Springer Oceanography

Shinya Shimokawa
Tomokazu Murakami
Hiroyoshi Kohno *Editors*

Geophysical Approach to Marine Coastal Ecology

The Case of Iriomote Island, Japan

Springer

Springer Oceanography

The Springer Oceanography series seeks to publish a broad portfolio of scientific books, aiming at researchers, students, and everyone interested in marine sciences. The series includes peer-reviewed monographs, edited volumes, textbooks, and conference proceedings. It covers the entire area of oceanography including, but not limited to, Coastal Sciences, Biological/Chemical/Geological/Physical Oceanography, Paleoceanography, and related subjects.

More information about this series at http://www.springer.com/series/10175

Shinya Shimokawa · Tomokazu Murakami · Hiroyoshi Kohno
Editors

Geophysical Approach to Marine Coastal Ecology

The Case of Iriomote Island, Japan

Springer

Editors
Shinya Shimokawa
Storm, Flood and Landslide
Research Division
National Research Institute for Earth
Science and Disaster Resilience
Tsukuba, Japan

Tomokazu Murakami
Storm, Flood and Landslide
Research Division
National Research Institute for Earth
Science and Disaster Resilience
Tsukuba, Japan

Hiroyoshi Kohno
Okinawa Regional Research Center
Tokai University
Yaeyama, Japan

ISSN 2365-7677 ISSN 2365-7685 (electronic)
Springer Oceanography
ISBN 978-981-15-1128-8 ISBN 978-981-15-1129-5 (eBook)
https://doi.org/10.1007/978-981-15-1129-5

This Springer imprint is published by the registered company Springer Nature Singapore Pte Ltd.
The registered company address is: 152 Beach Road, #21-01/04 Gateway East, Singapore 189721, Singapore

Preface

The presence of a coral reef, a sea grass bed of a shallow sea, a tidal flat, and a mangrove river will form a diverse tropical/subtropical coastal marine ecosystem and provide various benefits to humans. However, several coastal marine ecosystems are currently on the verge of crisis all over the world. In particular, the large-scale bleaching of coral due to the rising temperature of seawater observed in 2016 in all parts of the world is still fresh in our memory. Therefore, there is a strong demand for the global conservation of the coastal marine ecosystems and for environmental impact assessments.

Furthermore, the Iriomote Island, which is the target area of this book, has witnessed an increasing number of tourists in recent years after the inauguration of a new airport on the adjacent Ishigaki Island, and concerns regarding the impacts on the natural environment are intensifying. In addition, the Government of Japan is planning to register the area that includes the Iriomote Island (official name of the area: Amami-Oshima Island, Tokunoshima Island, the northern part of Okinawa Island, and Iriomote Island) as a world natural heritage site. Therefore, elucidating the relation between the ecology of organisms concerning the coastal marine ecosystem in the Iriomote Island, the physical environment corresponding to the ecological distribution of these organisms as well as the environmental impact assessment based on it is valuable immediate requirements.

To satisfy those requirements, investigations on the ecological distribution, observations of the ocean, atmosphere, and rivers, and numerical simulations have become important. Research with a comprehensive approach that combines the above has not necessarily been sufficient so far because close cooperation is required among specialists in different disciplines. Since 2011, the editors of this book, who are specialists in geophysics (Shinya Shimokawa and Tomokazu Murakaki) and ecology (Hiroyoshi Kohno), have been conducting a joint research on oceanographic observations during the occurrence of typhoons on the Iriomote Island, which is considered to be prone to typhoons. We noted that such a comprehensive research was possible, and we intended to contribute to the research on the conservation of the coastal marine ecosystem in areas, such as coral reefs, which are in a critically vulnerable situation.

Although the normal state and spatial environmental gradient related to coastal marine ecosystems, such as corals, are obviously important, the temporal environmental gradient of the oceanographic and meteorological phenomena and weather events, such as typhoons and monsoons, occurring in the region are also important. In particular, unlike tropical regions, subtropical regions, such as the Ryukyu Islands, which include the Iriomote Island, serve as the northern or southern limit for various marine species. In other words, for such species, a subtropical region offers marginal survival conditions. In such an area, the temporal environmental gradient of the oceanographic and meteorological phenomena can critically influence the distribution of marine species. For example, a strong wave and current due to a typhoon may destroy a coral. However, if no typhoon has occurred for a long time, the seawater temperature remains high, which may cause bleaching of the coral. Thus, all of the average state, spatial, and temporal environmental gradients are important to understand the physical environment, including the coastal marine ecosystem.

The Sakiyama and Amitori Bays in the Iriomote Island are the only nature conservation areas in the ocean environment in Japan. Because there is no land route to reach the area, the natural environment with minimal artificial influence is preserved and contains diverse coastal marine ecosystems such as coral. The Painta, Ubo, Ayanda, and Udara Rivers flow into the inner parts of the bays. The Amitori Bay is characterized by a sudden change in the depth of water and exhibits the second largest water depth in Okinawa. They yield various spatial environmental gradients. This area also provides a temporal environment gradient; the typhoons are surrounded by high-pressure systems in the Pacific Ocean in summer and by the northeasterly monsoon winds from continental anticyclones in winter. All these occurrences make the area very suitable to perform field research aimed at understanding the physical environment involving the coastal marine ecosystem.

For more than nine years since 2011, we have energetically promoted research on the physical environment involving the coastal marine ecosystems, such as coral, mainly in the Sakiyamawan–Amitoriwan Nature Conservation Area. We have benefited from the help of many researchers, and this book is the outcome.

In Part I, we introduce common basic items for specific research that are to be covered after Part II. It also describes the target areas of this book, including the Iriomote Island and the Sakiyamawan–Amitoriwan Nature Conservation Area, and their meteorological fields. Further, it provides an overview of the organisms that are studied in this book (coral, *Enhalus acoroides*, and *Coenobita brevimanus*), the observation equipment used for obtaining the physical environment data, and the numerical model used for replicating the oceanic flow and sediment transport fields. In Part II, we cover the physical environment of the Iriomote Island elucidated using various types of observation equipment and numerical models. It describes the oceanic flow field, sediment transport from rivers flowing into the inner parts of the bays, and underwater three-dimensional measurement using the SfM technique. Parts III and IV, which constitute the core of this book, present the research results obtained using a comprehensive approach by combining the investigations of ecological distribution, observations of ocean, atmosphere, and rivers, and

numerical simulations. In Part III, we study the relations between the distribution of the coastal marine ecosystem and the physical environments. The relation between the distribution of coral as well as *Enhalus acoroides* and the physical environment, particularly the relation between the oceanic flow and sediment transport fields, and a method to estimate the distribution of coral based on its physical environment are obtained. In Part IV, we study the relations between the physical environments and the retention and dispersion of eggs, larvae, seeds, and fruit of marine organisms. The bundles of *Acroporidae* that spawn simultaneously, the seeds and fruits of *Enhalus acoroides* whose male and female flowers bloom simultaneously and pollinate on the sea surface, and the larvae of *Coenobita brevimanus* simultaneously discharged on the seashore are described along with the relation of them with the physical environment, especially the oceanic flow field.

This book was completed not only with the help of each chapter's author but also with the help of several collaborators. We would like to extend our gratitude to all such collaborators. In particular, Prof. Dr. Ryohei Misumi and Mr. Ken Sakihara provided tremendous support while advancing the research work presented in this book. In addition, the research activities on which this book was based were supported by the following: the research project of National Research Institute for Earth Science and Disaster Resilience ("Development of the Water-Related Disaster Prediction Technology Based on Multi Sensing"); a research and education grant for Okinawa Regional Research Center, Tokai University ("Species Diversity and its Maintenance Mechanisms of the Coral Community in the Ocean Area Northwest of Iriomote Island"); and the joint study conducted by Tokai University and the National Research Institute for Earth Science and Disaster Resilience ("Elucidation of the Relationship Between Coastal Marine Ecosystem and Temporal–Spatial Gradient of Physical Environment in the Ocean Area Northwest of Iriomote Island"). We would like to take this opportunity to express our gratitude to all of them.

Tsukuba, Japan — Shinya Shimokawa
Tsukuba, Japan — Tomokazu Murakami
Yaeyama, Japan — Hiroyoshi Kohno
November 2019

Contents

Part I
Basic Information

Chapter 1
Iriomote Island, Japan

Shinya Shimokawa, Hiroyoshi Kohno, Akira Mizutani, Masako Nakamura and Wataru Doi

Abstract This chapter gives basic information on Iriomote Island, the target area of Iriomote Island. Sections 1.1–1.3 describes geophysical aspect of Iriomote Island: the geographical characteristics, Sakiyamawan–Amitoriwan Nature Conservation Area, and the meteorology, respectively. Sections 1.4–1.6 describe biological aspects of Iriomote Island: Corals, Tropical sea grass *Enhalus acoroides*, *Coenobita brevimanus*, respectively.

Keywords Iriomote Island · Sakiyamawan–Amitoriwan Nature Conservation Area · Coral · *Enhalus acoroides* · *Coenobita brevimanus*

S. Shimokawa (✉)
Storm, Flood and Landslide Research Division, National Research Institute for Earth Science and Disaster Resilience, Tsukuba, Japan
e-mail: simokawa@bosai.go.jp

H. Kohno · A. Mizutani
Okinawa Regional Research Center, Tokai University, Yaeyama, Japan
e-mail: hkohno@scc.u-tokai.ac.jp

A. Mizutani
e-mail: ma110267@tsc.u-tokai.ac.jp

M. Nakamura
School of Marine Science and Technology, Tokai University, Shizuoka, Japan
e-mail: mnakamura@tsc.u-tokai.ac.jp

W. Doi
Faculty of Fisheries, Kagoshima University, Kagoshima, Japan
e-mail: doiw@fish.kagoshima-u.ac.jp

S. Shimokawa et al. (eds.), *Geophysical Approach to Marine Coastal Ecology*, Springer Oceanography, https://doi.org/10.1007/978-981-15-1129-5_1

1.1 Geographical Characteristics of Iriomote Island

Shinya Shimokawa

Iriomote Island is located southwest of Japan at 24° 15–20′ N and 123° 40–55′ E on the East China Sea. It is around 100 km from the Tropic of Cancer and around 200 km from Taiwan, which is closer to it than Okinawa Island, Japan (Fig. 1.1a). The island belongs to the Ryukyu Islands, Okinawa, Japan and is included among the Yaeyama Islands with Ishigaki, Taketomi, Kohama, and other small islands.

Geologically, Iriomote Island belongs to the Ryukyu Arc. The Ryukyu Arc–Okinawa Trough system is one of several arc–backarc systems along the margin of the western Pacific and eastern Asia (Kizaki 1986). Ryukyu Arc is divided into the north, middle, and south Ryukyu arcs. The respective boundaries are the Tokara strait and the Miyako depression. The Yaeyama Islands, including Iriomote Island, belongs to the south Ryukyu Arc. The deepest area of the Okinawa Trough is at the submarine rift valley near the Yaeyama Islands: It reaches 2300 m depth.

The main target area of this book is the northwestern part of Iriomote Island (Fig. 1.1b), particularly Sakiyama and Amitori bays (Fig. 1.1c). Neither bay has a

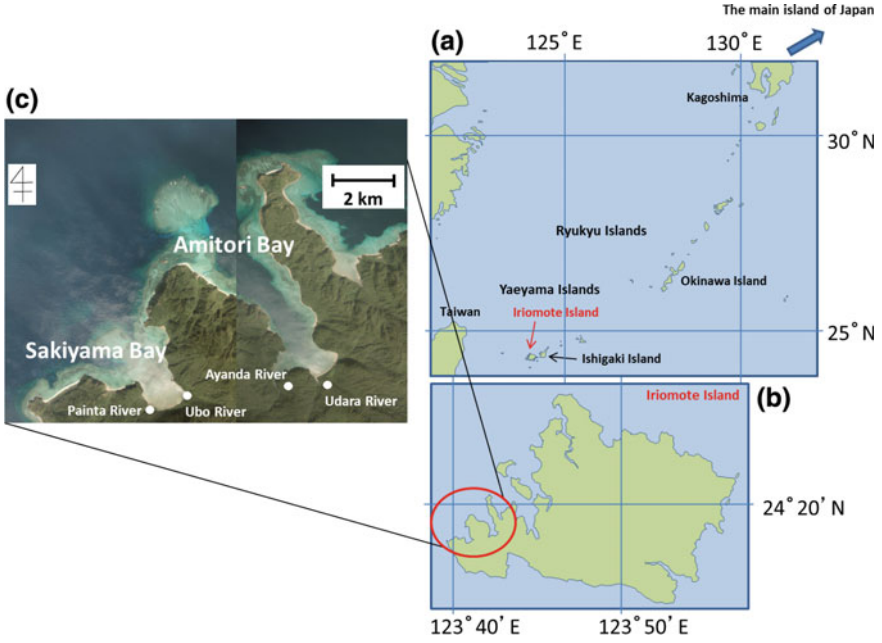

Fig. 1.1 Locations of Iriomote Island, Sakiyama Bay, and Amitori Bay. Our main study region lies on the southernmost tip of the Ryukyu Islands, Japan (**a**) and on Iriomote Island (**b**), and in the northwestern part of Iriomote Island, which includes the Sakiyamawan–Amitoriwan Nature Conservation Area (**c**) with its two bays: Sakiyama Bay and Amitori Bay. The white points in (**c**) show the river mouths of the four rivers: Painta, Ubo, Ayanda, and Udara rivers

road for access. Moreover, the bay perimeters are uninhabited. Consequently, the bays conserve widely diverse natural environments with little human impact. They belong to Sakiyamawan–Amitoriwan Nature Conservation Area. Details of the area are described in Sect. 1.2.

Iriomote Island, with an area of 290 km^2, is the second-largest island of Okinawa prefecture after Okinawa Island, with a shoreline length of 130 km. Over 90% of its mountainous topography is covered by subtropical virgin forest. Nevertheless, it has no steep mountains. The highest, Komi-dake, has height of 469.5 m. The second and third, Tedou-dake and Goza-dake, have respective heights of 441.2 and 420.4 m. These mountains overlap, with ridges extended, forming the complicated topography. Flatlands exist only around the mouths of the large rivers, as described later, and along the coast. They are used as residential areas, farmlands, and stock farms. The island has around 2000 residents.

On Iriomote Island, rivers are well developed by many rains and the complicated topography. Its many rivers and swamps include the 18.8 km long Urauchi River, which is the longest river in Okinawa prefecture. Nakama River is 7.45 km long. Urauchi River flows northwestward on the island from its southeastern origin. The Nakama River flows eastward from its southwestern origin. Many waterfalls are formed by their water flows and the complicated topography. Particularly Pinaisahra, which has the maximum height in Okinawa prefecture, and the Mariyudu and Kanbire waterfalls are famous as sightseeing spots. In addition, mangrove forests have developed around the riverbank near the river mouth. A mangrove forest in Nakama River is the largest in Japan.

The Ryukyu Islands, including Iriomote Island (Fig. 1.1a), have a subtropical marine climate, although they belong to humid subtropical climate (Cfa) according to the Köppen–Geiger Classification. Influenced by Kuroshio, among the world's major warm currents, and monsoons, among the world's major seasonal winds, annual precipitation reaches over 2000 mm. Subtropical rainforests thrive there. This is a distinguishing feature in the subtropical zone between 20–30° N and 20–30° S (Shimizu 2014). Much of the subtropical world is in the mid-latitude dry zone with low precipitation. Its vegetation is mostly dry series, including monsoon forest, savanna, steppe, and desert. Details of the atmospheric fields are presented in Sect. 1.3.

Many primitive characteristics have remained on Iriomote Island, home to characteristic and various animals and plants. One reason that the biome of the island has maintained its uniqueness up to the present day is that the Ryukyu Arc, including Iriomote Island, was separated from the Asian Continent and Japanese Islands (i.e., the Okinawa Trough was formed) at an early time: from Late Miocene to Early Pleistocene (Miki et al. 1990; Gallagher et al. 2015). It also was not submerged during the subsequent marine transgression periods (Ota 1998; Okamoto 2017). The Iriomote wildcat (*Prionailurus bengalensis iriomotensis*) and crested serpent eagle (*Spilornis cheela*) are designated as special national natural treasures. Also, the yellow-margined box turtle (*Cuora flavomarginata*), Kishinoue's giant skink (*Plestiodon kishinouyei*), Sakishima habu (*Protobothrops elegans*), and others are designated as national natural treasures. Most of those are

species endemic to Yaeyama Islands, although species endemic to Iriomote Island also exist, such as the Iriomote wildcat.

Moreover, the abundant ecosystems of Iriomote Island extend from land into the circumjacent coastal marine regions. Its biological environmental factors can be characterized mainly by coral reefs, seaweed forests, and tidelands. They can supply habitats and food for various living things beginning with fish and shellfish. Particularly, the coastal marine ecosystem in this region can be characterized mainly by the coral reefs which have been formed by sea level changes and accompanying glacial and interglacial cycles in Pleistocene and inflow of Kuroshio into the back arc side of the Ryukyu Arc at around 2 million years ago (Iryu et al. 2006). Details of the targets of this book, coral, *Enhalus acoroides* (a species of sea grass) and *Coenobita brevimanus* (a species of land hermit crab), are described, respectively, in Sects. 1.4, 1.5, and 1.6.

Iriomote Island has been designated as Iriomote Ishigaki National Park, Iriomote National Wildlife Sanctuary, and the Sakiyamawan–Amitoriwan Nature Conservation Area. Great efforts have been dedicated to the protection of the island's animals and plants and to the conservation of their habitats. Recently however, tourists are increasing rapidly with the opening of an airport on Ishigaki Island, neighboring Iriomote Island. Since then, concerns about nature destruction have intensified. In addition, the Government of Japan aims to register the region, including Iriomote Island (Amami-Oshima Island, Tokunoshima Island, the northern part of Okinawa Island, and Iriomote Island), on the world nature heritage list (Government of Japan 2017). Registration on the world heritage list can lead to the intensification of nature conservation and economic development through increased tourism, but such recognition can bring burdens to the natural environment with increased tourism. It should be recognized strongly that economic development by tourist businesses is based on nature conservation in the relevant area. For that purpose, assessments of environmental impact and consideration of measures for reducing environmental loads will be increasingly necessary for the area.

For environmental impact assessment, relations between distributions of living things there and physical environments of their habit must be investigated. This book specifically examines the relations among coastal marine ecosystems such as coral, sea grass, and land hermit crab, with the intention of providing basic information in support of assessments.

1.2 Sakiyamawan–Amitoriwan Nature Conservation Area

Hiroyoshi Kohno

The Sakiyamawan–Amitoriwan Nature Conservation Area is located at the westernmost end of Iriomote Island, the Yaeyama Islands, Okinawa-ken (Fig. 1.2). It consists of a marine area of 1077 ha including Sakiyama and Amitori bays opening

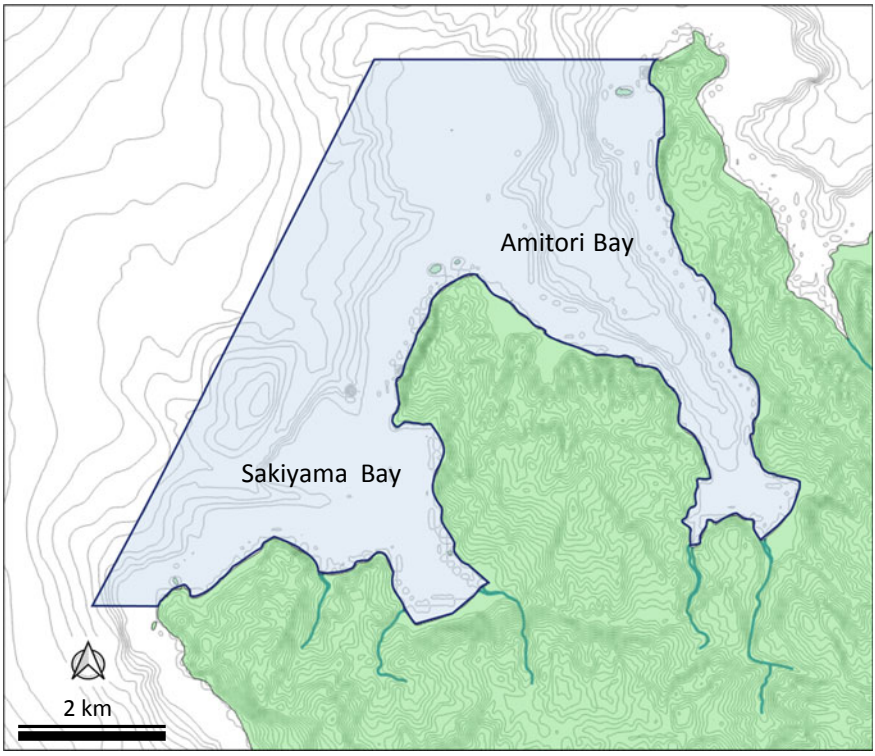

Fig. 1.2 Location of the Sakiyamawan–Amitoriwan Nature Conservation Area. Created by editing Geospatial Information Authority of Japan, 2017. http://fgd.gsi.go.jp/download/mapGis.php

to the northwest and their circumference, forming a clear sea area with rich natural beauty subject to little anthropogenic impact (Ministry of Environment 2015).

Originally, a sea area of 128 ha at the center of inner Sakiyama Bay was designated by the Environmental Protection Agency as the first marine Nature Conservation Area of Japan on June 28, 1983 (Marine Park Center Foundation 1984). Sakiyama Bay, about 1.3 km wide, with length of as little as 1.4 km, is shallow. It has a huge Galaxea colony at its mouth and well-developed reef-building coral assemblages to the center, comprising *Acropora*, *Montipora*, and *Porites*. Collectively, they form a complicated and rich marine biota in which one species among them is dominant and grows thickly at one place while several species are intermingled at other places. A submarine seaweed forest has formed at the bay head, mainly comprising communities of *E. acoroides*, a tropical sea grass for which the northern limit of distribution is the Yaeyama Islands. Furthermore, tidal flats around the mouth of small rivers flowing into the bay head are well developed (Ministry of Environment 2015). However, Amitori Bay is long and deep, with an inner bay environment that is affected little by waves and tidal

currents or by northeast monsoons in winter (see Sect. 1.3). Mangrove forests grow at the bay head, with the Udara and Ayanda rivers with developed tidal flats flowing there. This steep environmental gradient accompanying the length and water depth of the bay is also a notable characteristic of Amitori Bay. Moreover, coral assemblages are developed according to diverse environments inside the bay. There is a large-scale assemblage of *Leptoseris amitoriensis*, an endemic species of Iriomote Island in the depth of the bay. Consequently, both Sakiyama and Amitori bays have outstanding natural environments with rich natural character, large coral assemblages, seagrass meadows, and various species thriving and expanding. Those commonalities notwithstanding the bays differ in geographical features and environments inside the bays, so that a characteristic biocoenosis for each bay reflects their differences (Ministry of Environment 2015). The characteristics of physical environments such as waves, tidal current, and sediment transportation from rivers in both bays are described in Part 2.

This area including both bays and their circumference falls under "sea areas that sustain well-preserved nature including native flora and fauna, e.g., tropical fishes, corals, and seagrasses" prescribed by item 5, paragraph 1, Article 22 of Nature Conservation Act, so that it is necessary to conserve this whole area as a nature conservation area. For this reason, the area was re-designated as a nature conservation area with substantial expansion from the original Sakiyamawan Nature Conservation Area on February 17, 2015 (Ministry of Environment 2015).

Nature conservation areas are extremely important for the conservation of natural environments. However, it is fundamentally important to comprehend local ecosystems unerringly as well as the characteristics of flora and fauna with peculiarity, endemism, and scarcity, to preserve them for years to come. Therefore, the Ministry of Environment has been conducting surveys continuously since the re-designation (Marine Park Center Foundation 1984; Nature Conservation Bureau of Environmental Protection Agency 1990, 1999; Nature Conservation Bureau of Ministry of Environment and Kaiyu Ltd. 2004; Naha Natural Environmental Office of Ministry of Environment and Okinawa Regional Research Center of Tokai University 2016, 2017, 2018).

Coral assemblages and seagrass meadows, constituting the principal biological environment of the Sakiyamawan–Amitoriwan Nature Conservation Area, have so far undergone the influences of feeding damage of coral by a huge outbreak of corallivorous starfish, *Acanthaster planci* sensu lato, coral bleaching by high water temperature, and feeding damage to *E. acoroides* by green turtles *Chelonia mydas*. For example, although feeding damage of *A. planci* sensu lato was confirmed as only slight in Amitori Bay until 1979, a huge outbreak of this starfish arose in 1980–1982, entailing destructive feeding damage to the coral assemblage (Kohno 1984). These populations were assumed to have invaded Sakiyama Bay gradually since 1983, but they left without imparting severe feeding damage; a sound coral reef survived (Marine Park Center Foundation 1984; Ogura et al. 1989). This is one aspect of the background of Sakiyama Bay, designated as the first marine nature conservation area of Japan. The coral assemblages of Amitori Bay, once almost

annihilated but on the road to recovery, suffered from wide-area coral bleaching by high water temperatures in 1998, 2007, and 2016, so that coverage has been declining consistently. Especially, bleaching by high water temperature during the summer of 2016 extended to even the lower reaches of reef slopes. Coverage and egg production rates, as well as the number of Acropora larvae, recruited decreased extremely in 2017. Consequently, the influence of bleaching lasted into the following year. Details of coral issues are discussed in detail in Sect. 1.4. Medows of *E. acoroides* with monospecific or dominantly are formed scattered along the northwestern coast of Iriomote Island. However, the decline and disappearance of meadows because of overgrazing by herbivorous green turtles *C. mydas* are rapidly advancing recently (Takeyama et al. 2014; Naha Natural Environmental Office of Ministry of Environment and Okinawa Regional Research Center of Tokai University 2016, 2017, 2018). The ecological characteristics of habitat and sexual reproduction of *E. acoroides* at the northern limit of distribution and more detailed recent status are described in Sect. 1.5.

1.3 Meteorology of Iriomote Island

Akira Mizutani

Iriomote Island, located around 24° north latitude and 123° east longitude, is one island among the Yaeyama Islands of the southernmost end of the Ryukyu Islands from Kyushu, Japan to Taiwan. The Kuroshio Current (warm current) flows northward between Iriomote Island and Taiwan. By virtue of this warm current, heat flows into the atmosphere from the sea in winter, so that atmospheric temperatures do not drop to any great degree even during a souhing cold snap; also, heat flows into the sea from the atmosphere in summer, so that atmospheric temperature does not rise remarkably. The Okinawa province including Iriomote Island belongs to such a "subtropical oceanic climate." However, the Okinawa province is also governed by the East Asian monsoon belt: Northerly and southerly winds prevail, respectively, in winter and summer.

These two characteristics combine to produce the climate of the Okinawa province and Iriomote Island: roughly comprising a winter and a summer. In winter, high-pressure and low-pressure fronts pass over the Japanese Islands through the Sea of Japan by turns from the continent. The so-called pressure pattern of "high pressure to the west and the low pressure to the east" prevails when high-pressure areas cover the west side of the Japanese Islands and low-pressure areas cover the east side (Fig. 1.3a). Iriomote Island is located at the southern edge of this high-pressure zone; light rains fall; and a strong northeast winds are typical. Moreover, waves get higher and stormy weather comes from the sea under this pressure pattern. By contrast, in summer, the so-called pressure pattern of the "high

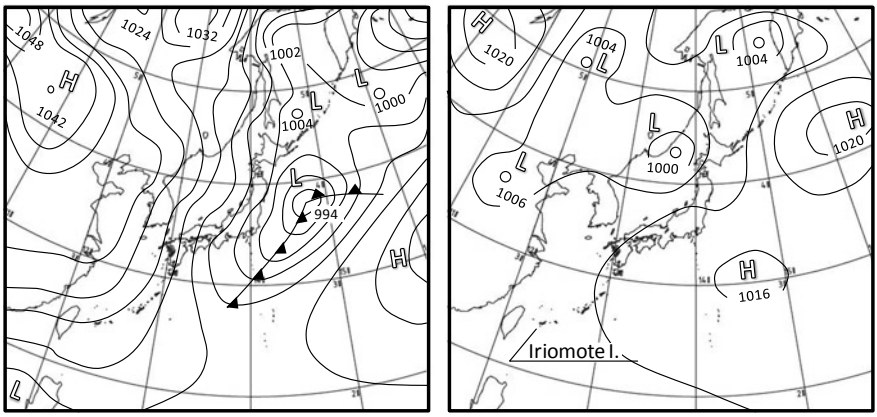

Fig. 1.3 Representative barometric arrangement in winter (**a**) and summer (**b**) around the Japanese archipelago. Created by editing Japan Meteorological Agency, 2014: https://www.data.jma.go.jp/fcd/yoho/hibiten/index.html

pressure to the south and the low pressure to the north" prevails when high-pressure areas cover the south side and low-pressure areas cover the north side, centering on the Japanese Islands (Fig. 1.3b). The weather on Iriomote Island is pleasant when covered by the Pacific High, and southeastern winds are typical.

However, a typhoon reverses the quiet oceanic conditions of a summer and produces a disturbance. Typhoons break out at around 15° north latitude to the east of the Philippines, move northwestward along the edge of the Pacific High, developing strength, and approach the Yaeyama Islands. The annual numbers of approaching typhoons at the Yaeyama Islands are reportedly 4.3 at Ishigakijima and 4.1 at Iriomote Island (Ishigakijima local meteorological observatory, Japan Meteorological Agency: http://www.jma-net.go.jp/ishigaki/obd/stats/sokuho/index_Stats.html browsed on August 3, 2018.).

This section presents an outline of a characteristic meteorological field in Iriomote Island based on records published during 2011–2016 (Mizutani and Sakihara 2012, 2014, 2015, 2016, 2017), from meteorological observations taken by the Okinawa Regional Research Center of Tokai University at Amitori Bay of Iriomote Island, providing research on natural and cultural sciences with environmental data.

Table 1.1 presents observation items and the outline of the equipment used. The observation equipment for atmospheric temperature and precipitation is placed on a lawn about 60 m inland from the seashore, and at the end of a pier for seawater temperature, wind direction, and wind velocity (Fig. 1.4). Seawater temperatures are measured on the sea bottom at about 3 m depth.

Table 1.1 Summary of observations

Observation equipment		Interval (min)
Data logger	CR1000 (Campbell)	
Air temperature and humidity	CVS-HMP155D-JM (Vaisala)	10
Precipitation	CTK-15PC-JM (Climatec)	10
Wind direction and speed	CYG-5106 (R. M. Young)	10
Water temperature	Tidvit v2 (Onset)	10

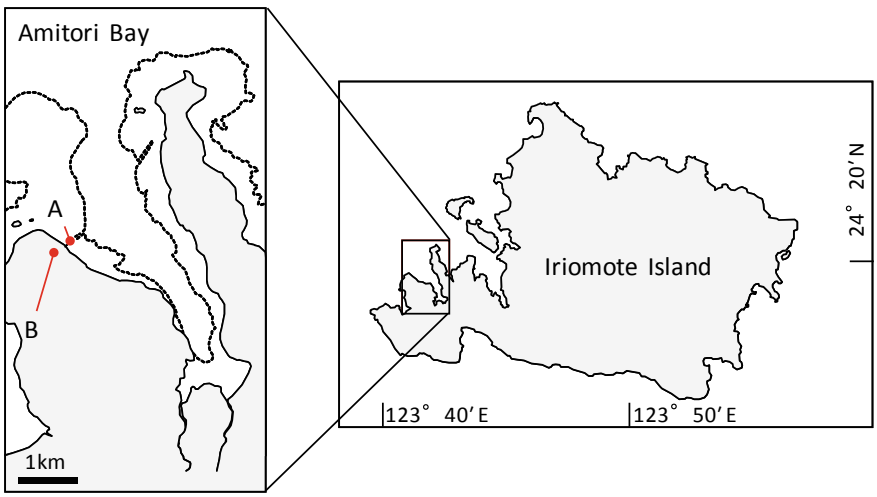

Fig. 1.4 Observation points at Amitori Bay, Iriomote Island: A, water temperature, wind direction, and speed; B, air temperature, humidity, and precipitation

For the period for which data were used, the observed values at Amitori for the six years of 2011–2016 indicate a warm and wet environment throughout the year, with average atmospheric temperature of 24.4 ± 4.44 SD °C (SD, standard deviation), average seawater temperature of 25.7 ± 2.72 SD °C, and average humidity of 80.1 ± 11.11 SD %. Annual accumulated rainfall was high, exceeding 1500 mm. Average wind velocity was 4.2 ± 2.83 SD m/s, and northeast and south–southeast winds prevailed, respectively, accounting for at 14.8 and 13.7% of all wind directions.

Seasonally, the lowest temperature was recorded in January, with a monthly average of 18.5 ± 2.44 SD °C. Subsequently, atmospheric temperatures rise gradually, becoming the highest in July to reach a monthly average of 28.9 ± 2.15 SD °C (Fig. 1.5). The seasonal change of seawater temperature was synchronizing mostly with atmospheric temperature, the lowest at a monthly average of

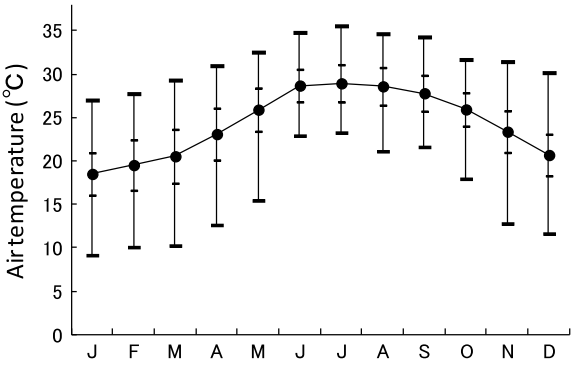

Fig. 1.5 Monthly change of the air temperature on the Amitori Bay, Iriomote Island (2011–2016): circle, average; shorter line, SD; longer line, minimum and maximum

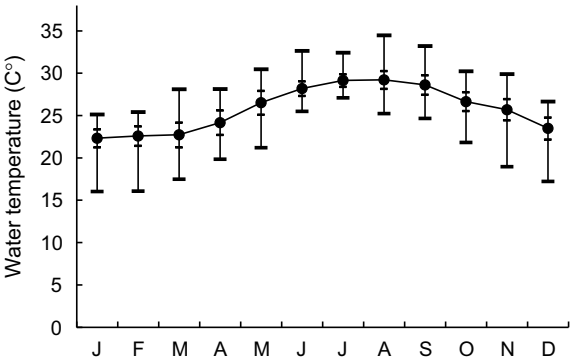

Fig. 1.6 Monthly change of the water temperature on the Amitori Bay, Iriomote Island (2011–2016): circles, average; shorter lines, SD; longer lines, minimum and maximum

22.3 ± 1.06 SD °C in January, and the highest at a monthly average of 29.2 ± 1.06 SD °C in August (Fig. 1.6). The ranges of atmospheric temperature and seawater temperature for the six years were 9.1–35.6 °C and 16.0–34.5 °C, respectively.

During October–March, northeast winds prevailed at 19–24% (Fig. 1.7), with wind velocity showing a monthly average of 4.7 ± 2.74 SD to 5.9 ± 3.01 SD m/s (Fig. 1.8). During April–August, south–southeast winds prevailed at 17–26%, with lower wind velocities showing a monthly average of 3.0 ± 1.50 SD to 3.9 ± 2.25 SD m/s. However, the maximum wind velocity (averaged for 10 min) of this period was over 20 m/s in July–October, where all cases were related to approaching typhoon phenomena.

Rainfall exceeded 100 mm almost every month. Especially, monthly accumulated rainfall of 200 mm or more was often recorded in August related to approaching typhoons and in May of the "rainy season" with enhanced rainfall under the influence of a stationary front stretching from east to west in the Okinawa

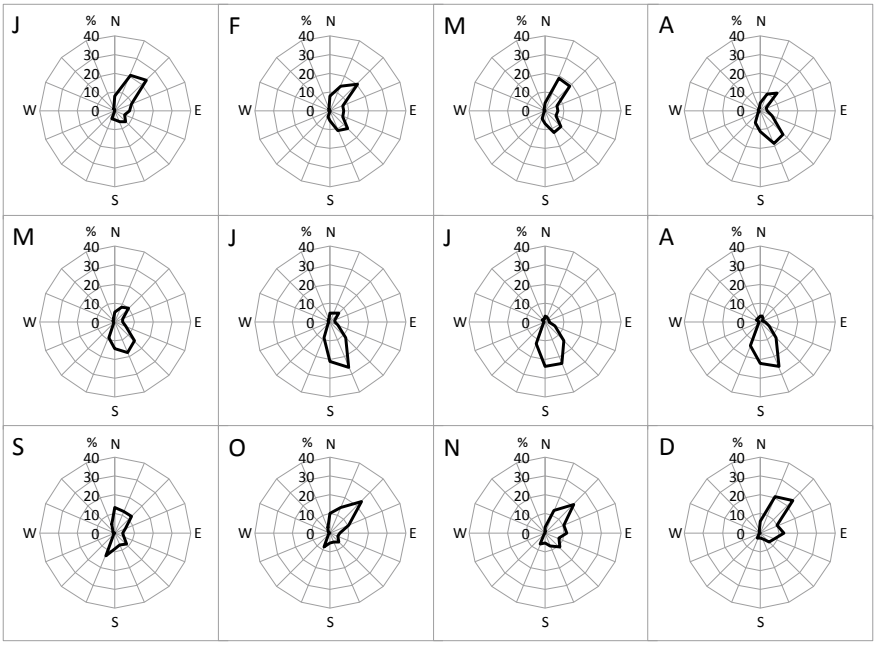

Fig. 1.7 Monthly change of the wind direction on the Amitori Bay, Iriomote Island (2011–2016)

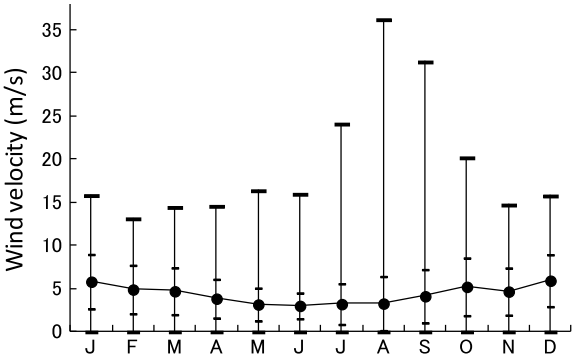

Fig. 1.8 Monthly change of the wind velocity on the Amitori Bay, Iriomote Island (2011–2016): circles, average; shorter lines, SD; longer lines, minimum and maximum

province (Fig. 1.9). Humidity was higher than 80% in April–September, and conversely lower than 80% in October–March (Fig. 1.10).

A total of 26 typhoons approached Iriomote Island during 2011–2016 (annual average: 4.3 times) (Ishigakijima Local Meteorological Observatory, Japan Meteorological Agency: http://www.jma-net.go.jp/ishigaki/obd/stats/sokuho/index_Stats.html browsed on August 3, 2018.). The maximum instantaneous

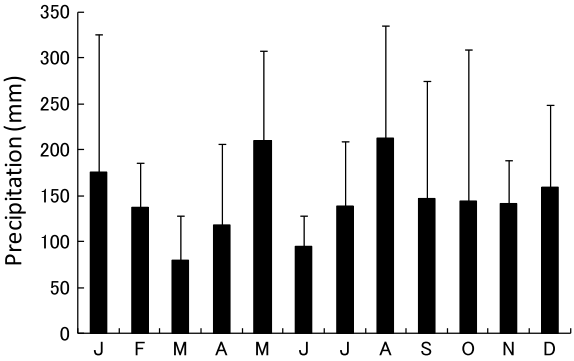

Fig. 1.9 Monthly change of the rainfall on the Amitori Bay, Iriomote Island (2011–2016): rod, average; bar, SD

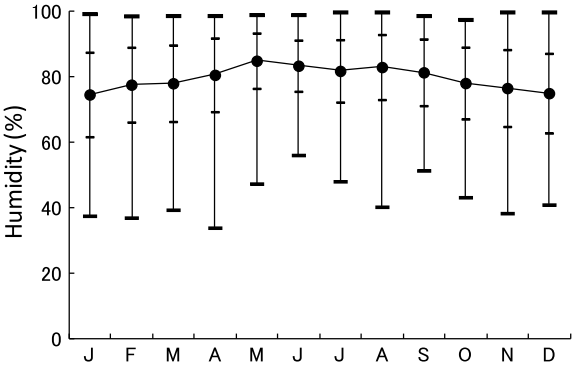

Fig. 1.10 Monthly change of the humidity on the Amitori Bay, Iriomote Island (2011–2016): circles, average; shorter lines, SD; longer lines, minimum and maximum

wind velocity of each year was recorded during the approach and passage of these typhoon storms. Noteworthy strong typhoons were No. 13 (SOUDELOR), No. 15 (GONI), and No. 21 (DUJUAN), all in 2015, with respective recorded maximum wind speeds and maximum instantaneous wind velocities of 28.9 m/s and 51.7 m/s, 36.3 m/s and 50.7 m/s, and 31.4 m/s, and 53.3 m/s (Fig. 1.11). Daily accumulated precipitation at the closest approach exceeded 100 mm in each case (Iriomote observation point, Ishigakijima local meteorological observatory, Japan Meteorological Agency: http://www.data.jma.go.jp/obd/stats/etrn/index.php). Furthermore, a storm and high surf occurred together and seawater temperatures dropped temporarily. Consequently, short-term disturbances in marine environments including seawater temperature are characteristic events of meteorological and oceanographic phenomena in this area, which has frequently approaching typhoons.

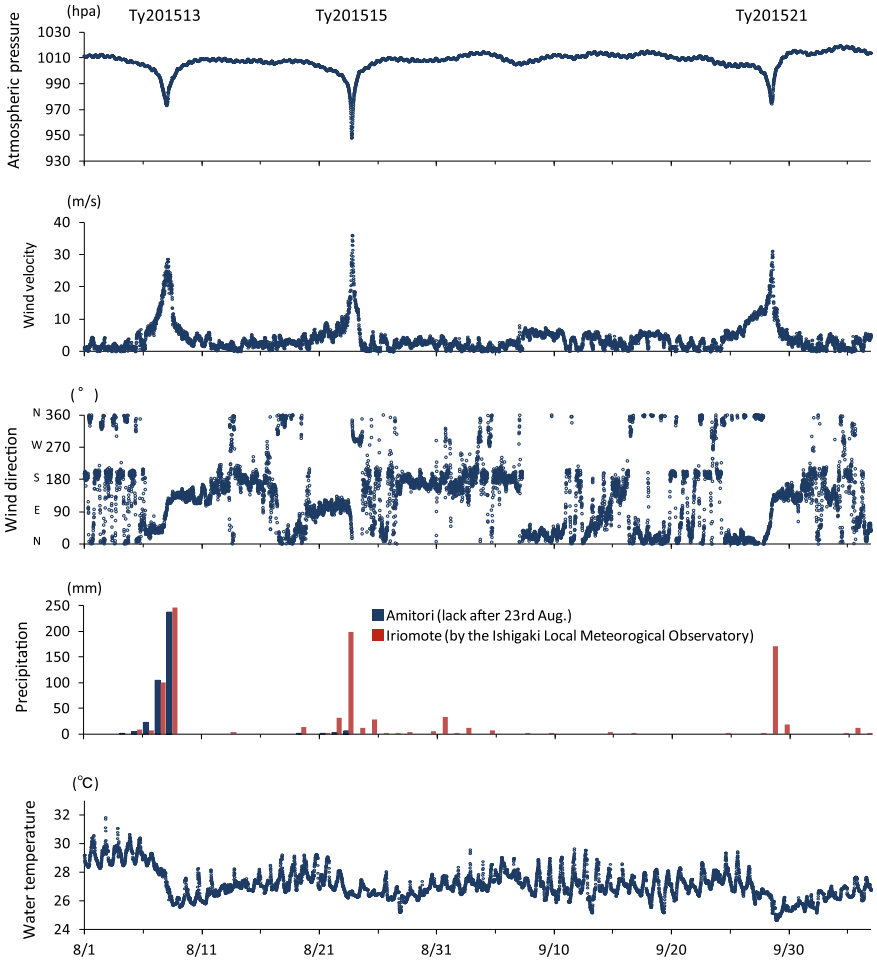

Fig. 1.11 Weather change with the three typhoons on the Amitori Bay, Iriomote Island in 2015. Precipitation on Iriomote was created by the author based on Ishigaki Local Meteorological Observatory, 2015. http://www.data.jma.go.jp/obd/stats/etrn/index.php?prec_no=91&blockno=47917&year=2015&month=09&day=&view= (referred from Mizutani and Sakihara 2016)

1.4 Corals in Amitori and Sakiyama Bay

Masako Nakamura and Hiroyoshi Kohno

1.4.1 State in the 1980s

Around Iriomote Island, outbreaks of corallivorous starfish, *A. planci* sensu lato have been observed since the beginning of the 1970s, e.g., Hatoma Island in 1972–1973 and Sekisei Lagoon in 1974–1981. In contrast, in Amitori and Sakiyama bays, damage caused by *A. planci* sensu lato has not been observed until the 1980s. First observations were made at the Amitori Bay entrance in the summer 1980. Branching acroporid corals and *Echinopora lamellosa* communities have largely been fed by *A. planci* sensu lato. Then, in the following year, coral communities in Amitori Bay were devastated by these corallivorous starfish. Only a part of the west side of the bay has not been affected (Marine Park Center Foundation 1984). In Sakiyama Bay, *A. planci* sensu lato were first observed 1983. In December 1983, *A. planci* sensu lato were observed, but only slightly, in Amitori Bay. However, fewer than 20 individuals per site were observed in Sakiyama Bay and northeastern areas of the entrance of Amitori Bay. The number of *A. planci* sensu lato in Sakiyama Bay increased toward August in 1984 (Ogura et al. 1989). According to the increase in the number of *A. planci* sensu lato, coral cover in Sakiyama Bay decreased in 1984. Coral communities in the northeast part of the bay showed 30–70% coverage in December 1983 (Marine Park Center Foundation 1984), but coral cover decreased to less than 10% in shallow waters in July (Ogura et al. 1989). Most of *Acropora* spp. were eaten in shallow lagoon to reef slope areas while branching and plate *Millepora* spp. and Fungiidae were not (Ogura et al. 1989). Ogura et al. (1989) estimated that the travel distance of *A. planci* sensu lato might be 0–15 m per day when there are corals on which to feed; they can travel for 6–10 h without prey. Moreover, the populations of *A. planci* sensu lato, which appeared in Amitori Bay in 1980, have been estimated as migrating to other areas along two routes, moving southwestward and northeastward (Marine Park Center Foundation 1984, Fig. 1.12). By the southwestward route, the population went to Sakiyama Bay and further west, passing through shallow areas of Yona-son or Sakuramizo. Along the northeastward route, the population followed reef edges and slopes to the end (closed-off section) of Amitori Bay and approached the bay entrance at the other bank (Sabasaki-side), subsequently proceeding northeastward.

In 1985, no *A. planci* sensu lato were observed; coral cover was less than 5% in most areas of Amitori and Sakiyama bays (Yokochi et al. 1991). Three years later, in 1988, coral cover started to increase from the entrance to the end of Amitori Bay (Habe 1989). In 1988, coral cover reached approx. 10%. In the entire bay, *A. planci* sensu lato was the dominant coral genus.

Fig. 1.12 Estimated migration routes at the beginning of the 1980s in Amitori and Sakiyama bays. Red arrows indicate southwestward route and blue arrows indicate northeastward route. A star shows the first area, where damage by *A. planci* sensu lato was first observed. Rewrite from Marine Park Center Foundation (1984). Map data© 2018 Google

The outbreaks of *A. planci* sensu lato in Amitori and Sakiyama Bays in the 1980s were expected to be attributable to numerous larvae entering the areas at the moment of increase of phytoplankton caused by heavy rainfall in 1976–1977 (Marine Park Center Foundation 1984).

1.4.2 State in the 1990s

At the end of the 1980s, coral cover in Sakiyama Bay varied from 1.1 to 21.6% (Nature Conservation Bureau 1999). However, 12.5–51.5% coral cover was observed in 1997, suggesting a recovery after the *A. planci* sensu lato outbreaks in the 1980s (Nature Conservation Bureau 1999). Dominant coral genera differed among sites in the bay. The highest coral cover was observed at S-RF.1, dominated mainly by branching *Acropora* spp. (Fig. 1.13). S-RS.1 and 2 were dominated by *Montipora* spp. and *Pocillopora* spp. Branching *Acropora* spp. were also dominant at S-EG.1. The lowest coral cover was observed at S-EW.1, where branching *Porites* spp. were the dominant coral genus.

Coral communities in Amitori Bay showed high cover: as much as those observed in Sakiyama Bay, which were 10–60% in 1995 (Nature Conservation Bureau 1999). Different from Sakiyama Bay, all of Amitori Bay were mostly dominated by *Acropora* spp. *Montipora* spp. were the second-most abundant coral genus in the bay. With lower cover, *Porites* spp. were also observed in the bay. At A-WM.1 and A-BB.1, acroporid coral covers decreased to 1997, although those at three other sites increased, especially at A-ER.1 and St.5; covers in 1997 were four

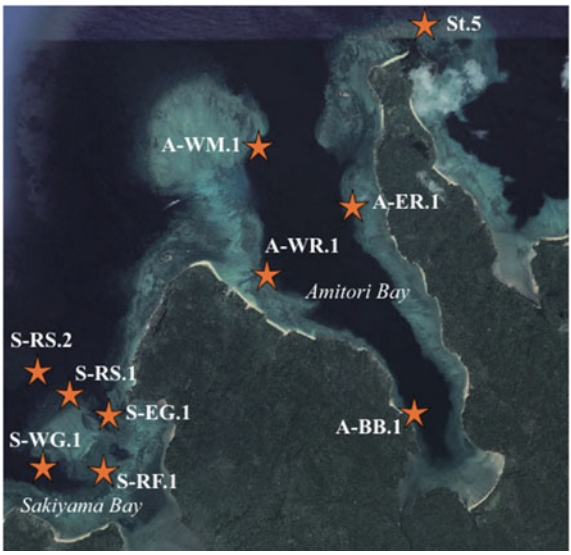

Fig. 1.13 Survey sites for observation of "State of Sakiyama Bay Nature Conservation Area, Okinawa, Japan" done by Nature Conservation Bureau, Environment Agency (Nature Conservation Bureau 1999). Map data© 2018 Google

times higher than those in 1995. As a result, coral cover was high in the bay, but it varied from 30 to 70% in 1997.

However, abnormally high seawater temperatures caused mass bleaching of corals in Ryukyu Islands, including Iriomote Is. More than 90% of branching *Acropor*a spp. and *Millepora* spp. in the lagoon in Sakiyama Bay died because of bleaching in 1998 (Nature Conservation Bureau 1999). However, coral communities at S-RS.1 and 2 were less affected.

1.4.3 State in 2000s

In spite of large coral losses because of mass bleaching in 1998, coral communities in Amitori and Sakiyama Bays already showed high coral cover and species diversity at the beginning of this century. Spot Check Surveys in 2004 found 40–60% coral cover at the entrances of the Sakiyama and Amitori Bays (Ministry of the Environment and Kaiyu 2004). In Sakiyama Bay, the maximum coral cover was 55%. The east side of Amitori Bay showed 60% coral cover. The communities in Sakiyama Bay consisted mainly of *Acropora* spp. and *Montipora* spp. In Amitori Bay, coral community compositions differed among areas. Reef flats around the entrance and middle of the bay were dominated by a mix of branching and table corals. Table corals were dominant at reef edges and reef slopes. In the shallow lagoon, there were mainly massive corals such as Poritidae. At the end of the bay, a mix of poritid corals, and branching and corymbose acroporids were major constituents of the community.

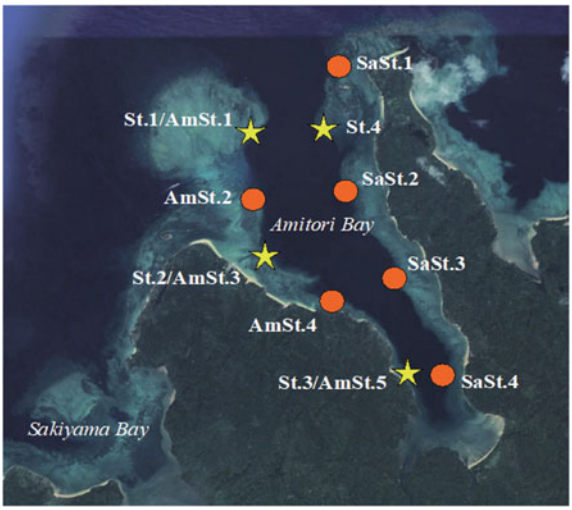

Fig. 1.14 Survey sites for coral community and larval supply in 2000s. Yellow stars show sites for 2005–2008 but St.3 was set from 2006. Orange circles show sites from 2016. AmSt.1, AmSt.3, and AmSt.5 were identical to St.1–3 in surveys for 2005–2008. These were also the same as A-WM.1, A-WR.1, and A-BB.1 in Fig. 1.13, respectively. Map data© 2018 Google

In Amitori Bay, surveys of the coral community and larval supply were conducted at four sites in the bay during 2005–2007; similar surveys have been done at nine sites since 2016 (Fig. 1.14). Coral cover was higher toward the bay entrance. The coral communities were acroporid-dominant, with low cover of pocilloporid corals (Fig. 1.15a). In addition, poritids were more abundant toward the end of the bay. These were also observed in 2016. For larval supply, estimated with artificial settlement plates, dominant coral families were also acroporid corals in 2006–2007. No relation between cover and larval supply for acroporid corals was observed, but a more detailed survey conducted in 2016 showed positive correlation between the cover and larval supply for acroporid corals (Nakamura et al. 2017; see Sect. 15). With results of the numerical model, designated as the Coastal ocean Current Model (Murakami et al. 2015a, see Sect. 2), the resilience and sustainability of acroporid coral communities in Amitori Bay can rely on self-seeded larvae (Nakamura et al. 2017; see Sect. 15). However, in the summer of 2016, mass coral bleaching was observed in the Yaeyama region, including Iriomote Island, where 94.3% of corals in Sakiyama Bay were observed to be bleached (Biodiversity Center of Japan 2017). In Amitori Bay, water temperatures exceeded 30 °C for more than 20 days in August 2016, resulting in high bleaching rates (Murakami et al. 2017; Fig. 1.15b). High seawater temperatures greater than 30 °C were not observed only at surface areas, but to 30 m depth. Coral bleaching rates were greater than 50% down to 20 m depth. The maximum rate, 86.6%, was observed at 15 m depth. Moreover, 32.5% of corals were bleached, even at 30 m depth. After mass bleaching in 2016, the percentage cover and larval supply of acroporid corals decreased drastically in Amitori Bay in 2017.

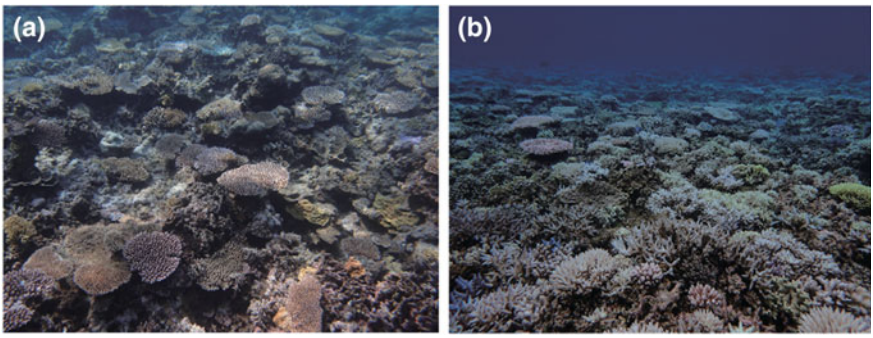

Fig. 1.15 Coral communities in Amitori Bay. **a** Before the bleaching event in 2016, **b** at the bleaching event in August 2016

1.4.4 Into the Future

Coral communities in both Amitori and Sakiyama Bays have experienced several severe disturbances since the 1980s. During this time, corals were again bleached dramatically. They died because of abnormal high seawater temperatures during summer 2016. In Sakiyama Bay, high bleaching rates were also observed in 2017 (84.7%; Biodiversity Center of Japan 2018). However, some areas had high density of juvenile corals of less than 5 cm in Amitori Bay, as observed from a qualitative survey in 2017. These data suggest the future recovery of coral communities, which we have also observed for the last 30 years after disturbances. Therefore, it is necessary to monitor the changes and dynamics of coral communities in these bays from biological, chemical, and physical aspects to elucidate the processes of recovery after severe disturbances. Such data can help to establish protective measures for the resilience and sustainability of coral communities and can help to propose new approaches for the protections based on scientific knowledge.

1.5 Tropical Sea Grass *Enhalus acoroides* in Sakiyama and Amitori Bays

Akira Mizutani and Hiroyoshi Kohno

Sea grasses, a unique group of flowering plants that have adapted to marine environments, fulfill a key role in coastal ecosystems and coral reefs in tropical regions. *E. acoroides* (Fig. 1.16) belongs to the monotypic genus in the family Hydrocharitaceae (den Hartog and Kuo 2006). This species is widespread

Fig. 1.16 Monospecific meadow of *Enhalus acoroides* in Sakiyama Bay

throughout the Indian Ocean and tropical areas of the western Pacific (den Hartog 1970). The species are found in brackish water canals down to lower intertidal and subtidal zones on mud, sand, and coral substrates (Green and Short 2003). It is a very large sea grass plant, with leaf length exceeding one meter and leaf width reaching two centimeters. Actually, *E. acoroides* is a perennial and dioeciously as other sea grass species.

In common with sea grasses, shoot recruitment is the addition of new individuals to the population occurring through vegetative production of new shoots through clonal growth or by the recruitment of new genets through production and germination of seed or fragments (Duarte et al. 2006). In large *E. acoroides*, the average specific recruitment rate of new shoots into population is 0.26 $year^{-1}$, which is less than one-tenth that of small species (Hemminga and Duarte 2000; Duarte et al. 2006). Conversely, shoot mortality of the species is low: less than 0.5 $year^{-1}$ (Hemminga and Duarte 2000; Duarte et al. 2006). Reportedly, the shoot life span is ten years (Vermaat et al. 1995).

Sexual reproduction of *E. acoroides* is an obligate surface-pollination (Ackerman 2006). During low tide in the daytime, male flowers detach underwater and float to the water surface (Fig. 1.17a). When they are freely drifting with the wind, they might encounter female inflorescence that remains attached to the

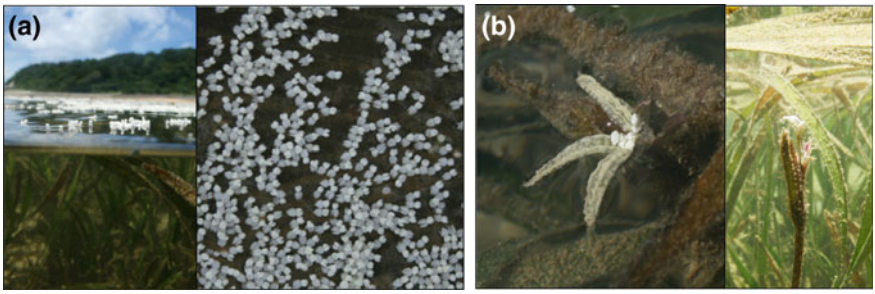

Fig. 1.17 Sexual reproduction of *Enhalus acoroides*. **a** Male flowers floating surface; **b** female flower capturing male flowers

submerged plat via a long spiral peduncle (Fig. 1.17b). As the tide begins to fill, female flowers close and male flowers are taken in. Pollen is transferred in a dry state from anther to stigma, and infructescence develops underwater. In the tropics, flowering occurs throughout the year (Bronus and Heijs 1986; Kenyon et al. 1997; Verheij and Erftemeijer 1993; Rattanchot et al. 2016; Rollón et al. 2003).

In Japan, *E. acoroides* are distributed only in the Yaeyama Islands, a southern group of Ryukyu Islands (Ohba and Miyata 2007; Toma 1999); this region is the northernmost habitat of the species. Based on recent genetic analyses, the Yaeyama and northeast Philippines populations are genetically similar, which suggests that recruitment occurs from the northeast Philippines to Yaeyama by the Kuroshio Current (Nakajima et al. 2014).

In the Yaeyama Islands, monospecific meadows of *E. acoroides* stand only around Iriomote Island: They are nonexistent or rare in other islands (Ohba and Miyata 2007; Toma 1999). At Iriomote Island, meadows of this species with monospecific or dominantly in multispecific habitats are distributed patchily along the complicated coast. Suitable conditions of waves and currents have been extracted, indicating that D. L. −0.76 m deep, 25–32 cm in $H_{1/3}$, 11–19 cm/s in bottom flow, and 0.1–0.3 cm in residual current (Nakase et al. 2015). The northernmost population has a clearer flowering phenology; the flowering period is limited to May–November, with a peak during July–September (Mizutani et al. in press). The period from flowering to fruit dehiscence is about 70–100 days; the proportion of fruit dehiscence is less than 10% (Mizutani et al. in press). The number of seeds per fruit is mainly 5–10 (Murakami et al. 2014a, 2015b, c), being similar to other populations in tropical areas (Bronus and Heijs 1986; Rollón et al. 2003).

Meadows of *E. acoroides* in this region provide spawning and feeding habitats for various animals (e.g., Tsuchiya 1981; Nakamura et al. 2003; Nakamura and Sano 2004, 2005), they are used as fishing grounds. Furthermore, simultaneous flowering and biodiversity of meadows are useful for instruction in environmental

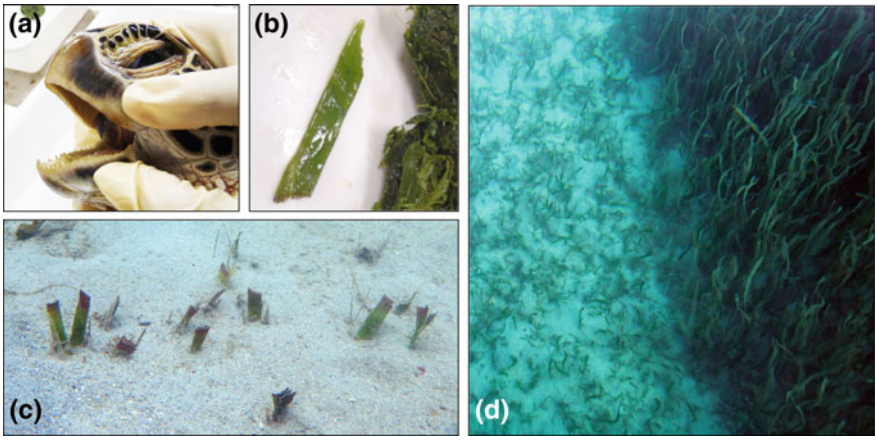

Fig. 1.18 *Enhalus acoroides* grazed by the green turtle *Chelonia mydas*. **a** Green turtle bill; **b** sharply cut leaves of *E. acoroides* detected in green turtle stomach contents; **c** and **d** shoots and meadow grazed by green turtles

education and ecotourism. However, *E. acoroides* meadows around Iriomote Island have declined and disappeared rapidly. A decrease of 38% was estimated to have occurred up to 2013 in comparison with areas analyzed in 1974 based on aerial photographs (Takeyama et al. 2014). The cause is overgrazing by increased population of the herbivorous green turtle *C. mydas* (Fig. 1.18). Leaves of *E. acoroides* with grazing scars are extremely short. The tips are cut linearly. Although shoots that have been grazed will not soon die, if they continue for more than a year, then the shoot growth will begin to decline as the width of the leaves narrows (Mizutani et al. 2016).

In the case of a meadow in Sakiyama Bay, grazing started between 2004 and 2011, thereafter expanding to the whole meadow by 2018, based on aerial photographs (Fig. 1.19) (Naha Natural Environmental Office of Ministry of Environment and Okinawa Regional Research Center of Tokai University 2018). In Amitori Bay, leaves of *E. acoroides* were markedly shorter in 2009 (Nakamura 2010), indicating grazing by the green turtle (Mizutani et al. 2016). Eventually, the whole meadow disappeared completely in 2013 (Takeyama et al. 2014). Changes in the meadow structure influence fish communities (Nakamura 2010; Kohno et al. unpublished).

Along the intricate coast of Iriomote Island, the possibility of dispersion and enrollment among meadows is estimated as very low because the floating period of seeds is extremely short (Murakami et al. 2014a, b, 2015c). If the fruit is separated before seed release, the floating period is much longer (Murakami et al. 2015b). However, it is necessary that the fruits develop for 8 weeks or more to germinate

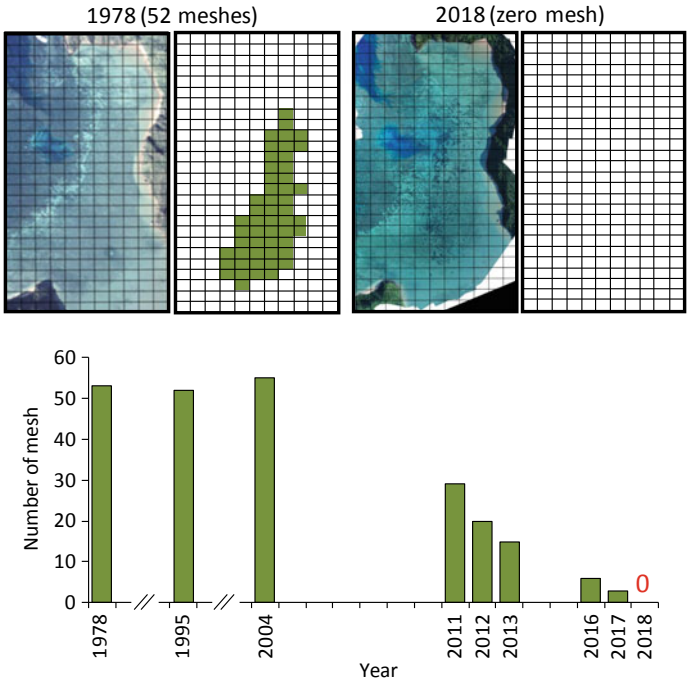

Fig. 1.19 Change of the *Enhalus acoroides* meadow in Sakiyama Bay. Aerial photographs were separated by a 50 × 50 m mesh. Meshes that appeared uniformly in green were counted each year. The photograph in 1978 was reprinted from Geospatial Information Authority of Japan, 2010. The photograph in 2018 was taken by authors using an unmanned aerial vehicle (altered from Naha Nature Environmental Office of Ministry of Environment and Okinawa Regional Research Center of Tokai University 2018)

those seeds (Murakami et al. 2015b). Therefore, the probability of recovery of meadow disappearance by sexual reproduction is inferred as very low.

The effectiveness of measures using steel piles as an obstacle to turtle grazing was assessed in Sakiyama Bay in 2016. The results showed that turtle grazing pressure was alleviated and leaf length increased in the area with a pile height of 50 cm and a pile intervals of 50 cm, wholeness no effect was observed in areas with shorter piles (20 cm) or with piles spaced at wider intervals (100 cm) (Fig. 1.20) (Mizutani et al. 2018).

To prevent extinction of the northernmost population of *E. acoroides* and its ecosystem, it is necessary to consider concrete measures such as the installation of turtle exclusion cages (Fourqurean et al. 2010) and a management system to control the appropriate population size of the green turtle.

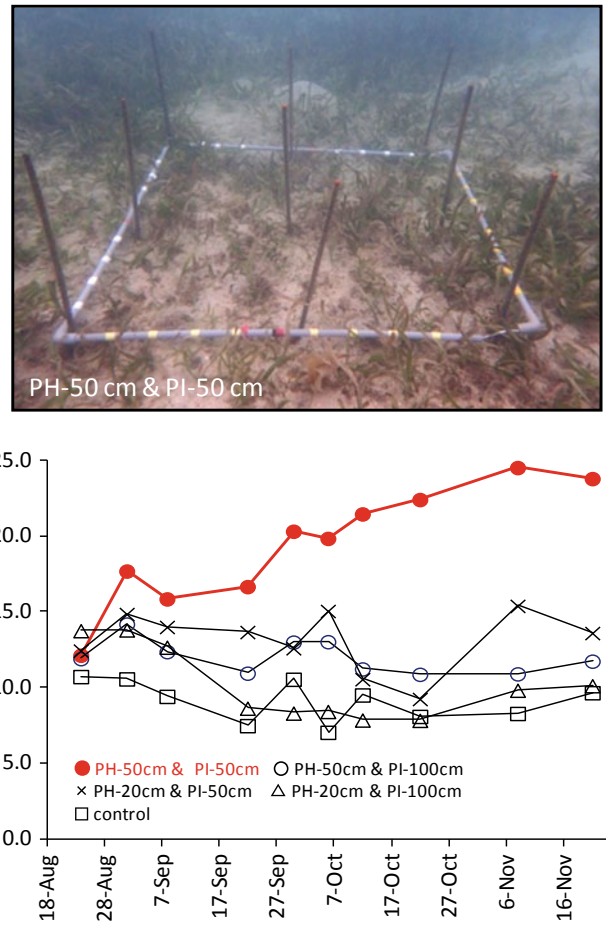

Fig. 1.20 Changes in leaf length of the *Enhalus acoroides* over time for different steel pile configurations. Piles with nine millimeters in diameter were installed in quadrates (1 × 1 m) on grazed area in Sakiyama Bay in 2016. Averages of a total 45 shoots with three-quadrates by each pile setting are shown. PH, pile height; PI, pile interval. Leaf length of *E. acoroides* on an area not grazed by turtles in Sakiyama Bay is about 50 cm and more (altered from Mizutani et al. 2018)

1.6 *Coenobita brevimanus* in Sakiyama and Amitori Bays

Wataru Doi and Hiroyoshi Kohno

1.6.1 General Biology of Land Hermit Crabs

Land hermit crabs are anomuran decapod crustaceans of the family Coenobitidae comprising the genus *Coenobita* Latreille 1829, with 17 species, and the monogeneric coconut or robber crab, *Birgus latro* Linnaeus, 1767 (Mclaughlin et al. 2010; Rahayu et al. 2016). They are adapted to desiccating environments, inhabiting small islands or narrow coastal strips worldwide in subtropical and tropical areas. Several species have the functional ability to live in a range of habitats, from rainforest to arid scrubland, but their penetration of these habitats is limited to small islands or to narrow coastal strips (Hartnoll 1988). Ovigerous females of coenobitid crabs must approach the shore when their embryos hatch because the larvae must spend their planktonic stage in the sea (Hartnoll 1988).

As with aquatic hermit crabs such as Paguroidea, *Coenobita* crabs and early juveniles of *B. latro* carry gastropod shells as a mobile home. The shells protect the spirally curved and less calcified abdomen of the crab from mechanical damage and desiccation. The shells also provide an egg chamber in which female hermit crabs attach the eggs to their pleopods during the period between laying and hatching. To grow larger, with increased survival rates, and producing more embryos, land hermit crabs must exchange suitably sized shells. They are adversely affected by a shortage of shells. Therefore, the availability of the shell resources can determine the abundance and size structure of *Coenobita* crabs in terrestrial environments.

1.6.2 Coenobita brevimanus *in Yaeyama Islands*

The species examined herein, *C. brevimanus* Dana, 1856 (Fig. 1.21) is widely distributed throughout the Indo-Pacific area. Individuals have been recorded from the East African mainland in the westernmost and from Tua-motu Islands (French Polynesia) in the easternmost (Hartnoll 1988; Vannini and Ferretti 1997). The Japanese archipelago's southern islands are the extreme northern limit of the biological range of *C. brevimanus*. In Japan, this species is found on Miyako and Yaeyama islands (Okinawa Prefectural Board of Education (OPBE), 1987; Fujita 2017), although they are rare in other areas. They are found in Okinawa Island, but no detailed information about them has been reported (OPBE 2006). A single ovigerous female was collected on Chichijima Island in the Bonin Islands (Sanda et al. 2018). Numerous individuals of *C. brevimanus* can be found especially in Iriomote and

Fig. 1.21 Photograph of a land hermit crab *Coenobita brevimanus* on Iriomote Island

Ishigaki islands. Of the six species of *Coenobita* found on the Ryukyu Islands (24–31° N, 121–131° E) (Nakasone 1988; Asakura 2004), *C. brevimanus*, which inhabits coastal forests (Hamasaki et al. 2017), is the most terrestrially adapted species along with *C. cavipes*. However, rather than in natural habitats, the abundance of *C. brevimanus* is higher in the settlement area and the abandoned village and adjacent beach (Kosuge and Kohno 2010; Mizutani and Kohno 2012; Mizutani et al. 2012; Nio et al. 2014; Doi et al. 2019, unpublished data).

Distributions of land hermit crabs in the Yaeyama Islands were studied frequently in the 2010s (Fig. 1.22). On Nakanokamishima, an uninhabited remote

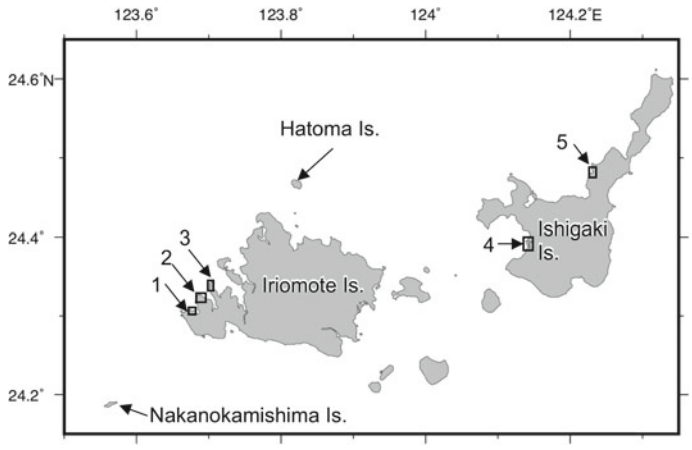

Fig. 1.22 Locations of distributions of land hermit crabs studied in Yaeyama Islands: 1 Sakiyama Village (Doi et al. unpublished data); 2 Amitori village (Doi et al. 2019) and Beach (Mizutani and Kohno 2012); 3 Sabazaki Beach (Mizutani and Kohno 2012); 4 Nagura Amparu (Hamasaki et al. 2017); 5 Itona Village (Kosuge and Kohno 2010)

island, of 41 adult crabs observed, 17 were identified as *C. brevimanus* (Kohno et al. 2012). Along the coasts around Ishigaki Island and Iriomote Island, 5961 and 1136 crabs were captured, respectively, through visual surveys and using bait traps (Fujikawa et al. 2017). The proportions of *C. brevimanus* were extremely low, only 0.7 and 1.1%, respectively. In coastal forests and along the shoreline of the sandbank in the Nagura Amparu, a brackish estuary system with a tidal flat on Ishigaki Island, a few *C. brevimanus* were collected only in the coastal forest, but not at the shoreline (Hamasaki et al. 2017). Tsuru et al. (2018) investigated the distributions of land hermit crabs on Hatoma Island using the same method as that reported by Fujikawa et al. (2017). Of the 1326 crabs from the coastal and inland habitats of the island, 6.5% were *C. brevimanus*. Consequently, in these natural habitats, the relative densities of *C. brevimanus* were lower than those of other *Coenobita*.

1.6.3 C. brevimanus *in Northwestern Iriomote Island*

In contrast, more *C. brevimanus* were found in some villages on Yaeyama Islands. Around the low-density residential area of Itona Village on Ishigaki Island, 69 *C. brevimanus* individuals were collected along with 117 *C. cavipes* (Kosuge and Kohno 2010). On the southern coast and at a settlement area on Hatoma Island, 27 and 84 individuals of *C. brevimanus* were collected, respectively (Mizutani et al. 2012). Nine individuals of *C. cavipes* were collected in the settlement area. As in Itona and Hatoma Villages, the numbers of *C. brevimanus* individuals were the same or larger than congeners; the size structures with the gastropod shell use patterns were comparable (Fig. 1.23; Mizutani and Kohno 2012; Doi et al. 2019; unpublished data). In Amitori Bay, on the sandy beach on the western coast and in Amitori Village, many crabs grow to greater than 20 mm in palm width (PW) using the turban snail *Turbo* (*Marmarostoma*) *argyrostomus* and the Persian purpura *Purpura persica* (Mizutani and Kohno 2012; Doi et al. 2019) as transportable shelters. In Sabazaki Beach, on the eastern coast of Amitori Bay, where no villages have been founded, the crawling crabs consisted mainly of smaller individuals of less than 20 mm PW using the smooth moon turban *Lunella cinerea* (Mizutani and Kohno 2012). In Sakiyama Village, most crabs were smaller. Those crabs mainly used the murex snail *Mancinella armigera* (Doi et al. unpublished data). In Hatoma Village, rather than that of Sabazaki and Sakiyama, larger crabs with *T. (M.) argyrostomus* appeared. Those gastropod shells in Fig. 1.23 are consumed as edible species from a prehistoric age to the present. The shells have been excavated from shell middens in the ruins of these areas (Hirata et al. 1973; Amitori Remains and Katura Shell Mound Excavation Team 2007). Amitori was inhabited by a maximum of 200 people between the seventeenth century and 1971. It is now used as a research center of Tokai University. The shell middens were created by hunter–gathers who stayed temporarily at a campsite during the fourth–fifth centuries and by the former residents during the existence of the village (Amitori Remains and Katura Shell Mound Excavation Team 2007). The discarded shells of the

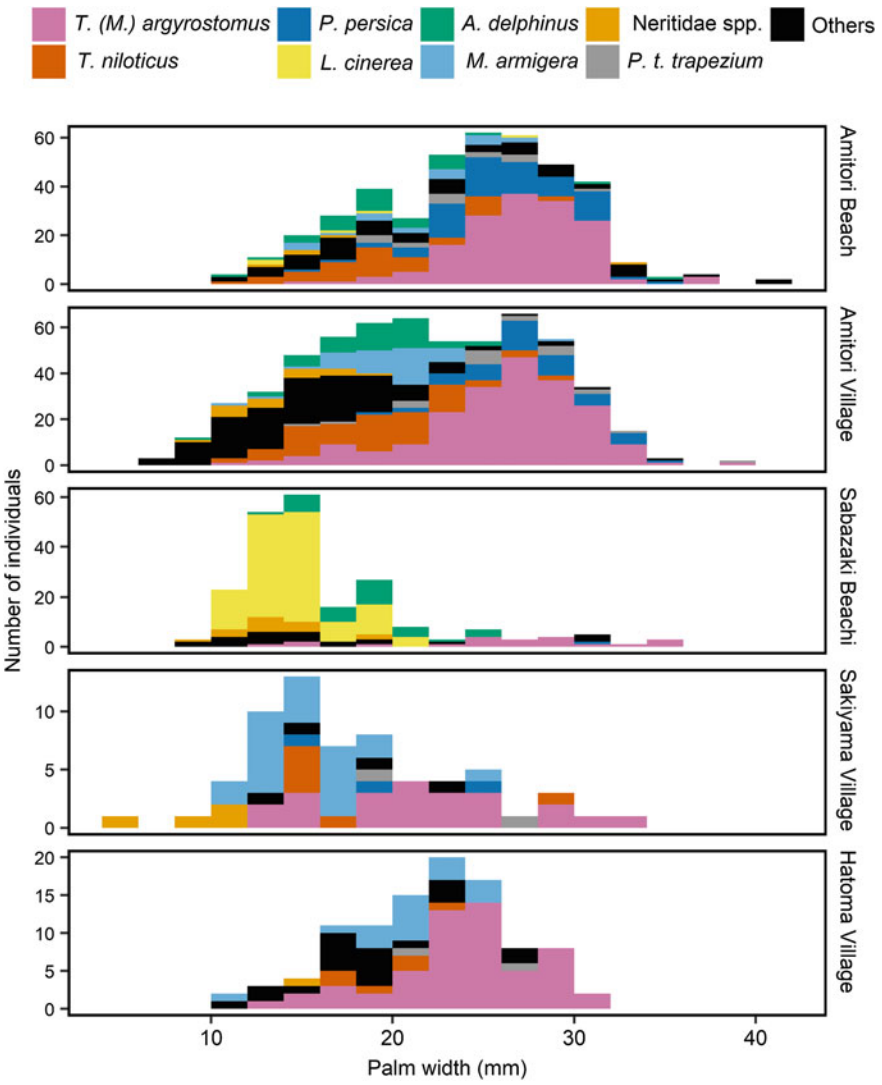

Fig. 1.23 Size frequency distributions (palm width) of the land hermit crab *Coenobita brevimanus* with gastropod shells in the Yaeyama Islands (Mizutani and Kohno 2012; Mizutani et al. 2012; Doi et al. 2019; unpublished data). The gastropod species are turban snail *Turbo* (*Marmarostoma*) *argyrostomus*, the Persian purpura *Purpura persica*, the common delphinula *Angaria delphinus*, the species of family Neritidae, the smooth moon turban *Lunella cinerea*, the murex snail *Mancinella armigera*, the trapezium horse conch *Pleuroploca trapezium*, and other species of gastropods and artificial materials. Data source: Mizutani and Kohno (2012), Mizutani et al. (2012), Doi et al. (2019)

gastropods on the land, which were caught by the sojourners and the residents from coral reefs in Amitori Bay, might be shell resources for *C. brevimanus*. In Sakiyama Village, which was founded in 1756 and which was abandoned in 1945, residents were forcibly transferred and engaged in agriculture. Shell middens were not found. In Sabazaki Beach, on the eastern coast of Amitori Bay, settlement by humans was not confirmed. Therefore, the artificial shell supply is limited in Sakiyama and Sabazaki. In Hatoma Village, some managers of local guesthouses discarded shells such as *T.* (*M.*) *argyrostomus* (Mizutani et al. 2012).

Although methods and efforts of sampling differed in those studies, the results might indicate that shell availability probably contributes to the size difference and abundance of *C. brevimanus* in the Yaeyama Islands. The hermit crabs in Amitori, which use shells of edible marine gastropods such as *Turbo* (*M.*) *argyrostomus*, likely discarded by the former residents, grow to be larger than crabs living on an adjacent uninhabited island and an inhabited village without discarded shell middens and piles. The population of the crabs in Amitori Bay, consisting of many large crabs, could be a source population through dispersal during pelagic larval stages in their northern marginal ranges because larger females might have higher fecundity, i.e., releasing more larvae. To consider the conservation of this near-threatened species (Ministry of the Environment, Japan 2018) showing the fragmented distributions, it is necessary to elucidate the dynamics of recruitment and the transition from the sea to land of juveniles through the pelagic larval stages. However, the coastal habitats where recruitment into terrestrial habitats occurs were still unknown for the present species. Hamasaki et al. (2018) collected and identified a total of 576 early juveniles of coenobitids using PCR–RFLP techniques, of which 0.7% were *C. brevimanus*. Spatiotemporal patterns of larvae releasing behavior of this species were studied in Amitori Beach (Nio et al. 2019). The starting points of the larval dispersals were determined. Therefore, the results of the ecological studies can be input as data in a numerical simulation of the larval dispersal using an ocean model (Murakami et al. 2014b; Sect. 16). Such results are expected to contribute to greater understanding of the dynamics of recruiting and source-sink relations of *C. brevimanus* larvae.

References

Ackerman JD (2006) Seagrass sexual reproduction. In: Larkum AWD, Orth RJ, Duarte CM (eds) Seagrasses: biology, ecology and conservation. Springer, The Netherland, pp 89–109

Amitori Remains and Katura Shell Mound Excavation Team (2007) Study of Amitori Remains and Katura Shell Mound. Amitori Remains and Katura Shell Mound Excavation Team, Hadano

Asakura A (2004) Recent topics on taxonomy of hermit crabs from Japanese waters – family Coenobitidae. Aquabiology 26:83–90 (in Japanese with English abstract)

Biodiversity Center of Japan (2017) Preliminary report on monitoring 1000 coral reef survey in fiscal year 2016. The Ministry of the Environment, Japan

Biodiversity Center of Japan (2018) Preliminary report on monitoring 1000 coral reef survey in fiscal year 2017. The Ministry of the Environment, Japan
Bronus JJWM, Heijs FML (1986) Production and biomass of the seagrass *Enhalus acoroides* (L.f.) royal and its epiphytes. Aquat Bot 25:21–45
den Hartog C (1970) The sea-grasses of the world. North Holland Publishing Company, Amsterdam
den Hartog C, Kuo J (2006) Taxonomy and biogeography of seagrasses. In: Larkum AWD, Orth RJ, Duarte CM (eds) Seagrasses: biology, ecology and conservation. Springer, The Netherland, pp 1–23
Doi W, Mizutani A, Yoshioka M, Kawai K, Kohno H (2019) Aspects of local population and gastropod shell use of the land hermit crab *Coenobita brevimanus* (Decapoda: Anomura) in Amitori, an abandoned village on Iriomote Island, Japan. Jpn J Benthol 73:75–83 (in Japanese with English abstract)
Duarte CM, Fourqurean JW, Krause-Jensen D, Olesen B (2006) Dynamics of seagrasses stability and change. In: Larkum AWD, Orth RJ, Duarte CM (eds) Seagrasses: biology, ecology and conservation. Springer, The Netherland, pp 271–294
Fourqurean JW, Manuel S, Coates KA, Kenworthy WJ, Smith SR (2010) Effects of excluding sea turtle herbivores from a seagrass bed: overgrazing may have led to loss of seagrass meadows in Bermuda. Mar Ecol Prog Ser 419:223–232
Fujikawa S, Hamasaki K, Sanda T, Ishiyama N, Tsuru T, Dan S, Kitada S (2017) Distributional characteristics of terrestrial hermit crabs along the coasts of Ishi-gakijima Island and Iriomotejima Island, Ryukyu Archipelago, Japan. Bull Biogeogr Soc Jpn 71:25–38 (in Japanese with English abstract)
Fujita Y (2017) Fauna of decapod crustaceans in Minna-jima Island, Miyako Island Group, southern Ryukyu Islands, Japan. Bull Miyakojima City Mus 21:91–110
Gallagher SJ, Kitamura A, Iryu Y, Itaki T, Koizumi I, Hoiles PW (2015) The Pliocene to recent history of the Kuroshio and Tsushima currents: a multi-proxy approach. Prog Earth Planet Sci 2. https://doi.org/10.1186/s40645-015-0045-6
Government of Japan (2017) Nomination of Amami-Oshima Island Tokunoshima Island the Northern Part of Okinawa Island, and Iriomote Island for inscription on the World Heritage List, 275 pp
Green EP, Short FT (2003) World atlas of seagrasses. Prepared by the UNEP World Conservation Monitoring Centre. University of California Press, Berkeley
Habe (1989) Studies on the conservation and management of coral reefs and the control of *Acanthaster planci* juveniles. Grant-in-Aid for General Scientific Research (A) (Project/Area Number: 60440017)
Hamasaki K, Fujikawa S, Sanda T, Tsuru T, Kitada S (2017) Distributions of land hermit crabs (Decapoda: Coenobitidae) on the coast of the tidal lagoon, Nagura Amparu, on Ishigakijima Island, Japan. Biogeography 19:142–149
Hamasaki K, Fujikawa S, Iizuka C, Sanda T, Tsuru T, Imai H, Kitada S (2018) Recruitment to adult habitats in terrestrial hermit crabs on the coast of Ishigakiji-ma Island, Ryukyu Archipelago, Japan. Invertebr Biol 137:3–16
Hartnoll RG (1988) Evolution, systematics, and geographical distribution. In: Burg-gren WW, McMahon BR (eds) Biology of the land crabs. Cambridge University Press, Cambridge, pp 6–54
Hemminga MA, Duarte CM (2000) Seagrass ecology. Cambridge University Press, Cambridge
Hirata Y, Nakasone Y, Shokita S (1973) Mollusks, crabs, prawns in Okinawa. Hu-dokisya, Naha (in Japanese)
Iryu Y, Matsuda H, Piller WE, Quinn TM, Mutti M (2006) Introductory perspective on the COREF Project. Island Arc 15:393–406
Kenyon RA, Conacher CA, Poiner IR (1997) Seasonal growth and reproduction of *Enhalus acoroides* (L.f.) Royle in a shallow bay in the Western Gulf of Carpentaria, Australia. J Mar Freshw Res 48:335–342
Kizaki Y (1986) Geology and tectonics of the Ryukyu Islands. Tectonophyics 125:193–207

Kohno H (1984) Hands of the devil reached Iriomote Island – *Acanthaster planci*. Marine Science Museum, vol 14, no 2, 2–3 (in Japanese)

Kohno H, Mizutani A, Murakoshi M, Nio T, Kosuge T (2012) Land hermit crabs in the seabirds colony of Nakanokamishima Island, South Ryukyus, Japan. Biol Mag Okinawa 50:49–59 (in Japanese with English abstract)

Kosuge T, Kohno H (2010) Preliminary study of shell-utilization by land hermit crabs *Coenobita brevimanus* Dana and *C. cavipes* Stimpson in Itona, Ishigaki Island, Ryukyu Islands, Japan. Nankiseibutsu 52:113–118 (in Japanese)

Marine Park Center Foundation (1984) Commission report to Ministry of Environment. Emergency survey report on conservation measures for Sakiyamawan nature conservation area, 134 pp (in Japanese)

Mclaughlin PA, Komai T, Lemaitre R, Rahayu DL (2010) Annotated checklist of anomuran decapod crustaceans of the world (exclusive of the Kiwaoidea and families Chirostylidae and Galatheidae of the Galatheoidea) part I – Lithodoidea, Lomisoidea and Paguroidea. Raffles Bull Zool 23(Suppl):5–107

Miki M, Matsuda T, Otofuji Y (1990) Opening mode of the Okinawa Trough: paleomagnetic evidence from the South Ryukyu Arc. Tectonophysics 175:335–347

Ministry of Environment (2015) Sakiyamawan – Amitoriwan nature conservation area certificate of designation, a maintenance plan document, 10 pp (in Japanese)

Ministry of the Environment, Government of Japan (2018) Red List 2018. https://www.env.go.jp/nature/kisho/hozen/redlist/RL2018_5_180604.pdf. Accessed 11 June 2018

Mizutani A, Kohno H (2012) Distribution of *Coenobita brevimanus* in Amitori, Iri-omote Island. Study Rev Iriomote Isl 2011:30–39 (in Japanese)

Mizutani A, Sakihara K (2012) The weather observation of ORRC (Okinawa Regional Research Center), Tokai University in 2011 – wind direction and speed, air temperature, humidity, precipitation, and water temperature in Amitori Bay, and water temperature and salinity in Urauchi River. Study Rev Iriomote Isl 2011:84–95 (in Japanese)

Mizutani A, Sakihara K (2014) The weather observation of ORRC (Okinawa Regional Research Center), Tokai University in 2012 to 2013 – wind direction and speed, air temperature, humidity, precipitation, and water temperature in Amitori Bay, and water temperature and salinity in Urauchi River. Study Rev Iriomote Isl 2013:62–83 (in Japanese)

Mizutani A, Sakihara K (2015) The weather observation of ORRC (Okinawa Regional Research Center), Tokai University in 2014 – wind direction and speed, air temperature, humidity, precipitation and water temperature in Amitori Bay, and water temperature and salinity in Urauchi River. Study Rev Iriomote Isl 2014:68–79 (in Japanese)

Mizutani A, Sakihara K (2016) The weather observation of ORRC (Okinawa Regional Research Center), Tokai University in 2015 – wind direction and speed, air temperature, humidity, precipitation and water temperature in Amitori Bay, and a summary of typhoons TY1513, 1515 and 1521. Study Rev Iriomote Isl 2015:74–84 (in Japanese)

Mizutani A, Sakihara K (2017) The weather observation of ORRC (Okinawa Regional Research Center), Tokai University in 2016 – wind direction and speed, air temperature, humidity, precipitation and water temperature in Amitori Bay. Study Rev Iriomote Isl 2016:75–84 (in Japanese)

Mizutani A, Nio T, Kosuge T, Kohno H (2012) Shell-utilization by the land hermit crab, *Coenobita brevimanus* Dana, 1852 (Crustacea, Anomura, Coenobitidae) on Hatomajima Island, Southern Ryukyus, Japan – the relationship between large individuals and shells of *Turbo (Marmarostoma) argyrostomus*. Biol Mag Okinawa 50:73–82 (in Japanese with English abstract)

Mizutani A, Sakihara K, Kawata N, Kohno H (2016) Influence of feeding of *Chelonia mydas* on *Enhalus acoroides* – verification by leaf slicing back experiment and progress observation of meadows with feeding scars. Study Rev Iriomote Isl 2015:42–51 (in Japanese)

Mizutani A, Inoue H, Inoue T, Takenaka Y, Kohno H (2018) Asseing the effectiveness of measures for alleviating grazing pressure by Green Turtles on tropical seagrass *Enhalus acoroides*. Study Rev Iriomote Isl 2017:33–45 (in Japanese with English abstract)

Mizutani A, Inoue H, Tamamoto M, Kitahara Y, Fujiyoshi M, Murakami T, Nakase K, Kohno H (in press) Sexual reproduction of the tropical seagrass *Enhalus acoroides* (L.f.) Royle around Iriomote Island, Japan: flowering period, fruit set, and fruit survival at the northern limit of the species. Jpn J Conserv Ecol (in Japanese with English abstract)

Murakami T, Kohno H, Iwasaki A, Kuramochi T, Shimokawa S, Kimura K (2014a) Particle tracking analysis based on ecological investigation of seed of *Enhalus acoroides* in Amitori Bay, Iriomote Island, Japan. Ann J Civ Eng Ocean B3 70:I_1074–I_1079 (in Japanese with English abstract)

Murakami T, Kohno H, Mizutani A, Jinno M, Shimokawa S (2014b) Particle tracking analysis of larvae of land hermit crab *Coenobita brevimanus* in Amitori Bay, Iri-omote Island, Japan. Ann J Civ Eng Ocean B2 70:1136–1140 (in Japanese with English abstract)

Murakami T, Kohno H, Yamamoto Y, Mizutani A, Shimokawa S (2015a) Numerical simulation for initial dynamic state of bundle based on field observations of Acroporidae spawning in Amitori Bay, Iriomote Island, Japan. J Jpn Soc Civ Eng B2 71:1225–1230 (in Japanese with English abstract)

Murakami T, Kohno H, Tamamoto M, Mizutani A, Shimokawa S (2015b) Numerical analysis of *Enhalus acoroides* fructification dispersal in the northwestern sea area of Iriomote Island, Japan. Ann J Civ Eng Ocean B2 71:I_1351–I_1356 (in Japanese with English abstract)

Murakami T, Kohno H, Tamamoto M, Mizutani A, Shimokawa S (2015c) Numerical analysis of *Enhalus acoroides* seed dispersal in the northwestern sea area of Iriomote Island, Japan. Ann J Civ Eng Ocean B3 70:I_1074–I_1079 (in Japanese with English abstract)

Murakami T, Kohno H, Nakamura M, Tamamura N, Mizutani A, Shimokawa S (2017) Bleaching of vertically distributed corals in Amitori Bay of Iriomote Island. J Jpn Soc Civ Eng B3 73:881–886 (in Japanese with English abstract)

Naha Natural Environmental Office of Ministry of Environment and Okinawa Regional Research Center of Tokai University (2016) 2015 Survey report on decline factors of *Enhalus acoroides* at Sakiyamawan – Amitoriwan nature conservation area in Iriomote Island, 33 pp (in Japanese)

Naha Natural Environmental Office of Ministry of Environment and Okinawa Regional Research Center of Tokai University (2017) 2016 Survey report on decline factors of *Enhalus acoroides* at Sakiyamawan – Amitoriwan nature conservation area in Iriomote Island, 37 pp (in Japanese)

Naha Natural Environmental Office of Ministry of Environment and Okinawa Regional Research Center of Tokai University (2018) 2018 Report on consideration of measures for decline factors of *Enhalus acoroides* at Sakiyamawan – Amitoriwan nature conservation area in Iriomote Island, 64 pp (in Japanese)

Nakajima Y, Matsuki Y, Lian C, Fortes MD, Uy WH, Campos WL, Nakaoka M, Nadaoka K (2014) The Kuoshio current influences genetic diversity and population genetic structure of a tropical seagrass, *Enhalus acoroides*. Mol Ecol 23:6029–6044

Nakamura Y (2010) Patterns in fish response to seagrass bed loss at the southern Ryukyu Islands, Japan. Mar Biol 157:2397–2406

Nakamura Y, Sano M (2004) Is there really lower predation risk for juvenile fishes in a seagrass bed compared with an adjacent coral area? Bull Mar Sci 74:477–482

Nakamura Y, Sano M (2005) Comparison of invertebrate abundance in a seagrass bed and adjacent coral and sand areas at Amitori Bay, Iriomote Island, Japan. Fish Sci 71:543–550

Nakamura Y, Horinouchi M, Nakai T, Sano M (2003) Food habits of fishes in a seagrass bed on a fringing coral reef at Iriomote Island, southern Japan. Ichthyol Res 50:15–22

Nakamura M, Murakami T, Khono H, Noda W, Matsushita Y, Mizutani A (2017) Coral recruitment on a local scale in Amitori Bay, Iriomote Island, estimated by settlement plates and numerical analysis. J Jpn Soc Civ Eng B2 72:1279–1284 (in Japanese with English abstract)

Nakase K, Murakami T, Ukai A, Mizutani A, Shimokawa S, Kohno H (2015) Distribution analysis of *Enhalus acoroides* vegetation using hydraulic model, in the northwest sea area of Iriomote Island, Okinawa, Japan. Ann J Civ Eng Ocean B3 71:I_957–I_962 (in Japanese with English abstract)

Nakasone Y (1988) Land hermit crabs from the Ryukyus, Japan, with a description of a new species from the Philippines (Crustacea, Decapoda, Coenobitidae). Zool Sci 5:165–178

Nature Conservation Bureau (1999) State of Sakiyama Bay nature conservation area, Okinawa, Japan. Environment Agency, 140 pp (in Japanese with English abstract)
Nature Conservation Bureau Environment Agency (1990) Survey report of the Sakiyama Bay nature conservation area, Okinawa, Japan, 239 pp (in Japanese)
Nature Conservation Bureau, Environment Agency (1999) State of Sakiyama Bay nature conservation area, Okinawa, Japan, 140 pp (in Japanese)
Nature Conservation Bureau of Ministry of Environment and Kaiyu Ltd. (2004) 2003 Survey report on nature conservation measures for Amitori Bay, 131 pp (in Japanese)
Nio T, Doi W, Mizutani A, Kohno H (2019) Seaward migration and larval release of the land hermit crab Coenobita brevimanus Dana, 1852 (Anomura: Coenobitidae) on Iriomote Island, Japan. Crust Res 48:67–80
Nio T, Suguri A, Mizutani A, Doi W, Kohno H (2014) Emergence of the mole crab *Hippa marmorata* around the land hermit crab *Coenobita brevimanus* releasing larvae. Cancer 23:39–42 (in Japanese)
Ogura M, Yokochi H, Ishimaru A, Kohno H, Suzuki Y, Minagawa H, Miyamoto Y, Habe T (1989) Movement of the aggregations of the crown-of-thorns starfish, *Acanthaster planci* (L.), in the northwestern coast of Iriomote-jima, Ryukyu Islands. Bull Inst Ocean Res Dev Tokai Univ 10:31–41 (in Japanese with English abstract)
Ohba T, Miyata M (2007) Seagrasses of Japan. Hokkaido University Press, Sapporo (in Japanese)
Okamoto T (2017) Historical biogeography of the terrestrial reptiles of Japan: a comparative analysis of geographic ranges and molecular phylogenies. In: Motokawa M, Kajihara H (eds) Species diversity of animals in Japan. Springer, Tokyo, Japan, pp 135–168
Okinawa Prefectural Board of Education (1987) AMAN: a report on the distribution and ecology of land hermit crabs in Okinawa Prefecture. Ryukurindo-Shoten, Ginowan, 254 pp (in Japanese)
Okinawa Prefectural Board of Education (2006) A report on the distribution and ecology of land hermit crabs in Okinawa Prefecture II. Cultural Assets Division, Okinawa Prefectural Board of Education, Naha, 262 pp (in Japanese)
Ota H (1998) Geographic patterns of endemism and speciation in amphibians and reptiles of the Ryukyu Archipelago, Japan, with special reference to their paleogeographical implications. Res Popul Ecol 40:189–204
Rahayu DL, Shih H, Ng PKL (2016) A new species of land hermit crab in the genus *Coenobita Latreille*, 1829 from Singapore, Malaysia and Indonesia, previously confused with *C. cavipes* Stimpson, 1858 (Crustacea: Decapoda: Anomura: Coenobitidae). Raffles Bull Zool 34 (Suppl):470–488
Rattanchot E, Short FT, Prathep A (2016) *Enhalus acoroides* responses to experimental shoot density reductions in Haad Chao Mai National Park, Trang Province, Thailand. Mar Ecol 37:411–418
Rollón RN, Steveninck EDR, Vierssen W (2003) Spatiotemporal variation in sexual reproduction of the tropical seagrass *Enhalus acoroides* (L.f.) Royle in Cape Bolinao, NW Philippines. Aquat Bot 76:339–354
Sanda T, Hamasaki K, Iizuka C, Kitada S (2018) Distribution of terrestrial hermit crabs on the coasts of Chichijima Island in the Bonin Islands and Hatchijojima Island in the Izu Islands, Japan. Bull Biogeogr Soc Jpn 72:65–74 (in Japanese with English abstract)
Shimizu Y (2014) Process of the formation of Japanese forest and typification of vegetation zone: from an East Asian viewpoint. Reg Views (Institute of Applied Geography, Komazawa University, Tokyo) 27:19–75 (in Japanese with English abstract)
Takeyama K, Kohno H, Kuramochi T, Iwasaki A, Murakami T, Kimura K, Ukai A, Nakase K (2014) Distribution and growth condition of *Enhalus acoroides* in Iriomote Island. Ann J Civ Eng Ocean B3 70:I_1068–I_1073 (in Japanese with English abstract)
The Ministry of the Environment, Kaiyu Ltd. (2004) 2003 Survey report on nature conservation measures for Amitori Bay. Biodiversity Center of Japan, The Ministry of the Environment, Japan, 131 pp

Toma T (1999) Seagrasses from the Ryukyu Islands – I, species and distribution. Biol Mag Okinawa 37:75–92 (in Japanese with English abstract)

Tsuchiya M (1981) On the spawning of the squid, *Sepioteuthis lessoniana* Lesson at Amitori Bay, Iriomote Island, Okinawa. Bull Inst Ocean Res Dev Tokai Univ Note 3:53–75 (in Japanese with English abstract)

Tsuru T, Hamasaki K, Sanda T, Fujikawa S, Kitada S (2018) Distribution of terrestrial hermit crabs on Hatomajima Island, Ryukyu Archipelago, Japan. Bull Biogeogr Soc Jpn 72:75–85 (in Japanese with English abstract)

Vannini M, Ferretti J (1997) Chemoreception in two species of terrestrial hermit crabs (Decapoda: Coenobitidae). J Crust Biol 17:33–37

Verheij E, Erftemeijer PLA (1993) Distribution of seagrass and associated macroalgae in South Sulawesi, Indonesia. Blumea-Biodivers Evol Biogeogr Plants 38:45–64

Vermaat JE, Agawin NSR, Duarte CM, Fortes MD, Marbà N, Uri JS (1995) Meadow maintenance, growth and productivity of a mixed Philippine seagrass bed. Mar Ecol Prog Ser 124:215–225

Yokochi H, Ueno S, Ogura M, Nagai A, Habe T (1991) Spatiotemporal changes of the distribution and abundance of *Acanthaster planci* (L.) and corals at northwestern Iroomote-jima, Ryukyu Islands: 1983–1988. J Sch Mar Sci Technol Tokai Univ 32:231–242 (in Japanese with English abstract)

Chapter 2
Observational Method

Tomokazu Murakami

Abstract Observations introduced into this book include current and wave observations mainly using WavesADCP, meteorological observation using an anemometer, and water quality observation using a portable multi-item water quality meter. This chapter presents a description of these observational methods.

Keywords Field observation · Ocean current · Temperature · Wave · Wind

2.1 Current Velocity and Wave Observation

WavesADCP was used for observation of current velocity and waves in studies introduced in this book. An Acoustic Doppler Current Profiler (ADCP), an ultrasonic current meter using the Doppler effect is upgraded to WavesADCP by augmentation with simultaneous observations of waves.

The WavesADCP employed for this study (Workhorse Sentinel; Teledyne RD Instruments Inc.). This WavesADCP operates at a frequency of 600 kHz and simultaneously emits four beams at beam angles of 20°. It has measurement accuracy of ±0.3% or ±0.3 cm/s, resolution of 0.1 cm/s, a current measurement range of ±5 m/s (standard) and ±20 m/s (maximum), and maximum measurement range of 66 m. A WavesADCP can also measure water temperature with an equipped water thermometer.

Layer thickness was set to 50 cm. The ensemble interval was set to 10 min (100 measurements during this period) for the acquisition of high-resolution data. The error of measurement of current velocity assumed from this setting was 0.01 m/s.

T. Murakami (✉)
Storm, Flood and Landslide Research Division, National Research Institute for Earth Science and Disaster Resilience, Tsukuba, Japan
e-mail: tmurakami@bosai.go.jp

S. Shimokawa et al. (eds.), *Geophysical Approach to Marine Coastal Ecology*, Springer Oceanography, https://doi.org/10.1007/978-981-15-1129-5_2

Fig. 2.1 Observation sites

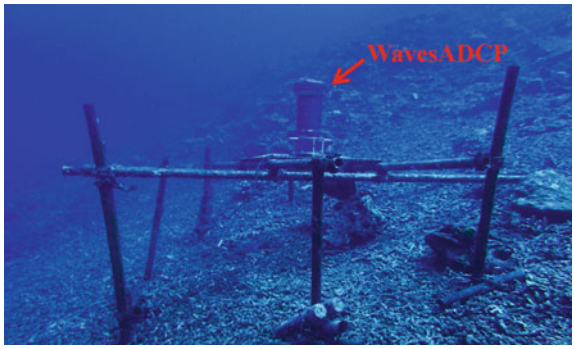

Fig. 2.2 Installation of WavesADCP

We constructed a solid frame that maintains a level necessary for high-precision observation and which can bear a strong current at the time of a typhoon on the sea bottom (12.4 m average water depth) of observation site A, as presented in Fig. 2.1. We installed WavesADCP described in Fig. 2.2.

2.2 Meteorological Observation

Meteorological observations were conducted at point B shown in Fig. 2.1 using an analog weather signal recording system (CR1000; Campbell Scientific Inc.), a humidity and temperature probe (1CVS-HMP155D-JM; Vaisala), a rain gauge (CTK-15 PC-JM; Climatec Inc.), and a marine wind monitor (CYG-5106; R. M. Young Co.) (Fig. 2.3). The anemometer is 4.2 m above the top plate of the landing bridge shown in Fig. 2.4 to the center of the windmill. The data logging interval of these observation instruments is 10 min.

Fig. 2.3 Analog weather signal recording system (CR1000), Hygrothermograph (1CVS-HMP155D-JM) and Rain gauge (CTK-15PC-JM)

Fig. 2.4 Anemometer (CYG-5106)

2.3 Water Quality Observation

A portable multi-item water quality meter (RINKO-Profiler ASTD102; JFE Advantech Co. Ltd.) (Fig. 2.5) was used in this study for water quality observations, which can simultaneously measure DO, turbidity, and chlorophyll as well as the water depth, water temperature, and salinity according to the specifications presented in Table 2.1.

Fig. 2.5 Portable multi-item water quality meter

Table 2.1 Profiler specifications (RINKO-Profiler ASTD102)

Measurement items	Depth	Water temperature	Electric conductivity	Salinity	DO	Chlorophyll	Turbidity
Sensor type	Semiconductor pressure sensor	Thermistor	Electrode	Practical salinity	Phosphorescence	Fluorometer	Backscattering
Measurement range	0–600 m	−5 to 40 °C	0–70 ms/cm	0–40	0–20 mg/l (0–200%)	0–400 ppb (Uranine reference)	0–1,000 FTU (Formazin reference)
Resolution	0.01 m	0.001 °C	0.001 ms/cm	0.001	0.001 mg/l (0.01%)	0.01 ppb	0.03 FTU
Accuracy	±0.3% FS	±0.01 °C	±0.01 ms/cm (2–65 ms/cm)	±0.01	±2% FS (± 2% FS)	±1% FS zero drift ±0.1 ppb	±0.3 FTU or ±2% of the measured value
Time constant (s)	0.2	0.2	0.2	0.2	0.4	0.2	0.2

Water quality is visible with 0.1 m resolution along the vertical direction by going to an observation point by ship and dropping it into the sea.

Acknowledgements This research was supported by JSPS KAKENHI Grant Number 18K04377.

Chapter 3
Numerical Simulation Method

Tomokazu Murakami

Abstract This chapter presents a description of models used for simulations performed in this book, including the Coastal ocean Current Model with a multi-sigma coordinate system (CCM) developed by the author and a colleague for computation of seawater flow, a wave model SWAN developed at Delft University of Technology, and the Lagrangian particle tracking model.

Keywords Numerical simulation · Ocean model · Wave model · Particle tracking model

3.1 Ocean Model CCM

This section presents a description of the Coastal ocean Current Model with a multi-sigma coordinate system (CCM) used in this book, developed by the author and colleagues for seawater flow computations (Murakami et al. 2004).

Seawater flow in inland seas such as Sakiyama Bay and Amitori Bay is closely involved with the vertical structure of water temperature, salinity, and density. These quantities are governed strongly by oceanic water entering from the bay mouth, as well as layering because of insolation and river water, circulation inside of the bay by wind, and upwelling. For that reason, the numerical computation of seawater flow in an inland sea requires correct evaluation not only of changes of geographical features but also the effects of meteorological fields such as insolation and wind, as well as solving from offshore to the inland sea continuously with sufficient accuracy.

This chapter is based on work reported by Murakami et al. (2004).

T. Murakami (✉)
Storm, Flood and Landslide Research Division, National Research Institute for Earth Science and Disaster Resilience, Tsukuba, Japan
e-mail: tmurakami@bosai.go.jp

S. Shimokawa et al. (eds.), *Geophysical Approach to Marine Coastal Ecology*, Springer Oceanography, https://doi.org/10.1007/978-981-15-1129-5_3

Seawater inflow from offshore is important for inland seas such as Sakiyama Bay and Amitori Bay. Accordingly, it is necessary to configure a computational domain widely including offshore areas. However, the water depth difference is highly extended between that in an inland sea and offshore in a computational domain that is so configured. Furthermore, geographical features change suddenly and intricately at the bay mouth. The σ coordinates, which implement correct expressions of complicated submarine topography and easy handling of boundary conditions, are in heavy use for the computation of seawater flow under such conditions. Ocean models using this scheme, including POM (Mellor 2004), have been developed.

The σ coordinate system is defined as

$$\sigma = \frac{z-\zeta}{\zeta+h} = \frac{z-\zeta}{H}, \tag{3.1}$$

where ζ represents the water surface displacement, h denotes the still water depth, and H stands for the total depth.

The primitive equations are converted into the σ coordinate system from the Cartesian coordinate system with Eq. 3.1. Then, they are discretized and solved using the finite difference method. The relation between the vertical difference of physical quantity in the Cartesian coordinate system ϕ and that of physical quantity in the σ coordinate system $\tilde{\phi}$ is expressed as

$$\frac{1}{\Delta z}(\phi_{k+1} - \phi_{k-1}) = \frac{1}{H}\frac{1}{\Delta\sigma}(\tilde{\phi}_{k+1} - \tilde{\phi}_{k-1}). \tag{3.2}$$

In the difference equation in the σ coordinate system of the right-hand side of Eq. 3.2, $\Delta\sigma$ is multiplied by total depth H having a horizontal variation as shown in relation $\Delta\sigma \cdot H = \Delta z$ obtained from Eq. 3.1. The difference value is calculated using Δz distorted for every lattice depending on the water depth. For example, Δz offshore with a depth of 100 m and in an inland sea with a depth of 3 m are 10 m and 0.3 m, respectively, in the configuration of 10 layers at a vertical regular interval in the σ coordinate system. The difference equation of Eq. 3.2 is apt to yield a numerical error at an enlarged Δz or when the vertical change of physical quantities is great. Accordingly, the accuracy of vertical difference deteriorates extremely offshore with a large water depth compared with an inland sea. When a physical quantity with a large numerical error is introduced from offshore into an inland sea as the target of computation, a large numerical error will arise in computation of a physical quantity in the inland sea. This difficulty requires more careful handling, especially when coupled with a meteorological field, because the vertical change of physical quantities is enhanced because of momentum transfer by wind, heat exchange by insolation, and water balance by precipitation and evaporation. Consequently, it is an important problem that the accuracy of vertical difference is dependent on water depth when solving continuously from offshore to an inland sea.

Simplified solutions to this problem include increasing the number of vertical layers and the concept of unequally spaced layers by making the interlayer spacing near the sea surface dense. However, a considerable number of vertical layers or extremely unequal layer spacing is indispensable for the method described above to reduce the differences of Δz between an inland sea and offshore. These measures are expected to increase the computation time and instability in computation. They are not conclusive solutions.

The present author and colleagues have newly proposed the multi-sigma coordinate system in which a calculation domain is divided into numerous regions along the vertical direction, and σ coordinates are applied to each region. This multi-sigma coordinate system is defined as follows, with divided regions designated sequentially from the sea surface as I, II, III, …:

$$\sigma_{\mathrm{I}} = \frac{z-\zeta}{\zeta + h_{\mathrm{I}}} \quad \text{in region I}\,(-h_{\mathrm{I}} \le z < \zeta) \tag{3.3}$$

$$\sigma_{\mathrm{II}} = \frac{S_{\mathrm{I}} + z}{h_{\mathrm{II}}} \quad \text{in region II}\,(-h_{\mathrm{II}} \le z < -h_{\mathrm{I}}) \tag{3.4}$$

$$\sigma_{\mathrm{III}} = \frac{S_{\mathrm{II}} + z}{h_{\mathrm{III}}} \quad \text{in region III}\,(-h_{\mathrm{III}} \le z < -h_{\mathrm{II}}) \tag{3.5}$$

$$\begin{cases} h_{\mathrm{I}} = h & \text{at } h \le S_{\mathrm{I}} \\ h_{\mathrm{I}} = S_{\mathrm{I}} & \text{at } h > S_{\mathrm{I}} \end{cases}$$

$$\begin{cases} h_{\mathrm{II}} = h - S_{\mathrm{I}} & \text{at } h \le S_{\mathrm{II}} \\ h_{\mathrm{II}} = S_{\mathrm{II}} - S_{\mathrm{I}} & \text{at } h > S_{\mathrm{II}} \end{cases}$$

$$\begin{cases} h_{\mathrm{III}} = h - S_{\mathrm{II}} & \text{at } h \le S_{\mathrm{III}} \\ h_{\mathrm{III}} = S_{\mathrm{III}} - S_{\mathrm{II}} & \text{at } h > S_{\mathrm{III}} \end{cases}$$

The definition of the σ coordinates of representative regions I, II, and III is described below, but this definition also applies to region IV and deeper regions. S_{I}, S_{II}, and S_{III}, respectively, represent the distance from $z = 0$ to the interface between regions I and II, II and III, and III and IV. Such S is designated as the interface depth. Figure 3.1 shows the grid points of the so-defined multi-sigma coordinates and those of the conventional σ coordinates. Conventional σ coordinates of Fig. 3.1 represent a big difference in Δz between the inland sea and offshore, influenced by water depth change. However, in the multi-sigma coordinate system, the influence of water depth change can be eliminated from region I by narrowing region I directly under the sea surface, so that Δz in the inland sea and offshore becomes uniform. Consequently, the water depth dependence of the accuracy of vertical difference in the top layer can be canceled, which is intrinsically important in coupled calculation with a meteorological field. Moreover, dividing a domain into multiple regions can cancel the water depth dependence of the accuracy of vertical difference, even in regions except near the sea bottom. Furthermore, the

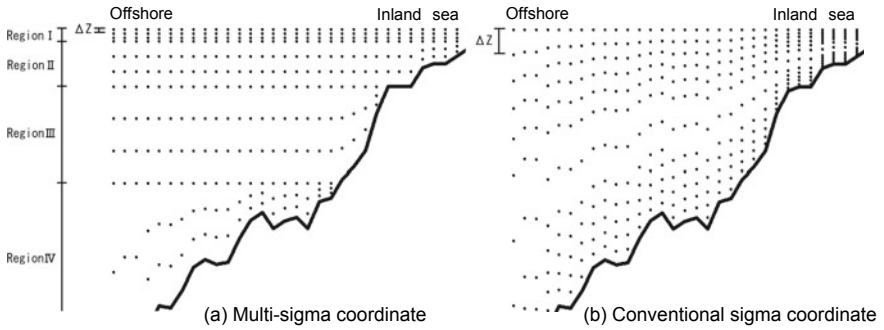

Fig. 3.1 Layouts of grid points using the multi-sigma coordinate system and the conventional sigma coordinate system. Black points signify the grid points

conventional problem of the numerical error of the horizontal pressure gradient term and horizontal diffusion term is improved because the level difference in a domain that includes no sea bottom becomes the same as that of the Cartesian coordinate system, even if geographical features are steep.

An oceanographic model using multi-sigma coordinates has been newly developed in this study. It is designated as the Coastal ocean Current Model (CCM). The major characteristics of this multi-sigma coordinate ocean model are the following.

- Hydrostatic pressure approximation and Boussinesq approximation are applied. The primitive equations include the equation of continuity, the *N*–*S* equation, the diffusion equation of temperature and salinity, and the equation of state in terms of density.
- The number of regions in which the σ coordinates is applied can be configured as arbitrary numbers.
- The fifth-order accurate upwind difference scheme is applied to the finite difference of the advective term. The fourth-order accurate central difference scheme is used for the finite difference of the diffusion term.
- The Mellor–Yamada Level 2.5 turbulent closure model (Mellor and Yamada 1982) is adopted as a turbulent model.

To investigate the usefulness of the multi-sigma coordinates, six cases of Table 3.1 were computed for Ise Bay in Japan in July 10–17, 2001 using an ocean model with the multi-sigma coordinate system.

Interface depth *S* was determined so that the number of horizontal grid points in a calculation domain was divided equally by *N* of each case. Case 1 is identical to the conventional σ coordinates.

Figure 3.2 shows the mean sea level temperature obtained using the analysis of data of a summer (July–September 2001) of the NOAA satellite. This figure shows the relative drop of the sea surface temperature only at the bay mouth. The temperature drop is regarded as taking place at the mouth where vertical mixing

Table 3.1 Cases for computation (referred from Murakami et al. 2004)

	N, Number of regions in which σ coordinates are applied	S, Interface depth (m)
Case 1	1	
Case 2	2	$S_{\mathrm{I}} = 3$
Case 3	3	$S_{\mathrm{I}} = 3$, $S_{\mathrm{II}} = 22$
Case 4	4	$S_{\mathrm{I}} = 3$, $S_{\mathrm{II}} = 19$, $S_{\mathrm{III}} = 35$
Case 5	5	$S_{\mathrm{I}} = 3$, $S_{\mathrm{II}} = 14$, $S_{\mathrm{III}} = 26$, $S_{\mathrm{IV}} = 69$
Case 6	6	$S_{\mathrm{I}} = 3$, $S_{\mathrm{II}} = 10$, $S_{\mathrm{III}} = 20$, $S_{\mathrm{IV}} = 29$, $S_{\mathrm{V}} = 55$

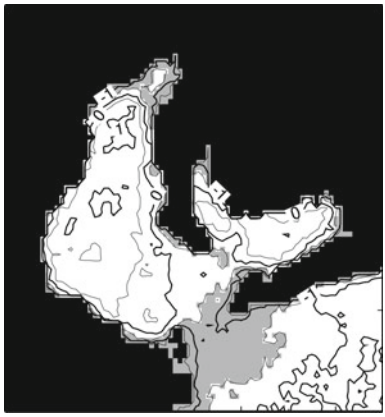

Fig. 3.2 Mean sea level temperature distribution in summer (July–September 2001); contour interval is 0.5 °C and low-temperature regions of a deviation not more than −0.5 °C are shaded (referred from Murakami et al. 2004)

prevails, although the calculation period of this study differs from the NOAA satellite analysis period. Accordingly, this phenomenon, which arises in the middle of an inland sea and offshore, is assumed as a suitable target for confirming the calculation accuracy of this model. The multi-sigma coordinate effects are examined from the viewpoint of reproducibility of this phenomenon.

Figure 3.3 shows the mean sea level temperature during the calculation period for each case. The temperature drop took place not at the mouth but offshore in Case 1. This is considered to be the result of Δz expansion offshore because of the water depth and the result of accuracy of the vertical difference deterioration. A slight temperature drop was observed at the mouth in addition to the temperature drop offshore in Case 2. This is considered to be the result of σ coordinates applied to two regions in Case 2; Δz was uniform over the inland sea and offshore near the sea surface ($z = -3$ m or above). Otherwise, in a deep region, Δz was enlarged offshore as in Case 1. In contrast to these, the temperature drop in Cases 3–6 was observed only at the mouth as shown in Fig. 3.2. Consequently, the multi-sigma coordinates are estimated as improving the calculation accuracy. Especially in Cases 4–6, in which σ coordinates were applied to four or more domains, almost no difference is indicated from the actual temperature distribution.

Fig. 3.3 Mean sea level temperature distribution during calculation period. The contour interval is 0.5 °C, with shaded low-temperature regions having deviation of not more than −0.5 °C (referred from Murakami et al. 2004)

Figure 3.4 compares the calculated density at 10:00 a.m. of each case with the measured density obtained from observational data of temperature and salinity acquired once a day (in the morning) at the bay center. Results of July 11, 12, and 16 are shown when typical characteristics were observed. The observed value was reproduced well with calculation on July 11 in Cases 1–6. In contrast, the layering was poorly reproduced on July 12 when the calculated values tended to be uniform along the perpendicular direction compared with the observed value, and on July 16 when a pycnocline appeared in the observed value because of a high river flow rate.

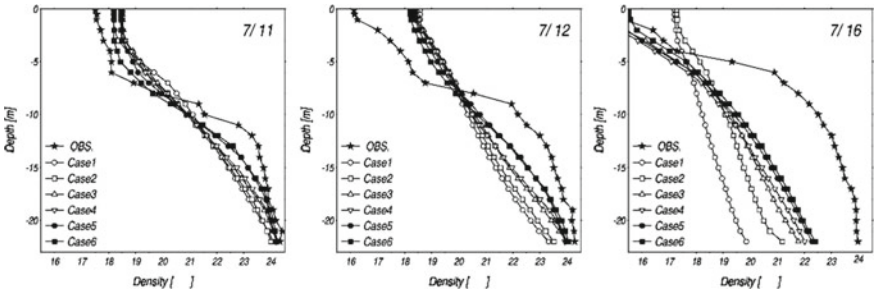

Fig. 3.4 Comparison of observed and calculated values of density distribution at point A: (left) density on July 11, (center) density on July 12, and (right) density on July 16 (referred from Murakami et al. 2004)

Calculations tended to make the density distribution too uniform along the perpendicular direction in any case. However, the density distribution of Cases 5 and 6 was approached. The calculation accuracy improved with all days as the σ coordinates were multiplexed more from Case 1 to Case 4.

Figure 3.5 shows the mean density distribution during the calculation period at cross section B of Fig. 3.1 for each case. This figure shows a difference in the density of seawater flowing in from offshore in each case (near x = 50 km in the figure). Thereby it is demonstrated that a difference occurred in the distribution of high-density water mass existing near the sea bottom of the inland sea. Moreover, the density contours fluctuated greatly in accordance with geographical features near the mouth in Cases 1–3. It is unnatural that the time-averaged density field fluctuates greatly depending on the water depth. It is regarded as a calculation difficulty. Actually, this difficulty is resolved gradually as the σ coordinates are multiplexed.

Figure 3.6 shows the surface residual current during the calculation period for each case. The trend of runoff to the west and inflow from the east, the characteristic of Ise Bay in the summer, is evident in the residual current field of the inland sea in all cases. However, a difference exists in the flow velocity of inflow from the east. A large vortex is observed near the open boundary of southwest and northeast in Cases 1 and 2. These vortices are known to appear on the open boundary even if a calculation domain is modified. They have been regarded as a calculation-related problem. These vortices cause an intense southwestward flow offshore. These vortices shrink in Case 3 and almost disappear in Cases 4–6. The flow offshore turns northeastward opposite to Cases 1 and 2. Consequently, it is regarded as one reason why the calculation accuracy of quantities such as temperature, salinity, and the density in the inland sea was improved that the calculative error near an open boundary was reduced using multi-sigma coordinates.

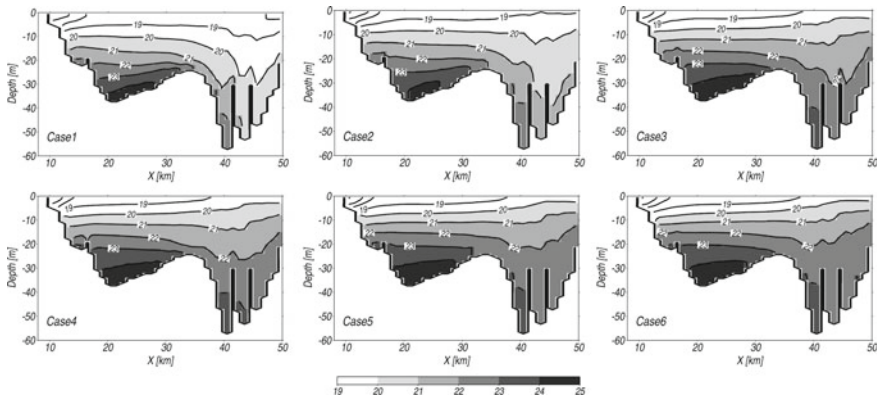

Fig. 3.5 Mean density distribution during the calculation period at cross section B. The contour interval is 1(σ_t) (referred from Murakami et al. 2004)

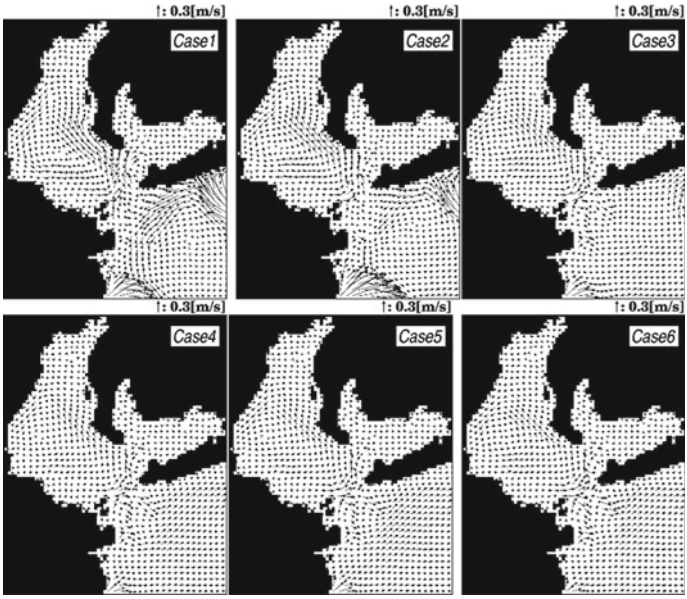

Fig. 3.6 Surface residual current during calculation period (referred from Murakami et al. 2004)

Consequently, results verified that the CCM is a suitable model for computing seawater flow, water temperature, salinity, and density in inland seas such as Sakiyama Bay and Amitori Bay, as described above.

3.2 Wave Model SWAN

SWAN (Booij et al. 1996) was used to calculate a wave field. SWAN is a wave forecasting and hindcasting model for shallow sea areas of the third-generation developed at Delft University of Technology. This section presents a description of the SWAN outline (Cycle III ver. 40.31) (Holthuijsen et al. 2004).

Because the directional wave spectrum is not conserved but the wave action density is conserved in a state with a flow, SWAN uses not the directional wave spectrum $E(s, q)$ but the wave action density spectrum $N(s, q)$, for which the independent variables are relative frequency s and wave direction q, and $N(s, q) = E(s, q)/s$. Actually, SWAN provides users with primitive equations of two types: a rectangular coordinate system and the spherical coordinate system. The primitive equation of the rectangular coordinate system is given as the following equation.

$$\frac{\partial}{\partial t}N + \frac{\partial}{\partial x}c_x N + \frac{\partial}{\partial y}c_y N + \frac{\partial}{\partial \sigma}c_\sigma N + \frac{\partial}{\partial \theta}c_\theta N = \frac{S}{\sigma} \tag{3.6}$$

In that equation, c_x, c_y, c_σ, and $c_{\theta,}$ respectively, denote the propagation velocities on the real space and the spectrum space x, y, s, and θ. They are used as components in the equations shown below using phase velocity of each component wave c, group velocity c_g, steady flow velocity vector $\overrightarrow{U} = (U, V)$, and wave number vector $\vec{k} = \left(k_{x,} k_y\right)$.

$$c_x = c_\mathrm{g} \cos\theta + U \tag{3.7}$$

$$c_y = c_\mathrm{g} \sin\theta + V \tag{3.8}$$

$$c_\sigma = \frac{\partial}{\partial_t}\left(\sqrt{gk\tan h(kh)} = \vec{k} \cdot \overrightarrow{U}\right) \tag{3.9}$$

$$c_\theta = \frac{c_\mathrm{g}}{c}\left[\sin\theta\frac{\partial c}{\partial x} - \cos\theta\frac{\partial c}{\partial y}\right] - \frac{1}{k}\left(\sin\theta\frac{\partial}{\partial x} - \cos\theta\frac{\partial}{\partial y}\right)\left(\vec{k} \cdot \overrightarrow{U}\right) \tag{3.10}$$

The first term of the left-hand side of Eq. 3.6 expresses the temporal rate of change of wave action density. The second and third terms express the spatial propagation of wave action density. c_x and $c_{y,}$ respectively, represent the propagation velocity along the x-direction and y-direction. The fourth term denotes the change of relative frequency according to the temporal change of water depth and a flow (propagation velocity in s space c_σ). The fifth term expresses wave refraction by water depth and a flow (propagation velocity in θ space c_θ). S on the right-hand side (= S (s, q)) is an energy source function representing the effects of wave generation, wave dissipation, and interaction between nonlinear wave components. This function S will be described later. Equations of propagation velocity (3.7)–(3.10) are derived using the linear kinematic wave theory (Whitham 1974; Dingemans 1997; Mei 1983). Equation (3.6), the wave action density equation in the rectangular coordinate system, is converted to the spherical coordinate system on the Earth as

$$\frac{\partial}{\partial t}N + \frac{\partial}{\partial \lambda}c_\lambda N + (\cos\varphi)^{-1}\frac{\partial}{\partial \varphi}c\varphi\cos\varphi N + \frac{\partial}{\partial \sigma}c_\sigma N + \frac{\partial}{\partial \theta}c_\theta N = \frac{S}{\sigma} \tag{3.11}$$

where c_λ, c_φ, c_σ, and c_θ are given, respectively, as shown below.

$$c_\lambda = \frac{c_\mathrm{g}\sin\theta + V}{R\cos\varphi} \tag{3.12}$$

$$c_\varphi = \frac{c_\mathrm{g}\cos\theta + U}{R} \tag{3.13}$$

$$c_\sigma = \frac{\partial}{\partial t}\left(\sqrt{gk\tan h(kh)} - \vec{k}\cdot\vec{U}\right) \tag{3.14}$$

$$c_\theta = \frac{c_g \sin\theta\tan\varphi}{R} + \frac{1}{kR}\left(\sin\theta\frac{\partial}{\partial\varphi} - \frac{\cos\theta}{\cos\varphi}\frac{\partial}{\partial\lambda}\right)\left(\sqrt{gk\tan(kh)} - \vec{k}\cdot\vec{U}\right) \tag{3.15}$$

Therein, φ, λ, and R, respectively, denote the latitude, longitude, and the Earth's radius. Energy source function S on the right-hand side of Eqs. 3.6 and 3.11 is expressed as shown below.

$$S(\sigma,\theta) = S_{\text{in}} + S_{\text{ds}} + S_{\text{br}} + S_{\text{bf}} + S_{\text{nl}} + S_{\text{tri}} \tag{3.16}$$

In that equation, S_{in} represents an energy transport term from wind to wave, S_{ds} denotes an energy dissipation term by whitecap breaking wave, S_{br} expresses an energy dissipation term by shallow water breaking wave, S_{bf} stands for an energy dissipation term by bottom friction, S_{nl} signifies an energy transport term by nonlinear interaction between four-wave components, and S_{tri} is an energy transport term by nonlinear interaction between three-wave components. An important characteristic of SWAN is that it takes S_{br} and S_{tri} into consideration directly.

Integration of the action balance equation in SWAN is conducted using a finite difference scheme in all five dimensions (time, real space, and spectrum space). The computation time is divided using a single time step for the simultaneous integration of the propagation term and the source term. The real space is also divided using a rectangle grid with fixed resolution Δx and Δy, respectively, along the x-direction and y-direction. The spectrum space is divided by a fixed directional division $\Delta\theta$ and relative frequency $\Delta\sigma/\sigma$ (logarithmic distribution). The range of the frequency spectrum, which can be chosen freely, is divided within a range, with the low-frequency and high-frequency portions cut off.

3.3 Particle Tracking Model

The three-dimensional particle tracking model used in this book is a numerical model that tracks each particle in a Lagrangian way. Particle tracking calculations are conducted based on a seawater flow field acquired from the CCM ocean model described above. The following conditions are imposed in the case of particle tracking: (1) Diffusion is not considered, (2) particles do not jump out of the sea surface, and (3) particles perform total reflection on a boundary with land. This numerical model can track virtual particles (water particles) having no mass. It is unaffected by specific gravity. It moves only by seawater flow. Soil particles form sediment with their own weight with the effects of specific gravity considered.

Acknowledgements This research was supported by JSPS KAKENHI Grant Number 18K04377.

References

Booij N, Holthuijsen LH, Ris RC (1996) The SWAN wave model for shallow water. In: Proceedings of 25th international conference on coastal engineering, vol 1, pp 668–676

Dingemans MW (1997) Water wave propagation over uneven bottoms. Part 1—linear wave propagation. In: Advanced series on ocean engineering (vol 13). World Scientific, p 471

Holthuijsen LH, Booij N, Ris RC, Haagsma IJG, Kieftenburg ATMM, Kriezi EE, Zijlema M, van der Westhuysen AJ (2004) SWAN Cycle III Ver. 40.31 User Manual

Mei CC (1983) The applied dynamics of ocean surface waves. Wiley, New York, p 740

Mellor GL (2004) Users guide for a three-dimensional, primitive equation, numerical ocean model, 56 pp. http://www.aos.princeton.edu/WWWPUBLIC/htdocs.pom

Mellor GL, Yamada T (1982) Development of a turbulence closure model for geophysical fluid problems. Rev Geophys Space Phys 20(4):851–875

Murakami T, Yasuda Y, Ohsawa T (2004) Development of a multi-sigma coordinate model coupled with an atmospheric model for the calculation of coastal currents. Ann J Coast Eng JSCE 51:366–370 (in Japanese with English abstract)

Whitham GB (1974) Linear and nonlinear waves. Wiley, New York, p 636

Part II
Observation and Estimation of Physical Environments

Chapter 4
Dynamical Properties of Coastal Currents in the Northwestern Part of Iriomote Island Part. 1—Sakiyama and Amitori Bays

Jun Yoshino, Tomokazu Murakami, Akiyuki Ukai, Hiroyoshi Kohno, Shinya Shimokawa, Kouta Nakase, Akira Mizutani and Takashi Yasuda

Abstract The physical properties of coastal currents in semi-closed bays (e.g., Sakiyama and Amitori bays) in the northwestern part of Iriomote Island are discussed in this chapter, based on the results of theoretical, observational, and numerical investigations. According to the tidal flow dynamics in a single channel, these bays in this region are categorized as "deep bays," in which little difference in

This chapter is based on works reported by Yoshino et al. (2011, 2016).

J. Yoshino (✉)
Faculty of Engineering, Gifu University, Gifu, Japan
e-mail: jyoshino@gifu-u.ac.jp

T. Murakami · S. Shimokawa
Storm, Flood and Landslide Research Division, National Research Institute for Earth Science and Disaster Resilience, Tsukuba, Japan
e-mail: tmurakami@bosai.go.jp

S. Shimokawa
e-mail: shimokawa@bosai.go.jp

A. Ukai · K. Nakase
Environment Business Division, Penta-Ocean Construction Co., Ltd., Tokyo, Japan
e-mail: Akiyuki.Ukai@mail.penta-ocean.co.jp

K. Nakase
e-mail: Kouta.Nakase@mail.penta-ocean.co.jp

H. Kohno · A. Mizutani
Okinawa Regional Research Center, Tokai University, Yaeyama, Japan
e-mail: hkohno@scc.u-tokai.ac.jp

A. Mizutani
e-mail: ma110267@tsc.u-tokai.ac.jp

T. Yasuda
Aichi University of Technology, Gamagori, Japan
e-mail: yasuda@aut.ac.jp

S. Shimokawa et al. (eds.), *Geophysical Approach to Marine Coastal Ecology*, Springer Oceanography, https://doi.org/10.1007/978-981-15-1129-5_4

phase and amplitude of the tidal levels exists from the open ocean. Ocean waters therefore flow in a bay in the incoming tide. By contrast, bay waters flow out to the open ocean in the outgoing tide. In Sakiyama Bay with its shallower waters, surface seawater exchange between the bay and ocean is active under near-calm conditions, leading to an environment in which the river water mass near the surface layer is more likely to flow out to the open ocean. By contrast, in Amitori Bay with the deeper waters, near-surface river water is stagnant under near-calm conditions. It selectively distributes to the eastern side of the bay because of the Earth's rotation. The theory of tidal flow dynamics in a single channel suggests that differences of coastal currents between Sakiyama and Funauki bays are mainly attributable to the difference of the aspect ratio, the length to depth ratio, between the two bays. Such a difference in physical properties in the coastal currents is expected to affect the coastal ocean ecosystem distribution in this region.

Keywords Amitori Bay · Coastal current · Iriomote Island · Sakiyama Bay · Seawater exchange · Tidal flow · River flow

4.1 Introduction

The northwestern part of Iriomote Island has rich coastal oceanic ecosystems with intricate topography, leading to the considerable spatial variation of reef-building corals (Sect. 1.4), mangrove forests, and *Enhalus acoroides* (Sect. 1.5). Its coastal oceanic ecosystems are strongly influenced by various environmental factors, which comprise physical factors (i.e., radiations, temperature, wave, current, and turbidity), chemical factors (i.e., dissolved oxygen, salinity, and nutrients), topographical/geological factors (i.e., depth and bottom sediments), biological factors (i.e., competitors and enemies), and anthropogenic factors (i.e., landfill and sediment discharge). Because the physical factors are especially important in this region, we require quantitative estimation of the coastal current fields to develop the strategies to improve biodiversity and to preserve natural ecosystems.

In the northwestern part of Iriomote Island, semi-enclosed bays continue from south to north: Sakiyama Bay, Amitori Bay, Funauki Bay, and Shirahama Bay (see Sects. 1.1 and 1.2, and Fig. 1.1). In addition, each of the bays has a few rivers. Sakiyama Bay is a shorter and shallower bay of about 2 km length and about 10 m depth, with two major rivers: Painta River and Ubo River. Amitori Bay next to Sakiyama Bay is longer and deeper, about 3 km long and about 70 m deep, with two major rivers: Ayanda River and Udara River. Such topographical differences among the bays might engender differences of physical factors, consequently influencing the distributions of respective coastal oceanic ecosystems in this region.

In this chapter, differences of coastal current fields in Sakiyama and Amitori bays located in the northwestern part of Iriomote Island are discussed based on theoretical, observational, and numerical perspectives.

4.2 Tidal Flow Dynamics in a Single Channel

(a) Theoretical Formulae

First, the theory of the tidal flow dynamics in a single channel, which is simplified as a rectangular bay portrayed in Fig. 4.1, is introduced. Then, the physical properties of tidal currents in Sakiyama and Amitori bays are discussed. The basic equation system of this theory comprises a momentum equation and a mass continuity equation describing an idealized rectangular semi-closed bay (Unoki 1993). In these equations, η_0 represents the tidal level in the open ocean given by a simple sine curve with a period of T, and η denotes the resultant tidal level homogeneous in a channel (bay) with area of A. The width, length, and depth in a channel are expressed, respectively, as w, l, and h. Therefore, the channel area is expressed as $\mathrm{A} = wl$. The current velocity is u in a channel, where the direction from offshore to onshore is positive. We assume that the meteorological forcing and river discharge can be ignored under calm conditions. Then, the momentum equation and mass continuity equation in a channel are described as follows:

$$\frac{\mathrm{d}u}{\mathrm{d}t} = -g\frac{\eta - \eta_0}{l} - \frac{\beta u}{h} \tag{4.1}$$

$$\frac{\mathrm{d}\eta}{\mathrm{d}t} = \frac{whu}{\mathrm{A}} = \frac{hu}{l} \tag{4.2}$$

where the first term on the right side of the momentum equation Eq. (4.1) is the sea surface gradient force and g represents the gravitational force. The second term on the right side of Eq. (4.1) expresses the ocean bottom drag as linearly approximated by $\beta = (8/3\pi)C_f\hat{U}$ and $C_f = 0.0026$. Also, $\hat{U}$ stands for the amplitude of tidal current velocity u of which optimal value is found by the successive iteration

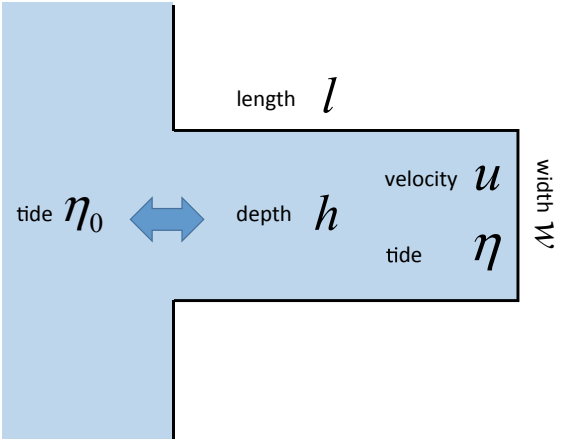

Fig. 4.1 Schematic diagram of tidal flow dynamics in a single channel

method. The right side of the mass continuity equation Eq. (4.2) expresses the rate of discharge in a channel. The linear equation systems Eqs. (4.1) and (4.2) are solvable by assuming that variations of the tidal level η and current velocity u in a channel responded by the tidal level η_0 in the open ocean can be represented in the following exponential forms.

$$\eta_0 = M\mathrm{e}^{i\sigma t}, \eta = \hat{\eta}\mathrm{e}^{i\sigma t}, u = \hat{u}\mathrm{e}^{i\sigma t} \tag{4.3}$$

Therein, M (real number) denotes the amplitude of tidal level in the open ocean, $\hat{\eta}$ and $\hat{u}$ (complex number), respectively, express the amplitude and phase change of tidal level and current velocity in a channel. The amplitudes of tidal level and current in a channel are expressed, respectively, by $|\hat{\eta}|$ and $|\hat{u}|$. The phase change of tidal level and current in a channel are written, respectively, by $\arg(\hat{\eta})$ and $\arg(\hat{u})$. $\sigma(=2\pi/T)$ is the radian frequency of tidal level in the open ocean with a period T of 12 h. Based on Eqs. (4.1), (4.2), and (4.3), we obtain the following first-order algebraic equation system.

$$\hat{\eta} + A\hat{u} = M \tag{4.4}$$

$$\hat{\eta} - a\hat{u} = 0 \tag{4.5}$$

Then, we can solve $\hat{\eta}$ and $\hat{u}$ as shown below.

$$\hat{u} = \frac{1}{A+a}M \tag{4.6}$$

$$\hat{\eta} = \frac{a}{A+a}M \tag{4.7}$$

In those equations, A and a are the complex number expressed in seconds.

$$A = \left(\frac{\beta}{h} + i\sigma\right)\frac{l}{g} \tag{4.8}$$

$$a = -i\frac{wh}{\sigma \mathrm{A}} = -\frac{i}{\sigma}\frac{h}{l} \tag{4.9}$$

Therein, i is the imaginary unit. Denominator $A+a$ in Eqs. (4.6) and (4.7) is derived as the following.

$$A + a = \frac{\beta l}{gh} + i\left(\frac{\sigma l}{g} - \frac{h}{\sigma l}\right) \tag{4.10}$$

Then, the relations between the complex parameters A and a defined by Eqs. (4.8) and (4.9) are compared. In these definitions, A and a include two parameters "length l" and "depth h" of a channel, implying that the aspect ratio

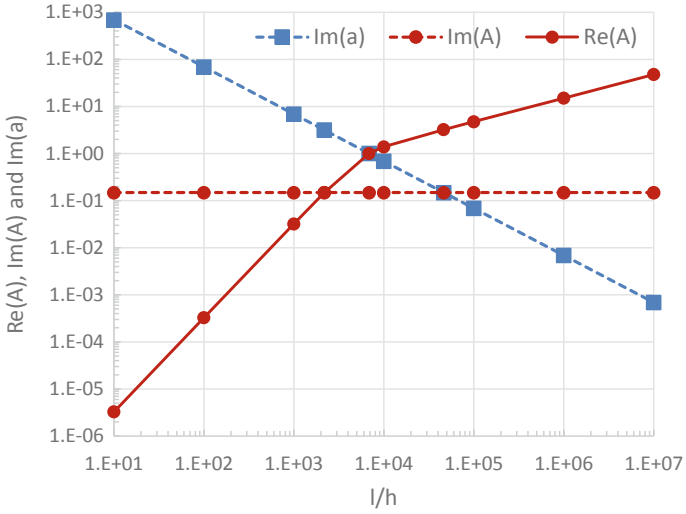

Fig. 4.2 Relations between the aspect ratio of the channel l/h and complex parameters (Re(A), Im(A), and Im(a))

"l/h" is an important parameter to express tidal currents in a channel. Figure 4.2 presents the relations of aspect ratio (l/h) and complex parameters (A and a) with fixed length of l = 10,000 m. Because A is a complex number obtained from the momentum equation Eq. (4.1) and because a is pure imaginary number obtained from the mass continuity equation Eq. (4.2), the real part (solid lines) and imaginary part (dashed lines) are individually compared. Figures 4.3 and 4.4,

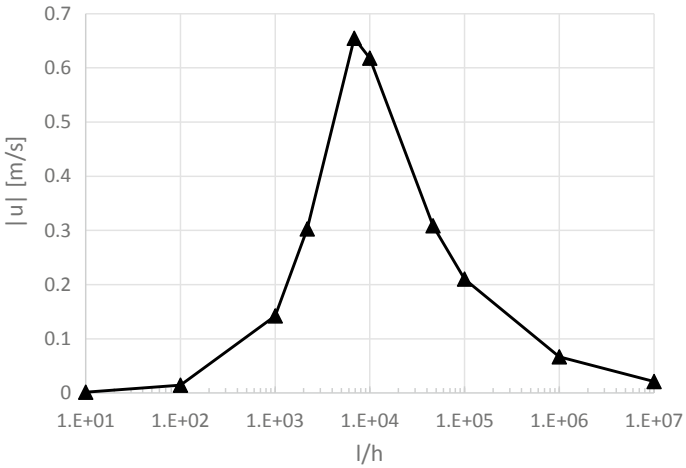

Fig. 4.3 Relation between the channel aspect ratio l/h and the amplitude of the current velocity $|\hat{u}|$

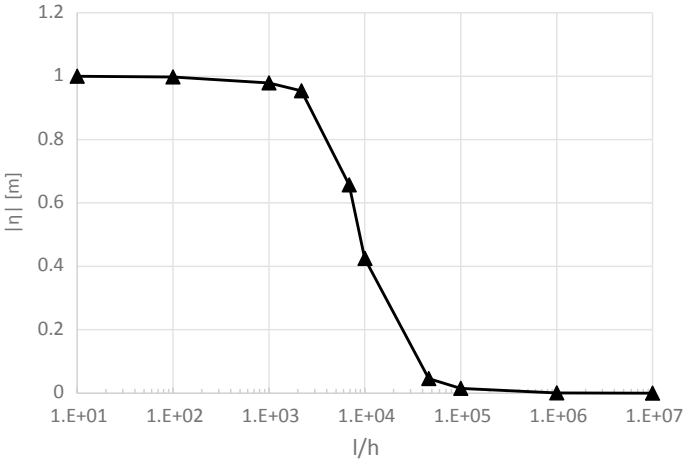

Fig. 4.4 Relation between the aspect ratio l/h and tidal amplitude $|\hat{\eta}|$

respectively, show the relations of aspect ratio (l/h) and the amplitude of current velocity $|\hat{u}|$ and tidal level $|\hat{\eta}|$ with a fixed ocean tide of $M = 1\,\mathrm{m}$. In this comparison, the radian frequency of ocean tide and gravitational force are set, respectively, to $\sigma = 1.45 \times 10^{-4}\,1/\mathrm{s}$ and $g = 9.8\,\mathrm{m/s^2}$.

In the smaller aspect ratio of a channel ($l/h < 2.18 \times 10^3$), complex parameter a derived from the mass continuity equation becomes more dominant. Such a bay is designated as a "deep bay" in this study. In this case, the larger the aspect ratio l/h of a bay, the lager the amplitude of current velocity $|\hat{u}|$ in a bay. Then, the amplitude of tidal level $|\hat{\eta}|$ in a bay is nearly 1.0 m, which is same size as the amplitude of the tidal level M in the open ocean.

In the moderate aspect ratio of a channel ($2.18 \times 10^3 \leq l/h < 4.63 \times 10^4$), two complex parameters, A and a, are mutually comparable, implying that the each of the terms in both the momentum equation and mass continuity equation must act comparably on the tidal currents. Such a bay is designated as a "shallow bay" in this study. When the aspect ratio of a bay becomes $l/h = 6.85 \times 10^3$, the amplitude of current velocity $|\hat{u}|$ in a bay corresponds roughly to a peak value of 0.7 m/s. The amplitude of tidal level $|\hat{\eta}|$ in a bay is about 0.7 m, which is less than that (M = 1.0 m) of the open ocean.

In the larger aspect ratio of a channel ($l/h \geq 4.63 \times 10^4$), the complex parameter A derived from the momentum equation Eq. (4.1) dominates the complex parameter a obtained from the mass continuity equation Eq. (4.2). Such a bay is designated as a "very shallow bay" in this study. In this case, the larger the aspect ratio l/h of a bay, the smaller the amplitudes of tidal current $|\hat{u}|$ and level $|\hat{\eta}|$, respectively, approaching 0 m/s and 0 m.

Next, we intend to extend the detailed discussion to elucidate the bays' three types: "very shallow bay," "shallow bay," and "deep bay."

(b) **Case of "very shallow bay"**

First, we consider $l/h = 4.63 \times 10^4$ in which $\mathrm{Im}(A)$ and $\mathrm{Im}(a)$ are the same size but which are at least one order of magnitude smaller than $\mathrm{Re}(A)$, according to Fig. 4.2. Such a shallow-floor bay is categorized as a "very shallow bay" for this study. In this situation, the term of the mass continuity equation in Eq. (4.2) is smaller, but the terms of the momentum equation, especially for the second term of the ocean bottom drag (β/h in $\mathrm{Re}(A)$) in Eq. (4.1), become more dominant. Because the imaginary part of $A + a$ in Eq. (4.10) is nearly 0, one can obtain depth h of this case as presented below.

$$h = \frac{\sigma^2 l^2}{g} \tag{4.11}$$

If depth h satisfies Eq. (4.11) (i.e., l = 10,000 m and h = 0.22 m), then $A + a$ in Eq. (4.10) can be approximated as shown below.

$$A + a \approx \frac{\beta l}{g h} \tag{4.12}$$

In addition, one can obtain the approximated forms of Eqs. (4.6) and (4.7) such that

$$\hat{u} \approx \frac{g}{\beta}\left(\frac{l}{h}\right)^{-1} M \tag{4.13}$$

$$\hat{\eta} \approx -i\frac{g}{\sigma\beta}\left(\frac{l}{h}\right)^{-2} M \tag{4.14}$$

The amplitudes of current velocity $|\hat{u}|$ and tidal level $|\hat{\eta}|$ in a bay, shown in Eqs. (4.13) and (4.14), provide high accuracy in a "very shallow bay" with the larger aspect ratio of a channel. In $l/h \geq 4.63 \times 10^4$, the effect of ocean bottom drag contributes greatly to the temporal change of tidal current velocity $\hat{u}$, as shown in Eq. (4.13) and Fig. 4.3. Therefore, $|\hat{u}|$ is proportional to depth h in a bay and is inversely proportional to length l of a bay. That is, $|\hat{u}|$ is inversely proportional to the aspect ratio l/h of a bay. The positive maximum of u in a bay (from ocean to bay) appears at the high-tide time, although the negative minimum of u in a bay (from bay to ocean) appears at the low-tide time. Therefore, no phase difference exists between tidal flow $\arg(\hat{u})$ in a bay and tidal level $\arg(M)$ in the open ocean. The ocean bottom drag effect also influences the temporal change of tidal level $\hat{\eta}$, as shown in Eq. (4.14) and Fig. 4.4, so $|\hat{\eta}|$ is proportional to the square of depth h in a bay and is inversely proportional to the square of length l in a bay. Consequently,

$|\hat{\eta}|$ is inversely proportional to the square of the aspect ratio l/h of a bay. The phase of tidal level $\arg(\hat{\eta})$ in a bay lags behind that $\arg(M)$ of the open ocean by 1/4 T (3 h) because of the existence of "$-i$" in Eq. (4.14).

(c) **Case of "shallow bay"**

If $l/h = 6.85 \times 10^3$, which is smaller than the previous threshold ($= 4.63 \times 10^4$), then the amplitude of tidal velocity $|\hat{u}|$ in a bay reaches a peak, as presented in Fig. 4.3. In such a case, $\mathrm{Re}(A)$ and $\mathrm{Im}(a)$ are the same size, but are almost one order larger than $\mathrm{Im}(A)$, according to Fig. 4.2. In other words, the effect of ocean bottom drag gradually decreases with depth h, although the effect of mass conservation gradually increases with depth h. These effects on the amplitude of tidal velocity $|\hat{u}|$ in a bay are mutually compensatory, becoming a peak of $|\hat{u}|$. Such a transitional bay is categorized as a "shallow bay" in this study. Because the real part of Eq. (4.8) is just equal to the imaginary part of Eq. (4.9), the following holds.

$$h = l\sqrt{\frac{\sigma\beta}{g}} \tag{4.15}$$

If the depth h satisfies Eq. (4.15) (i.e., $l = 10{,}000$ m and $h = 1.53$ m), then $A + a$ in Eq. (4.10) can be approximated as shown below.

$$A + a \approx \frac{\beta l}{gh} - i\,\frac{\beta l}{gh} \tag{4.16}$$

One can obtain the approximated forms of Eqs. (4.6) and (4.7) as the following.

$$\hat{u} \approx \frac{1}{2}\frac{g}{\beta}\left(\frac{l}{h}\right)^{-1}(1+i)M \tag{4.17}$$

$$\hat{\eta} \approx \frac{1}{2}\frac{g}{\sigma\beta}\left(\frac{l}{h}\right)^{-2}(1-i)M \tag{4.18}$$

The amplitude of tidal velocity $|\hat{u}|$ and tidal level $|\hat{\eta}|$ in a bay, estimated by Eq. (4.17) and (4.18), are 0.7 m/s and 0.7 m, respectively, which are consistent with the values estimated by exact solutions in Eqs. (4.6) and (4.7). In this case, the ocean bottom drag effect decreases gradually with depth h, thereby increasing $|\hat{u}|$. In contrast, the effect of mass conservation also increases with depth h, leading to the decrease of $|\hat{u}|$. When these two effects approximately balance, then the amplitude of tidal current $|\hat{u}|$ in a bay shows a peak. The phase of tidal current $\arg(\hat{u})$ in a bay is earlier by 1/8 T (1.5 h) from that $\arg(M)$ in the open ocean. For this reason, Eq. (4.17) includes "$1 + i$" making the phase shift earlier. According to Eq. (4.18), although the magnitude of tidal level $|\hat{\eta}|$ in a bay is decayed by the ocean bottom drag, the phase of tidal level $\arg(\hat{\eta})$ in a bay is delayed by 1/8 T

(1.5 h) from that $\arg(M)$ of the open ocean, because of "$1 - i$", making the phase shift later.

(d) **Case of "deep bay"**

If aspect ratio l/h is smaller than 6.85×10^3, then the amplitude of tidal velocity $|\hat{u}|$ declines thereafter, according to Fig. 4.3. Also, Fig. 4.2 shows that, in the case of $l/h = 2.18 \times 10^3$, $\mathrm{Re}(A)$ and $\mathrm{Im}(A)$ are mutually comparable and are one order smaller than $\mathrm{Im}(a)$. In other words, the ocean bottom drag effect can be safely neglected. The mass conservation becomes a dominant effect. Such a bay is categorized as a "deep bay" in this study. Because the real part $\mathrm{Re}(A)$ in Eq. (4.8) is equal to the imaginary part $\mathrm{Im}(A)$ in Eq. (4.8), the following expression can be obtained.

$$h = \frac{\beta}{\sigma} \tag{4.19}$$

If depth h satisfies with Eq. (4.19) (i.e., l = 10,000 m and h = 4.58 m), then the complex parameter $A + a$ is approximated to the complex parameter a. For h = 4.58 m, $A + a$ in Eq. (4.10) become a simple form as shown below, because of $|A| << |a|$.

$$A + a \approx a = -\frac{i}{\sigma}\frac{h}{l} \tag{4.20}$$

As a result, Eqs. (4.6) and (4.7) can be simplified.

$$\hat{u} \approx \frac{1}{a}M = i\sigma\left(\frac{l}{h}\right)M \tag{4.21}$$

$$\hat{\eta} \approx M \tag{4.22}$$

These two equations, Eqs. (4.21) and (4.22), are sufficiently accurate to account for the tidal velocity $\hat{u}$ and tidal level $\hat{\eta}$ in the deep bay with an aspect ratio l/h of less than 6.85×10^3. In this case, the ocean bottom drag effect seldom influences the tidal currents. According to Eq. (4.21) and Fig. 4.3, the effect of the mass conservation equation Eq. (4.2) mainly dominates that of the momentum equation Eq. (4.1). Also, Eq. (4.21) includes "i". Therefore, the phase of tidal current $\arg(\hat{u})$ in a bay is 1/4 T (3 h) earlier than that $\arg(M)$ of the ocean tide. As a consequence, the maximum peaks of u in a bay appear at incoming tide. The minimum peaks of u in a bay emerge at outgoing tide. The tidal velocity magnitude $|\hat{u}|$ is proportional to length l and inversely proportional to depth h. Actually, $|\hat{u}|$ is proportional to aspect ratio l/h. Apparently, Eq. (4.22) and Fig. 4.4 suggest that the amplitude of tidal level $|\hat{\eta}|$ is no longer affected by the ocean bottom drag and is nearly corresponding to the amplitude of the ocean tide M. The phase of tidal level $\arg(\hat{\eta})$ is no longer delayed from that $\arg(M)$ of the open ocean, irrespective of the aspect ratio l/h.

(e) Cases of Sakiyama and Amitori bays

Based on the discussions presented above, one can then turn to consider the properties of tidal currents in the Sakiyama and Amitori bays, which are similar to the idealized rectangular semi-closed bays discussed in the previous subsections.

In Sakiyama Bay, the representative length l and depth h are estimated, respectively, as approximately 2000 and 2 m. Figure 4.5 shows a time series of tidal velocity and tidal level during one day under the settings of Sakiyama Bay, when M = 0.5 m. The tidal level in the bay corresponds to that of the open ocean. Amplitude decay and phase lag no longer occur. The amplitude of tidal velocity $|\hat{u}|$ in the bay is 0.073 m/s, and the phase of tidal velocity $\arg(\hat{u})$ in the bay is 1/4 T (3 h) earlier than that $\arg(M)$ of the open ocean. The aspect ratio l/h in Sakiyama Bay is 1000, which is categorized as a "deep bay" ($A = 0.00164 + i0.0297$, $a = -6.88i$). Its physical features are consistent with those presented in the earlier discussion.

In Amitori Bay, located at the next to Sakiyama Bay, the representative length l and depth h are estimated, respectively, as about 3000 and 50 m. Figure 4.6 shows a time series of tidal velocity u and tidal level η during one day under the settings of Amitori Bay, when M = 0.5 m. The amplitude of tidal level $|\hat{\eta}|$ in the bay corresponds to that M of the open ocean. The amplitude decay and phase lag no longer occur as they do in Sakiyama Bay. The amplitude of tidal velocity $|\hat{u}|$ in the bay is 0.0043 m/s. The phase of tidal current $\arg(\hat{u})$ is 1/4 T (3 h) earlier than that $\arg(M)$ of the ocean tide. The aspect ratio l/h of Amitori Bay is 60, which is also categorized as a "deep bay" (A = 0.0000581 + i0.0445, a = −114i).

Both Sakiyama and Amitori bays show "deep bay" behavior, but the aspect ratio l/h of Sakiyama Bay is about 17 times higher than that of Amitori Bay. Furthermore, the amplitude of tidal velocity u in Sakiyama Bay is about 17 times larger than that of Amitori Bay, consistent with Eq. (4.21) in the "deep bay" theory.

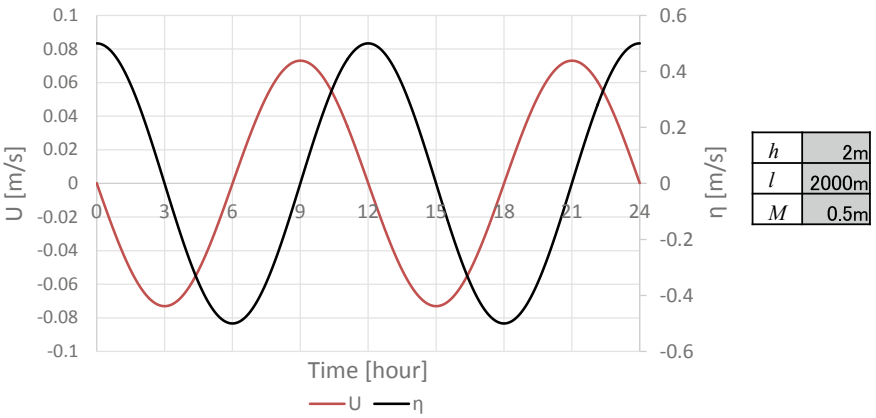

Fig. 4.5 Time series of tidal level $\hat{\eta}$ and current velocity $\hat{u}$ in Sakiyama Bay, as predicted by the theory of tidal flow dynamics in a single channel

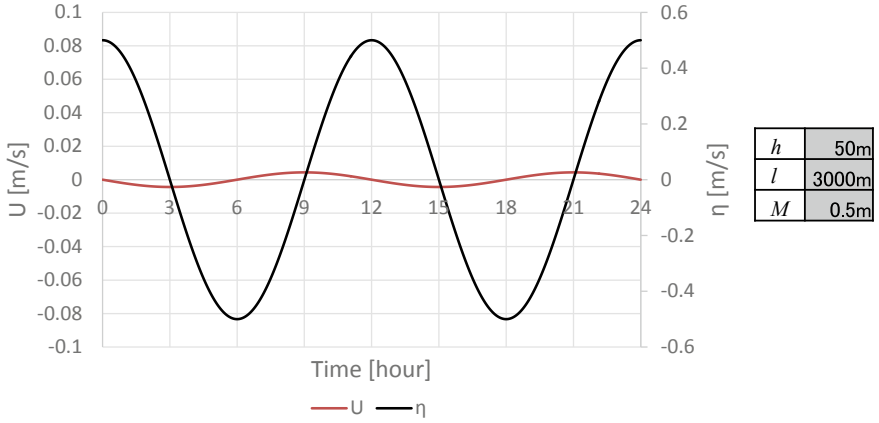

Fig. 4.6 Time series of tidal level $\hat{\eta}$ and current velocity $\hat{u}$ in Amitori Bay, as predicted using the theory of tidal flow dynamics in a single channel

In Sakiyama Bay with larger l/h, the seawater exchange at the near-surface layer might take place actively. In Amitori Bay with smaller l/h, surface seawater is likely to stagnate in a bay. Such a difference of physical properties might strongly influence the soil particle transport from rivers and the resultant distributions of coastal oceanic ecosystems.

Any bay in the northwestern part of Iriomote Island is classified as a "deep bay," which is explainable by Eqs. (4.21) and (4.22) in the previous subsection. It should be remembered that the distributions of physical properties are never homogeneous in a realistic bay, while the tidal flow theory in this study is assumed to be horizontally homogeneous in an idealized bay.

4.3 Observations and Simulations

In this section, we next examine detailed current fields within Amitori Bay, based on results of in situ observations and numerical simulations.

(a) **In situ observations**

First, observational results of coastal currents within Amitori Bay are discussed in this subsection. We conducted in situ observations during two months from October 2010. Detailed explanations have been made of the observational instruments used for this study in Chap. 2. As presented in Fig. 4.7, a total of five observational points are present within the area in Amitori Bay. Those points are distributed uniformly and broadly within Amitori Bay to identify the horizontal properties of coastal currents in the semi-closed bay. Observed data are the temperature (Points 1, 2, 3, 4, and 5 at three depths), salinity (Points 1 and 5 at two depths), illuminance

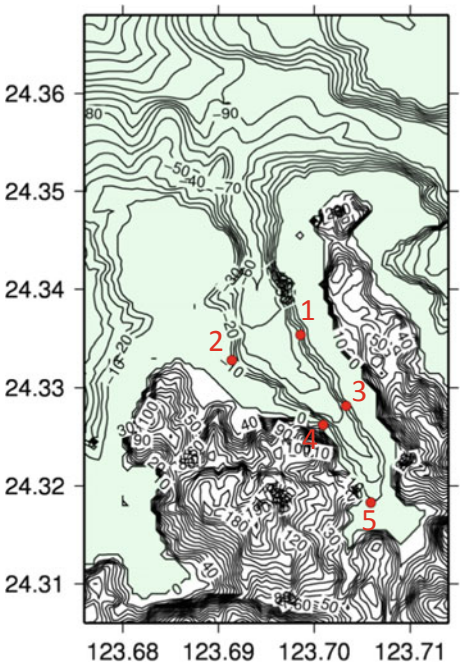

Fig. 4.7 Computational domain of CCM shown with five observational points in Amitori Bay. Referred from Yoshino et al. (2011)

(Points 1, 3, 4, and 5 at a one depth), tidal level (Point 2), significant wave height (Point 2), wave direction (Point 2), wave direction (Point 2), and current velocity (Point 2).

As described herein, we specially examine the observational results of temperature and salinity. Figure 4.8 shows time series of three-depth temperatures at the five observational points during November 2–7, 2010, under mostly cloudy conditions with weaker meteorological forcing. Especially at Points 1, 3, and 5, a considerable temperature drop is apparent at a 1 m depth. Such a large temperature drop in the surface layer might be regarded as attributable to "radiative cooling" during night time. However, that reason might be excluded from several possible causes, suggesting cloudy conditions during this period and no temperature drop at Point 2. Radiative cooling might occur homogeneously, depending not on the observational points because the target bay is sufficiently narrow that it is not affected by inhomogeneities of meteorological forcing. Granting that there may be substantial radiative cooling at the ocean surface, one might infer that temperature drops would take place anywhere in Amitori Bay. One another reason for surface temperature drops might be "vertical mixing (entrainment)" with cold deep water. However, that might be incorrect because the deeper water has higher temperature than the surface water, as presented in Fig. 4.8. The "horizontal advection" of cold river water may be another reason for partial temperature drops in Amitori Bay. We can infer that the river water with a lower temperature at the surface layer in this season flows out from the bay to the ocean. It would hardly be surprising if

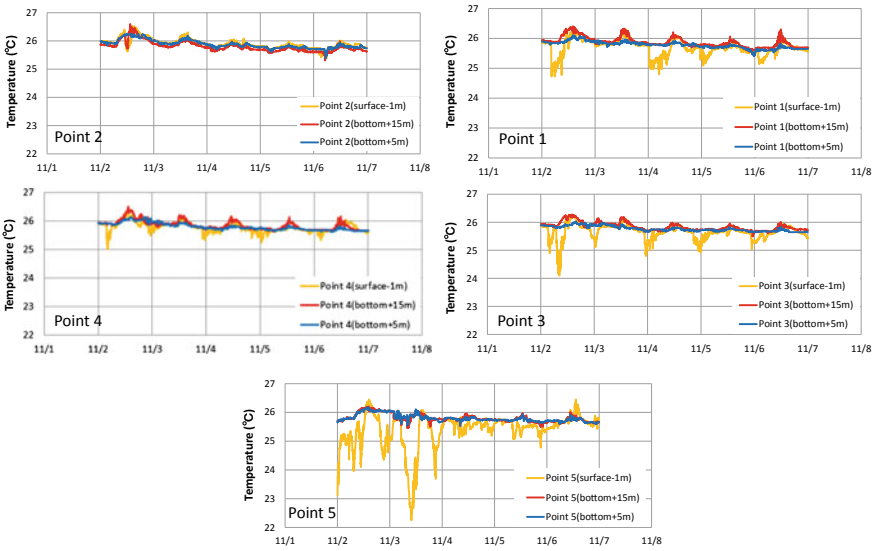

Fig. 4.8 Time series of temperature at −1 m from the sea surface, +15 m from the bottom, +5 m from the bottom, and at the five observational points shown in Fig. 4.7. Referred from Yoshino et al. (2011)

horizontal advection of the river water occurs selectively in the bay, except for Points 2 and 4.

The assumption of "horizontal advection" can be justified by the tidal flow dynamics discussed in the previous section. Figure 4.9 shows a time series of the tidal level at Point 2 during the same period as Fig. 4.8. Because Amitori Bay is classified as a "deep bay," the tidal level within the bay changes in phase with the ocean tide, and the tidal current within the bay stagnates uniformly. Comparison between Figs. 4.8 and 4.9 indicates that surface temperature drops are synchronized with outgoing tide during night time. The phase lag of temperature drop at Point 1 is regarded as resulting from the longer traveling time from the river mouth to Point 1. The night-time temperature drops in the outgoing tide are visible at the eastern side of Amitori Bay (e.g., Point 1), but not at the opposite (western) side (e.g., Point 2). The amount of temperature drop at Point 3 is larger than that at the opposite side (Point 4). The temperature drops in the outgoing tide have not been observed during the daytime, perhaps because of the compensation of low-temperature advections and weak radiation heating. Consequently, a distinct west–east asymmetry is apparent in the mixing processes between tidal water flow and river water flow within Amitori Bay.

Figure 4.10 shows the horizontal distributions of observed surface temperatures averaged temporally over six-day periods and interpolated horizontally. Higher ocean water temperatures are located at the western side of Amitori Bay. Lower river water temperatures are shifted to the opposite (eastern) side. It is readily

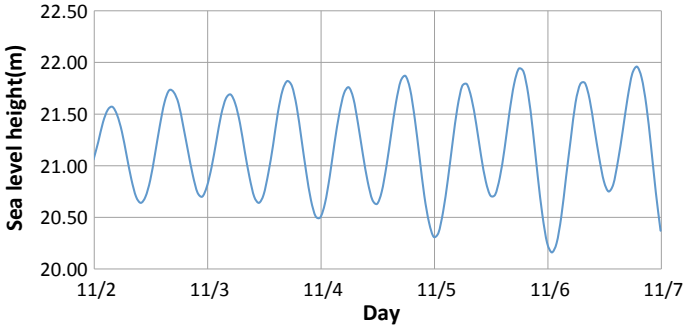

Fig. 4.9 Time series of sea level height at Point 2 in Amitori Bay. Referred from Yoshino et al. (2011)

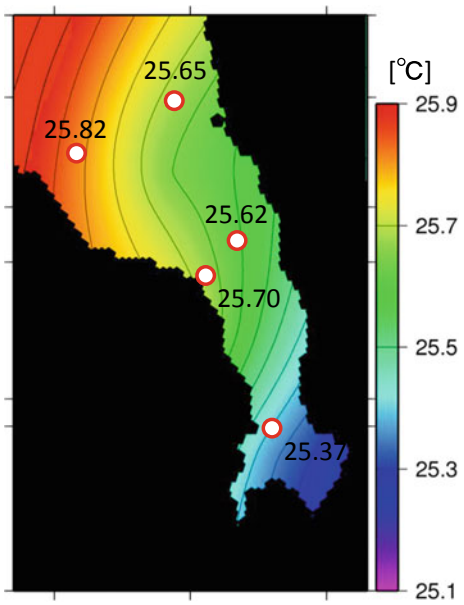

Fig. 4.10 Horizontal distribution of sea surface temperatures averaged during 6 days observed in Amitori Bay. Referred from Yoshino et al. (2011)

apparent that there is a strong west–east asymmetry of surface temperature. The averaged distributions show clear asymmetry, implying that asymmetric tidal currents dominates steadily under calm conditions with cloudy skies and low wind speeds. In situ observations suggest that for some reason, low-temperature and low-salinity river water is likely to flow selectively in the eastern side in Amitori Bay. By contrast, high-temperature and that high-salinity ocean water is prone to dominate in the western side in Amitori Bay.

(b) **Numerical simulations**

Next, the physical properties of tidal currents in Amitori Bay can be discussed based on the results of numerical simulations obtained using a multi-sigma-coordinate coastal current model (CCM) (Murakami et al. 2004). Detailed information related to the CCM is presented in Chap. 3. The computational domain having grid size of 50 m is presented in Fig. 4.7. In the lateral boundary conditions of CCM, the tidal level is defined by the outputs of ocean tidal model NAO (Matsumoto et al. 2000). The salinity in the open ocean is set to 34.4 ‰, held constant during the simulation periods. In the two rivers located at the head of Amitori Bay, the river flow rate and salinity are fixed, respectively, at 0.01 m^3/s and 0‰ during the simulation periods. The momentum, temperature, mass, and salinity conservation equations are numerically integrated during October 4–9, 2010 (a total of five days) with a time step interval of 1 s.

Because the numerical simulations in this study are designed to elucidate the mixing processes between the ocean water and river water in Amitori Bay, meteorological forcing at the sea surface (the fluxes of water, heat, radiation, and momentum) is fixed at zero in CCM. Therefore, no circulation occurs in the bay driven by wind and buoyancy. We can consider the salinity as a passive tracer.

Figure 4.11 portrays the horizontal distributions of salinity and current velocity vectors at the surface layer in the outgoing tide (21:00UTC October 7, 2010) and incoming tide (15:00UTC October 7, 2010). In the outgoing tide presented in

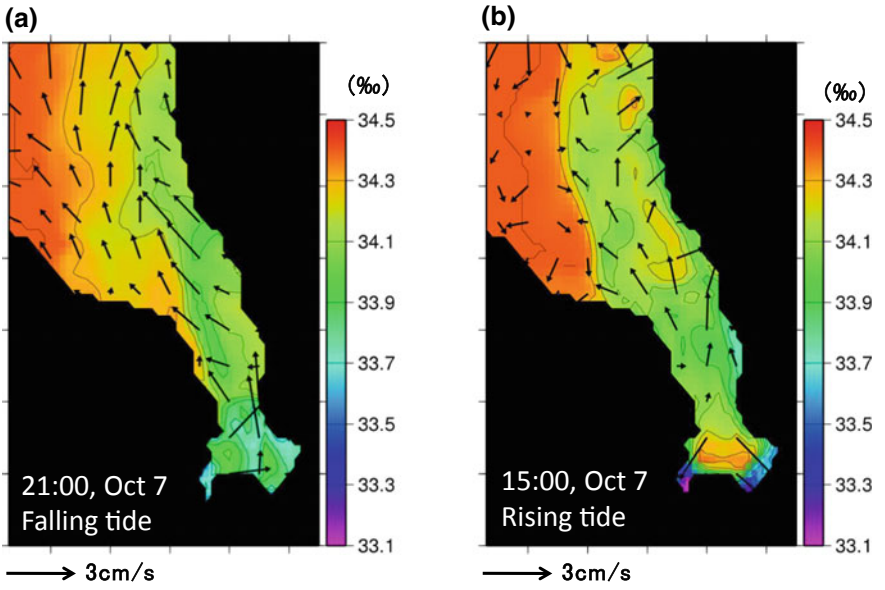

Fig. 4.11 Horizontal distributions of surface current vectors and surface salinity simulated in Amitori Bay in **a** falling tide and **b** rising tide. Referred from Yoshino et al. (2011)

Fig. 4.11a, low-salinity water originating from two rivers spreads from the head to the mouth of Amitori Bay. As shown previously, the low-salinity river water selectively flows out to the eastern side of Amitori Bay (right side of the figure). In the incoming tide presented in Fig. 4.11b, the upwelling of the high-salinity water originating from the open ocean is apparent near the head of the bay. Upwelling flows near Point 5 result from the exit of the sea valley portrayed in Fig. 4.7. At the time of the incoming tide, the low-salinity river water from the river mouth is trapped close to the head of the bay. The low-salinity river water in the middle of the bay, which is transported in the previous incoming tide, is mixed with the high-salinity ocean water near the center. The mixing processes between river water and ocean water never reach to the western side of Amitori Bay. Such physical properties of tidal flow in Amitori Bay are characterized as a deep bay in which tidal velocity is weaker and as calm conditions in which the meteorological forcing is weaker.

Figure 4.12 shows the horizontal distributions of salinity and current velocity vectors at the surface layer averaged during the three-day periods (last half of the simulation periods). It is readily apparent that the river water, on average, is consistently flowing out to the eastern side of the bay and that it is unlikely to affect the opposite (western) side of the bay. Such a west–east asymmetry of tidal currents is expected to control, indirectly, the asymmetries of the horizontal distribution and coverage of coral reefs, which is apparent in Amitori Bay.

Why does the west–east asymmetry of tidal currents appear at the surface layer in Amitori Bay? When we assume that river water flows at the surface without the

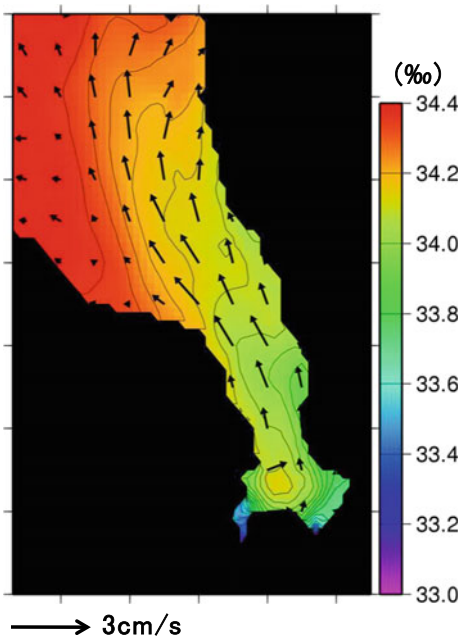

Fig. 4.12 Horizontal distributions of surface current vectors and surface salinity averaged during 3 days simulated in Amitori Bay. Referred from Yoshino et al. (2011)

effects of friction and entrainment, then the potential vorticity PV of a river water mass should be conserved as shown below.

$$\mathrm{PV} = \frac{\zeta_z + f}{h} = \text{const.} \tag{4.23}$$

In that equation, h represents the river water depth, ζ_z signifies the vertical vorticity of the river water, f denotes the planetary vorticity ($= 2\Omega\sin\phi$), Ω expresses the angular velocity of the Earth's rotation, and ϕ stands for the latitude. In Amitori Bay, located in the Northern Hemisphere, the initial value of PV is expected to be greater than 0 because of $\zeta_z = 0$ and $f > 0$. When a water mass flows out from the mouth of river, then the water mass will spread out with decreasing depth h. To conserve the potential vorticity PV, the vertical vorticity ζ_z is expected to be less than 0. As a result, negative vertical vorticity ($\zeta_z < 0$) may cause a counterclockwise rotation of the river flow. In other words, the Earth's rotation changes northward currents from the river to the eastward. Therefore, the river flow is steered toward right side (left side) in the Northern (Southern) Hemisphere. At the equator, the Earth's rotation never affects the river flow in the bay.

Figure 4.13 shows the horizontal distributions of salinity and current velocity vectors at the surface layer averaged during the three-day periods (last half of the simulation periods) in the case of (a) Northern Hemisphere ($\phi = +24°$), (b) equator ($\phi = 0°$), and (c) Southern Hemisphere ($\phi = -24°$). These sensitivity experiments indicate that, in Amitori Bay, the surface river water is likely to flow to the eastern (western) side of the bay in the case of the Northern (Southern) Hemisphere, and shows no west–east asymmetry in the case of the equator. Consequently, it can be concluded that the asymmetric flow of a surface river water mass, which can be confirmed in observations and simulations, results from the effect of the Earth's rotation called as the "Colioris force."

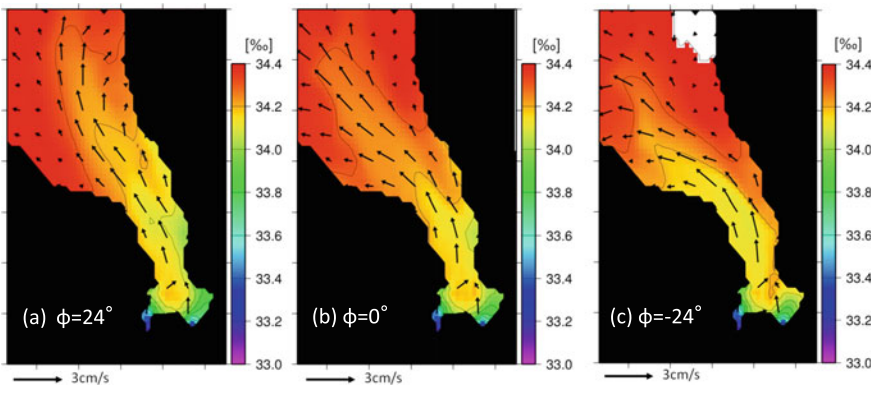

Fig. 4.13 Horizontal distributions of surface current vectors and surface salinity averaged during 3 days simulated as **a** $\phi = 24°$, **b** $\phi = 0°$ and **c** $\phi = -24°$

However, when entrainment, ocean bottom drag, and meteorological forcing are strong, then the conservation law of potential vorticity expressed in Eq. (4.23) is not valid, leading to a lack of asymmetric pattern of a surface river flow. It is expected that such an asymmetric pattern is a typical phenomenon under the "deep bay" (i.e., small aspect ratio of a bay) with the "calm conditions" (i.e., low wind speeds).

4.4 Concluding Remarks

The physical properties of coastal currents in semi-closed bays in the northwestern part of Iriomote Island were examined as described in this chapter based on theoretical, observational, and numerical investigations.

The tidal flow dynamics in a single channel, introduced in this chapter, indicated that Sakiyama and Amitori bays were classified as "deep bays," for which the amplitude and phase of tidal level in the bay were the almost same as those in the open ocean and for which the tidal velocity in incoming tide (outgoing tide) showed a maximum (minimum) peak. In Sakiyama Bay with its lager aspect ratio (with shallower floor), the tidal seawater exchange was relatively high. Surface river water flowed easily out to the open ocean under calm conditions. In Amitori Bay with a smaller aspect ratio (with deeper floor), the tidal seawater exchange was relatively weak. Surface river water from the head of the bay was likely to stagnate. Under calm conditions, the stagnant river water flowed selectively out to the eastern side of the bay because of the effects of Earth's rotation. The differences of physical properties between Sakiyama and Amitori bays can be explained by the different aspect ratio of the bays.

Such influential differences of tidal flow patterns are regarded as affecting the differences of distribution and structure of coastal ocean ecosystems in this area.

Acknowledgements Technical assistance with observational and numerical investigations was graciously provided by Mr. Kota Noguchi in Penta-Ocean Construction Co., Ltd.

References

Matsumoto K, Takanezawa T, Ooe M (2000) Ocean tide models developed by assimilating TOPEX/POSEIDON altimeter data into hydrodynamical model: a global model and a regional around Japan. J. Oceanography 56:567–581

Murakami T, Yasuda T, Ohsawa T (2004) Development of a multi-sigma coordinate model coupled with an atmospheric model for the calculation of coastal currents. Ann J Coast Eng 51:366–370 (in Japanese with English abstract)

Unoki S (1993) Coastal ocean physics, Tokai University Press, 672 p (in Japanese)

Yoshino J, Noguchi K, Ukai A, Nakase K, Kohno H, Kimura K, Murakami T, Yasuda T (2011) Relationships between ocean current fields and coral habitat environment in Amitori Bay, Iriomote Is., Japan. Ann J Civil Eng Ocean 67(2):I_43–I_48 (in Japanese with English abstract)
Yoshino J, Murakami T, Ukai A, Kohno H, Kita K, Shimokawa S, Sakihara K, Mizutani A (2016) Seawater exchange processes through the bays of Shiarahama and Funauki in Iriomote Island, Okinawa, Japan. J Japan Soc Civil Eng B2 72(2):I_1207–I_1212 (in Japanese with English abstract)

Chapter 5
Dynamical Properties of Coastal Currents in the Northwestern Part of Iriomote Island Part. 2—Funauki and Shirahama Bays

Jun Yoshino, Tomokazu Murakami, Akiyuki Ukai, Hiroyoshi Kohno, Shinya Shimokawa, Kouta Nakase and Akira Mizutani

Abstract This chapter presents investigation of the physical properties of tidal flows in two semi-closed bays connected with a channel based on theoretical, observational and numerical frameworks. Shirahama Bay with shallower water and Funauki Bay with deeper water in the northwestern part of Iriomote Island are mutually connected by a channel. Tidal flows in both bays are expected to be much more complex than those of Sakiyama and Amitori bays, discussed in Chap. 4. According to the tidal flow dynamics in Chap. 4, the seawater exchange in Shirahama Bay is more active because of its shallower water floor, whereas the seawater exchange in Funauki Bay is more stagnant because of its deeper water

This chapter is based on works reported by Yoshino et al. (2016, 2018).

J. Yoshino (✉)
Faculty of Engineering, Gifu University, Gifu, Japan
e-mail: jyoshino@gifu-u.ac.jp

T. Murakami · S. Shimokawa
Storm, Flood and Landslide Research Division, National Research Institute for Earth Science and Disaster Resilience, Tsukuba, Japan
e-mail: tmurakami@bosai.go.jp

S. Shimokawa
e-mail: shimokawa@bosai.go.jp

A. Ukai · K. Nakase
Environment Business Division, Penta-Ocean Construction Co., Ltd., Tokyo, Japan
e-mail: Akiyuki.Ukai@mail.penta-ocean.co.jp

K. Nakase
e-mail: Kouta.Nakase@mail.penta-ocean.co.jp

H. Kohno · A. Mizutani
Okinawa Regional Research Center, Tokai University, Yaeyama, Japan
e-mail: hkohno@scc.u-tokai.ac.jp

A. Mizutani
e-mail: ma110267@tsc.u-tokai.ac.jp

S. Shimokawa et al. (eds.), *Geophysical Approach to Marine Coastal Ecology*, Springer Oceanography, https://doi.org/10.1007/978-981-15-1129-5_5

floor. Consequently, the low-salinity water originating from a river is likely to be retarded in Funauki Bay under near-calm conditions. In the case of a smaller aspect ratio (shallower and longer) of the connecting channel, the seawater exchange among the bays becomes inactive. In the case of the moderate aspect ratio of the connecting channel, which is comparable with those of both bays, the seawater exchange among the bays reaches a maximum. For a larger aspect ratio (deeper or shorter) of the connecting channel, the seawater exchange will stagnate not only between the bays, but also between the bays and the open ocean. The aspect ratio of the connecting channel, which strongly affects the tidal currents in both bays, is expected to strongly influence on the dispersions of eggs and seeds in the coastal ocean ecosystems in this region.

Keywords Iriomote Island · Shirahama Bay · Funauki Bay · Coastal current · Seawater exchange · Tidal flow · River flow · Connecting channel

5.1 Introduction

In the coastal area in the northwestern part of Iriomote Island, there are intricate semi-closed bays consisting of (from south to north) Sakiyama Bay, Amitori Bay, Funauki Bay and Shirahama Bay (referred to Sect. 1.1, Sect. 1.2 and Fig. 1.1). Funauki and Shirahama bays, which are located north of the Sakiyama and Amitori bays discussed in Chap. 4, have respective vertical depths of 80 m and 40 m, giving rise to a great difference in the depth. We can infer that such a great difference leads to differences in the physical properties of coastal currents among the bays. The heads of Funauki and Shirahama bays have river mouths of Kuira River and Nakara River, respectively. Moreover, they are mutually linked by a connecting channel. The existence of that connecting channel might cause complicated tidal flows. The behaviors will therefore be more complex than those of Sakiyama and Amitori bays discussed in Chap. 4.

The heads of Funauki and Shirahama bays are home to the tropical seaweed *Enhalus acoroides*, as discussed in Sect. 1.5, in which the Yaeyama Islands, Okinawa, Japan are situated at the northern extreme. The *Enhalus acoroides* generally develop colonies near the river mouth, where waves are constantly calm (Yoshida et al. 2007). Recently, however, *Enhalus acoroides* has come to be listed as a category II endangered species in the Red List by the Ministry of the Environment. Its colonies are reported to be decaying and disappearing from Funauki and Shirahama bays (Takeyama et al. 2014). Especially in Funauki Bay, although some colonies of *Enhalus acoroides* have existed in the past, most are currently disappearing, because of feeding damage inflicted by green turtles (Mizutani et al. 2016) among other reasons. To conserve and restore the *Enhalus acoroides* colonies in this region, the seed and fruit dispersion processes in this region must be understood. To elucidate those processes, it is important in turn to

discuss the physical properties of tidal flows in Funauki and Shirahama bays with their connecting channel.

This chapter describes the theoretical, observational and numerical investigations on the coastal currents in Funauki and Shirahama bays, which are mutually connected by a single channel.

5.2 Tidal Flow Dynamics in a Complex Channel Network

(a) Theoretical formula

We first examine the physical properties of tidal flow in Funauki and Shirahama bays in the northwestern part of Iriomote Island, based on the tidal flow theory in a complex channel network (Unoki 1993). The existence of a connecting channel linking Funauki and Shirahama bays is expected to complicate the flow structure, compared to a single channel such as that in Sakiyama and Amitori bays, discussed in Chap. 4. This section explains the tidal flow dynamics in the complex channel network. Subsequently, we discuss the influence of the connecting channel on Funauki and Shirahama bays.

Funauki and Shirahama bays with a connecting channel are simplified and idealized herein by three channels and two bays, as shown in the schematic diagram in Fig. 5.1. Bay 1 and Bay 2 have the same area A. They are connected respectively with the open ocean by Channel 1 and Channel 2. Bay 1 and Channel 1 are associated with Shirahama Bay. Bay 2 and Channel 2 correspond to Funauki Bay. Bay 1 and Bay 2 are mutually connected by Channel 3, analogous to the connecting channel. η_0 represents the tidal level in the open ocean. Also, η_1 and η_2 respectively stand for the tidal levels in Bay 1 and Bay 2. In the three channels, u, w, l and h respectively denote the velocity, width, length, and depth. Their suffix represents the number of three channels. The current velocity u_1 (u_2) from the open ocean to Bay 1 (Bay 2) is positive. Velocity u_3 from Bay 1 to Bay 2 is positive. Consequently, the momentum equations in Channel 1, Channel 2 and Channel 3 and the mass continuity equations in Bay 1 and Bay 2 are described as shown below.

$$\frac{\mathrm{d}u_1}{\mathrm{d}t} = -g\frac{\eta_1 - \eta_0}{l_1} - \frac{\beta u_1}{h_1} \tag{5.1}$$

$$\frac{\mathrm{d}u_2}{\mathrm{d}t} = -g\frac{\eta_2 - \eta_0}{l_2} - \frac{\beta u_2}{h_2} \tag{5.2}$$

$$\frac{\mathrm{d}u_3}{\mathrm{d}t} = -g\frac{\eta_2 - \eta_1}{l_3} - \frac{\beta u_3}{h_3} \tag{5.3}$$

$$\mathrm{A}\frac{\mathrm{d}\eta_1}{\mathrm{d}t} = w_1 h_1 u_1 - w_3 h_3 u_3 \tag{5.4}$$

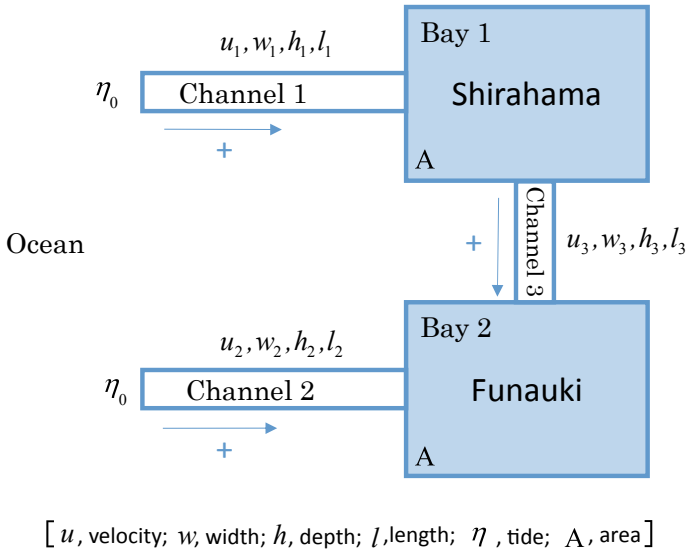

Fig. 5.1 Schematic diagram showing tidal flow dynamics in a complex channel network, simplifying Shirahama and Funauki bays with a connecting channel. Referred from Yoshino et al. (2016)

$$\mathrm{A}\frac{\mathrm{d}\eta_2}{\mathrm{d}t} = w_2 h_2 u_2 + w_3 h_3 u_3 \tag{5.5}$$

In those equations, g represents gravitational acceleration. The ocean bottom drag expressed by the second terms in Eqs. (5.1), (5.2), and (5.3) is assumed to be proportional to the first power of the current velocity, where $\beta = (8/3\pi)C_f\hat{U} = 6.85 \times 10^3$. In these equations, the meteorological forcing is negligible under near-calm conditions.

To solve the linear equations system above, the temporal variations of the tidal level η and current velocity u respondent to the tidal level η_0 in the open ocean can be represented as the following exponential forms.

$$\begin{aligned} &\eta_0 = M\mathrm{e}^{i\sigma t}, \eta_1 = \hat{\eta}_1\mathrm{e}^{i\sigma t}, \eta_2 = \hat{\eta}_2\mathrm{e}^{i\sigma t}, \\ &u_1 = \hat{u}_1\mathrm{e}^{i\sigma t}, u_2 = \hat{u}_2\mathrm{e}^{i\sigma t}, u_3 = \hat{u}_3\mathrm{e}^{i\sigma t} \end{aligned} \tag{5.6}$$

In those expressions, M (real number) stands for the amplitude of the tidal level in the open ocean. Also, $\hat{\eta}$ and $\hat{u}$ (complex number) represent the amplitude and phase change of the tidal level and current velocity. The amplitude of tidal level and current is expressed, respectively, by $|\hat{\eta}|$ and $|\hat{u}|$. The phase change of the tidal level and current is presented, respectively, as $\arg(\hat{\eta})$ and $\arg(\hat{u})$. σ $(= 2\pi/T)$ is the radian frequency of the tidal level η_0 in the open ocean with a period T of 12 h.

Substituting Eq. (5.6) into Eqs. (5.1), (5.2), (5.3), (5.4) and (5.5), we can obtain the following first-order algebraic equations system as

$$\hat{\eta}_1 + A\hat{u}_1 = M \tag{5.7}$$

$$\hat{\eta}_2 + B\hat{u}_2 = M \tag{5.8}$$

$$\hat{\eta}_1 - \hat{\eta}_2 + C\hat{u}_3 = 0 \tag{5.9}$$

$$\hat{\eta}_1 - a\hat{u}_1 + c\hat{u}_3 = 0 \tag{5.10}$$

$$\hat{\eta}_2 - b\hat{u}_2 - c\hat{u}_3 = 0 \tag{5.11}$$

where A and a in Eqs. (5.7), (5.8), (5.9), (5.10) and (5.11) are complex number as

$$\begin{aligned} A &= \left(i\sigma + \frac{\beta}{h_1}\right)\frac{l_1}{g}, \quad a = -i\frac{w_1 h_1}{\sigma A} \\ B &= \left(i\sigma + \frac{\beta}{h_2}\right)\frac{l_2}{g}, \quad b = -i\frac{w_2 h_2}{\sigma A} \\ C &= \left(i\sigma + \frac{\beta}{h_3}\right)\frac{l_3}{g}, \quad c = -i\frac{w_3 h_3}{\sigma A} \end{aligned} \tag{5.12}$$

where i is the imaginary unit. It is better to express these equations in matrix form as

$$\begin{bmatrix} 1 & 0 & A & 0 & 0 \\ 0 & 1 & 0 & B & 0 \\ 1 & -1 & 0 & 0 & -C \\ 1 & 0 & -a & 0 & c \\ 0 & 1 & 0 & -b & -c \end{bmatrix} \begin{bmatrix} \hat{\eta}_1 \\ \hat{\eta}_2 \\ \hat{u}_1 \\ \hat{u}_2 \\ \hat{u}_3 \end{bmatrix} = \begin{bmatrix} M \\ M \\ 0 \\ 0 \\ 0 \end{bmatrix} \tag{5.13}$$

Because Eq. (5.13) is described in the form of $\mathbf{Ax} = \mathbf{b}$, the solution vector $\mathbf{x}$ is solvable using the Cramer's rule. Consequently, the exact solutions of $\hat{u}_1, \hat{u}_2, \hat{u}_3, \hat{\eta}_1$, and $\hat{\eta}_2$ are obtainable as presented below.

$$\hat{u}_1 = \frac{2Bc + (B+b)C}{A(B+b)c + (A+a)Bc + (A+a)(B+b)C}M \tag{5.14}$$

$$\hat{u}_2 = \frac{2Ac + (A+a)C}{A(B+b)c + (A+a)Bc + (A+a)(B+b)C}M \tag{5.15}$$

$$\hat{u}_3 = \frac{-A(B+b) + (A+a)B}{A(B+b)c + (A+a)Bc + (A+a)(B+b)C}M \tag{5.16}$$

$$\hat{\eta}_1 = \frac{(Ab + aB)c + a(B + b)C}{A(B + b)c + (A + a)Bc + (A + a)(B + b)C} M \tag{5.17}$$

$$\hat{\eta}_2 = \frac{(Ab + aB)c + (A + a)bC}{A(B + b)c + (A + a)Bc + (A + a)(B + b)C} M \tag{5.18}$$

As discussed in the preceding chapter, because both Funauki and Shirahama bays are categorized as deep bays, the assumptions of $A + a \approx a$ and $B + b \approx b$ can be valid. Therefore, Eqs. (5.14), (5.15), (5.16), (5.17) and (5.18) can be simplified as

$$\hat{u}_1 = \frac{2Bc + bC}{Abc + aBc + abC} M \tag{5.19}$$

$$\hat{u}_2 = \frac{2Ac + aC}{Abc + aBc + abC} M \tag{5.20}$$

$$\hat{u}_3 = \frac{-Ab + aB}{Abc + aBc + abC} M \tag{5.21}$$

$$\hat{\eta}_1 = \frac{Abc + aBc + abC}{Abc + aBc + abC} M = M \tag{5.22}$$

$$\hat{\eta}_2 = \frac{Abc + aBc + abC}{Abc + aBc + abC} M = M \tag{5.23}$$

which are the approximate solutions in deep bays. These equations indicate that the tidal flows in Channel 1 (Bay 1) and Channel 2 (Bay 2) are influenced by the flow of Channel 3 (connecting channel), because Eqs. (5.19), (5.20), and (5.21) include complex parameters C and c representing the Channel 3 shape. Conversely, the tidal flow in Channel 3 also depends on the flows in Channel 1 (Bay 1) and Channel 2 (Bay 2), implying that all channels mutually interact in a complex manner. However, the amplitudes of tidal levels in Bay 1 and Bay 2 are nearly equal to the amplitude in the open ocean M, suggesting that the amplitude reduction and phase shift are sufficiently small to be negligible when Bay 1 and Bay 2 are "deep bays."

(b) **Case of Funauki and Shirahama bays**

Based on the exact solutions of Eqs. (5.14), (5.15), (5.16), (5.17) and (5.18), one can next consider the tidal flows in Funauki and Shirahama bays. The depth of Shirahama Bay (i.e., Channel 1) is estimated as $h_1 = 40$ m. The depth of Funauki Bay (i.e., Channel 2) is estimated as $h_2 = 80$ m. In this study, to simplify the problem, width w and length l in Funauki and Shirahama bays are mutually coincident. Therefore, the areas of the two bays are set to the same values. We herein assume the representative values $l_1 = l_2 = 5000$ m, $w_1 = w_2 = 500$ m and $A = 2,500,000$ m^2. Then, the aspect ratio of Shirahama Bay (Channel 1) is $l_1/h_1 = 125$. That of Funauki Bay (Channel 2) is $l_2/h_2 = 62.5$. Furthermore, the

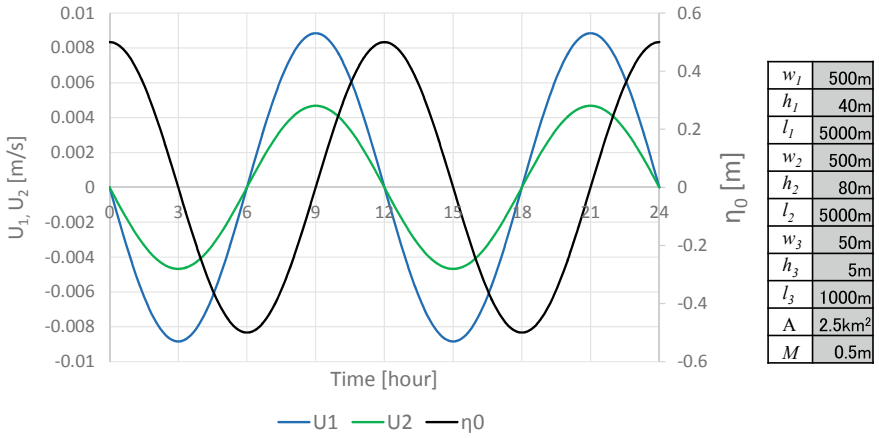

w_1	500m
h_1	40m
l_1	5000m
w_2	500m
h_2	80m
l_2	5000m
w_3	50m
h_3	5m
l_3	1000m
A	2.5km^2
M	0.5m

Fig. 5.2 Time series of ocean tidal level and current velocity in Channel 1 and Channel 2

width, length, and depth of the connecting channel (i.e., Channel 3) are assumed to be $w_3 = 50$ m, $l_3 = 1000$ m, and $h_3 = 5$ m, resulting in an aspect ratio of $l_3/h_3 = 500$, which is much larger than those of Channel 1 and Channel 2. Under the topographic conditions, the tidal flows in Funauki and Shirahama bays are calculated using a tidal level of $M = 0.5$ m in the open ocean.

Figure 5.2 shows time series of current velocities u_1 and u_2 in Channel 1 (Shirahama Bay) and Channel 2 (Funauki Bay) during a one-day period. Because both Channel 1 and Channel 2 are categorized as "deep bays," a greater aspect ratio in those channels (with shallower and longer water) produces a greater amplitude of the current velocity. For example, Shirahama Bay, with its lager aspect ratio, has amplitude of about 0.009 m/s, which is double the corresponding value (0.0045 m/s) in Funauki Bay. It is consistent with Eq. (4.21) in Chap. 4 that the aspect ratio of Channel 1 is double the aspect ratio of Channel 2, and that the phases of tidal currents $\arg(\hat{u}_1)$ and $\arg(\hat{u}_2)$ are $1/4T$ (3 h) earlier than the phase of the ocean tide $\arg(M)$.

Figure 5.3 presents a time series of current velocity u_3 in Channel 3 (the connecting channel) during a one-day period. The tidal current amplitude is close to 0.02 m/s, which is much larger than that of either Channel 1 or Channel 2. Another characteristic is that the phase of tidal current $\arg(\hat{u}_3)$ is delayed by $1/4T$ (3 h). That result indicates that the flow from Bay 1 (Bay 2) to Bay 2 (Bay 1) occurs in the outgoing tide (incoming tide).

(c) Physical properties of the connecting channel

The previous subsection describes a strong tidal flow in Channel 3 between Bay 1 and Bay 2, in which the phase of current velocity $\arg(\hat{u}_3)$ is $1/4T$ (3 h) earlier than the phase of the ocean tide $\arg(M)$. Consequently, the water and material exchanges that occur near the surface are expected to be active between Bay 1 (Shirahama Bay) and Bay 2 (Funauki Bay). We herein discuss what physical processes can

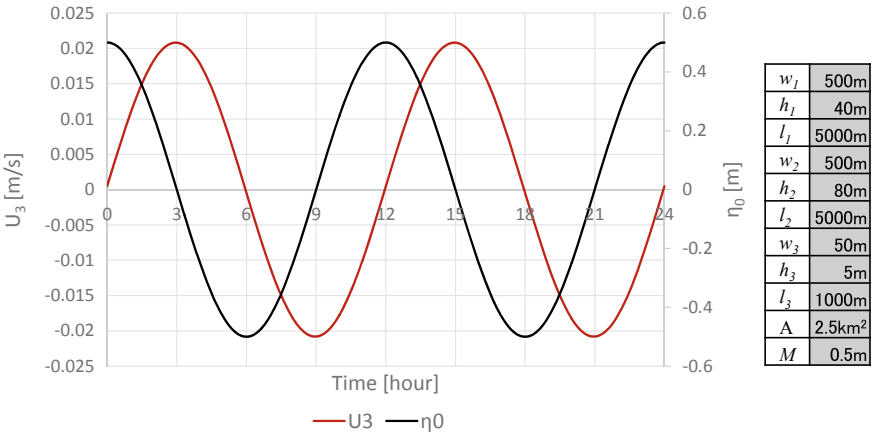

Fig. 5.3 Time series of tidal level $\hat{\eta}$ and current velocity $\hat{u}$ in Channel 3, simulated using the theory of tidal flow dynamics in a complex channel network. Referred from Yoshino et al. (2016)

control the tidal current in Channel 3. The width, length and depth of Channel 3 are set as $w_3 = 50$ m, $l_3 = 1000$ m, and $h_3 = 5$ m as the reference state. Then the respective sensitivities of depth h_1 and length l_1 are investigated.

First, Fig. 5.4 shows the time series of the current velocities u_3 of tidal flows simulated with depths h_1 of seven types in Channel 1: 10, 20, 40, 80, 160, 320, and 640 m, assuming that all other parameters are fixed. The results indicate that the amplitude of current velocity $|\hat{u}_3|$ is intensified by the difference of depth between Channel 1 and Channel 2. For $h_1 < h_2$, the phase of current velocity $\arg(\hat{u}_3)$ is shifted by $-1/4T$ (-3 h) from that of the ocean tide $\arg(M)$. In the case of $h_1 = h_2$,

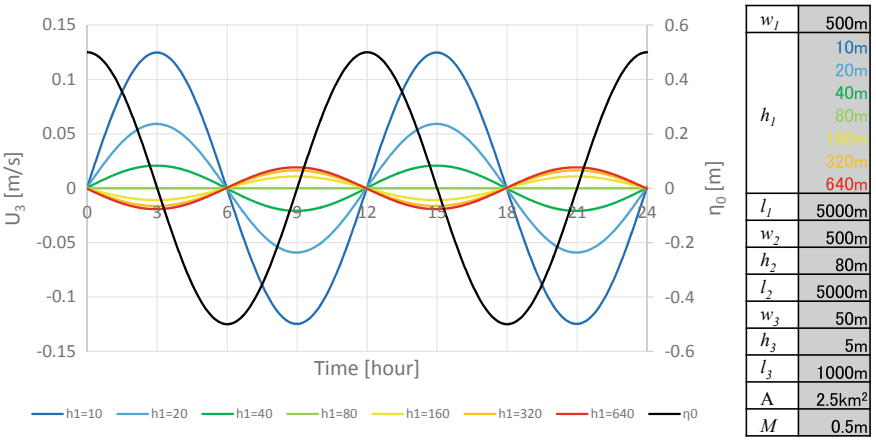

Fig. 5.4 Time series of tidal level $\hat{\eta}$ and current velocity $\hat{u}$ in Channel 3 in each of sensitivity experiments with changing depth of Channel 1. Referred from Yoshino et al. (2016)

the amplitude of the tidal velocity $|\hat{u}_3|$ will be zero, implying that no tidal flow passes through Channel 3. In the case of $h_1 > h_2$, the phase of current velocity $\arg(\hat{u}_3)$ is shifted by +1/4T (+3 h) from that of the ocean tide $\arg(M)$. Consequently, it is suggested that the flow pattern in the connecting channel is mainly controlled by the differences of depth among Funauki and Shirahama bays.

Such a phase shift presented in Fig. 5.4 is explainable by the approximated Eq. (5.21). The inequality $Ab \gg aB$ in Eq. (5.21) will hold if the Channel 1 depth is assumed to be much larger than that of Channel 2 ($h_1 \ll h_2$). Equalities $A \gg C$ and $B \gg C$ in Eq. (5.21) will be valid if the aspect ratio of Channel 3 is assumed to be much larger than those of Channel 1 and Channel 2 ($l_3/h_3 \gg l_1/h_1$ and $l_3/h_3 \gg l_2/h_2$). Then, Eq. (5.21) can be approximated as shown below.

$$\hat{u}_3 \approx \frac{-Ab}{Abc}M = -\frac{M}{c} = -i\frac{\sigma A}{w_3 h_3}M \tag{5.24}$$

Therefore, the approximated equation indicates that the large difference of depth between Channel 1 and Channel 2 ($h_1 \ll h_2$) causes the phase delay of the current velocity $\arg(\hat{u}_3)$ of Channel 3 by 1/4T (3 h) from the ocean tide $\arg(M)$ (T = 12 h) because of the "$-i$" multiplier in Eq. (5.24).

Next, Fig. 5.5 presents a time series of the current velocities u_3 of tidal flows simulated with lengths l_1 of seven types in Channel 1: 625, 1,250, 2,500, 5,000, 10,000, 20,000, and 40,000 m, assuming that all the other parameters are fixed. The results suggest that the amplitude of current velocity $|\hat{u}_3|$ in Channel 3 is intensified by the difference of length between Channel 1 and Channel 2. In the case of $l_1 < l_2$, Channel 3 will have a phase shift $\arg(\hat{u}_3)$ of +1/4T (+3 h) from the ocean tide $\arg(M)$. In the case of $l_1 = l_2$, the amplitude $|\hat{u}_3|$ and phase shift $\arg(\hat{u}_3)$ in Channel 3 will be zero. In the case of $h_1 > h_2$, the phase of current velocity $\arg(\hat{u}_3)$ in

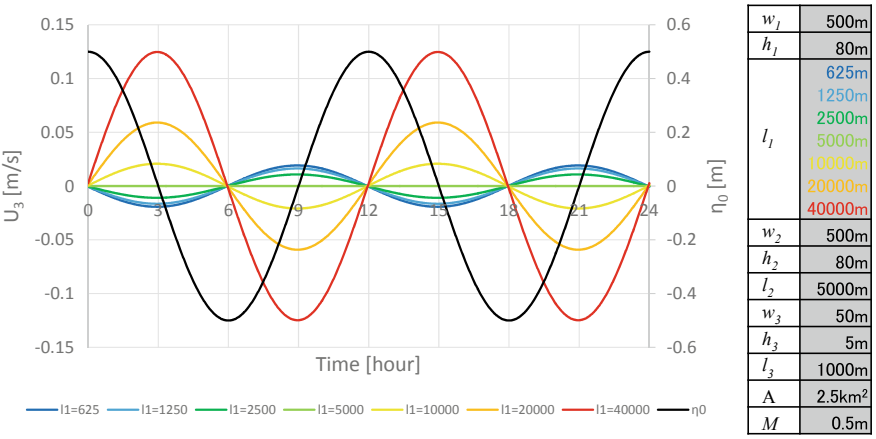

w_1	500m
h_1	80m
l_1	625m 1250m 2500m 5000m 10000m 20000m 40000m
w_2	500m
h_2	80m
l_2	5000m
w_3	50m
h_3	5m
l_3	1000m
A	2.5km^2
M	0.5m

Fig. 5.5 Time series of tidal level $\hat{\eta}$ and current velocity $\hat{u}$ in Channel 3 in each of sensitivity experiments with changing length of Channel 1. Referred from Yoshino et al. (2016)

Channel 3 will be delayed by $-1/4T$ (-3 h) from the ocean tide $\arg(M)$. Consequently, the difference of length between Channel 1 and Channel 2 shows an opposite response to that of depth presented in Fig. 5.4, implying that not only depths but also lengths in both Funauki and Shirahama bays control the tidal flow in the connecting channel.

Such a phase shift $\arg(\hat{u}_3)$ depicted in Fig. 5.5 can be understood from the rearrangement of the theoretical equation written in Eq. (5.21). The inequality $Ab \ll aB$ in Eq. (5.21) will hold if the difference of length between Channel 1 and Channel 2 is sufficiently large ($l_1 \ll l_2$). The equalities $A \gg C$ and $B \gg C$ in Eq. (5.21) will be valid if the aspect ratio of Channel 3 is much larger than those of Channel 1 and Channel 2 ($l_3/h_3 \gg l_1/h_1$ and $l_3/h_3 \gg l_2/h_2$). Then Eq. (5.21) can be approximated as presented below.

$$\hat{u}_3 \approx \frac{aB}{aBc}M = \frac{M}{c} = i\frac{\sigma A}{w_3 h_3}M \tag{5.25}$$

As a result, the large difference of length between Channel 1 and Channel 2 induces the tidal flow u_3 in Channel 3 with a phase shift of $+1/4T$ ($+3$ h) from the ocean tide $\arg(M)$ ($T = 12$ h) because of the "$+i$" multiplier in Eq. (5.25).

Based on the results described above for the sensitivity experiments of changes of depth and length in Channel 1 on the tidal flows in Channel 3, results show that the difference of aspect ratio l/h between Channel 1 and Channel 2 mainly influences the response of tidal flows u_3 in the connecting channel. The aspect ratio of Shirahama Bay is 125, which is double the aspect ratio of Funauki Bay (62.6). The greater the difference in aspect ratio between the two bays, the greater the magnitude of tidal velocity $|\hat{u}_3|$ in Channel 3. The phase of tidal velocity $\arg(\hat{u}_3)$ in Channel 3 is delayed by $1/4T$ (3 h) from the ocean tide $\arg(M)$.

5.3 Tidal Flow Simulations in a Complex Channel Network

(a) Basic equation system

Next, to identify the degree to which the aspect ratio of Channel 3 influences the tidal flows and seawater exchanges in Shirahama Bay (Channel 1 and Bay 1) and Funauki Bay (Channel 2 and Bay 2), the numerical experiments using a two-layer nonlinear tidal flow model in a complex channel network are conducted in this section. The tidal flow model will include the effects of river flow and mass transport, which are ignored in the one-layer linear model used in the preceding section.

As presented in Fig. 5.6, an idealized topography representing Shirahama Bay (Channel 1 and Bay 1) and Funauki Bay (Channel 2 and Bay 2) with the connecting channel (Channel 3) is applied in this model. Assuming that the difference of depth

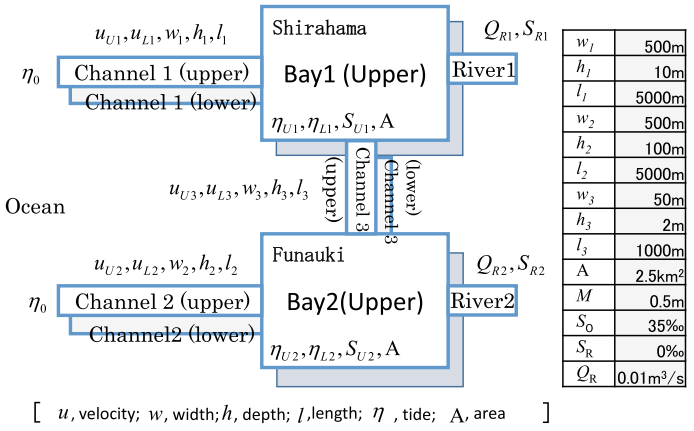

w_1	500m
h_1	10m
l_1	5000m
w_2	500m
h_2	100m
l_2	5000m
w_3	50m
h_3	2m
l_3	1000m
A	2.5km^2
M	0.5m
S_O	35‰
S_R	0‰
Q_R	0.01m^3/s

Fig. 5.6 Schematic diagram showing two-layer tidal flow model in a complex channel network representing Shirahama and Funauki bays with a connecting channel. Referred from Yoshino et al. (2018)

between Channel 1 and Channel 2 is sufficiently large, the respective depths of Channel 1 and Channel 2 are set as 10 and 100 m. Bay 1 and Bay 2 are connected to the open ocean by Channel 1 and Channel 2, respectively, and are mutually linked by Channel 3. Furthermore, the river waters of River 1 and River 2 flow respectively into Bay 1 and Bay 2. Under near-calm conditions in summers, a saltwater wedge among the upper-level freshwater and low-level saltwater can be often observed in the bays, implying that the bay areas can be generally categorized as a type of "weak mixing." Therefore, the momentum and mass continuity equations in the tidal flow model can be divisible into two layers, consisting of upper-level freshwater layer (denoted by suffix U) and lower-level saltwater layer (denoted by suffix L).

η_{U0} and η_{L0} respectively stand for the sea-level anomalies in the open ocean at the upper and lower layers. η_{U1} and η_{L1} (η_{U2} and η_{L2}) respectively represent the sea-level anomalies in Bay 1 (Bay 2) at the upper and lower layers. The area is defined as A in both Bay 1 and Bay 2, assuming the same length and width as each other. u_{U1} and u_{L1} (u_{U2} and u_{L2}) respectively show current velocities at the upper and lower layers in Channel 1 (Channel 2), assuming that a flow from the open ocean to Bay 1 (Bay 2) is positive. u_{U3} and u_{L3} are the same but in Channel 3, assuming that a flow from Bay 1 to Bay 2 is positive. The respective width, length and depth of the three channels are w, l and h, which are labeled with suffixes by the channel layer (U and L) and channel number (1, 2, and 3). Consequently, the momentum conservation equations at the upper layer in Channel 1, Channel 2 and Channel 3 are the followings.

$$\frac{\mathrm{d}u_{U1}}{\mathrm{d}t} = -g\frac{\eta_{U1} - \eta_{U0}}{l_1} - \frac{\tau_{i1}}{\rho_{U1}h_{U1}} \tag{5.26}$$

$$\frac{\mathrm{d}u_{U2}}{\mathrm{d}t} = -g\frac{\eta_{U2} - \eta_{U0}}{l_2} - \frac{\tau_{i2}}{\rho_{U2}h_{U2}} \tag{5.27}$$

$$\frac{\mathrm{d}u_{U3}}{\mathrm{d}t} = -g\frac{\eta_{U2} - \eta_{U1}}{l_3} - \frac{\tau_{i3}}{\rho_{U3}h_{U3}} \tag{5.28}$$

Also, the momentum conservation equations at the lower layer in Channel 1, Channel 2 and Channel 3 are expressed as,

$$\frac{\mathrm{d}u_{L1}}{\mathrm{d}t} = -g(1-\varepsilon)\frac{\eta_{U1} - \eta_{U0}}{l_1} - g\varepsilon\frac{\eta_{L1} - \eta_{L0}}{l_1} + \frac{\tau_{i1}}{\rho_{L1}h_{L1}} - \frac{\tau_{b1}}{\rho_{L1}h_{L1}} \tag{5.29}$$

$$\frac{\mathrm{d}u_{L2}}{\mathrm{d}t} = -g(1-\varepsilon)\frac{\eta_{U2} - \eta_{U0}}{l_2} - g\varepsilon\frac{\eta_{L2} - \eta_{L0}}{l_2} + \frac{\tau_{i2}}{\rho_{L2}h_{L2}} - \frac{\tau_{b2}}{\rho_{L2}h_{L2}} \tag{5.30}$$

$$\frac{\mathrm{d}u_{L3}}{\mathrm{d}t} = -g(1-\varepsilon)\frac{\eta_{U2} - \eta_{U1}}{l_3} - g\varepsilon\frac{\eta_{L2} - \eta_{L1}}{l_3} + \frac{\tau_{i3}}{\rho_{L3}h_{L3}} - \frac{\tau_{b3}}{\rho_{L3}h_{L3}} \tag{5.31}$$

where g represents the gravitational acceleration, ρ_U and ρ_L respectively denote the density of seawater at the upper and lower layers, leading to $\varepsilon = (\rho_L - \rho_U)/\rho_L = 0.03$. The interfacial and bottom friction drags τ_i and τ_b are parameterized by the following equations.

$$\tau_i = \frac{1}{2}\rho_U f_i |u_U - u_L|(u_U - u_L) \tag{5.32}$$

$$\tau_b = \rho_L C_f |u_L| u_L \tag{5.33}$$

Therein, f_i signifies the coefficient of interfacial friction drag. The empirical formulas of Nakayama et al. (1998) are used in this study. In addition, C_f denotes the dimensionless coefficient of bottom friction drag. It is set as 0.0026 and ignores the presence of seaweed and coral at the bottom.

Furthermore, mass conservation equations at the upper layer in Bay 1 and Bay 2 are described as,

$$A\frac{\mathrm{d}\eta_{U1}}{\mathrm{d}t} = w_1 h_{U1}u_{U1} + w_1 h_{L1}u_{L1} - w_3 h_{U3}u_{U3} - w_3 h_{L3}u_{L3} + Q_{R1} \tag{5.34}$$

$$A\frac{\mathrm{d}\eta_{U2}}{\mathrm{d}t} = w_2 h_{U2}u_{U2} + w_2 h_{L2}u_{L2} + w_3 h_{U3}u_{U3} + w_3 h_{L3}u_{L3} + Q_{R2} \tag{5.35}$$

where Q_{R1} and Q_{R2}, respectively, represent the river flow rates into Bay 1 and Bay 2. They are set as a constant value of 0.01 [m^3/s] in both of the rivers, based on the observations made near other similar rivers under calm conditions. The mass conservation equations at the lower layer in Bay 1 and Bay 2 are given as

$$A\frac{d\eta_{L1}}{dt} = w_1 h_{L1} u_{L1} - w_3 h_{L3} u_{L3} - AE(u_{U1} - u_{L1}) \tag{5.36}$$

$$A\frac{d\eta_{L2}}{dt} = w_2 h_{L2} u_{L2} + w_3 h_{L3} u_{L3} - AE(u_{U2} - u_{L2}) \tag{5.37}$$

where E is the coefficient of entrainment at the interface between upper and lower layers. It is estimated using the empirical formula reported by Suga and Takahashi (1976). Moreover, the salinity conservation equations at the upper layer in Bay 1 and Bay 2 are introduced as

$$\begin{aligned} V_1\frac{\partial S_{U1}}{\partial t} = {} & S_0 \max(w_1 h_{U1} u_{U1}, 0.0) + S_{U1} \min(w_1 h_{U1} u_{U1}, 0.0) \\ & - S_{U1} \max(w_3 h_{U3} u_{U3}, 0.0) - S_{U2} \min(w_3 h_{U3} u_{U3}, 0.0) \\ & + EA(S_{U1} - S_0)(u_{U1} - u_{L1}) + S_{R1} Q_{R1} \end{aligned} \tag{5.38}$$

$$\begin{aligned} V_2\frac{\partial S_{U2}}{\partial t} = {} & S_0 \max(w_2 h_{U2} u_{U2}, 0.0) + S_{U2} \min(w_2 h_{U2} u_{U2}, 0.0) \\ & + S_{U1} \max(w_3 h_{U3} u_{U3}, 0.0) + S_{U2} \min(w_3 h_{U3} u_{U3}, 0.0) \\ & + EA(S_{U2} - S_0)(u_{U2} - u_{L2}) + S_{R2} Q_{R2} \end{aligned} \tag{5.39}$$

where S_{U1} and S_{U2}, respectively, denote the salinities at the upper layer in Bay 1 and Bay 2. They can be considered as passive tracer in the bays. Furthermore, V_1 and V_2 are the respective volumes of seawater at the upper layer in Bay 1 and Bay 2. S_0 represents the salinity of the open ocean which is fixed at 35.0 ‰. Also, S_{R1} and S_{R2} respectively represent the salinities of the river water incoming to Bay 1 and Bay 2, and are set as a constant of 0.0 ‰. Because the volume of the lower layer is much greater than that of the upper layer, the salinities at the lower layer in Bay 1 and Bay 2 are assumed to be fixed at 35.0 ‰, which is same as that in the open ocean.

The differential equations presented above in Eqs. (5.26)–(5.39) are numerically integrated using the Runge–Kutta method during a period of 200 days. The tidal level in the open ocean at the upper level and lower level (η_{U0} and η_{L0}) is given by a sine function with a period of 12 h and a peak value of 0.5 m. The last 24 h in the simulations are used for analysis.

(b) **CNTRL: moderate aspect ratio for the connecting channel**

First, we discuss the result of a control experiment (CNTRL), in which the parameters used in the model are presented in Fig. 5.6. The parameters in CNTRL are set to realistic values in Channel 1 (Bay 1), Channel 2 (Bay 2) and Channel 3. Those

orders are in good agreement with the actual conditions. The aspect ratio of Channel 1 is $l_1/h_1 = 500$; that of Channel 2 is $l_2/h_2 = 50$. The aspect ratio of Channel 3 is assumed to be $l_3/h_3 = 500$, which is the same value as that of Channel 1.

Figure 5.7 shows a time series of the tidal level in each bay and the upper-level water flow rate in each channel during 24 h in CNTRL. Figure 5.8 presents a time series of the salinity in the respective bays during 24 h in CNTRL. Upper-level flows in both Channel 1 and Channel 2 are oscillating with a phase shift of +1/4T (+3 h) from the ocean tide (T = 12 h). The upper-level flow rate in Channel 1 with shallower water ($h_1 = 10$ m) is much greater than that in Channel 2 with deeper water ($h_2 = 100$ m). The upper-level flow rate in Channel 3 is considerably higher than that in Channel 2. It is about half of that in Channel 1. Moreover, it oscillates with a phase shift of $-1/4T$ (−3 h) from the ocean tide (T = 12 h). The connecting channel therefore transports surface waters from Bay 2 (Bay 1) to Bay 1 (Bay 2) in the incoming tide (outgoing tide). The salinity in Bay 2 with lower seawater exchanges is lower than that in Bay 1 with higher seawater exchanges because of the stagnation of flow and freshwater in Bay 2.

Figure 5.9 presents a summary of the tidal exchange rate and constant flow rate in respective channels and the salinity in respective bay, averaged during 24 h in CNTRL. Although the upper-level tidal exchange in Channel 3 is quite large (0.065 m^3/s), a clear difference in salinities is apparent between Bay 1 (32.8 ‰) and Bay 2 (30.6 ‰). This difference derives from a large difference in the tidal exchange between Channel 1 (0.173 m^3/s) and Channel 2 (0.021 m^3/s). According to the linear theory for "deep bays" in Chap. 4, the tidal exchange in Channel 1 with shallower water ($h_1 = 10$ m) is active, but that in Channel 2 with deeper water ($h_2 = 100$ m) is inactive.

One can consider the physical properties of tidal current in each channel in CNTRL based on the theoretical equations in the previous subsection. Under the

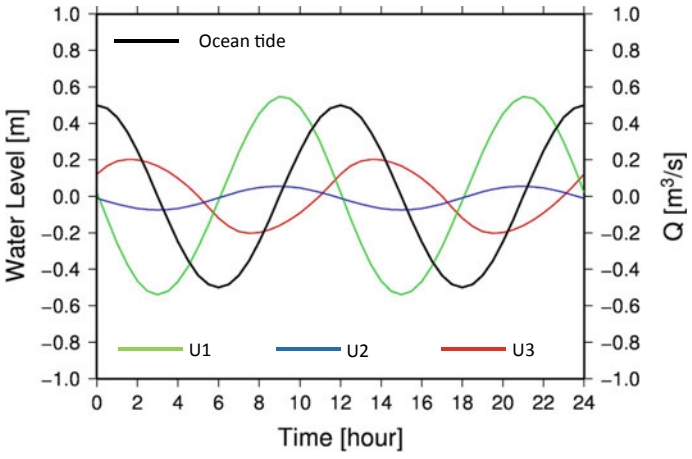

Fig. 5.7 Time series of tidal-level and upper-level water flows in Channel 1, Channel 2 and Channel 3 simulated using CNTRL. Referred from Yoshino et al. (2018)

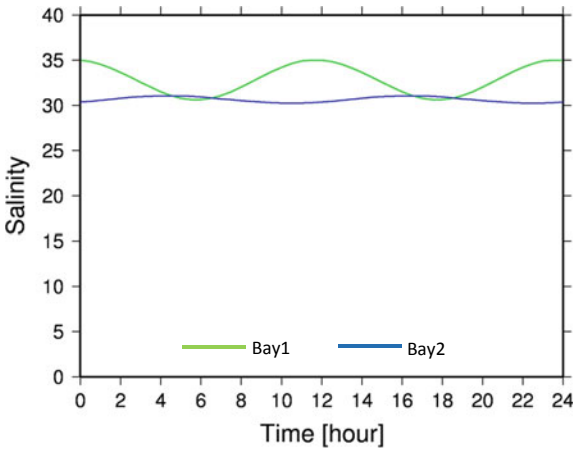

Fig. 5.8 Time series of tidal level and upper-level salinity in Bay 1 and Bay 2 simulated using CNTRL. Referred from Yoshino et al. (2018)

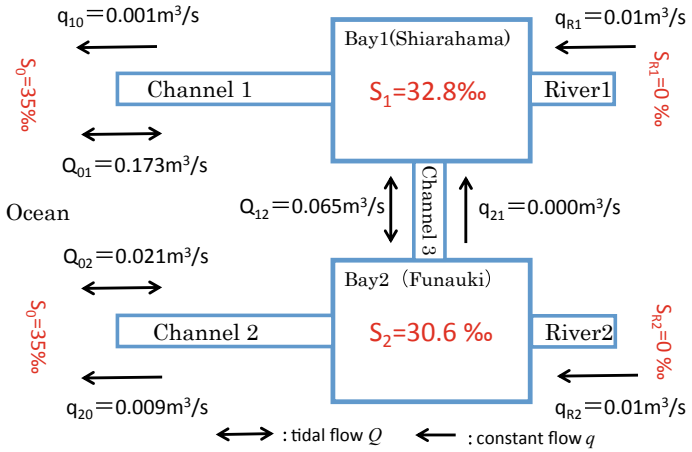

Fig. 5.9 Tidal flows, constant flows and salinity in respective channels and bays simulated using CNTRL. Referred from Yoshino et al. (2018)

aspect ratios of three channels in CNTRL, the assumptions $C \approx A \gg B$ and $c \approx a \ll b$ will hold; then Eqs. (5.19), (5.20), and (5.21) can be approximated as shown below.

$$\hat{u}_1 \approx \frac{bC}{Abc + abC} M = \frac{M}{c + a} \tag{5.40}$$

$$\hat{u}_2 \approx \frac{Ac + aC}{Abc + abC} M = \frac{M}{b} (\to 0) \tag{5.41}$$

$$\hat{u}_3 \approx \frac{-Ab}{Abc + abC} M = -\frac{M}{c + a} \tag{5.42}$$

In the case of the moderate aspect ratio of the connecting channel, the tidal flow in Channel 1 is strong, but that in Channel 2 is weak. It is noteworthy that the tidal exchange in Channel 3 is comparable with that in Channel 1.

(c) CASE 1: large aspect ratio for the connecting channel

Next, we discuss the result of a sensitivity run (CASE 1), in which the aspect ratio of Channel 3 is set at an extremely high value of 50,000. The experimental setting assumes that the connecting channel in CASE 1 is much longer and shallower than that in CNTRL. The other parameters used are the same as the CNTRL run, as presented in Fig. 5.6.

Figure 5.10 summarizes the tidal exchange rate and constant flow rate in each channel and the salinity in each bay, averaged during 24 h in CASE 1. The upper-level tidal exchange in the connecting channel is 0.017 m^3/s, which is about 4 times lower in CASE 1 than in CNTRL. As a consequence, the difference in salinity between Bay 1 (33.1 ‰) and Bay 2 (27.3 ‰) is enlarged in CASE 1. In common with CNTRL, the tidal exchange in Channel 1 is active (0.181 m^3/s), and that in Channel 2 is inactive (0.019 m^3/s). The longer and shallower Channel 3 in CASE 1 weakens the mutual interference among the bays and distinguishes different intrinsic features among individual bays.

One can then assess the physical properties of tidal currents in each channel in CASE 1 based on the theoretical equations presented in the preceding subsection.

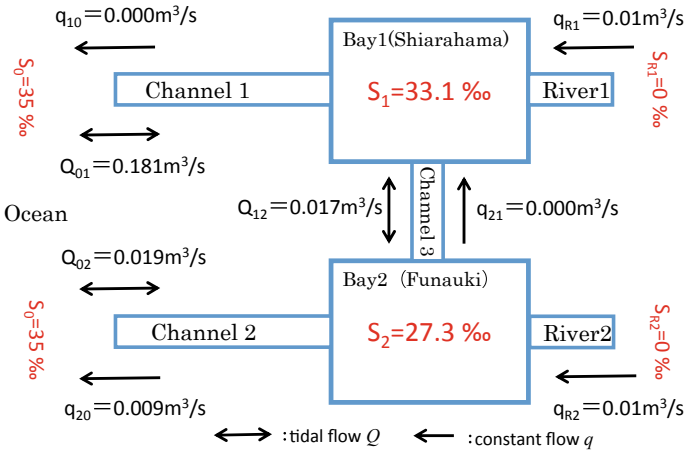

Fig. 5.10 Tidal flows, constant flows and salinity in respective channels and bays simulated using CASE 1. Referred from Yoshino et al. (2018)

Under the aspect ratios of three channels in CASE 1, the assumptions $C \gg A \gg B$ and $c \ll a \ll b$ will hold; then Eqs. (5.19), (5.20), and (5.21) can be approximated as presented below.

$$\hat{u}_1 \approx \frac{bC}{abC} M = \frac{M}{a} \tag{5.43}$$

$$\hat{u}_2 \approx \frac{aC}{abC} M = \frac{M}{b} (\to 0) \tag{5.44}$$

$$\hat{u}_3 \approx \frac{-Ab}{abC} M = -\left(\frac{A}{C}\right) \frac{M}{a} (\to 0) \tag{5.45}$$

In the case of a large aspect ratio of the connecting channel, the tidal exchange in Channel 3 is expected to be inactive. For that reason, Channel 1 and Channel 2 will not mutually interact. As a result, the tidal flows in both channels show clear individual features as a single bay, as described in Chap. 4.

(d) **CASE 2: small aspect ratio for the connecting channel**

Next, one can discuss the sensitivity run results (CASE 2) in which the aspect ratio of Channel 3 is set at an extremely low value of 0.5. The experimental setting includes the assumption that the connecting channel in CASE 2 is much shorter and deeper than that in CNTRL. The other parameters are the same as those used for the CNTRL run, as presented in Fig. 5.6.

Figure 5.11 presents a summary of the tidal exchange rate and constant flow rate in each channel and the salinity in each bay, as averaged during 24 h in CASE 2. The upper-level tidal exchange in the connecting channel is reduced to nearly 0.0 m^3/s in

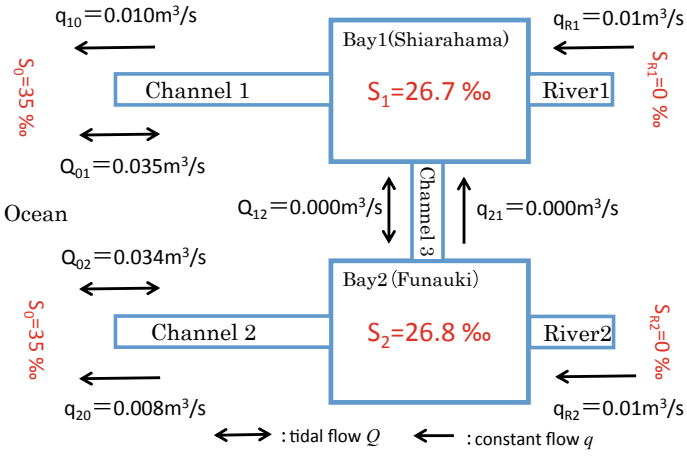

Fig. 5.11 Tidal flows, constant flows, and salinity in respective channels and bays simulated using CASE 2. Referred from Yoshino et al. (2018)

CASE 2. Not only Channel 3 but also Channel 1 decreases the upper-level tidal exchange to 0.035 m^3/s, which is equivalent to that (0.034 m^3/s) in Channel 2. Consequently, the tidal current over the entire channel network stagnates because of the small aspect ratio of the connecting channel. The upper-level salinity is also decreased by the stagnations of freshwater in both Bay 1 (26.7 ‰) and Bay 2 (26.8 ‰). The shorter and deeper (smaller aspect ratio) characteristics of the connecting channel can contribute to a slower tidal exchange over the whole channel network because of the dominance of the effects of Channel 2.

One can consider the physical properties of tidal current in each channel in CASE 2 based on the theoretical equations given in the previous subsection. Under the aspect ratios of three channels in CASE 2, the assumptions $C \ll B \ll A$ and $c \gg b \gg a$ will hold; then Eqs. (5.19), (5.20) and (5.21) can be approximated as shown below.

$$\hat{u}_1 \approx \frac{Bc}{Abc} M = \left(\frac{B}{A}\right) \frac{M}{b} (\to 0) \tag{5.46}$$

$$\hat{u}_2 \approx \frac{Ac}{Abc} M = \frac{M}{b} (\to 0) \tag{5.47}$$

$$\hat{u}_3 \approx \frac{-Ab}{Abc} M = -\frac{M}{c} (\to 0) \tag{5.48}$$

In the case of the small aspect ratio of the connecting channel, the tidal flow by Channel 3 will stagnate. Then the tidal exchange in Channel 1 is influenced by those in Channel 2, resulting in tidal flow suppression over the whole channel network.

(e) **Relations between aspect ratio and tidal flow**

The sensitivities of the aspect ratio of the connecting channel (Channel 3) are investigated next. Figure 5.12 shows the relations between the aspect ratio l_3/h_3 of Channel 3 and upper-level tidal exchange rates in each bay. When aspect ratio l_3/h_3 of Channel 3 is a moderate value equivalent to l_1/h_1, the tidal exchange in Channel 3 becomes maximum, leading to active exchange between Bay 1 and Bay 2. Whether l_3/h_3 is larger or smaller than the value, the seawater exchange at the connecting channel will be suppressed. The tidal flow in Channel 2 (i.e., Funauki Bay) responds only slightly to the change of l_3/h_3 at all. It is always inactive through the open ocean because of its deeper water floor. By contrast, the tidal flow in Channel 1 (i.e., Shirahama Bay) is strongly affected by the change of l_3/h_3. The active (inactive) tidal flow in Channel 1 is attributed mainly to a larger (smaller) l_3/h_3 in Channel 3. Consequently, when it comes to the upper-level tidal exchange, Shirahama Bay rather than Funauki Bay is likely to be affected by the topographic change of the connecting channel.

Figure 5.13 presents relations between the aspect ratio l_3/h_3 of Channel 3 and upper-level salinity in each bay. The upper-level mass exchanges, such as fruits and

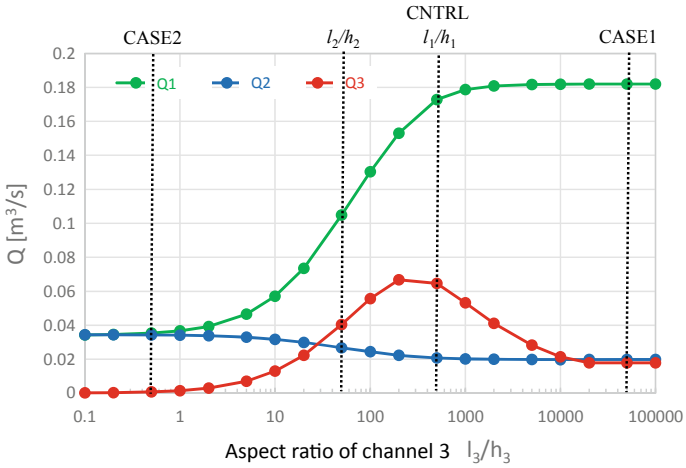

Fig. 5.12 Relations between aspect ratio of Channel 3 l_3/h_3 and tidal flow in respective channels. Referred from Yoshino et al. (2018)

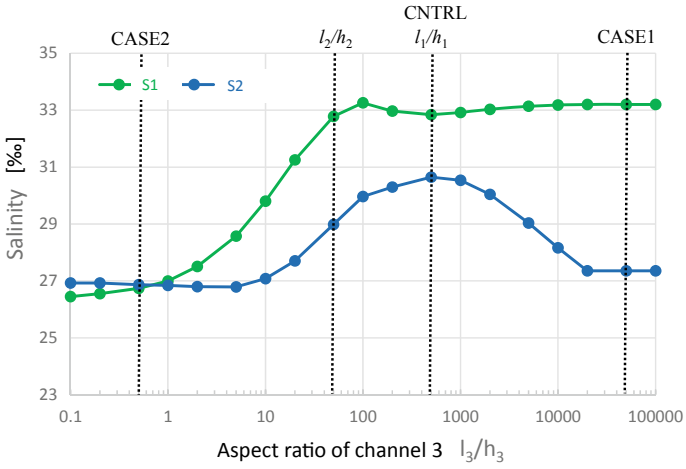

Fig. 5.13 Relations between the aspect ratio of Channel 3 l_3/h_3 and salinity in respective bays. Referred from Yoshino et al. (2018)

seeds of coastal ocean ecosystems, can be estimated indirectly because salinity at the surface level can be regarded as a passive tracer. In the case of the larger l_3/h_3, the upper-level tidal exchange in Channel 3 becomes inactive, leading to an independent environment with the greater difference in salinity between Bay 1 and Bay 2. It is considered that in such a condition, the dispersion of fruits and seeds from coastal ocean ecosystems is stronger in Shirahama Bay than in Funauki Bay. Moreover, the dispersion through the connecting channel is weaker. For smaller

l_3/h_3, the upper-level tidal exchanges in the whole channel network become inactive, resulting in a stagnant environment with the lower salinity in Bay 1 and Bay 2 than in the open ocean. The dispersion ability in the whole bays is regarded as weakened. In the case of the moderate l_3/h_3, the upper-level tidal exchange in Channel 3 becomes active, creating a mutually interactive environment with less difference in salinity between Bay 1 and Bay 2. The dispersion capability among the bays is probably enhanced. Consequently, the upper-level dispersion of fruits and seeds in both Funauki and Shirahama bays are likely to be influenced by the topographic changes of their mutually connective channel.

5.4 Observations and Simulations

This section presents examination of details of the physical features of tidal flows in Funauki and Shirahama bays with the connecting channel, based on results of in situ observations and CCM simulations. Detailed information is presented in relation to observational instruments in Chap. 2. The coastal current model "CCM" is explained in Chap. 3.

(a) **In situ observations**

First, observational features of water quality in Funauki and Shirahama bays are discussed in this subsection. We conducted in situ observations using a conductivity-temperature-depth profiler (CTD) during high-tide and low-tide periods on September 15, 2014, August 15, 2014, and October 20, 2015. The moving observations were conducted using a small boat with the CTD profiler at 26–36 points and at every 0.1-m depth. Influences of the movements of the small boat may be reduced to a great degree, because the observations were done during the near-calm conditions with a wind speed of less than 6 m/s, at AMeDAS Iriomote (observed by JMA: referred to Sect. 1.3). The CTD profiler used for this study (RINKO-Profiler ASTD102; JFE Advantech Co. Ltd.) can detect depth, temperature, salinity, dissolved oxygen, turbidity and chlorophyll simultaneously.

We herein specifically examine the results of the observations taken at 6:50 JST (low tide) and 14:00 JST (high tide) on October 20, 2015.

Figure 5.14 depicts the horizontal distributions of salinity in 0.1-m depth at 6:50 JST (low tide) and 14:00 JST (high tide) on October 20, 2015. Figure 5.15 portrays the horizontal distributions of temperature in 0.1-m depth at 6:50 JST (low tide) and 14:00 JST (high tide) on October 20, 2015. In both of the low and high tides, a low-salinity water mass (less than 20 ‰) is apparent near the connecting channel in Funauki Bay. Low-salinity areas tend to show a low temperature. Although low-salinity water exists in a small area of Shirahama Bay, most of it tends to show high-salinity water (30–36 ‰) over the bay. The low-salinity water mass observed in Funauki Bay is regarded as originating a freshwater from Kuira River located at the head of Funauki Bay, or partially originating in freshwater via the connecting

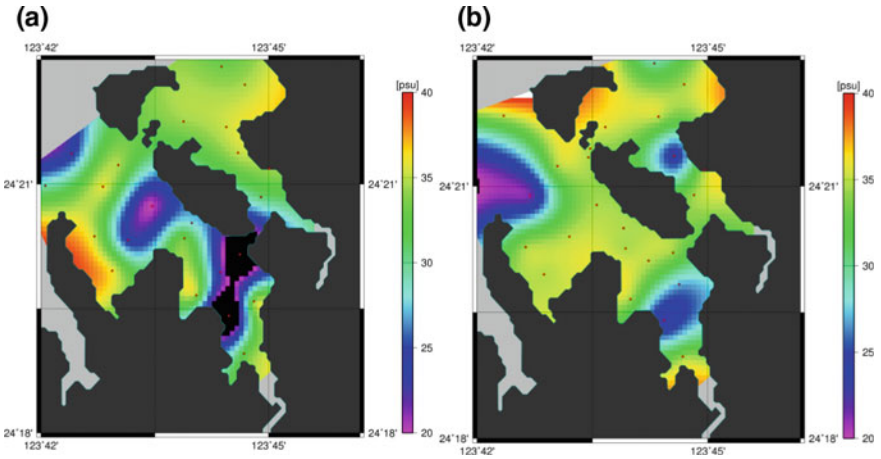

Fig. 5.14 Observed distributions of salinity in surface 0.1-m layer at **a** 6:50 JST October 20, 2015 (low tide) and **b** 14:00 JST October 20, 2015 (high tide). Referred from Yoshino et al. (2016)

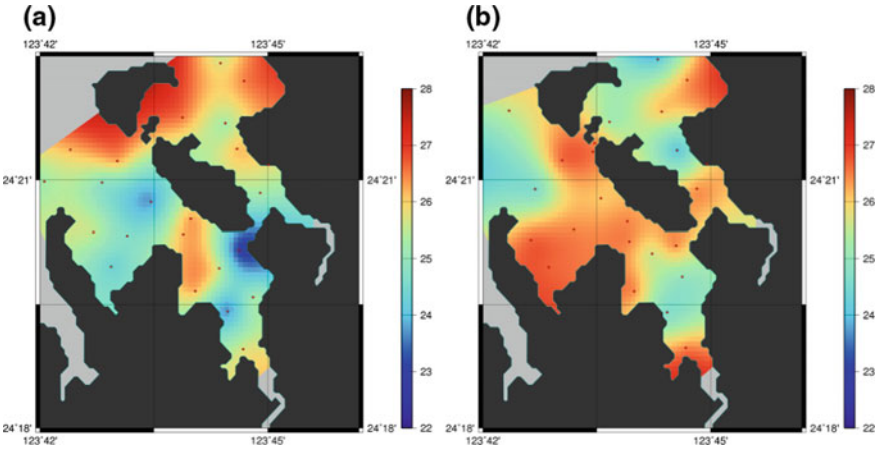

Fig. 5.15 Observed distributions of temperature in surface 0.1-m layer at **a** 6:50 JST October 20, 2015 (low tide) and **b** 14:00 JST October 20, 2015 (high tide)

channel from Nakara River located at the head of Shirahama Bay because of tidal exchanges.

Figure 5.16 presents vertical profiles of salinity and temperature at five points at the low tide time (6:50 JST on October 20, 2015). Figure 5.17 also presents vertical profiles of salinity and temperature at five points at the high tide time (14:00 JST on October 20, 2015). St. 2 and St. 3 close to the head of Funauki Bay show tendencies of low salinity and low temperature near 10 cm depth. The river-originating water mass at the surface layer is visible in both low-tide and high-tide periods. Seawater

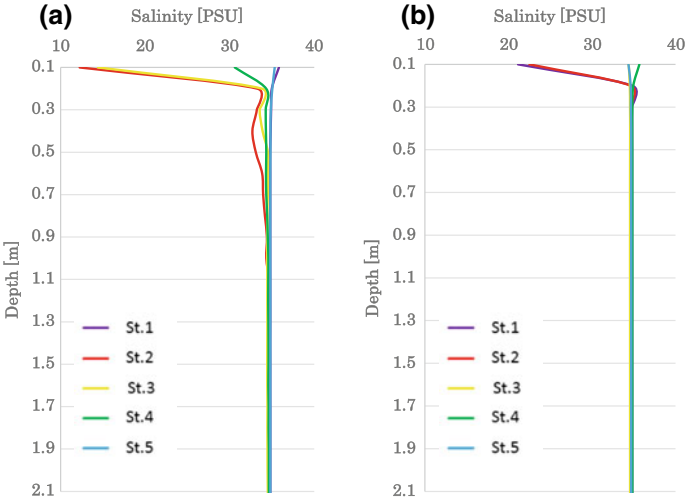

Fig. 5.16 Vertical profiles of salinity at five observational points at **a** 6:50 JST October 20, 2015 (low tide) and **b** 14:00 JST October 20, 2015 (high tide). Referred from Yoshino et al. (2016)

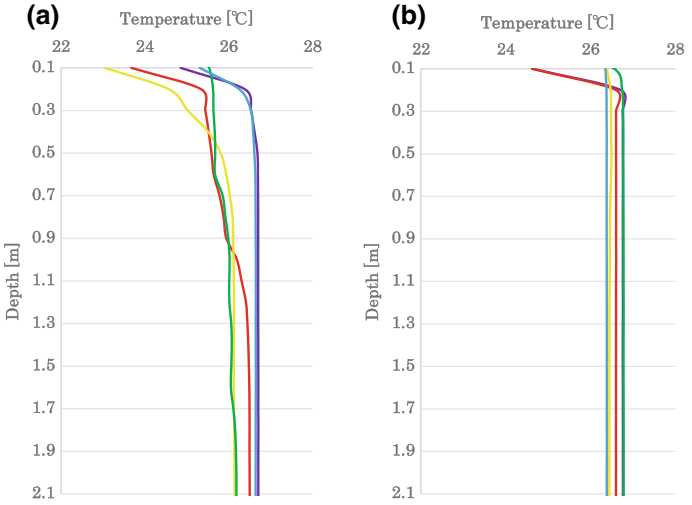

Fig. 5.17 Vertical profiles of temperature at the five observational points at **a** 6:50 JST October 20, 2015 (low tide) and **b** 14:00 JST October 20, 2015 (high tide)

exchange in Funauki Bay is regarded as stagnant for a longer period under the calm conditions. In Shirahama Bay, although transient low-salinity water is visible occasionally, it disappears promptly because of the strong seawater exchange.

Consequently, in situ observations by the CTD profiler indicate that the low-salinity and low-temperature water mass originating from the rivers is likely to

be stagnant, especially in Funauki Bay with deeper water. This feature is consistent with our findings related to the theory and simulations of tidal flow dynamics in a complex channel network described in previous sections.

(b) **CCM simulations**

Next in this subsection, we discuss the physical features of tidal flow in Funauki and Shirahama bays with the connecting channel, which might influence the surface layer water quality. To identify the tidal flow behavior in complex terrain, a numerical simulation is conducted using the multi-sigma coordinate coastal current model CCM (Murakami et al. 2004). In these simulations, salinity and temperature conservation equations are not included to simplify the problem, so the barotropic structures in the ocean are solved using momentum equations and mass continuity equations. The horizontal grid spacing of CCM is 50 m × 50 m. Two simulation periods are employed: June 9–May 16, 2014 (7 days) in summer and November 2–November 9, 2014 (7 days) in winter. The lateral boundary conditions for the sea-level height are added along the open boundaries using NAO.99jb (Matsumoto et al. 2000). As the meteorological forcing, the wind speed and direction observed at Amitori Village (operated by Okinawa Regional Research Center, Tokai University) are inputted homogeneously at the upper ocean boundary. Consequently, the currents in CCM are induced by current by tide (lateral boundary) and by current by wind (upper boundary). To compare tidal and wind influences, a CCM simulation without meteorological forcing, in which the wind speed is set to 0 m/s during the simulation period, is also conducted.

Figure 5.18 presents the horizontal distributions of the 7-day averaged surface current speed and vectors in summer and winter, as simulated by CCM. The time-average procedure can eliminate the high-frequency periodic tidal currents and can retain the steady-state residual currents only. In summer, the main wind direction is southwesterly winds, but its wind speeds are very weak. As a result, the surface residual current is not readily visible in the bays and channel. By contrast, in

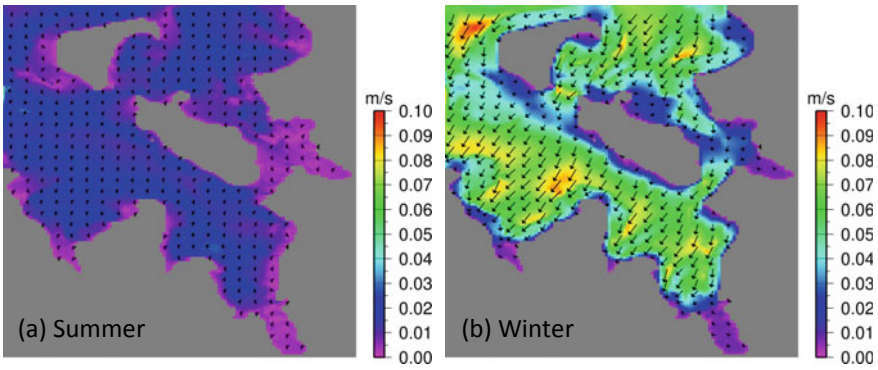

Fig. 5.18 Horizontal distributions of surface current speed and vectors averaged during 7 days in **a** summer and **b** winter simulated by CCM with wind forcing

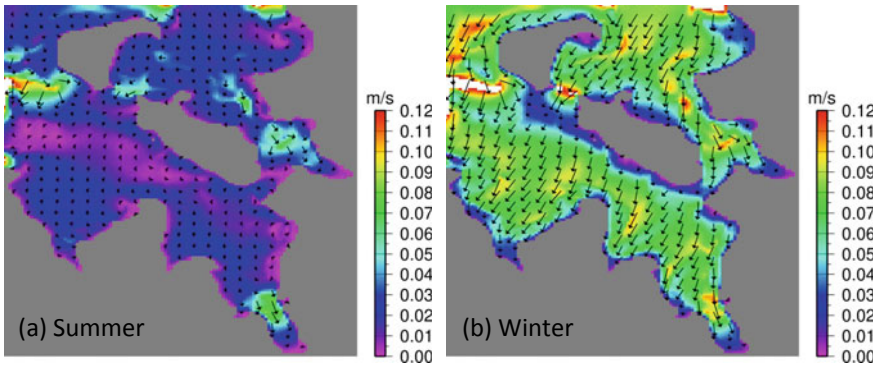

Fig. 5.19 Horizontal distributions of surface current speed and vectors averaged at incoming tide in **a** summer and **b** winter simulated by CCM with wind forcing

winter, northeasterly monsoon winds dominate. Strong residual currents develop from the north to the south in the bays. In winter, surface water is advected steadily from Shirahama Bay (north) to Funauki Bay (south) because of by the strong northeasterly wind.

Figure 5.19 shows the horizontal distributions of the surface current speed and vectors averaged at the incoming tides in summer and winter, as simulated by CCM. For comparison between tide-induced currents and wind-induced currents, Fig. 5.20 shows the values as portrayed in Fig. 5.19, but without wind forcing. Such a time-average procedure can identify the typical flow structure in the incoming tides. The current velocities become maximum in the direction from the open ocean to the bays because those bays are categorized as "deep bays." In summer, no clear difference is apparent in surface currents between those with and without wind forcing. Strong incoming flow dominates in the head of the bays. The surface tidal current in the connecting channel is directed from Funauki Bay (south)

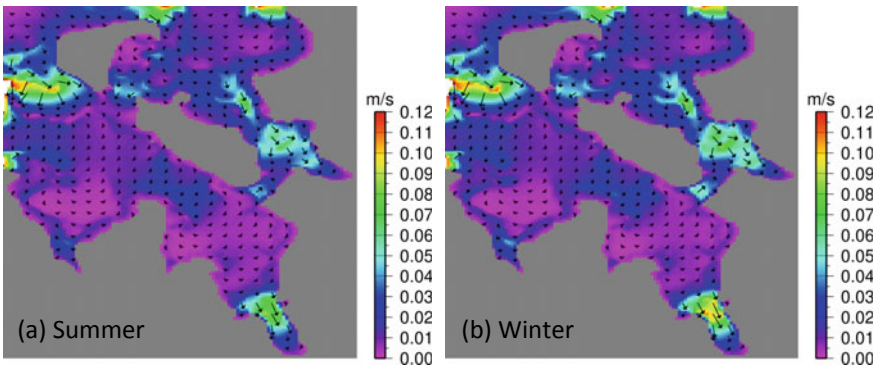

Fig. 5.20 Same as Fig. 5.19, but without wind forcing

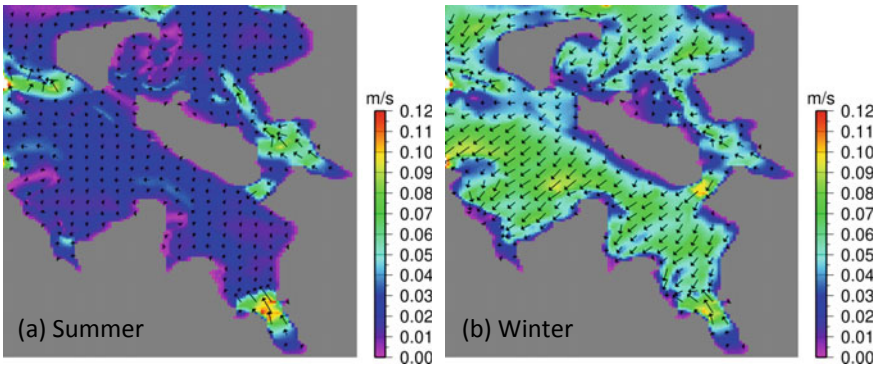

Fig. 5.21 Horizontal distributions of surface current speed and vectors averaged at outgoing tide in **a** summer and **b** winter simulated by CCM with wind forcing. Referred from Yoshino et al. (2016)

to Shirahama Bay (north). In winter, the strong northerly (southward) winds compensate for the northward tidal current in the connecting channel.

Figure 5.21 presents the horizontal distributions of the surface current speed and vectors averaged at the outgoing tides in summer and winter, as simulated by CCM. For comparison between tide-induced currents and wind-induced currents, Fig. 5.22 shows the values as shown in Fig. 5.21, but without wind forcing. The current velocities become maximum in the direction from the bays to the open ocean, as described above. In summer, no clear difference is apparent in surface currents between those with and without wind forcing. Strong outgoing flow dominates in the head of the bays. The surface tidal current in the connecting channel is directed from Shirahama Bay (north) to Funauki Bay (south). In winter, strong northerly (southward) winds further enhance the southward tidal current in the connecting channel.

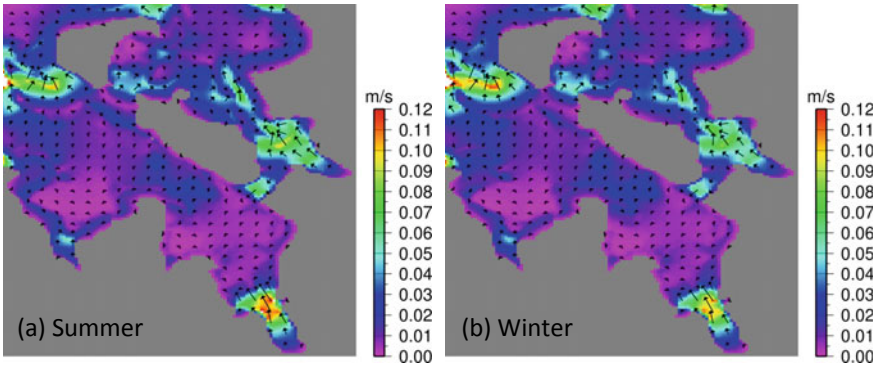

Fig. 5.22 Same as Fig. 5.21, but without wind forcing

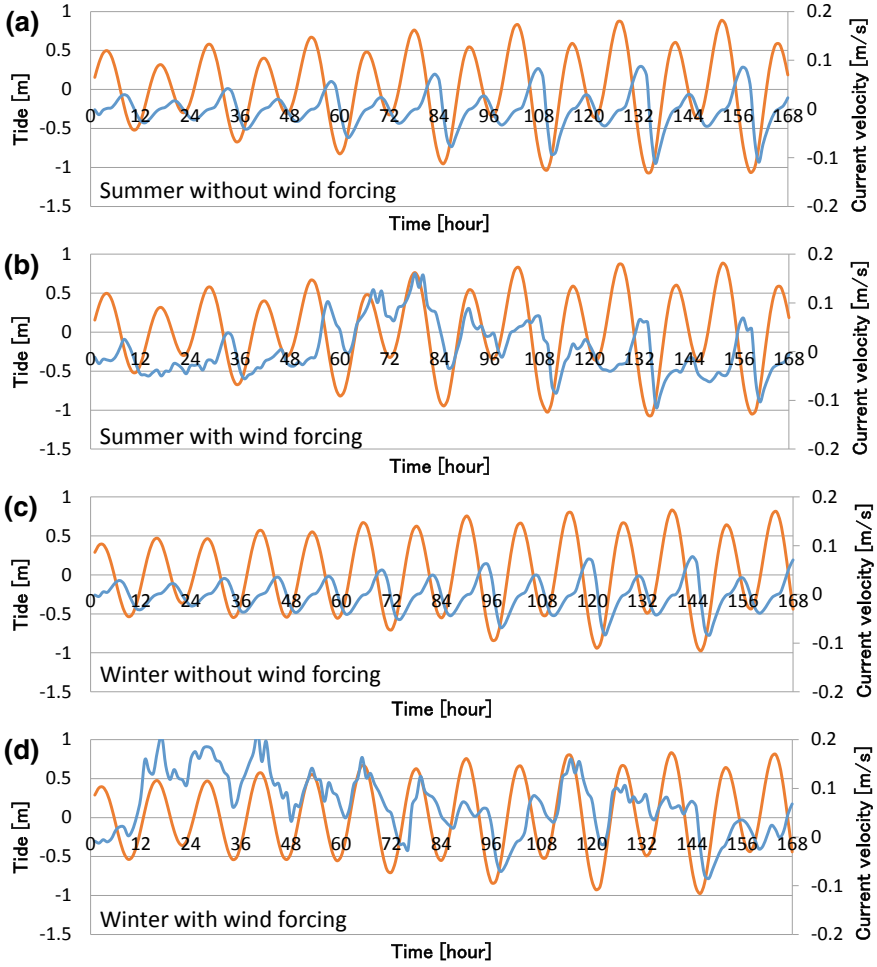

Fig. 5.23 Time series of tidal level (orange color lines) and surface current component (blue color lines) at the connecting channel in **a** summer simulated without wind forcing, **b** summer simulated with wind forcing, **c** winter simulated without wind forcing, and **d** winter simulated with wind forcing

Figure 5.23 presents time series of the tidal level and surface current velocity in the connecting channel. In these figures, the positive velocity denotes the current in the direction from Shirahama Bay to Funauki Bay. Negative velocity denotes the current in the direction from Funauki Bay to Shirahama Bay. Without wind forcing, a periodic tidal current develops in the connecting channel. The phase of the current velocity is delayed by $1/4T$ (3 h) from that of the tidal level (T = 12 h). In other words, the ocean tide induces strong flows from Funauki Bay (Shirahama Bay) to Shirahama Bay (Funauki Bay) in the incoming (outgoing) tide. The amplitude of the

current velocity in the connecting channel is on the order of 0.01 m/s when the amplitude of the sea level in the open sea is 0.5 m. Such a change is consistent with results of theory (Sect. 5.2) and simulations (Sect. 5.3) of tidal flow dynamics in a complex channel network. It is noteworthy that the theory and simulations produce a sine wave pattern for the tidal velocity in the connecting channel, but the CCM simulations indicate an asymmetric pattern in which the velocity component increases more slowly in the outgoing tides, although the velocity component decreases more rapidly in the incoming tides. The underlying causes of the asymmetric velocity changes might not be understood up to this point, but they might be related to the unconsidered processes in the theory of tidal flow dynamics explained in preceding sections. Considering wind forcing at the ocean surface, the current velocity in the connecting channel in summer has a phase shift of $-1/4T$ (−3 h) for the tidal level (T = 12 h). In winter, the periodic flows by the ocean tide are not readily discernable. It is noteworthy that the phase shift of the current velocity in the connecting channel does not occur under the strong meteorological forcing and that strong southward currents in the high tide are enhanced by the strong northerly winds. Meteorological forcing such as that which occurs by strong wind is expected to change the tidal flow pattern considerably, but further study is necessary to ascertain the effects of meteorological forcing on the coastal currents in this region.

It is readily apparent that the connecting channel linking Funauki and Shirahama bays causes the surface water exchange among the bays under near-calm conditions in summer. Their amplitude is closely related to the aspect ratio of the channels. As a consequence, the existence of the connecting channel drastically changes the water quality in the bays. Moreover, it might affect the dispersions of fruits and seeds of their respective coastal ocean ecosystems.

5.5 Concluding Remarks

This chapter presented discussion of the physical features of coastal current in Funauki and Shirahama bays in the northwestern part of Iriomote Island, based on theoretical, observational, and numerical investigations.

Because Shirahama Bay with shallower water and Funauki Bay with deeper water are connected by a channel, the respective flow pattern in the bays is very complex compared with those of Sakiyama Bay and Amitori Bay, as discussed in Chap. 4. Seawater exchange in Shirahama Bay would be more active than that in Funauki Bay if there is no connecting channel. As a result, the low-salinity water originating from rivers is more stagnant in Funauki Bay than in Shirahama Bay. Theoretical considerations have indicated that the flow in the connecting channel is controlled by the aspect ratio (ratio of length to depth) of the bays. The existence of the connecting channel strongly influences the flow and water quality patterns throughout the bays. In the realistic case (the moderate aspect ratio of the connecting channel), the connecting channel actively exchanges surface water among the bays. In the case of the smaller aspect ratio (longer or shallower) of the

connecting channel, the seawater exchange at the connecting channel becomes inactive, leading to the greater difference in salinity among the bays. For a higher aspect ratio (shorter or deeper) of the connecting channel, not only bay–bay exchange but also ocean–bay exchange becomes inactive, resulting in stagnant and low-salinity conditions throughout the bays.

The possibility exists that the existence of the connecting channel changes the tidal currents and water quality in both bays and affects the dispersion processes of fruits and seeds of coastal ocean ecosystems.

Acknowledgements The technical assistance with observational and numerical investigations was graciously provided by Mr. Keigo Kita in Kasugai City Office.

References

Matsumoto K, Takanezawa T, Ooe M (2000) Ocean tide models developed by assimilating TOPEX/POSEIDON altimeter data into hydrodynamical model: a global model and a regional around Japan. J Oceanogr 56:567–581

Mizutani A, Sakihara K, Kawata N, Kohno H (2016) Influence of feeding by green turtles on the stock of *Enhalus Acoroides*: experiments of pruning back of leaves and monitoring on seaweed beds with feeding marks. Study Rev Iriom Island 2015:42–51 (in Japanese)

Murakami T, Yasuda T, Ohsawa T (2004) Development of a multi-sigma coordinate model coupled with an atmospheric model for the calculation of coastal currents. Ann J Coast Eng 51:366–370 (in Japanese with English abstract)

Nakayama S, Hasegawa K, Fuzita M (1998) Experiments and prediction of a cold air flow which causes snow clouds in Ishikari Bay. J Japan Soc Civil Eng 607(II-45):1–17 (in Japanese with English abstract)

Suga K, Takahashi A (1976) Entrainment coefficient of brackish two-layer flow. Proc 31st Ann Conf Japan Soc Civil Eng 31(2):383–384 (in Japanese)

Takeyama K, Kohno H, Kuramochi T, Iwasaki A, Murakami T, Kimura K, Ukai A, Nakase K (2014) Distribution and growth condition of *Enhalus Acoroides* in Iriomote Island. J Japan Soc Civil Eng B3. 74(2):I_1068–I_1073, 2014 (in Japanese with English abstract)

Unoki S (1993) Coastal ocean physics. Tokai University Press, 672 p

Yoshida M, Kawachi N, Nakaoka M (2007) Spatial dynamics of seagrass beds analyzed with an integrated approach using remote sensing and citizen-based monitoring, Japanese J Conserv Ecol 12:10–19 (in Japanese with English abstract)

Yoshino J, Murakami T, Ukai A, Kohno H, Kita K, Shimokawa S, Sakihara K, Mizutani A (2016) Seawater exchange processes through the bays of Shiarahama and Funauki in Iriomote Island, Okinawa, Japan. J Japan Soc Civil Eng B2 72(2):I_1207-I_1212 (in Japanese with English abstract)

Yoshino J, Murakami T, Ukai A, Kohno H, Shimokawa S, Nakase K, Mizutani A (2018) Influence of aspect ratio of a connecting channel on seawater exchange in the bays of Shiarahama and Funauki in Iriomote Island, Okinawa, Japan. J Japan Soc Civil Eng B3 74(2):I_976–I_981 (in Japanese with English abstract)

Chapter 6
Sediment Monitoring in Sakiyama and Amitori Bays

Takumi Okabe, Tomokazu Murakami, Hiroyoshi Kohno, Akira Mizutani and Shinya Shimokawa

Abstract This chapter focuses on a technique for directly measuring suspended sediment or directly collecting coastal sediment for analysis. Simple and low-cost techniques employing sediment traps using a polyvinyl chloride pipe to capture suspended sediment and a handheld analyzer for X-ray fluorescent analysis and a digital scanner for image analysis were employed for sediment measurement and analysis. In laboratory experiments, the sediment catch performance of a cylindrical sediment trap was evaluated according to differences in the intake and outlet sizes. The characteristics of the measurement principle of the X-ray fluorescence analysis were described. Furthermore, a technique for digital image analysis that can estimate sediment diameter was constructed. In addition, color measurements using the CIE L^* a^* b^* color space system ascertained sediment color characteristics. Next, these measurement and analysis techniques were applied to sediment monitoring in the Sakiyama and Amitori bays. Fine sediment was captured in the sediment traps. The element content of the coastal sediment from multiple points within the bays and their spatial distributions obtained through X-ray fluorescence analysis were

This chapter is based on Okabe et al. (2016, 2017).

T. Okabe (✉)
Department of Architecture and Civil Engineering, Toyohashi University of Technology, Toyohashi, Japan
e-mail: okabe@ace.tut.ac.jp

T. Murakami · S. Shimokawa
Storm, Flood and Landslide Research Division, National Research Institute for Earth Science and Disaster Resilience, Tsukuba, Japan
e-mail: tmurakami@bosai.go.jp

S. Shimokawa
e-mail: simokawa@bosai.go.jp

H. Kohno · A. Mizutani
Okinawa Regional Research Center, Tokai University, Yaeyama, Japan
e-mail: hkohno@scc.u-tokai.ac.jp

A. Mizutani
e-mail: ma110267@tsc.u-tokai.ac.jp

S. Shimokawa et al. (eds.), *Geophysical Approach to Marine Coastal Ecology*, Springer Oceanography, https://doi.org/10.1007/978-981-15-1129-5_6

ascertained. The color, diameter, and chemical composition of the sediments were classified using clustering analysis, and the distribution of the cluster within the bays matched the topographical features.

Keywords Sediment transport · Sediment characteristics · Cylindrical sediment trap · X-ray fluorescence analysis · Image analysis

6.1 Introduction

The sediment in coral reef areas is an important environmental element, which serves as the foundation of ecosystems therein. Sediment has a major influence on coral. While natural sediment influences the growth of coral reefs (MacIntyre et al. 1992), it has been indicated that suspended sediment, typically produced by dredging, damages coral (Erftemeijer et al. 2012; Bessell-Browne et al. 2017). In addition, it has been reported that sediment deposition in coral reefs, which was supplied from a river, may influence the recruitment and growth of tabular coral (Murakami et al. 2012). As indicated by these previous studies, ascertaining the state and distribution of the sediment characteristics in a coral reef area is essential for ecosystem conservation, including coral (see Sect. 1.4) and *Enhalus acoroides* (see Sect. 1.5). The utilization of various sediment observation and monitoring techniques is required to grasp the spatial characteristics and dynamics of sediment in coral reefs, estuaries, and the rivers flowing into these areas.

Many monitoring techniques have been developed and applied to spatially investigate ecosystems in coral reef areas. These include a study attempting to identify and map coral reefs using a multibeam echosounder (MBES) (Roberts et al. 2005), and a comparative study evaluating coral reef ecosystems utilizing MBES and an airborne light detection and ranging (LiDAR) system, which uses aircraft-based lasers (Costa et al. 2009). In addition, a technique has been developed to map coral reefs as well as seagrass beds and mangroves using satellite images with high spatial resolution (Chauvaud et al. 1998; Andréfouët and Riegl 2004).

In general, the assessment of sediment environments requires a sample collected in the research area and its analysis. Well-established collection methods for sediment samples involve grab samplers, coring, and scuba diving (Mudroch and Azcue 1995). Collected sediments are then generally analyzed using sieve analysis (Jordan et al. 2010), chemical analysis (Entsch et al. 1983), and loss-on-ignition tests (Griffin et al. 2003). However, broader sediment spatial data are sought to evaluate sediment dynamics and diverse sediment environments in complex ecosystems in coral reefs. To achieve this objective with a huge number of spatiotemporal samples and data, observation and monitoring techniques must be simple and low-cost.

In this chapter, we address the sediment trap device for sediment collection and techniques for analyzing sediments using X-ray fluorescence (XRF) and digital images. A sediment trap suites monitoring suspended sediment. Sediment catch performance is the basis for its design, which was evaluated through laboratory

experiments. There has been an increase in cases using XRF to analyze the element content of coastal sediments in recent years; a handheld version of an XRF analyzer was introduced in this study. Image analysis for sediment diameter and color was also described. Finally, the above techniques were applied to monitor sediment in the Sakiyama and Amitori bays (see Sects. 1.1 and 1.2 and Fig. 1.1) and to assess the sediment environments in these bays.

6.2 Cylindrical Sediment Trap

Sediment samplers used in the observations of coastal sediment transport have various shapes. A bucket-type trap buried on the sea or river bottom with the intake at the floor is intended mainly for bed loads (Garcia et al. 2000). If the sediment transport is oriented predominantly in one direction, then the observation results are likely to be assessed as sediment flux. Thus, this type of trap is often used in monitoring wind-blown sand in coastal dunes and bed load in rivers. Logging devices were incorporated within the bucket to record time series of the catchweight (Jackson 1996).

Sediment traps intended for suspended sediment may be broadly divided into those with upward intakes and sideways intakes. A cylindrical sediment trap with an upward intake is utilized to catch falling solid particles and ascertain vertical substance transportation in offshore or enclosed bays (Rowe and Gardner 1979). These are utilized when sedimentary components contribute significantly to the sediment deposition process. A sampler with a sideways opening is employed to perceive horizontal sediment movements. These require a multilayer opening to ascertain the vertical distribution of suspended sediment. A sampler with long vertical intake slits, ensuring ventilation slits on the opposite side with a screen (metal or other mesh), traps the integrated sediments along the slit. These are mainly used for eolian sediment observations on land (Bauer and Namikas 1998). Among other possibilities, those constructed of polyvinyl chloride (PVC) pipe are inexpensive and easy to machine, and therefore, various sizes and designs are created for each study and survey.

The shape and performance of sediment samplers vary according to monitoring target and purpose, and therefore, it is difficult to evaluate and report sediment dynamics based on observation results among different samplers in a uniform manner. In addition, there have been few reports on a quantitative evaluation of the trap performance of sediment samplers. Bloesch and Burns (1980) have evaluated the performances of vertical cylindrical traps. Furthermore, there have been experimental investigations into the performances of cylindrical MultiPIT sediment traps (Gust et al. 1996) and a sampler for fine sediments (Phillips et al. 2000).

Here, a cylindrical sampler is employed to catch suspended sediments in sand drift surveys of shallow sea areas. In a water tank experiment, the relationship between the flow velocity and sizes of the intake and outlet was quantitatively evaluated with respect to performance.

6.2.1 Experiment Setup

The suspended sediment sampler was based on a cylindrical shape. Figure 6.1 depicts the external appearance and size of the sampler. To investigate the sediment flux in detail, the direction of the sediment movement needs to be measured as accurately as possible. This sampler can catch suspended sediment arriving from one direction and thus conforms to the requirements for the flux survey. The circular shape was selected for the intake and outlet because of machining ease. The experiment evaluated the capture performance based on the diameter size of the intake and outlet. A stainless-steel mesh was mounted on the outlet hole to ensure the incoming sediment was only from the intake side.

The sampler was installed within a water tank, and a belt conveyor located upstream then introduced glass particles to the stream to imitate suspended sediment (Fig. 6.2). The distance between the sampler and belt conveyor was changed according to the flow velocities, such that the intake was located where the suspended sediment concentration was at its highest.

In this experiment, different experimental combinations were set for the flow velocity v (0.15, 0.20, and 0.25 m/s), hole (intake and outlet) diameter D (5, 10, and 15 mm), and mesh aperture A (no mesh, 0.06, 0.28, 0.154, and 0.67 mm). The A value indicates the size by which the mesh was actually opened. For the particles, only glass beads (particle diameter 0.2 mm, density 2500 kg/m^3) were used, introducing approximately 7 g for each experiment case. In the experiment, characteristics of the capture performance according to the flow velocity and conditions of intake and outlet holes were evaluated; therefore, the particle diameter or the size of the sampler itself was not altered. The glass particle concentration in the flow was almost constant for each case.

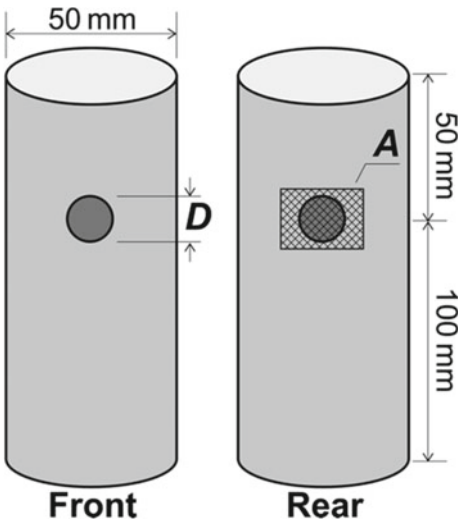

Fig. 6.1 Cylindrical suspended sediment sampler constructed from PVC pipe for laboratory experiments. Modified from Okabe et al. (2016)

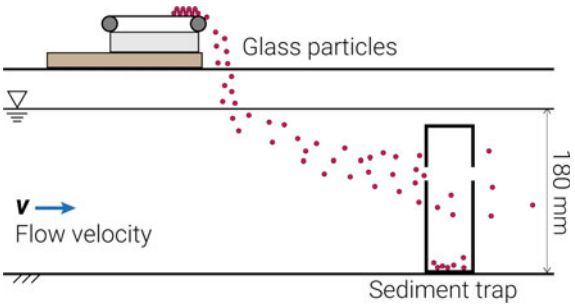

Fig. 6.2 Schematic diagram of suspended sediment sampler experiments. From Okabe et al. (2016)

The procedure for the experiment involved first arranging a set quantity of particles into a predetermined rectangular area on the belt conveyor using a frame. Thereafter, particles overflowing the frame were gathered and measured for weight and then used to compute the weight actually introduced to the water tank. Next, the belt conveyor was driven at a constant speed, and the time during which particles were introduced was measured. In addition, a digital camera was utilized to video the experiment from the side of the tank. After being introduced, the particles circulated through the water flow, and then the sampler captured the suspended particles. The particles remaining inside the sampler were then filtered through a strainer and left to dry. The dry weight of the particles was recorded as the capture weight. The experimental results for each case were obtained by repeating the experiment five times and taking the average.

6.2.2 *Experimental Results*

Figure 6.3 depicts the relationship between the aperture A and particle catch rate of the sampler with $D = 15$ mm. Thus, the catch rate increased as A became larger. This occurred because as the aperture enlarges, the water-conducting feature of the sampler improves, and more particles were introduced into the sampler. The catch rate with no mesh remained within a $\pm$ 4% difference from the results with $A = 0.67$ mm.

Figure 6.4 illustrates the relationship between the flow velocity v and catch rate for the three-hole diameters. According to the figure, the catch rate increased significantly as the flow velocity increased with $D = 5$ mm; however, this tendency decreased as D increased. Another factor in sampler performance was the diagonal direction of particles settling to the slit hole. The relationship between flow velocity and particle condition (diameter and density) results this vertical inflow angle to the intake hole. However, regarding the relationship with the aperture size A, differences in the catch rate increased as D increased. The catch rate was characterized by the flow velocity if D is small, and by A as D became larger.

Figure 6.5 illustrates the relationship between the flow direction to the intake hole and catch rate. When $D = 15$ mm, the inflow at 45° to the intake accounted for

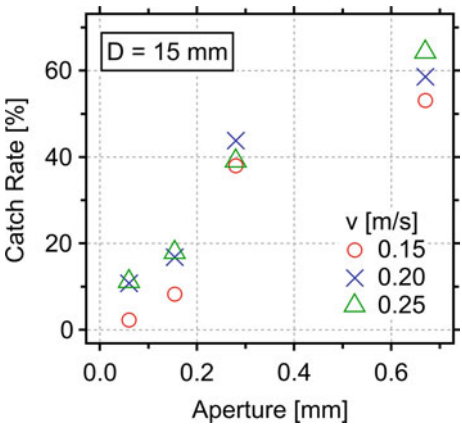

Fig. 6.3 Relationship between outlet mesh aperture and catch rate of sampler. Modified from Okabe et al. (2016)

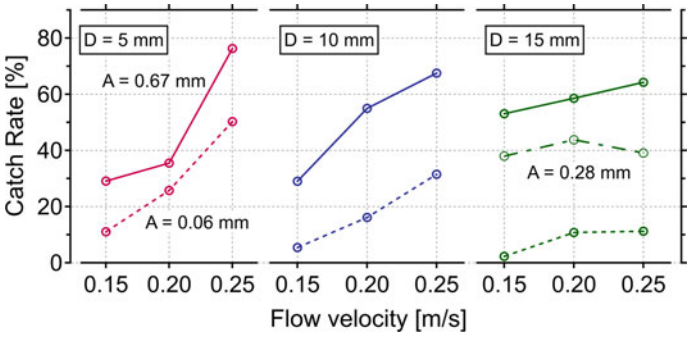

Fig. 6.4 Relationship between flow velocity and particle catch rate of sampler. Modified from Okabe et al. (2016)

approximately half of the catch rate compared to the inflow from the front (0°). Conversely, when D is small, the sampler directivity is enhanced. Regarding the current from the rear (outlet, mesh side), if the aperture allows particles to pass through, then the catch rate is the same as at the front. Hence, it should be noted that particles larger than A are reliably caught in the front intake.

Experiment results show that the catch rate is proportional to flow velocity v. This relationship was related to the water-conducting feature owing to the hole diameter and mesh conditions and the inflow angle of the suspended particles to the intake hole. Therefore, a theoretical analysis plays an important role in elucidating sampler performance under various inflow conditions. The performance is easier to evaluate in terms of data analysis if the catch rate is constant irrespective of the flow velocity. From this perspective and the results from Fig. 4.6, it is considered that a larger hole diameter is suited for suspended sediment surveys.

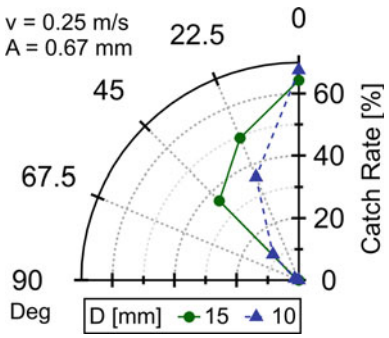

Fig. 6.5 Catch rate directivity of sampler. Modified from Okabe et al. (2016)

6.3 X-Ray Fluorescence Analysis

In recent years, XRF analysis has become a versatile means of examining and analyzing sediment environments. For example, an estimation technique for transport range using the chemical composition and sediment diameter distribution of bottom sediment has been proposed (Okada et al. 2009). In addition to ascertaining the characteristic chemical composition of tidal flat deposition (Rahman and Ishiga 2012), the distribution of gravel supplied from rivers to coasts was utilized to examine a coastal region (Caridi et al. 2016). This includes the use of portable XRF analyzers, which enable easy analysis of sediments in the field and in laboratories, in multi-point sediment investigations. Energy-dispersive X-ray spectroscopy (EDX)-based XRF analyzers, capable of simultaneously analyzing many elements within a short time, have been applied for various purposes. However, compared to wavelength dispersive X-ray spectroscopy (WDX), these analyzers cannot fully separate characteristic X-ray peaks; hence, their analytical precision is inferior. Nevertheless, they are small in size, superior in ease and speed of analysis, and can quickly analyze sediment samples of different volumes. Here, we employed a portable XRF analyzer (XLt792YW, NITON, Fig. 6.6). This analyzer can measure the content of 23 elements, excluding gaseous, volatile, and strongly magnetic elements, from atomic number 19 (K) to 83 (Bi) in the periodic table, at parts per million (ppm) accuracy.

6.4 Digital Image Analysis

The continued development and lower prices of image sensors have spurred the analysis of sediment using digital cameras and image scanners. Subsequent studies have found it simple to obtain sediment particle diameter information from field photography or small samples (Francus 1998; Rubin 2004). This approach can also be utilized for larger particle diameters, from fine sand to gravel (Buscombe and Masselink 2009). As such, it is now possible to perform multi-point and frequent

Fig. 6.6 Handheld X-ray fluorescence analyzer (NITON XLt792YW)

investigations of various sediment environments. Owing to an abundance of temporospatial information on sediments, new findings on coastal sediment dynamics are being obtained. In addition, particle diameter as well as color comprises important information indicating the characteristics of sediment environments.

6.4.1 Sediment Diameter

In sediment diameter analysis, a digital image scanner was employed to obtain sediment images (Fig. 6.7). After the images underwent binarization, the sizes of individual particles in the image were obtained through contour detection. Here, the mean sediment diameter d_m was defined as the ensemble average of the detected sediment diameters. The number of particles in each diameter was also counted from the images and processed statistically. Based on a sieve analysis of reference sediment from a natural beach, the median diameter d_{50} was 0.204 mm. The sediment diameter was then analyzed using image analysis with 1200 dpi images. This resulted in a d_{50} and d_m error of 0.035 mm. The targeted coastal areas in Iriomote

Fig. 6.7 Digital image of sediments from coral reef area

Island contain various sediments differing in density and origin, such as coral sand and sediment from rivers. It should be noted that the derived sediment diameters were different from those derived using a mass-based sieve analysis because the analysis is only reported in terms of shape.

Next, fine soil particles affecting coral were evaluated quantitatively by using the content of suspended particles in sea sediment (SPSS), a technique for assessing the quantity of fine particles originating from land (Omija 2004). Sediment samples from 58 sites in the Sakiyama and Amitori bays were analyzed, and the mean diameters d_m obtained from SPSS (Shibayama et al. 2016) and image analysis were compared. Figure 6.8 illustrates the relationship between the two. SPSS is shown on a logarithmic axis. Larger irregularities were observed for smaller d_m values, and the analysis of the fine particles in this image was poor. However, both approaches were relevant.

6.4.2 *Sediment Color*

The sediment color also represents crucial information. Niu et al. (2009) ascertained the movement of sediments owing to waves and flows in estuaries through field surveys using colored sand as a tracer and image analysis of the sediment samples. Many techniques have been established for tracking sediment movements through illumination and photography with fluorescent dyes and ultraviolet light (Black et al. 2007). Such image analysis techniques often provide the sand particle count and concentration, which were converted from estimated or statistical values based on image analysis. Thus, by rounding detection inaccuracies in the analysis, an easy-to-use and low-cost measurement technique is achieved.

In the technique described here, the red–green–blue (RGB) color values of image pixels were converted into the CIE L^* a^* b^* color space. The mean value and variance of brightness L^* and chromaticity a^* and b^* of all pixels within the

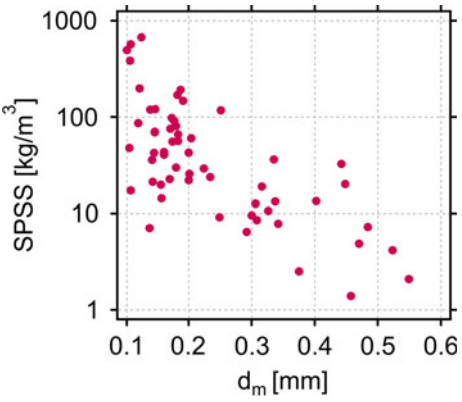

Fig. 6.8 Comparison of mean sediment diameters obtained from image analysis and SPSS. Modified from Okabe et al. (2017)

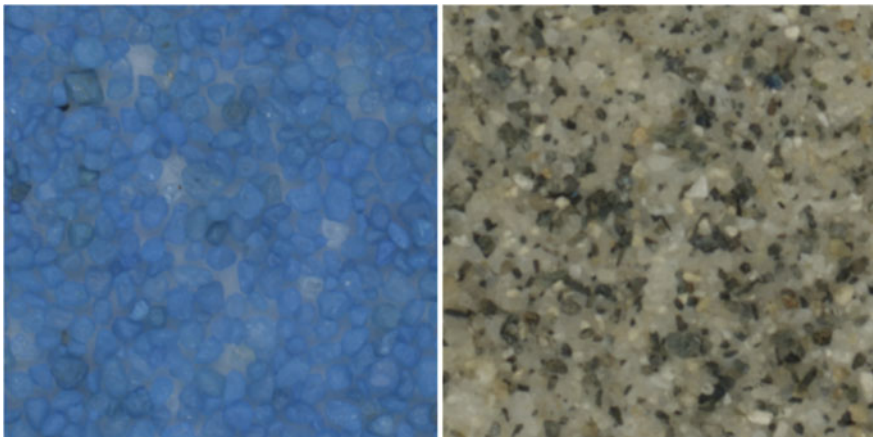

Fig. 6.9 Digital images of sediment samples (left: colored sand, right: natural beach sand)

images were calculated. Here, L^* is the brightness, a^* is the perceived chromaticity from red to green, and b^* is the perceived chromaticity from yellow to blue. For example, Fig. 6.9 presents images of sediment samples, blue colored and natural beach sands digitized by a scanner. Both image data were converted from RGB to an L^* a^* b^* color system. Figure 6.10 plots the relationship between the b^* and L^* of the images. The color differences between the two sands were separated clearly with the dotted line in the figure. By converting to a CIE L^* a^* b^* color system with a wide color gamut, the potential of deriving sediment characteristics is enhanced. For example, Nederbragt et al. (2006) reported a strong correlation between L^* and the results of a scientific analysis of sediments.

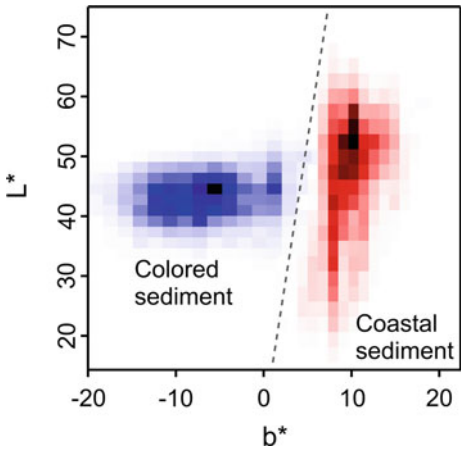

Fig. 6.10 Relationship between L^* and b^* from sediment images

6.5 Application: Characterization of Coastal Sediments in the Sakiyama and Amitori Bays

The survey and analysis techniques described previously were applied to investigate the sediment environment in the coral reef areas of the Sakiyama and Amitori bays. First, to monitor the status of suspended sediment in coastal zones, we set cylindrical sediment traps, which then captured sediment drifting through the nearshore. Next, XRF and image analyses were utilized to identify the characteristics of sediment in the bays. In addition, we combined this information and then classified the characteristics of the sediment distributions within the bays spatially, according to a principal component analysis.

6.5.1 Observations for Suspended Sediment

We set cylindrical bed load samplers at two sites in Amitori Bay, as shown in Fig. 6.11 (Stn. A1 and A2 at water depths of approximately 2.5 and 13 mm, respectively), facing in two directions at each site (south and north). The samplers were set for the period from September 23 to November 18, 2015. The suspended sediment sampler shape and material were the same as shown in Fig. 6.1, with D = 10 mm and A = 0.67 mm. The samplers were set in a vertical stack, such that the slit holes were located 0.2 and 0.5 m from the sea bottom surface, respectively.

Figure 6.12 depicts the changes over time in the significant wave height $H_{1/3}$ and peak period T_p during the period of observation with an acoustic Doppler current

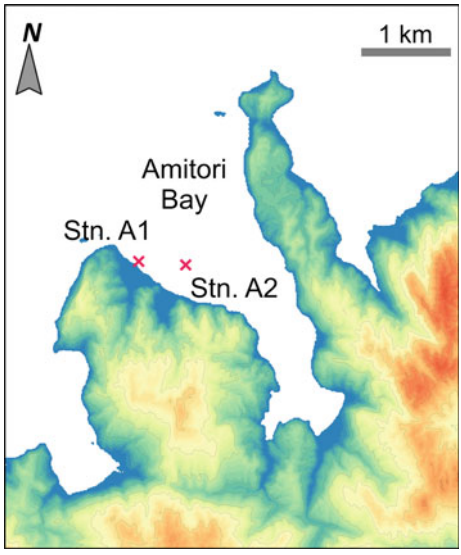

Fig. 6.11 Two locations (Stn. A1 and Stn. A2) where sediment traps were set in Amitori Bay. Modified from Okabe et al. (2016)

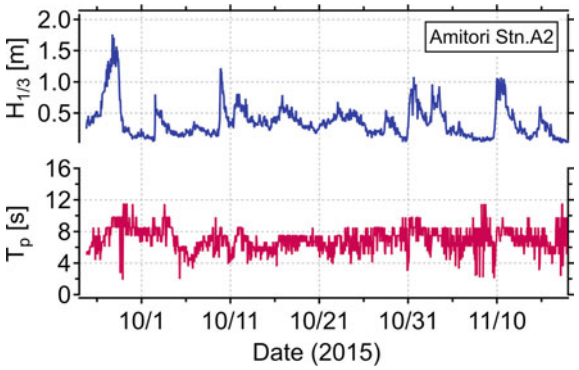

Fig. 6.12 Temporal variations of significant wave height and peak period at Stn. A2 in Amitori Bay. Modified from Okabe et al. (2016)

profiler (ADCP) deployed at Stn. A2. High waves from the 21st typhoon of the year at the end of September were observed; however, during other periods, the waves approximately satisfied $H_{1/3} < 1$ m and $4 < T_p < 8$.

Table 6.1 presents the results for the bed load. The terms southward and northward represent the inflow directions. There were differences on the order of one to two in the bed load size, owing to differences in the water depth at the two site locations. In addition, sediment from the south had the same weight for both the top and bottom layers; however, all of the caught sediment came from the fine particle fraction below the silt. Therefore, it is considered that there were no major differences in the sediment diameters and vertical concentration distributions of the suspended sediment. The aperture was large relative to the sediment diameter, and thus it is possible that the bed load results flowed in from both the north and south directions. Qualitatively, this resulted in a large quantity of drift sand observed at Stn. A1, which was in shallow water close to the shore compared to A2.

6.5.2 *Spatial Characteristics of the Coastal Sediment*

To spatially understand the characteristics of the sediments in the Sakiyama and Amitori bays, sediments were collected from multiple sites in shallow coastal zones and rivers. Sediments were collected from a total of 76 sites, as shown in Fig. 6.13.

Table 6.1 Weight of suspended sediment captured by sampler

	A1 southward (g)	A1 northward (g)	A2 southward (g)	A2 northward (g)
Upper trap	3.943	5.925	0.227	0.040
Lower trap	3.123	1. 582	0.271	0.025

From Okabe et al. (2016)

Of this total, we collected from 58 sites (blue ●) in August 2015 and 18 sites (red ■) in May 2016, including four sites in upstream river areas. In nearshore areas, dive collections of sediments were performed within shallow reefs and estuary tidal flats with water depths of 5 m or less. Much of the river sediments consists of gravel; hence, collection was from sites where sediments gather that are small in sediment diameter. The points at the Idumari River are the site of a blocked estuary, and the Ayanda River is a site where tidal effects are observed. In each sampling, the volume of collected sediments was 100 mL in a water-containing state.

The collected sediments were rinsed with water, dead leaves, algae, and other matter were removed, and they were then left to dry. Subsequently, sieving was performed to remove sediments with particle diameters less than 2 mm, and this was used for analysis. The focus was on the diameter of sediment flowing out from rivers to the bays and the sand constituting beaches. Furthermore, sediments collected from the 58 sites in August 2015 have been utilized for SPSS analysis in previous research (Shibayama et al. 2016).

6.5.2.1 Element Content

We prepared specimens for XRF analysis using sediments and a dedicated analyzer sample cup (outer diameter 30.7 mm, height 22.9 mm). Analysis was conducted on the samples with the analyzer on a fixed stand, rather than handheld. A decision was made to eliminate the effects of sediment diameter on the measurement values as much as possible by increasing the number of measurements and taking the average. Without pulverizing any sediments, we measured each sample three times, then used the mean value as the analysis result.

From the analysis results, 13 common chemical elements (chlorine (Cl), potassium (K), calcium (Ca), scandium (Sc), titanium (Ti), vanadium (V), chromium (Cr), manganese (Mn), iron (Fe), cobalt (Co), zinc (Zn), rubidium (Rb), and

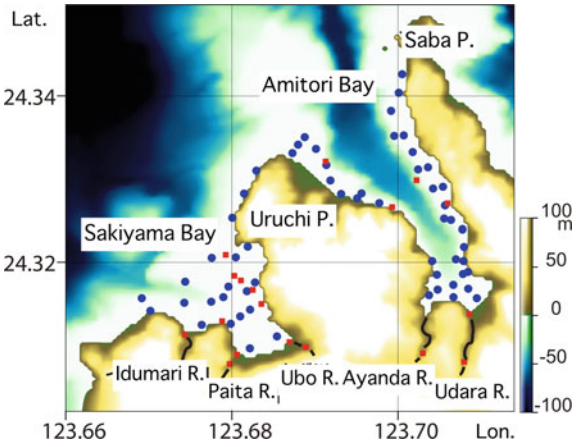

Fig. 6.13 Sediments collection sites. Modified from Okabe et al. (2017)

strontium (Sr) were detected in the survey site samples. However, a somewhat high amount of Co was detected at 24 sites, or approximately one-third of all sites, the content being on the order of several hundred ppm. Hence, Co was incorporated as a characteristic element.

Table 6.2 shows the correlation coefficients between each element. K and Sc had the highest correlation coefficient of $r = 0.99$, while Ca also had a strong connection with Sr and Ti. Sorting the elements in order of the highest correlation coefficient, we find that Cl is first, followed by elements with a high correlation with Ca (K, Sc, Ti, Cr, Rb, and Sr), elements with a high correlation with Fe (Mn, Co, and Rb), V, and finally Zn.

Figure 6.14 presents the detection results for the element content at the A1 site, located approximately in the middle of the eastern shore of Amitori Bay. According to the results, the Ca content is the highest, followed by K, Cl, and Fe content which are all smaller than Ca on the order of one to two. In addition, Fig. 6.15 shows the content of Ca and Fe at three sites in Sakiyama Bay. Dividing the bay longitudinally, we compared a river site (S1), an estuary tidal flat site (S2), and a site at the mouth of the bay (S3). The Ca content increased from the river to the mouth of the bay; however, at the mouth of the bay it was approximately 20 times larger than at the tidal flat, with a sudden change in the sign of the spatial increase. Conversely, Fe was abundant in the river, though signs of a linear decrease toward the mouth of the bay are observed.

Figure 6.16 illustrates the relationship between the distance from the inner part of Amitori Bay to the mouth of the bay and the Ca content. Using the A2 site in the inner part of the bay as a reference, this distance is the linear distance from the tidal flat to each site on the mouth side of the bay. Thus, even if the Ca content in the longitudinal direction of Amitori Bay is somewhat irregular, it increases roughly in proportion to the distance from the inner part of the bay to the mouth. In addition, there were no clear differences in this relationship on the east and west shores of the bay.

Figure 6.17 shows the spatial distribution of the Co content. The black dots in the figure signify non-detection sites. The Co content was characterized by being the highest in the Paita River. The detected Co content was mostly within a range of approximately 200 ppm and was present in the estuaries, tidal flats, and eastern reefs of both bays. In addition, it was also detected at three sites in the middle of Sakiyama Bay.

6.5.2.2 Diameter and Sediment Color

To utilize digital photographs in sediment diameter analysis, digital images of the sediment were captured at a resolution of 2400 dpi (0.0106 mm pixel size) using a flatbed scanner. In the color information analysis, the bottom surface of the sediments sample cup used in the XRF analysis (6 μm thick sample-holding transparent polypropylene thin film) was imaged with a scanner for analysis. We used an approximately 17 mm square (2400 dpi) area and obtained the mean value and

Table 6.2 Correlation coefficients between each element in the sediments

	Cl	K	Ca	Sc	Ti	V	Cr	Mn	Fe	Co	Zn	Rb
K	0.10											
Ca	0.27	0.76										
Sc	0.09	0.99	0.81									
Ti	−0.30	−0.83	−0.89	−0.88								
V	−0.33	0.34	−0.26	0.24	0.17							
Cr	−0.39	−0.75	−0.77	−0.78	0.70	0.26						
Mn	−0.22	−0.27	−0.45	−0.29	0.35	0.27	0.21					
Fe	−0.24	−0.45	−0.60	−0.51	0.46	0.15	0.28	0.88				
Co	−0.25	−0.27	−0.32	−0.19	0.44	−0.11	0.07	0.90	0.91			
Zn	0.03	0.22	0.26	0.23	−0.10	−0.05	−0.14	0.26	0.10	0.39		
Rb	−0.19	−0.70	−0.85	−0.74	0.75	0.18	0.56	0.67	0.75	0.59	−0.09	
Sr	0.28	0.75	0.97	0.80	−0.87	−0.25	−0.75	−0.44	−0.59	−0.30	0.30	−0.85

From Okabe et al. (2017)

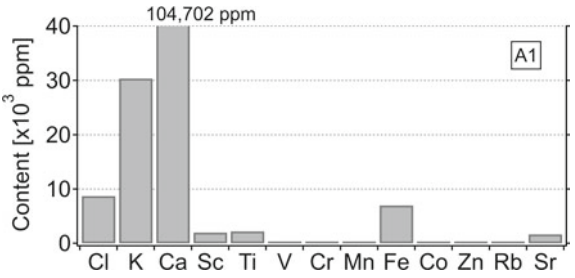

Fig. 6.14 Element content of sediments at A1 site in Amitori Bay. Modified from Okabe et al. (2017)

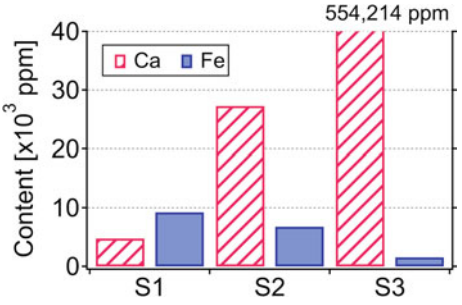

Fig. 6.15 Ca and Fe content of sediments at three sites (S1, S2, and S3) in Sakiyama Bay. Modified from Okabe et al. (2017)

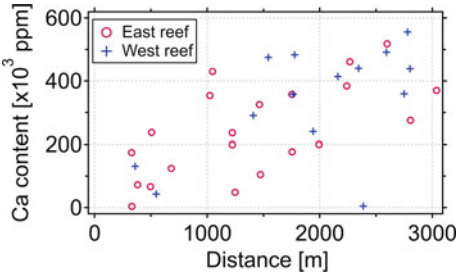

Fig. 6.16 Relationship between distance from the inner part of Amitori Bay and Ca content. Modified from Okabe et al. (2017)

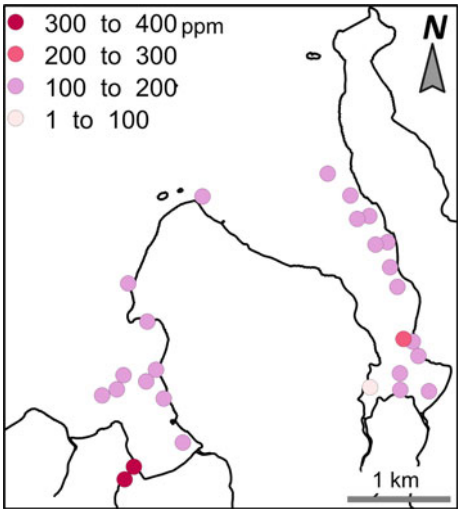

Fig. 6.17 Co content spatial distribution. Modified from Okabe et al. (2017)

variance of all images from the brightness L^* and chromaticity a^* and b^* for each pixel in a CIE L^* a^* b^* color system.

Table 6.3 presents the correlation coefficients between each of the sediment components, including sediment diameter d_m, brightness L^*, chromaticity a^* and b^*, and variance of color information (var subscript in the table) obtained at all survey sites. Thus, L^* has a low correlation relative to all other components; however, d_m has a high positive correlation with the color variance. In addition, it was found that the variance of color information has a mutually high correlation coefficient. Sorting the components in order of the highest correlation coefficient, first were components with a high correlation with d_m (respective variances with a^* and L^* a^* b^*), followed by components with a high correlation with b^* (a^*), and finally L^*.

6.5.2.3 Cluster Analysis

A cluster analysis is a technique that involves dividing targeted individuals and groups of variables into groups that are similar in nature and is employed for spatial categories of sediments and habitats along shores (Danielsson et al. 1999; Frontalini and Coccioni 2008). Understanding sediments and locations that are highly similar in a variety of aspects is believed to provide information that is beneficial to future ecosystem evaluations. Here, we attempted a cluster analysis through hierarchical clustering, using the element content (Cl, Ca, V, and Fe), sediment diameter d_m, and color (L^* and b^*), to analyze sediments similarities in many components. Furthermore, components with mutually high correlations and low detection site Zn content were excluded from the analysis. A median (median value) method was employed to compute the Euclidean distance between clusters. Figure 6.18 presents the dendrogram (tree diagram) obtained from the cluster analysis. The vertical axis represents the distance between clusters, with survey sites arranged on the horizontal axis. These results correspond to the spatial arrangement within the bay and are categorized into multiple regions. Each cluster in the figure includes a brief description of its characteristics. Figure 6.19 shows this in a map, where A to G in the figure corresponds to the categories in Fig. 6.18. From this, the characteristics of regions are obtained from the cluster analysis results, such as the clear division of

Table 6.3 Correlation coefficients between brightness and chromaticity with sediments color information

	d_m	L^*	a^*	b^*	L^* var.	a^* var.
L^*	0.32					
a^*	0.62	0.24				
b^*	0.36	−0.05	0.65			
L^* var.	0.77	0.13	0.52	0.28		
a* var.	0.73	−0.02	0.71	0.54	0.74	
b^* var.	0.62	−0.22	0.50	0.47	0.80	0.80

From Okabe et al. (2017)

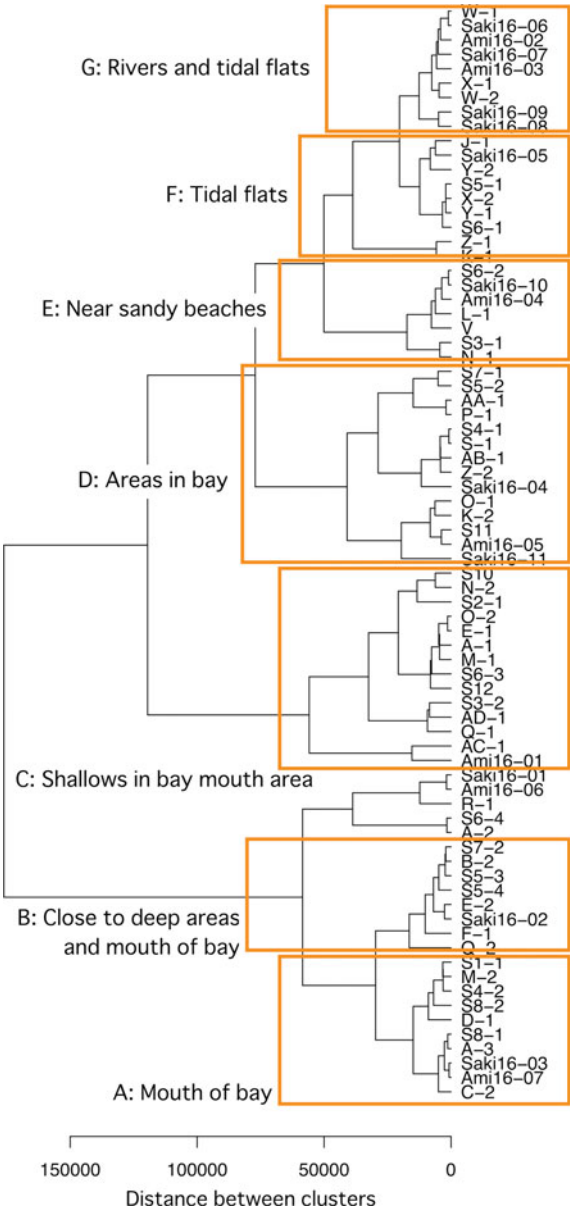

Fig. 6.18 Result of cluster analysis using the sediments chemical element content, sediment diameter, and color information. Modified from Okabe et al. (2017)

rivers and tidal flats. In Sakiyama Bay, the clusters change from the inner part of the bay to the mouth, and no major differences are observed at the eastern and western shores. In addition, the scattered cluster E is suggested to reflect bottom sampling close to the seashore.

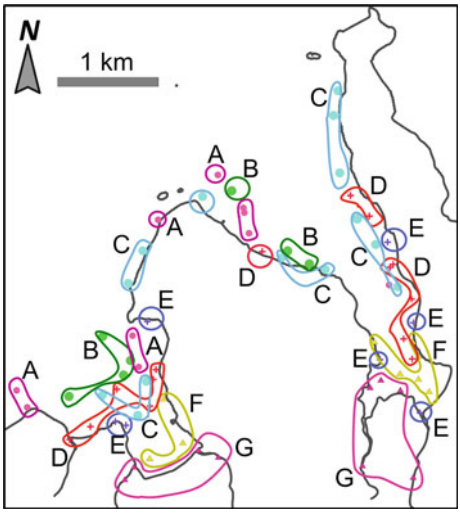

Fig. 6.19 Spatial arrangement of hierarchical clustering results showing spatial categories apply to the sediments. Modified from Okabe et al. (2017)

In Table 6.3, the sediment diameter d_m is observed to have a high positive correlation with the sediment color variance. This corresponds to the relationship between biologically derived yellow-white-colored sand with a large sediment diameter and fine dark-colored sand. In addition, d_m is related to SPSS (Fig. 6.8), and it is considered that outflowing sediment is contained in proportions corresponding with the sediment diameter. Both bays have coral reef areas in which there are mixtures of biologically derived sand and sediment supplied from rivers and other sources, the proportions of which are the main factors in spatially characterizing the sediments. Ca is a biologically derived index of coral and foraminifera, and its content increases corresponding to the distance from the inner part of a bay, as shown in Figs. 6.15 and 6.16. In contrast, outflowing sediment from rivers is distributed in a quantity and location corresponding to the external sediment transport forces of the waves and flow. Murakami et al. (2012) (see Chap. 9) similarly showed, according to numerical calculation results, that toward the mouth of Amitori Bay the quantity of outflowing sediment particles from rivers reaching the bottom decreases, while this feature is different on the eastern and western shores. On the eastern shore, outflowing sediment has a significant effect. In this study, Co detection was observed on the eastern shores of both bays (Fig. 6.17); however, additional detailed surveying and analysis are required to verify if the results support this finding. Nevertheless, this suggests possible differences in the sediments at the eastern and western shores of both bays.

A cluster analysis based on this information indicates that the spatial categories for the bays apply to the sediments (Fig. 6.19). This is particularly clear for rivers and tidal flats in the inner part of a bay, indicating that areas with a strong influence from outflowing sediment have different sediments from reefs. It is believed that differences in the cluster arrangements at the east and west shores are small in Sakiyama Bay, and that unlike the Co content distribution, changes in the sediments

predominate along the bay axis. The distributions of coral and Enhalus acoroides in Sakiyama Bay, presented by Shimokawa et al. (2016) (see Chap. 10), naturally indicate the shifting distributions of both along the bay axis, and spatial changes in the characteristics of biological and sediments distributions tend to be largely similar. However, because the additional physical factors of water depth distribution and wave exciting forces have a strong effect, these components may have complex mutual effects in forming the environments within the bays.

6.6 Conclusions and Future Work

In this chapter, the sediment-catching performance of a sediment trap utilized for suspended sediment monitoring in coastal areas was evaluated through a laboratory experiment. Based on the results of the experiment, it is clear that the intake mesh aperture is related to the permeability of the suspended sediment sampler, and the increase in the catch rate as the flow velocity increases is more prominent as the slit-hole diameter decreases. If the hole diameter is large, the catch rate is dependent upon the aperture. In addition, the directionality properties of the sampler were clarified. Next, we performed an XRF analysis and described the characteristics of relevant techniques and devices. We also described image analysis techniques frequently employed for sediment analysis in recent years. We established a method for acquiring sediment diameter and color information from sediment images obtained with a digital scanner.

Next, these observation and analysis techniques were applied to sediment monitoring in the Sakiyama and Amitori bays, and attempts were made to investigate the sediment environments in the bays. We captured small quantities of fine sediment using cylindrical samplers set in multiple layers and qualitatively investigated the differences in the drift sand quantity according to the water depth. In the XRF analysis, 13 shared chemical elements were detected from 76 sediment collection sites. At the mouths of both bays, the Ca content, indicating biologically derived sediments, was predominant. The spatial distributions increased roughly in proportion to the distance from the inner part of each bay. In addition, Co was detected at one-third of all the survey sites located in rivers, the tidal flats of the Amitori Bay and eastern reefs of both bays. Through a hierarchical cluster analysis using the sediments element content, sediment diameter, and color information, we found that these characteristics are spatially distributed from the inner part of the bay to the mouth.

Various techniques have been proposed to estimate the sediment diameter through image analysis. A technique using fractal theory (Martin and Taguas 1998) differs from methods in which a computer measures individual particle sizes, instead of performing a sieve analysis or visual observation, as in the example in this chapter. In addition, studies have also appeared using artificial neural networks to predict the sediment diameter in suspended sediment (Thompson et al. 2016) and continued attempts are being made to more accurately estimate sediment

information. If a large volume of environmental sediment data could be more easily obtained from coral reef areas through these techniques, it would be possible to obtain big data. Already, steps are being initiated to utilize big data for coastal zone disaster prevention and management (Gutierres et al. 2018), and it may be possible to achieve coral reef conservation in the future through big data on environments along shores.

Acknowledgements We would like to thank Mayumi Suzuki and Seishichi Miyauchi, graduates of Tokai University's School of Marine Science and Technology; and Takumi Shibayama, a graduate of University of Tsukuba, Graduate School of Life and Environmental Sciences, for helping to collect survey data. We also received advice from Professor Shigeru Kato of Toyohashi University of Technology concerning X-ray fluorescence and image analyses. For analytical work, we received the cooperation of Yusuke Aoki and Kazuki Furukawa, both graduates of Toyohashi University of Technology.

References

Andréfouët S, Riegl B (2004) Remote sensing: a key tool for interdisciplinary assessment of coral reef processes. Coral Reefs 23:1–4

Bauer BO, Namikas SL (1998) Design and field test of a continuously weighing, tipping—bucket assembly for aeolian sand traps. Earth Surf Proc Land 23(13):1171–1183

Bessell-Browne P, Negri AP, Fisher R, Clode PL, Duchworth A, Jones R (2017) Impacts of turbidity on corals: the relative importance of light limitation and suspended sediments. Mar Pollut Bull 117(1–2):161–170

Black KS, Athey S, Wilson P, Evans D (2007) The use of particle tracking in sediment transport studies: a review. Geological Society, London, Special Publications 274:73–91

Bloesch J, Burns NM (1980) A critical review of sedimentation trap technique. Schweiz Z Hydrol 42(1):15–55

Buscombe D, Masselink G (2009) Grain-size information from the statistical properties of digital images of sediment. Sedimentology 56(2):421–438

Caridi F, D'Agostino M, Marguccio S, Belvedere A, Belmusto G, Marcianò G, Sabatino G, Mottese A (2016) Radioactivity, granulometric and elemental analysis of river sediments samples from the coast of Calabria, south of Italy. The Eur Phys J Plus 131(5):136

Chauvaud S, Bouchon C, Maniere R (1998) Remote sensing techniques adapted to high resolution mapping of tropical coastal marine ecosystems (coral reefs, seagrass beds and mangrove). Int J of Remote Sens 19(18):3625–3639

Costa BM, Battista TA, Pittman SJ (2009) Comparative evaluation of airborne LiDAR and ship-based multibeam SoNAR bathymetry and intensity for mapping coral reef ecosystems. Remote Sens Environ 113(5):1082–1100

Danielsson Å, Cato I, Carman R, Rahm L (1999) Spatial clustering of metals in the sediments of the Skagerrak/Kattegat. Appl Geochem 14(6):689–706

Entsch B, Boto KG, Sim RG, Wellington JT (1983) Phosphorus and nitrogen in coral reef sediments. Limnol Oceanogr 28(3):465–476

Erftemeijer PL, Riegl B, Hoeksema BW, Todd PA (2012) Environmental impacts of dredging and other sediment disturbances on corals: a review. Mar Pollut Bull 64(9):1737–1765

Francus P (1998) An image-analysis technique to measure grain-size variation in thin sections of soft clastic sediments. Sed Geol 121(3–4):289–298

Frontalini F, Coccioni R (2008) Benthic foraminifera for heavy metal pollution monitoring: a case study from the central Adriatic Sea coast of Italy. Estuar Coast Shelf Sci 76(2):404–417

Garcia C, Laronne JB, Sala M (2000) Continuous monitoring of bedload flux in a mountain gravel-bed river. Geomorphology 34(1–2):23–31

Griffin SP, Garcia RP, Weil E (2003) Bioerosion in coral reef communities in southwest Puerto Rico by the sea urchin Echinometra viridis. Mar Biol 143(1):79–84

Gust G, Bowles W, Giordano S, Hüttel M (1996) Particle accumulation in a cylindrical sediment trap under laminar and turbulent steady flow: an experimental approach. Aquat Sci 58(4):297–326

Gutierres F, Gomes P, Rocha J and Teodoro AC (2018) Spatially explicit models in local dynamics analysis: the potential natural vegetation (PNV) as a tool for beach and coastal management. In: Botero C, Cervantes O, Finkl C (eds) Beach management tools—concepts, methodologies and case studies. Coastal Research Library, vol 24. Springer, Cham

Jackson DWT (1996) A new, instantaneous aeolian sand trap design for field use. Sedimentology 43(5):791–796

Jordan LKB, Banks KW, Fisher LE, Walker BK, Gilliam DS (2010) Elevated sedimentation on coral reefs adjacent to a beach nourishment project. Mar Pollut Bull 60(2):261–271

MacIntyre IG, Glynn PW, Cortés J (1992) Holocene reef history in the eastern Pacific: mainland Costa Rica, Caño Island, Cocos Island, and Galápagos Islands. In: Proceedings 7th international coral reef symposium (2):1174–1184

Martin MA, Taguas FJ (1998) Fractal modelling, characterization and simulation of particle-size distributions in soil. Proc R Soc Lond A: Math, Phys Eng Sci 454(1973):1457–1468

Mudroch A, Azcue JM (1995) Manual of aquatic sediment sampling. CRC Press, Florida, p 219

Murakami T, Ukai A, Kohno H, Mizutani A, Shimokawa S, Nakase K, Yasuda T (2012) Relationships between distributions of coral and physical environments in Amitori Bay, Iriomote island, Japan. Ann J Civil Eng Ocean B3(68):1133–1138 (in Japanese with English abstract)

Nederbragt AJ, Dunbar RB, Osborn AT, Palmer A, Thurow JW and Wagner T (2006) Sediment color analysis from digital images and correlation with sediment composition. Geological Society, London, Special Publications 267: 113–128

Niu X, Ueyama S, Sato S, Tajima Y, Liu H (2009) Sediment movement under combined waves, tide and river discharge in a river mouth. Proc Coastal Dynamics 2009: Paper No. 67 (1–13)

Okabe T, Aoki Y, Kato S, Murakami T, Shimokawa S, Kono H (2016) Experimental evaluation and field applications of a cylindrical sediment trap for suspended sediment. J Jpn Soc Civil Eng B3 72(2): I_922–I_927 (in Japanese with English abstract)

Okabe T, Murakami T, Kono H, Mizutani A, Shimokawa S (2017) Spatial characterization of a coastal sediment in Sakiyama and Amitori bays by X-ray fluorescence and digital image analysis. J Jpn Soc Civil Eng B3 73(2):I_1036–I_1041 (in Japanese with English abstract)

Okada T, Thi MTN and Furukawa K (2009) Estimation of the Spatial Distribution of Sediment Using Chemical Composition and Particle-size Distribution. J Japan Soc Civil Eng B2 65(1): 976–980 (in Japanese with English abstract)

Omija T (2004) Terrestrial inflow of soils and nutrients. Coral Reefs Jpn 47:64–68

Phillips JM, Russell MA, Walling DE (2000) Time-integrated sampling of fluvial suspended sediment: a simple methodology for small catchments. Hydrol Process 14(14):2589–2602

Rahman MA, Ishiga H (2012) Trace metal concentrations in tidal flat coastal sediments, Yamaguchi Prefecture, southwest Japan. Environ Monit Assess 184(9):5755–5771

Roberts JM, Brown CJ, Long D, Bates CR (2005) Acoustic mapping using a multibeam echosounder reveals cold-water coral reefs and surrounding habitats. Coral Reefs 24(4):654–669

Rowe GT, Gardner WD (1979) Sedimentation rates in the slope water of the northwest Atlantic Ocean measured directly with sediment traps. J Marine Res 37(3):581–600

Rubin DM (2004) A simple autocorrelation algorithm for determining grain size from digital images of sediment. J Sediment Res 74(1):160–165

Shibayama T, Shimokawa S, Kohno H, Ukai A, Mizutani A, Nakase K, Murakami T (2016) Property of soil particles related to reef-building coral distribution in Amitori and Sakiyama bays, Iriomote Island. In: Proceedings of Japan Geoscience Union Meeting 2016: ACG15-P06

Shimokawa S, Kohno H, Murakami T, Miyauchi S, Suzuki M, Mizutani A (2016) Relation between coral distributions and Physical variables in Sakiyama Bay, Iriomote Island, Japan. Ann J Civil Eng Ocean B2(72):1435–1440 (in Japanese with English abstract)

Thompson J, Sattar AM, Gharabaghi B, Warner RC (2016) Event-based total suspended sediment particle size distribution model. J Hydrol 536:236–246

Chapter 7
Transport Properties of Soil Particles in Sakiyama and Amitori Bays

Shinya Shimokawa, Tomokazu Murakami, Hiroyoshi Kohno and Akira Mizutani

Abstract The actual states of soil particle transport in and exchange between the Sakiyama and Amitori bays, Iriomote Island, Japan, were investigated using atmosphere–ocean–river observations and numerical simulations. Results show that in both bays in summer, large particles (≥ 15 μm) do not move from areas near the river mouths. Small particles, however, do move to the respective east sides of the bays. In winter in both bays, large particles move to the respective centers of the bays from areas near the river mouths, whereas small particles move to the respective west sides of the bays. Furthermore, soil particles move mainly from Sakiyama Bay to Amitori Bay in summer, but this direction is reversed in winter. These features are explainable mainly by seasonal differences in wind speed and direction, but the combination of seasonal differences in wind speed and direction, the wind-driven current and the topography are also important for them. The results are useful for assessing soil particle effects on coastal oceanic ecosystems, such as those containing reef-building coral and *Enhalus acoroides*, and their effective conservation in natural conservation areas of the Sakiyama and Amitori bays.

Keywords Coastal oceanic ecosystem · Environmental impact assessment · Iriomote Island · Sakiyamawan–Amitoriwan Nature Conservation Area · Soil particle

This chapter is based on work reported by Shimokawa et al. (2017).

S. Shimokawa (✉) · T. Murakami
Storm, Flood and Landslide Research Division, National Research Institute for Earth Science and Disaster Resilience, Tsukuba, Japan
e-mail: simokawa@bosai.go.jp

T. Murakami
e-mail: tmurakami@bosai.go.jp

H. Kohno · A. Mizutani
Okinawa Regional Research Center, Tokai University, Yaeyama, Japan
e-mail: hkohno@scc.u-tokai.ac.jp

A. Mizutani
e-mail: ma110267@tsc.u-tokai.ac.jp

S. Shimokawa et al. (eds.), *Geophysical Approach to Marine Coastal Ecology*, Springer Oceanography, https://doi.org/10.1007/978-981-15-1129-5_7

7.1 Introduction

The Sakiyamawan–Amitoriwan Nature Conservation Area of Iriomote Island is the only oceanic nature conservation area in Japan. Sakiyama Bay was designated as a nature conservation area in 1983. In 2015, the area was extended to include the adjacent Amitori Bay (Ministry of the Environment, Government of Japan 2015a, b; see also Sects. 1.1, 1.2 and Fig. 1.1). The area has no access roads. The bay perimeter is uninhabited. Therefore, it is a natural environment with very little human impact. Additionally, it has various environmental gradients, such as freshwater and soil inputs from rivers at the innermost parts of the bays, the existence of mangrove forests aside from the rivers, and differences of water depth, length, and reef slope zones between the bays (Kawana 1990; Ukai et al. 2012). The environmental gradients affect the distribution of coastal marine systems such as those including reef-building corals (see Sect. 1.4, Chaps. 9, 10 and 11) and *Enhalus acoroides* (see Sect. 1.5 and Chap. 12). For example, soil particles provide nutrients to them, but disturb the respiration of corals and photosynthesis of zooxanthellae. Consequently, the conservation and the assessment of environmental impact are urgently and critically necessary.

Previous reports have described that the distributions of reef-building corals (Murakami et al. 2012; Shimokawa et al. 2014b, 2015, 2016; Ukai et al. 2015) and *Enhalus acoroides* (Murakami et al. 2014, 2015a, b; Nakase et al. 2015, 2016) are influenced strongly by the environmental gradients. They vary with location in the Sakiyama and Amitori bays. However, the effects of soil input from rivers on the coastal marine ecosystems have not been investigated thoroughly in the area, especially in Sakiyama Bay.

This study was conducted to provide transport properties of soil particles in the region as basic information for analysis. Because of the remoteness of the study area and limited access, broad and continuous observations are difficult to obtain. Therefore, in addition to the observations conducted on site, we used numerical modeling that integrated observational data into the models. Based on the results, we were able to elucidate the transport properties of soil particles in the study area and the exchange properties between the Sakiyama and Amitori bays in summer and winter.

7.2 Numerical Model and Method

First, we conducted observations of wind speed, wind direction, and precipitation at point A (continuous meteorological observation station, Fig. 7.1), and flow rates at the four rivers using an acoustic Doppler current profiler (see Chap. 2). Tables 7.1 and 7.2 show average meteorological field data observed at point A in the summer and winter, with average flow rates observed respectively at the four rivers in the summer and winter. For flow rates of the Painta and Ubo rivers (Fig. 7.1) in

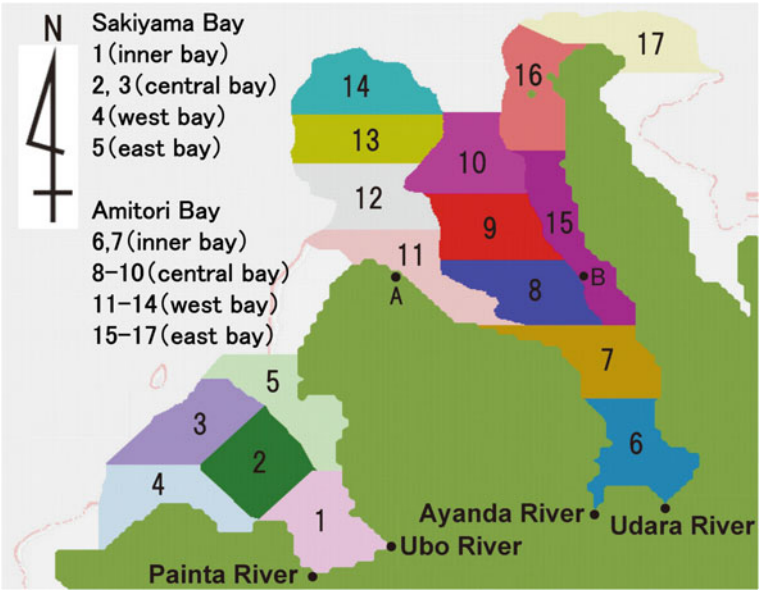

Fig. 7.1 Calculated domain and 17 regions investigated in this study. Particles are released from the mouths of the Painta, Ubo, Ayanda, and Udara rivers. A and B, respectively, show the meteorological observation point and oceanic flow observation point (Shimokawa et al. 2014b). Reprinted from Shimokawa et al. (2017) by The Authors licensed under CC BY 4.0

Table 7.1 Average meteorological field observations at point A (Fig. 7.1) in the summer and winter

	Summer	Winter
Ayanda river (m^3/s)	0.012	0.041
Udara river (m^3/s)	0.010	0.023
Painta river	0.011 m^3/s	Same as that in summer
Ubo river	0.097 m^3/s	Same as that in summer

Reprinted from Shimokawa et al. (2017) by The Authors licensed under CC BY 4.0

Table 7.2 Average flow rates observed at the four rivers (Fig. 7.1) during summer and winter

	Summer	Winter
Average wind speed (m/s)	3.1	5.8
Maximum wind speed (m/s)	8.6	13.5
Average wind direction (°)	SSE (160)	ENE (73)
Average precipitation (mm/day)	1.5	2.9
Maximum precipitation (mm/day)	15.5	42.5

Reprinted from Shimokawa et al. (2017) by The Authors licensed under CC BY 4.0

Sakiyama Bay, we used the same values for both summer and winter because winter observations could not be conducted.

Next, we reproduced current velocity fields in the Amitori and Sakiyama bays using CCM (Coastal ocean Current Model with a multi-sigma coordinate system, see Chap. 3; Murakami et al. 2011; Shimokawa et al. 2014a) with our field observations, the astronomical tide calculated using a tide model (Matsumoto et al. 2000) as the boundary values, and the water temperature and salinity observed using a conductivity–temperature–depth profiler (see Chap. 2; Murakami et al. 2012) for initial values. The calculated domain is portrayed in Fig. 7.1. Time periods of the calculations were June 9 to June 29, 2014, and November 1 to November 22, 2014, which are, respectively, periods of typical summer and winter atmospheric conditions in this area. The space resolution is 50 m horizontally and 42 layers vertically. The time step is 1 s.

Then, using the calculated current velocity fields, Lagrangian particle tracing analysis (see Chap. 3; Cushman-Roisin and Beckers 2011) was applied. The mass percentage passing of soil particles from the Ayanda and Udara rivers (Fig. 7.1) in Amitori Bay, obtained by sediment trap observation at the mouths of the rivers (Shimokawa et al. 2014b) demonstrated that the soil particle diameters were distributed mainly from 0.1 to 50 μm. This study specifically examines soil particle distributions. To investigate the soil particle distributions, the size difference of soil particles must be included because fine particles reach distant places, but coarse particles do not. Therefore, soil particles with diameters of 0.1, 1, 3, 5, 8, 10, 15, 20, and 30 μm were released every 10 s from the river mouths of the four rivers (Painta, Ubo, Ayanda, and Udara rivers, with six grid points for each river. Therefore, 24 particles were released every 10 s for each diameter value. See also Fig. 7.1.). We assumed that total sediment loads are equal among the four rivers in numerical experiments because no exact data are available, although the actual loads and the watershed sizes might be different. The initial state is that with no particle. Then, the states of the soil particles were classified into bottom (on the seafloor), floating (in the sea), and landed (from the sea). Time series of soil particle positions was obtained. Additional information for the numerical models and methods is presented in Chap. 3.

7.3 Results and Discussion

Figure 7.2 portrays a snapshot of the soil particle distributions with a diameter of 3 μm calculated via Lagrangian particle tracing analysis in the final states for the summer and winter (0:00 UTC, June 30 and 0:00 UTC, November 23 in 2014, respectively). Particles with yellow, red, violet, and pink, respectively, represent sources of the Painta, Ubo, Ayanda, and Udara rivers. The results demonstrate that for both bays, soil particles tend to accumulate on the east side in summer and the west side in winter and move from Sakiyama Bay to Amitori Bay in summer and from Amitori Bay to Sakiyama Bay in winter.

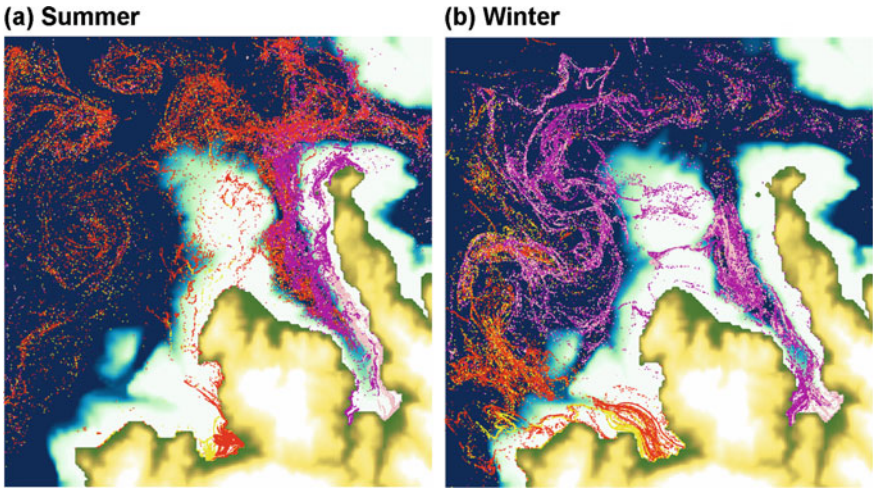

Fig. 7.2 Distributions of soil particles with a diameter of 3 μm in final states during **a** summer and **b** winter (0:00 UTC, June 30 and 0:00 UTC, November 23 in 2014, respectively). Yellow, red, violet, and pink dots, respectively, represent soil particles from the Painta, Ubo, Ayanda, and Udara rivers: Fig. 7.1. Reprinted from Shimokawa et al. (2017) by The Authors licensed under CC BY 4.0

To examine the characteristics of soil particle distributions, including the difference of distribution by the diameters and moving state (bottomed or floated) of soil particles, Sakiyama and Amitori bays were divided into 17 regions: 5 regions for Sakiyama Bay and 12 regions for Amitori Bay (Fig. 7.1). The divisions reflected the distributions of reef-building coral (Murakami et al. 2012; Shimokawa et al. 2016) and *Enhalus acoroides* (Murakami et al. 2014; Nakase et al. 2015). Each region has almost equal areal extent. For example, the west (11–14) and east regions (15–17) of Amitori Bay, respectively, correspond to the top of the reef slope (Fig. 1.1). The inner region of Sakiyama Bay (1, 2) corresponds to the *Enhalus acoroides* habitat.

Figure 7.3 presents the number of soil particles by region, particle diameter, and particle state (bottomed or floated) integrated in summer and winter. In summer, large particles, defined here as particles with >15 μm diameter, moved only slightly from the river mouth of each bay. Particularly, floating large particles were found only in the innermost regions of the bays. For Sakiyama Bay, the total number of soil particles was large on the east side, although the number of bottomed particles was large in the west side and the floating particles were numerous on the east side. For Amitori Bay, the total number of soil particles was large in the central bay, but the number of bottomed particles was large on the east side. In winter, for Sakiyama Bay, large particles moved from the river mouth over a broad region of the bay. For Amitori Bay, large particles moved from the river mouths to the inner bay, although the region over which they were distributed was smaller than that for Sakiyama Bay. For Sakiyama Bay, the numbers of both bottomed and floated particles were greater on the west side than those on the east side. For Amitori Bay, the total

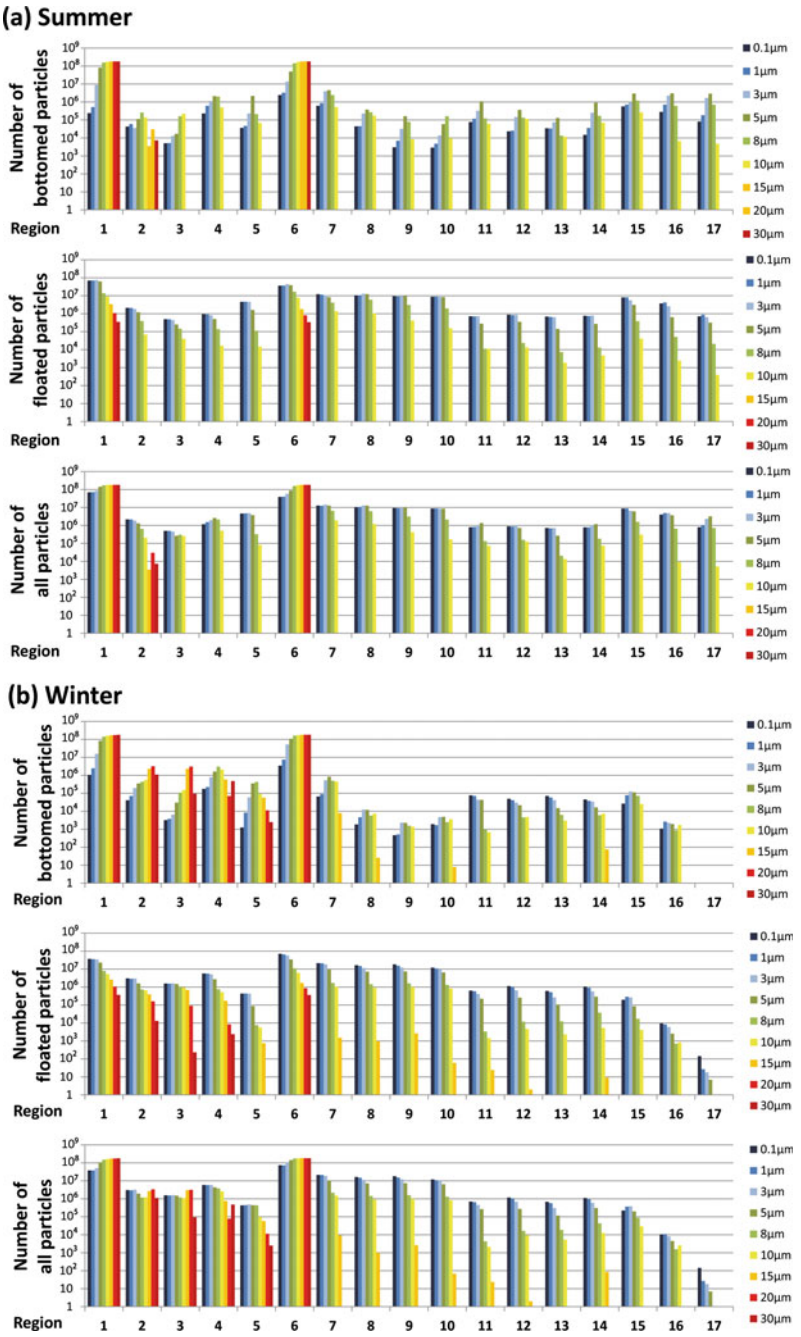

Fig. 7.3 Numbers of soil particles by region, particle diameter, and particles state (bottom and floating) integrated into **a** summer and **b** winter. Reprinted from Shimokawa et al. (2017) by The Authors licensed under CC BY 4.0

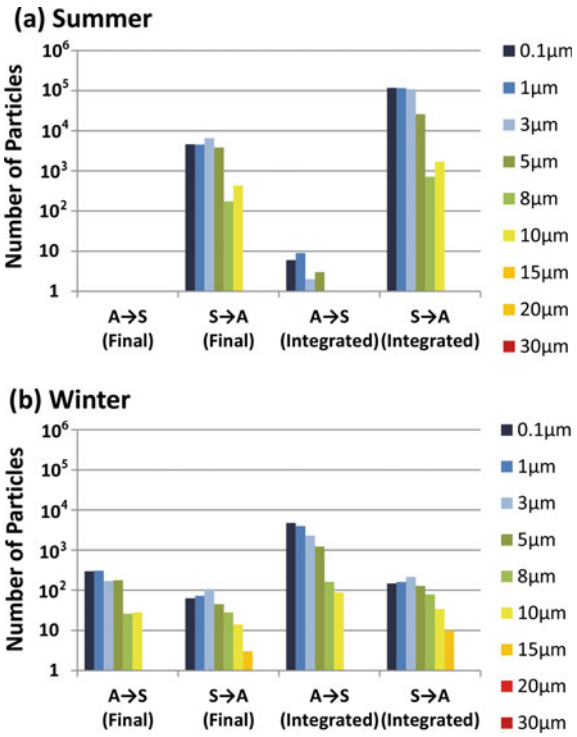

Fig. 7.4 Final and integrated numbers and size distributions of soil particles exchanged between Sakiyama and Amitori bays during **a** summer and **b** winter. Final and integrated values, respectively, represent the values at the end of the simulations and those integrated during the simulations. Reprinted from Shimokawa et al. (2017) by The Authors licensed under CC BY 4.0

number of soil particles was large in the central bay, but the number of bottomed particles was large on the west side. These characteristics of soil particle distributions and movements in winter were remarkably different from those in summer. The strong ENE winds in winter have the same effect on both bays. Therefore, the lengths along which the winds affect the soil transport are almost equal for both bays. However, the sizes and depths of the bays differ: Sakiyama Bay is smaller and shallower than Amitori Bay. Consequently, differences in soil particle transport between bays in winter are regarded as a cause.

Figure 7.4 shows the final and integrated numbers of soil particles exchanged between Sakiyama and Amitori bays in the summer and winter. Final and integrated values represent values at the end of the simulations and those integrated during the simulations. They are shown as respectively representative of instant and averaged values. For the soil particle exchange numbers, regions 13, 14, and 17 of Amitori Bay were excluded because they include open ocean regions. In summer, soil particles moved mainly from Sakiyama Bay to Amitori Bay. By contrast, in winter, soil particles moved mainly from Amitori Bay to Sakiyama Bay. However, in winter, movements from Sakiyama Bay to Amitori Bay also occurred for large particles, which is not observed in other cases examined in this study.

This fact agrees with the characteristics presented in Fig. 7.3, which shows that in winter for Sakiyama Bay, large particles moved from the river mouths to cover a

broad region of the bay. Comparison of the final values with integrated values reveals that, in summer, the final values from Amitori Bay to Sakiyama Bay were not observed but the integrated values are present. In winter, the final values from Amitori Bay to Sakiyama Bay are on the same order of magnitude as those in the reverse direction, but the integrated values from Amitori Bay to Sakiyama Bay are a few orders of magnitude larger than those in the reverse direction.

Figure 7.5 presents a time series of wind speed and direction observed at point A (Fig. 7.1) during summer and winter. The averaged wind speed in winter is about two times larger than that in summer because of the existence of strong seasonal winds from the Asian continent in winter. The averaged wind direction is SSE in summer and ENE in winter. It is almost constant except for temporal variations that include the passage of low-pressure systems such as the storm event of June 12, 2014. The respective averaged values of wind speed and direction are 3.1 m/s and 160° in summer and 5.8 m/s and 73° in winter (Table 7.1). Comparing features of wind speed and direction (Fig. 7.5) with those of soil particles shown in the snapshot (Fig. 7.2), one might note that the soil particles released from the river mouth at the inner bay in summer flow in the direction of the wind (SSE). In winter, the spread soil particles shift to the direction of the wind (ENE) in both bays but those in Amitori Bay are apparently trapped in the center of the bay. Figure 7.6 shows ocean currents in winter. In Amitori Bay, the current flows to the west coast at 0 m, but it flows to the east coast at 30 and 50 m as the return flow. Therefore, the current rotates in the direction of depth. As time passes, the soil particles are trapped in the rotating current. In Sakiyama Bay, this mechanism does not occur because the bay is shallow: depths in most areas of the bay are within a few meters;

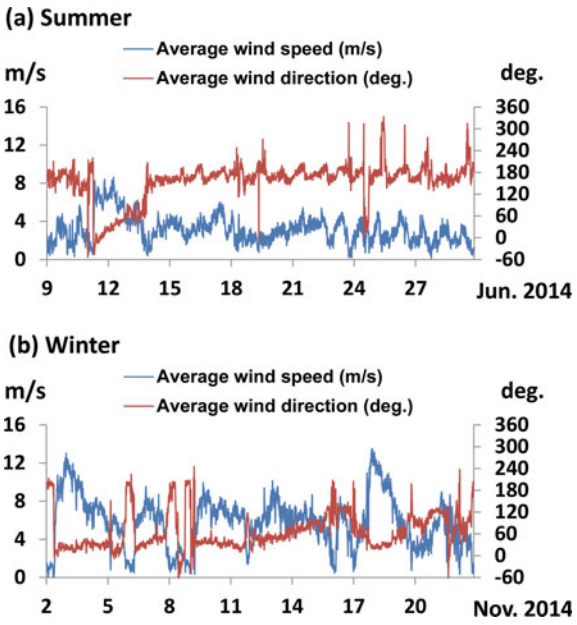

Fig. 7.5 Time series of wind speed and direction observed at point A (Fig. 7.1) in **a** summer and **b** winter. Reprinted from Shimokawa et al. (2017) by The Authors licensed under CC BY 4.0

the maximum is about 13 m at a reef pool of 200 m radius (Kawana 1990). In addition, comparison of the features of wind speed and direction with those of soil particles shown in Figs. 7.3 and 7.4 reveals differences in large particle movements for both bays between seasons. The differences are regarded as controlled mainly by differences in wind speed that occur with the seasons. Furthermore, differences in the number of soil particles exchanged between the Sakiyama and Amitori bays with the season are regarded as determined mainly by differences of wind direction that occur with the seasons. A certain amount of soil particle transport from Sakiyama Bay to Amitori Bay occurs in winter in the inverse direction of the winds. However, from Fig. 7.6, it is apparent that the averaged ocean currents, especially

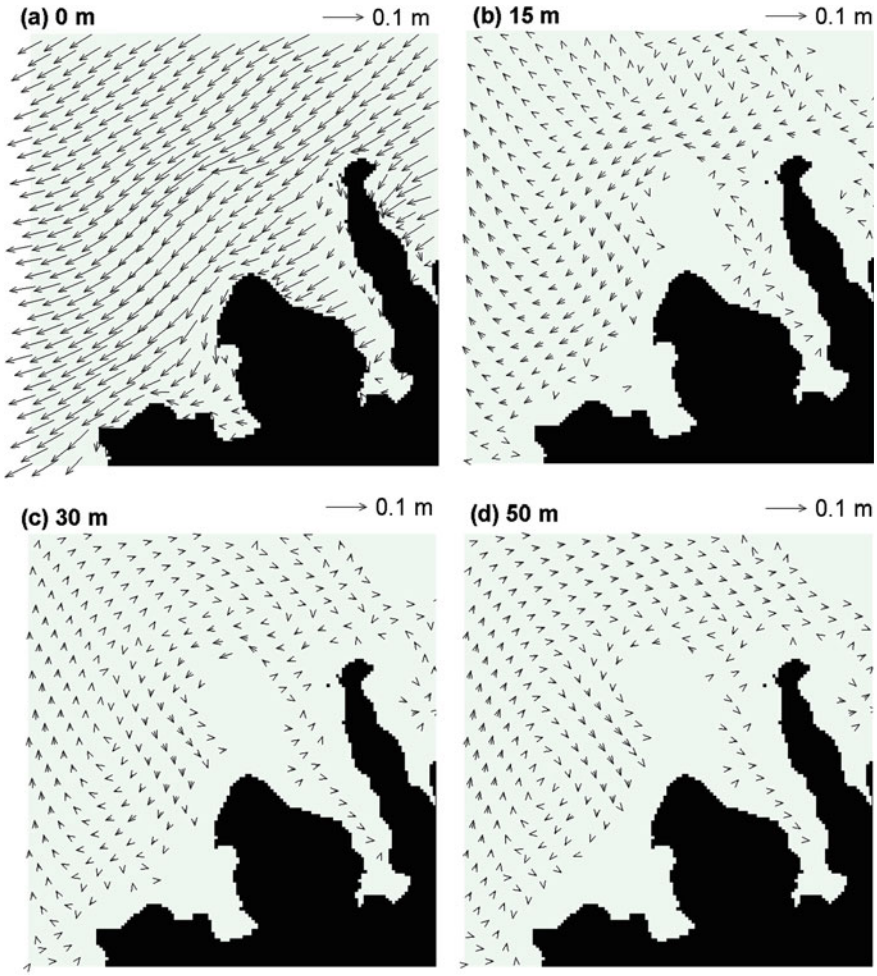

Fig. 7.6 Ocean current averaged in winter at depths of **a** 0 m, **b** 15 m, **c** 30 m, and **d** 50 m. Reprinted from Shimokawa et al. (2017) by The Authors licensed under CC BY 4.0

offshore, flow from Sakiyama Bay to Amitori Bay at 30 and 50 m, but flow from Amitori Bay to Sakiyama Bay at the surface. Moreover, the averaged wind direction was ENE in winter but, as portrayed in Fig. 7.5, the wind directions in winter changed considerably and became almost south around 2nd, 6th, 8th, 16th, 19th, and 22nd November. For the reasons described above, the soil particle transport from Sakiyama Bay to Amitori Bay in winter is regarded as occurring in winter. Consequently, the features in transport properties of soil particles in the Sakiyama and Amitori bays and soil particle exchange properties between the bays are explainable mainly by seasonal differences in wind speed and direction, but the combination among seasonal differences in wind speed and direction, wind-driven current and topography is also important for them.

However, some points of analyses must be improved to assess the actual states of soil particle transport in and exchange between the Sakiyama and Amitori bays more precisely. Particularly regarding the numerical simulations for the Painta and Ubo rivers in Sakiyama Bay, the flow rate used for winter was the same as that used for summer because we were unable to obtain a winter observational value, which is required as input for the numerical model. Furthermore, the critical Shields number was constant over the whole region in the numerical simulations conducted for the present study. Instead of them, observational values, which depend on the location, should be used in future studies.

7.4 Conclusions

For our target region, the only oceanic nature conservation area in Japan, conservation and environmental impact assessment are urgently and critically necessary. Nevertheless, investigations of the region, especially Sakiyama Bay, have not been thorough. To provide basic information for analyses, this study assessed the transport properties of soil particles in the region.

The Sakiyamawan–Amitoriwan Nature Conservation Area, designated as a nature conservation area in 2015 (Ministry of the Environment, Government of Japan 2015a, b), requires an immediate environmental impact assessment for its coastal marine ecosystems, such as those containing reef-building corals and *Enhalus acoroides*. As basic information for analyses, we assessed transport properties of soil particles in the region in this study. We conducted atmosphere–ocean–river observations and numerical simulations for the area to elucidate the transport properties of soil particles in the study area and the exchange of soil particles between the Sakiyama and Amitori bays during summer and winter.

The results are summarized as follows: (1) for each bay, soil particles tended to accumulate on the east side in summer and on the west side in winter; (2) for each bay, in summer, large particles (≥ 15 μm) did not move from areas near the river mouth, but in winter, large particles moved from the river mouth to the inner parts of the bay; and (3) soil particles moved mainly from Sakiyama Bay to Amitori Bay in summer, but the direction was reversed in winter.

These features are explainable mainly by seasonal differences in wind speed and direction, but the combination of seasonal differences in wind speed and direction, wind-driven current and topography also strongly affect them. For Amitori Bay, we conducted studies of soil particle effects on coastal oceanic ecosystems such as corals (Murakami et al. 2012; Shimokawa et al. 2014b; Ukai et al. 2015; Shimokawa et al. 2015, 2016) and *Enhalus acoroides* (Murakami et al. 2014, 2015a, b; Nakase et al. 2015, 2016). Those results provide basic information about whether the control of soil input from the rivers should be done or not and how much it should be done. Therefore, the results are expected to be useful to assess soil particle effects on coastal oceanic ecosystems and their effective conservation in the Sakiyamawan–Amitoriwan Nature Conservation Area.

Future studies will include observations related to the flow rate and critical Shields number described at the end of the preceding section. We shall assess soil particle effects on coastal oceanic ecosystems more precisely. Such results will enable us to clarify the relation between the distributions of coastal oceanic ecosystems, such as those containing reef-building corals *Enhalus acoroides*, and physical factors including the soil particle environment in the Sakiyamawan–Amitoriwan Nature Conservation Area.

Acknowledgements We thank Ms. Seina Miyauchi, Ms. Mayumi Suzuki, Mr. Yuichi Yoshioka, and Mr. Yuji Kitahara of Tokai University for their help. This work is supported by the Japan Society for the Promotion of Science through Grant No. 16K13879 and 18K04377.

References

Cushman-Roisin B, Beckers JM (2011) Introduction to geophysical dynamics. 2nd edn, Elsevier, Amsterdam, 828 pp

Kawana T (1990) Geomorphology, geology, climate and marine conditions in and around the Sakiyama Bay, Iriomote Island, The south Ryukyus, Japan. Report of investigation for Sakiyamawan nature conservation area (Ministry of the Environment, Government of Japan), pp 9–26. (in Japanese with English abstract)

Matsumoto K, Takanezawa T, Ooe M (2000) Ocean tide models developed by assimilating TOPEX/POSEIDON altimeter data into hydrodynamical model: a global model and a regional around Japan. J Oceanogr 56:567–581

Ministry of the Environment, Government of Japan (2015a) The Red Data Book of Japan (2014–9), 580 pp. (in Japanese)

Ministry of the Environment, Government of Japan (2015b) Plan for Sakiyamawan–Amitoriwan nature conservation area, 17 pp. (in Japanese)

Murakami T, Yoshino J, Yasuda T, Iizuka S, Shimokawa S (2011) Atmosphere–ocean–wave coupled model performing 4DDA with a tropical cyclone bogussing scheme to calculate storm surges in an inner bay. Asian J Environ Disaster Manag 3:217–228

Murakami T, Ukai A, Kohno H, Mizutani A, Shimokawa S, Nakase K, Yasuda T (2012) Relationships between distributions of coral and physical environments in Amitori Bay, Iriomote island, Japan. Ann J Civil Eng Ocean B3 68:1133–1138 (in Japanese with English abstract)

Murakami T, Kohno H, Iwasaki A, Kuramochi T, Shimokawa S, Kimura K (2014) Particle tracking analysis based on ecological investigation of seeds of *Enhalus acoroides* in Amitori Bay. Ann J Civil Eng Ocean B3(70):1074–1079 (in Japanese with English abstract)

Murakami T, Kohno H, Tamamoto M, Mizutani A, Shimokawa S (2015a) Numerical analysis of seed dispersal of *Enhalus acoroides* in the northwest sea area of Iriomote Island, Japan. Ann J Civil Eng Ocean B3 71:951–956. (in Japanese with English abstract)

Murakmai T, Kohno H, Tamamoto M, Mizutani A, Shimokawa S (2015b) Numerical Analysis of fructification dispersal of *Enhalus acoroides* in the northwest sea area of Iriomote Island, Japan. Ann J Civil Eng Ocean B2(71):1351–1356 (in Japanese with English abstract)

Nakase K, Murakami T, Ukai A, Mizutani A, Shimokawa S, Kohno H (2015) Distribution analysis of *Enhalus acoroides* vegetation, using hydraulic model, in the northwest sea area of Iriomote Island, Okinawa, Japan. Ann J Civil Eng Ocean B3 71:957–962 (in Japanese with English abstract)

Nakase K, Murakami T, Kohno H, Mizutani A, Ukai A, Shimokawa S (2016) Estimation of the *Enhalus acoroides* distribution using monthly condition of external forces by wave model in northwest coast of the Iriomote Island. Ann J Civil Eng Ocean B2 72:429–434 (in Japanese with English abstract)

Shimokawa S, Murakami T, Iizuka S, Yoshino J, Yasuda T (2014a) New typhoon bogusing scheme to obtain the possible maximum typhoon and its application for assessment of impacts of the possible maximum storm surges in Ise and Tokyo Bays in Japan. Nat Hazards 74:2037–2052. https://doi.org/10.1007/s11069-014-1277-2

Shimokawa S, Murakami T, Ukai A, Kohno H, Mizutani A, Nakase K (2014b) Relationship between coral distributions and physical variables in Amitori Bay, Iriomote Island, Japan. J Geophys Res: Oceans 119:8336–8356. https://doi.org/10.1002/2014JC010307

Shimokawa S, Kohno H, Murakami T, Mizutani A, Shibayama T, Yamamoto Y, Ukai A, Nakase K (2015) Relationship between massive coral distribution and physical variables in Amitori Bay, Iriomote Island, Japan. Ann J Civil Eng Ocean B3 71:969–974 (in Japanese with English abstract)

Shimokawa S, Kohno H, Murakami T, Miyauchi S, Suzuki M, Mizutani A (2016) Relation between coral distributions and Physical variables in Sakiyama Bay, Iriomote Island, Japan. Ann J Civil Eng Ocean B2 72:1435–1440 (in Japanese with English abstract)

Shimokawa S, Murakami T, Kohno H, Mizutani A (2017) Transport properties of soil particles in Sakiyamawan–Amitoriwan nature conservation area, Iriomote Island, Japan, Geosci Lett 4. https://doi.org/10.1186/s40562-017-0084-5

Ukai A, Kohno H, Kohta K (2012) Database on environmental information (sea depth, land height and wave height) in Amitori Bay, Iriomote Island, Japan. Study Rev Iriomote Is 2011:67–70 (in Japanese)

Ukai A, Murakami T, Mizutani A, Nakase K, Shimokawa S, Kohno H (2015) Estimation technique of spatial coral distribution in Amitori Bay, Iriomote Island, Japan. Ann J Civil Eng Ocean B3 71:963–968 (in Japanese with English abstract)

Chapter 8
Underwater Three-Dimensional Measurements

Hiroyuki Obanawa, Yu Tabayashi, Tomokazu Murakami, Hiroyoshi Kohno, Shinya Shimokawa and Akira Mizutani

Abstract The main objective of this study is to demonstrate the possibility of underwater three-dimensional measurement (underwater SfM) in a coral reef area by structure from motion (SfM). The possibility of underwater SfM using a small submarine (small remotely operated vehicle, sROV) was also investigated. After we conducted underwater SfM and conventional measurements simultaneously for dendritic coral, massive coral, and seaweed *Enhalus acoroides* in a coral reef area in Amitori Bay of Iriomote Island, we compared and examined the results. Underwater SfM allowed us to measure the heights, major and minor axes, and branch thicknesses of dendritic coral with the accuracy of a maximum and minimum error of 4.5 cm and 0.1 cm, respectively. Consequently, it was verified to be useful for monitoring coral preservation. However, three-dimensional measurements of *Enhalus acoroides* by SfM were not satisfactory because of swaying of

H. Obanawa (✉)
Hokkaido Agricultural Research Center, National Agriculture and Food Research Organization, Sapporo, Japan
e-mail: obanawah924@affrc.go.jp

Y. Tabayashi
College of Business Administration, Kanto Gakuin University, Yokohama, Japan
e-mail: forh-he@hotmail.co.jp

Y. Tabayashi
Center for Spatial Information Science, The University of Tokyo, Kashiwa, Japan

T. Murakami · S. Shimokawa
Storm, Flood and Landslide Research Division, National Research Institute for Earth Science and Disaster Resilience, Tsukuba, Japan
e-mail: tmurakami@bosai.go.jp

S. Shimokawa
e-mail: simokawa@bosai.go.jp

H. Kohno · A. Mizutani
Okinawa Regional Research Center, Tokai University, Yaeyama, Japan
e-mail: hkohno@scc.u-tokai.ac.jp

A. Mizutani
e-mail: ma110267@tsc.u-tokai.ac.jp

S. Shimokawa et al. (eds.), *Geophysical Approach to Marine Coastal Ecology*, Springer Oceanography, https://doi.org/10.1007/978-981-15-1129-5_8

leaves by waves or currents during the taking of sequential photographs. Investigation by sROV provided a clear three-dimensional model, but some technological problems were also revealed.

Keywords Amitori Bay · Coral reef · Remotely operated vehicle (ROV) · Structure from motion · Underwater photography

8.1 Introduction

The structure from Motion and Multi-View Stereo (SfM-MVS) measurement method (hereinafter, SfM method) is attracting attention recently as a three-dimensional geometry measurement method for geographical and planimetric features (Fonstad et al. 2013; Hayakawa et al. 2016). This method is a photogrammetric technique in which the three-dimensional geometry of a photographic object is reproduced using many overlapping photographs of the object shot from multiple directions. Photographs of the object are the only fundamentally necessary data. Therefore, this method presents the benefits of noncontact and nondestructive measurement.

The UAV-SfM method especially attracts attention because measurements are conducted by SfM processing of aerial images recorded using an unmanned aerial vehicle (UAV, drone) undergoing remarkable technological innovation recently. The method is superior to many conventional measurement methods used to date in many points such as high resolution, labor saving, and cost saving. It is even superior to aerial photogrammetry and aerial laser measurement using manned aircraft (light airplanes and helicopters), ground-based laser measurement, total station (equipment to measure distance and angle to a target point) measurement, and global navigation satellite system (GNSS) measurement. The UAV-SfM method is therefore applied to many study cases in diverse disciplines such as disaster prevention, environment, construction, forestry, and archaeology. Furthermore, its social implementation is in progress in some fields. For example, the Ministry of Land, Infrastructure and Transport of Japan is promoting i-Construction, aiming at the productivity revolution at a construction site by the full introduction of information and communication technology (ICT). The UAV-SfM method is positioned as a principal high technology (Ministry of Land, Infrastructure and Transport 2018).

As described above, the efficacy of the SfM method, which in principle enables measurement using only photographs of the object, is anticipated for underwater measurements that cannot be conducted with conventional surveying instruments. Actually, SfM measurement is regarded as especially advantageous to objects that favor noncontact and nondestructive measurements from a viewpoint of environmental protection, such as undersea coral reefs, which have geometry that is difficult to comprehend because of their complicated structure. For example, underwater SfM has been used in the UK, for the detection and investigation of

sunken ships and submarine ruins (e.g., McCarthy and Benjamin 2014; Jaklič et al. 2015). Other studies have evaluated the roughness of coral by underwater SfM at coral reef areas in Australia and Hawaii (Burns et al. 2015; Leon et al. 2015). However, the accuracy of parameters such as the height, major axis, and minor axis of coral, which are important for monitoring of them, has not been verified in those studies. Figueira et al. (2015) verified the accuracy of these parameters, but all measurements were conducted with coral samples left at rest in a pool. Because no disturbance such as a wave or current occurred, and because homogeneous lighting conditions attributable to high transparency are assured in a pool, higher performance is expected than that obtained in an actual environment. It is therefore unknown whether this result is applicable to actual environment. Furthermore, these studies specifically examine only coral although important living things aside from coral, such as seaweed, inhabit and grow in a coral reef. Accordingly, it is unknown that underwater SfM can survey with how much accuracy during monitoring in a coral reef area. Underwater SfM is inapplicable for monitoring in a coral reef area at present for that reason.

We surveyed coral and seaweed in a coral reef area using underwater SfM and conventional methods of high cost simultaneously and clarified the efficacy of underwater SfM by comparing both in this study. In addition, the case of underwater SfM in which photographs are taken not by diving or snorkeling but by remotely operated vehicle (ROV) is introduced at the end of this chapter.

8.2 Survey Procedure

8.2.1 Survey Site

Rich coral reefs centering on Okinawa Prefecture spread out widely in Japan. Sakiyama Bay and Amitori Bay of Iriomote Island are the only sea areas in Japan designated as nature conservation areas. Continuous monitoring is regarded as necessary for presenting adaptive measures for ecosystem conservation and against climate change and their limits (Sects. 1.1 and 1.2, and Fig. 1.1). Underwater SfM of low cost might be effective as a method for realizing continuous monitoring in such a coral reef area as described above.

This study specifically examines Amitori Bay, Iriomote Island, Okinawa Prefecture as a coral reef area. Amitori Bay is located in the western part of Iriomote Island. The influence of human activities on the environment has been minimal because of a lack of an overland route to the bay. Amitori Bay, a small bay with about 2 km width and about 4 km length, accommodates the Ayanda and Udara rivers, mangrove flats, coral reefs, and submarine topography of a maximum water depth of 70 m. Consequently, an extremely large environmental gradient exists inside the bay. For this study, underwater SfM was applied to coral (Sect. 1.4) and *Enhalus acoroides* (Sect. 1.5) at six survey sites inside the bay (Fig. 8.1).

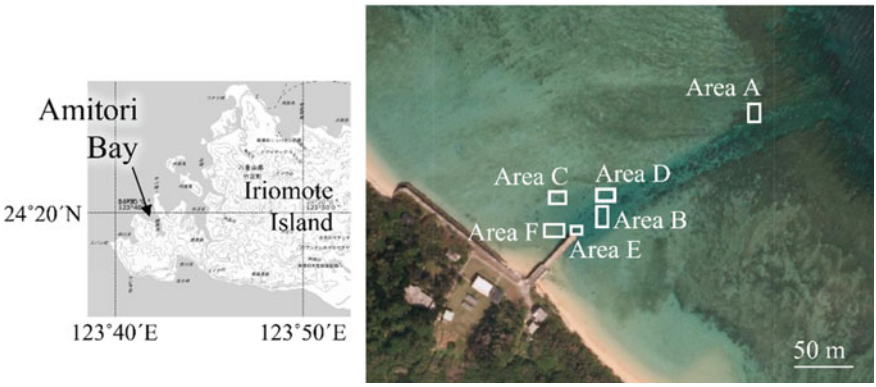

Fig. 8.1 Survey sites (created by editing Geospatial Information Authority of Japan 2018)

8.2.2 Photography

Sequential photographs of an object are required for SfM processing. Markers were placed to encircle the target coral or *Enhalus acoroides*; a snorkeling observer took sequential photographs from the sea surface in this study. Photographs taken from the side of the object were taken from underwater by another observer wearing diving equipment (Fig. 8.2). A staff (level rod) was placed nearby. Length information was acquired by photographing this together with the object, to give scale to the three-dimensional model explained later. Furthermore, the water depth of the placed markers was measured using a depth gauge for the adjustment of the inclination of the entire three-dimensional model.

8.2.3 SfM Processing

Using SfM, a three-dimensional measurement method based on images, multiple photographs (multiple images) of a measurement object are taken from various directions. Then, the location of the camera, the shooting direction, and the three-dimensional geometry of the object are estimated using parallax. For this study, SfM processing of photography data acquired using the method described above was conducted using photogrammetry software (PhotoScan Professional; AgiSoft LLC). The specific data processing procedure is described below.

First, the multiple photographic images are incorporated into the photogrammetry software. It is common to use several tens to 2000 photographs considering the performance and computation time of a computer that processes the data, depending on the object dimensions, distance from a camera, etc.

Next, characteristic points (points with abrupt change in color or luminance) are extracted from each photograph. An algorithm, SIFT, is used for the extraction of

Fig. 8.2 Underwater photography

characteristic points and for the description of feature quantities. It is robust to variation of the scale (dimensions in a photograph) of an object, rotation (direction), brightness, etc. Therefore, it is suitable for the processing of photographs taken from various angles and distances of an object with a complicated shape, as in this study.

Then, correspondence of each characteristic point in a photograph to that in another photograph is determined, such characteristic points are associated, and the shooting position and direction and the three-dimensional arrangement of the characteristic points of the object are estimated based on the deviation of locations of characteristic points in the photographs. Factors intrinsic in a camera lens—such as the focal distance, deviation of a principal point position, and distortion aberration—are also dealt with as unknown. Their optimum solutions are calculated simultaneously in this process. This picture processing is conducted almost automatically using software, designating some parameters and processing methods.

Then, a group with numerous points, called a dense cloud, is generated based on data of the estimated location and direction of cameras and photographs using conventional photogrammetry, far more than the characteristic points obtained using the SfM method. A dense cloud with a high point density enables us to visualize the detailed three-dimensional geometry of an object. Furthermore, it facilitates understanding of the situation of the surface of an object visually because each point holds the color information of the original photograph. Dense cloud data carry no information related to scale (dimensions of a three-dimensional model) or

direction (orientation, top and bottom) at this time. Accordingly, scale information is provided to the three-dimensional model using the length information of a staff visible in photographs taken at the time of underwater photography. The inclination of the whole three-dimensional model was adjusted based on the top face of tabular coral verified as almost horizontal by field surveys and information related to depth recorded at the time of diving photography.

The final three-dimensional model of this study has proper scale and inclination information but no orientation information as described above. This study was aimed at investigation of the shape measurement of an underwater object; it is intended neither as an investigation of orientation nor superposition with other spatial information. Therefore, the lack of orientation information does not matter for the present purposes.

Mesh data (surface data) and ortho images (images corrected the distortion of an object on a photograph by central projection) were generated from dense clouds with positional information after these processings using software (PhotoScan Professional; AgiSoft LLC). These data were exported. The coral dimensions were then measured using GIS software.

Consequently, underwater SfM enables us to measure the three-dimensional geometry of an object with high resolution by continuous photography from various angles using a digital camera. It excels in the simplicity of photographing work and the degrees of freedom of a three-dimensional measurable range.

8.3 Verification Results

About 1200–2400 photographs were taken at each research object area (A–E of Fig. 8.1). The number of dense clouds in the three-dimensional model created by SfM processing was about 2–50 million, corresponding to an average point density as high as about 2–100 points/cm^2. The time required for their SfM processing by a workstation was about 15–80 h: CPU—3.40 GHz, 6 cores, 12 threads; memory—64 GB. An example of a three-dimensional model created by SfM processing is presented in Fig. 8.3, in which the shapes of submarine geographical feature, complicated-shaped dendritic coral, tabular coral, and a staff (level rod) are reproduced.

The computational results were compared with actual measurements by a diver at several parts to verify the measurement accuracy of the three-dimensional model. The comparison objects included the height of tabular coral (one part), the major and minor axes (four parts), and height (four parts) of massive coral, and the major and minor axes (four parts), and branch thickness (one part) of dendritic coral (Fig. 8.4). The results of comparison of both data (Fig. 8.5) showed absolute error of 0.1–4.5 cm and relative error of 0.1–15.0%, which were regarded as demonstrating the efficacy of underwater SfM as a measurement method, despite some dispersion.

The computational results and actual measurements of seaweed (*Enhalus acoroides*) were compared. However, the shape of neither the patch nor the leaves of *Enhalus acoroides* was reproduced satisfactorily by the three-dimensional

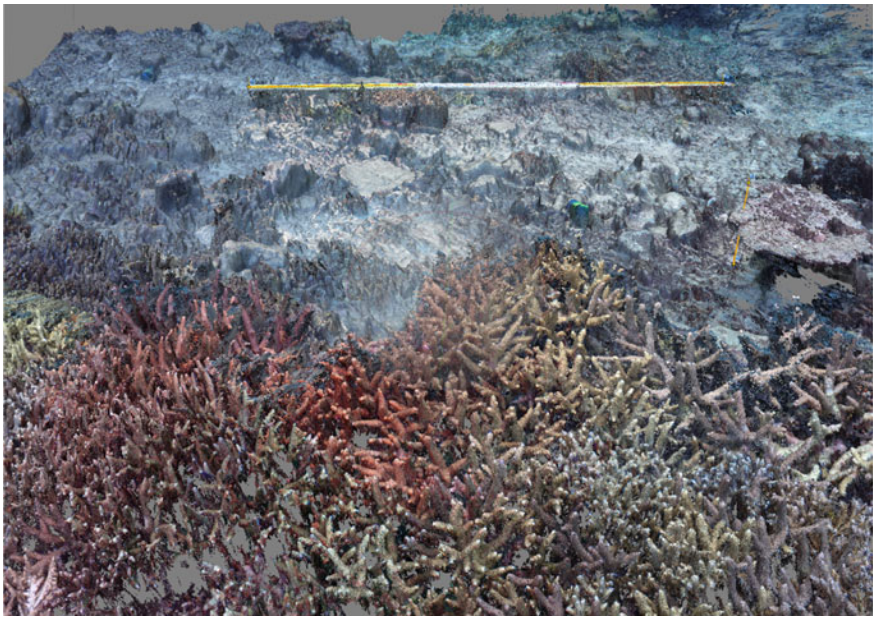

Fig. 8.3 Three-dimensional model created using SfM processing

model, as presented in Fig. 8.6, so that the major and minor axes and leaf width of *Enhalus acoroides* patches were not able to be evaluated using SfM. The reason for the poor shape reproducibility is regarded as being the following. The leaves of *Enhalus acoroides* swayed by a wave or current during the taking of sequential photographs, and the leaves changed their shape on each photograph. Accordingly, characteristic points corresponding between adjoining photographs were not correlated, no three-dimensional model was created by SfM processing correctly, and no shapes of leaves were reproduced satisfactorily.

Results show that underwater SfM is effective for objects such as coral with a shape that does not change in a short time, but that it is not applicable to objects such as *Enhalus acoroides*, with a shape that changes during photographing.

8.4 Underwater SfM Using ROV

An ROV, equipped with cameras, robot arms, etc. on its main part, is often used for underwater surveys. Conventionally, it is often controlled through a communication cable from the mother ship. Lighter-weight ROVs have been developed recently for use in managing culture facilities and for hobbies. These weigh only several to 10 kg and are compact, whereas many conventional ROVs are heavier than 100 kg. This small ROV is designated in this report as an sROV, with small s as a prefix.

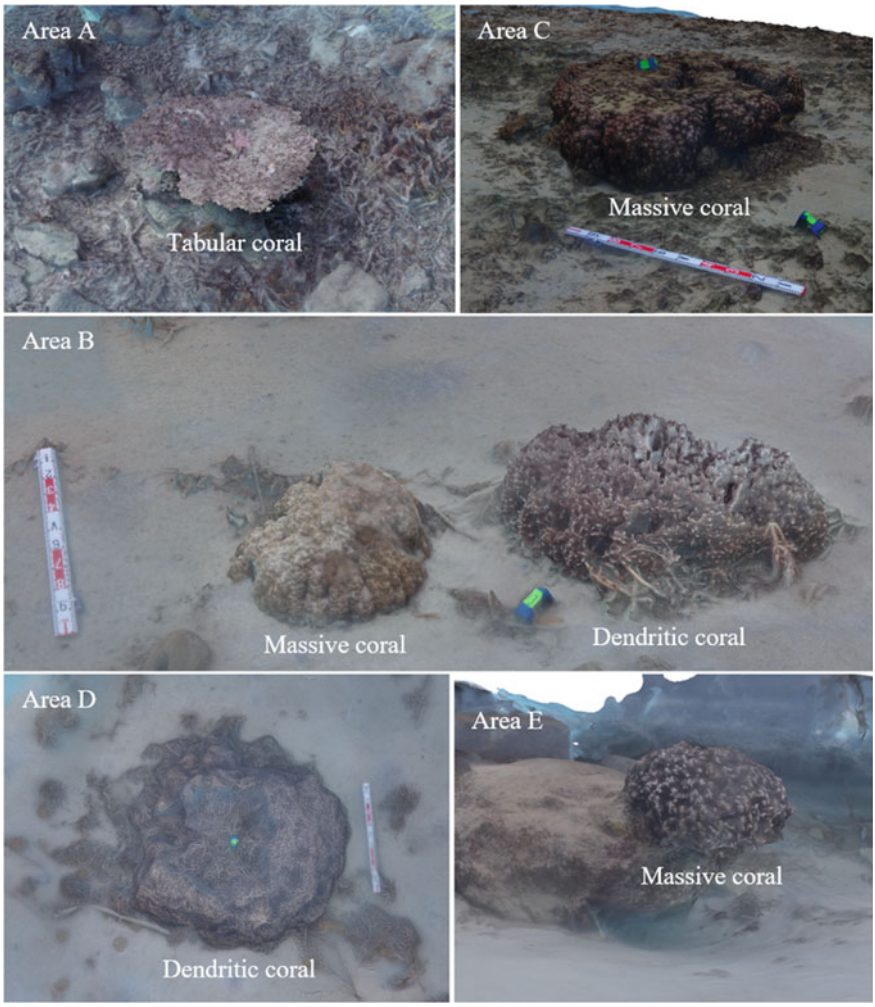

Fig. 8.4 Three-dimensional model of tabular, massive, and dendritic coral

The following benefits are anticipated by mounting a camera on an sROV and photographing an object over photographing by snorkeling or diving.

(1) Prolonged photographing is enabled and the shooting range is extended.
(2) Photographing of an object with complicated geometry is enabled by shooting from free angles.
(3) Shooting in narrow space is enabled.
(4) No disturbance is caused at a photographing site.

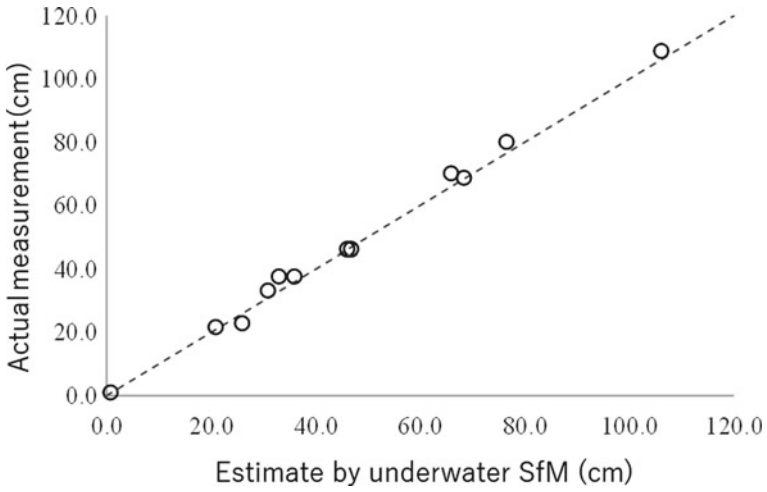

Fig. 8.5 Comparison between estimates produced using underwater SfM and actual measurements (broken line denotes equality ($y = x$))

Surveys were conducted at Suganuma, Gunma Prefecture (36° 49′ 29″ N, 139° 22′ 44″ E), and Aio Bay, Yamaguchi Prefecture (33° 59′ 50″ N, 131° 24′ 21″ E) (Tabayashi and Komuro, in preparation). DTG2 by Deep Trekker was used as an sROV (Fig. 8.7). Its controller and body are connected by a 70-m cable, through which control signals and video images are transferred. Video pictures recorded by the body are displayed on the screen of the controller. A digital camera (GR2; Ricoh Co. Ltd.) was used. Modeling computation of the acquired photographs was conducted in a computation environment equivalent to the case of coral.

A lake bottom with *Ranunculus nipponicus* var. submersus was modeled at Suganuma (Fig. 8.8). The geometry of objects was reproduced vividly; advantages (3) and (4) described above were especially realized. The remarkable benefits of sROVs were demonstrated: They allowed photography around complicated vegetation easily and without disturbing the sandy lake bottom.

Gravels and some shells in Aio Bay were modeled vividly (Fig. 8.9). Each individual shell is countable, which allows a complete count survey instead of sampling inspection. This might constitute a great benefit of sROVs for biological research. sROVs are also anticipated for their contributions to research investigating underwater pebble migration and changes of geographical features using periodical photography.

In contrast to these benefits described above, advantages (1) and (2) were not well realized, mainly because of the performance of the body of present sROVs. The SfM method requires overlapping photographs of an object when creating a

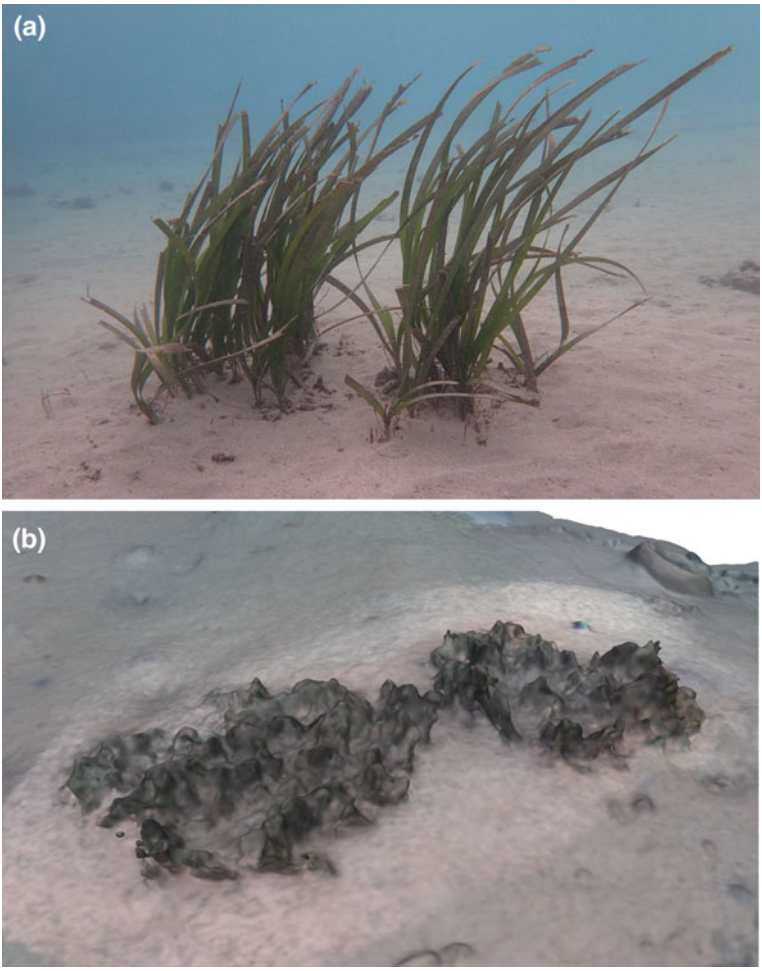

Fig. 8.6 **a** Photograph and **b** three-dimensional model of seaweed (*Enhalus acoroides*)

three-dimensional model. However, it is difficult to take moderate overlapping images using remote photography with the sROV. Missing images often occurred, even with the prolonged photographing period used for this study. Photographing activities were conducted with a narrow shooting range because of a short distance between the sROV and an object in this study, so that some areas were not modeled where sufficient overlapping of photographs was not implemented: Even the body of the sROV was operated at a low speed. It was also difficult to photograph an object from free angles. However, these issues can be resolved through the progress

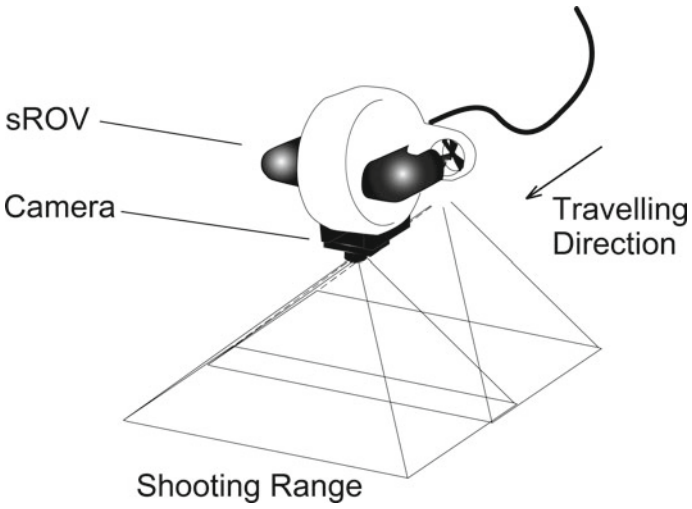

Fig. 8.7 Survey equipment and actual survey scene

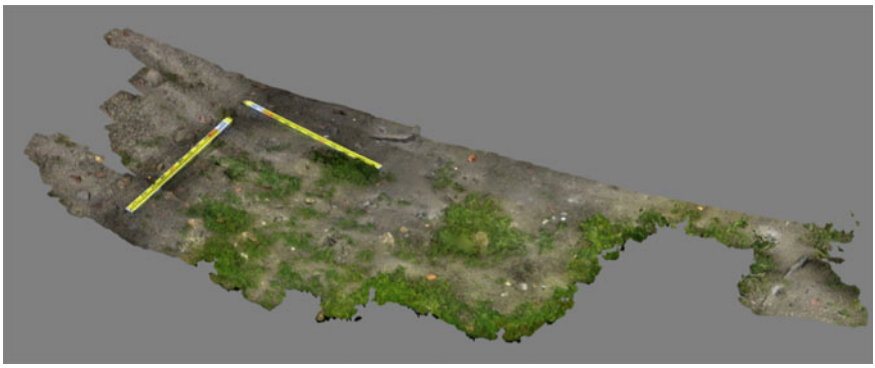

Fig. 8.8 Three-dimensional model of lake bottom and *Ranunculus nipponicus* var. submersus (after Tabayashi and Komuro (in preparation)). The length of the scales is around 1.15 m

of technologies such as controlling performance of the body. Water transparency and light environment are other important factors. As we could not take clear pictures in the turbid water or in the dark conditions, we could not make precise 3D model with them. Some improvements such as shedding strong light on the object are necessary for the future research in such conditions.

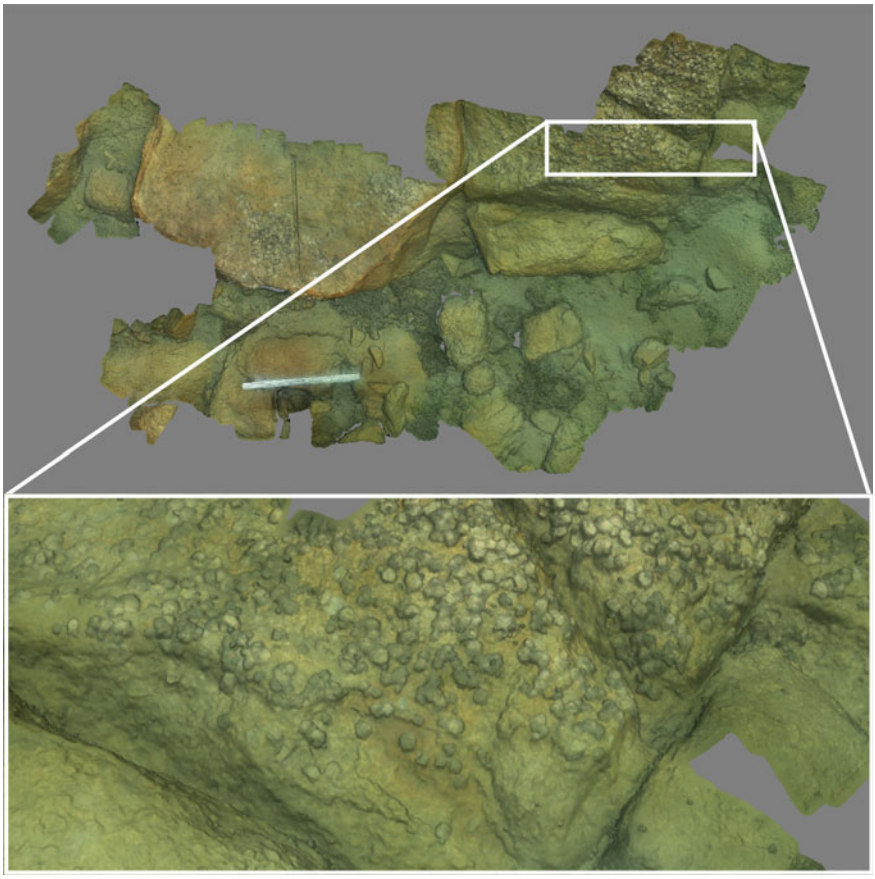

Fig. 8.9 Three-dimensional model of gravels and some shells (enlarged) on the seashore (from Tabayashi and Komuro (in preparation)). The length of the scale on the upper panel is around 1 m

8.5 Conclusion

After underwater SfM measurements were taken of the height, major axis, minor axis of coral and seaweed in a coral reef area in this study, we examined the measurement accuracy. The results demonstrated that underwater SfM can facilitate measurement of the height, major axis, minor axis, and branch thickness of dendritic coral, respectively, with the accuracy of a maximum and minimum error of 4.5 and 0.1 cm. Accordingly, underwater SfM was verified as useful for the monitoring of coral preservation and of the reaction of a coral reef ecosystem against climate change. However, three-dimensional measurement of *Enhalus acoroides* by SfM was not satisfactory because of swaying of leaves by a wave or current during the taking of sequential photographs. Consequently, it is difficult at

present to apply underwater SfM for the monitoring of swinging or undulating objects such as seaweed. Investigation using sROVs provided a clear three-dimensional model, but some technological problems were also revealed.

Acknowledgements Field observations at Iriomote Island were conducted with the cooperation of Ken Sakihara of the Okinawa Regional Research Center and of Mayumi Suzuki and Seina Miyauchi, who were then students of the School of Marine Science and Technology, Tokai University. The survey conducted in Suganuma and Aio Bay was assisted by Takashi Komuro. This study was conducted as a research project of National Research Institute for Earth Science and Disaster Resilience, joint research by Tokai University and National Research Institute for Earth Science and Disaster Resilience, and JSPS Grants-in-Aid for Scientific Research Nos. 26281055 and 17K18534. The authors extend their deepest gratitude for this kind support from so many sources.

References

Burns J, Delparte D, Gates R, Takabayashi M (2015) Integrating structure-from-motion photogrammetry with geospatial software as a novel technique for quantifying 3D ecological characteristics of coral reefs. PeerJ 3:e1077

Figueira W, Ferrari R, Weatherby E, Porter A, Hawes S, Byrne M (2015) Accuracy and precision of habitat structural complexity metrics derived from underwater photogrammetry. Remote Sens 7(12):16883–16900

Fonstad MA, Dietrich JT, Courville BC, Jensen JL, Carbonneau PE (2013) Topographic structure from motion: a new development in photogrammetric measurement. Earth Surf Proc Land 38 (4):421–430

Geospatial Information Authority of Japan (2018) GSI maps https://maps.gsi.go.jp. Accessed 12 July 2019

Hayakawa YS, Obanawa H, Saito H, Uchiyama S (2016) Geomorphological applications of structure-from-motion multi-view stereo photogrammetry: a review. Trans, Jpn Geomorphol Union 37(3):321–343

Jaklič A, Erič M, Mihajlović I, Stopinšek Ž, Solina F (2015) Volumetric models from 3D point clouds: the case study of sarcophagi cargo from a 2nd/3rd century AD Roman shipwreck near Sutivan on island Brač, Croatia. J Archaeol Sci 62:143–152

Leon JX, Roelfsema CM, Saunders MI, Phinn SR (2015) Measuring coral reef terrain roughness using 'structure-from-motion' close-range photogrammetry. Geomorphology 242:21–28

McCarthy J, Benjamin J (2014) Multi-image photogrammetry for underwater archaeological site recording: an accessible, diver-based approach. J Marit Archaeol 9(1):95–114

Ministry of Land, Infrastructure, Transport and Tourism Japan (2018) i-Construction. http://www.mlit.go.jp/tec/i-construction/index.html. Accessed 12 July 2018

Tabayashi Y, Komuro T (in preparation) Underwater 3D measurement using ROV and SfM-MVS

Part III
Relationship Between Distributions of Marine Coastal Ecosystem and Physical Environments

Chapter 9
Coral Distributions and Physical Environments in Amitori Bay

Shinya Shimokawa, Tomokazu Murakami, Akiyuki Ukai, Hiroyoshi Kohno, Akira Mizutani and Kouta Nakase

Abstract The relation between coral distribution and physical characteristics was investigated for Amitori Bay, Iriomote Island, Japan. Field observations were conducted to obtain data for the coral distribution, sea temperature, sea salinity, wind speed, and river flow rate. Then, the observed data were used in ocean and wave model numerical simulations and soil particle tracking analyses to ascertain the spatial and temporal distributions of wave height and the numbers of soil particles. The main results of this study indicate that the wave height and the number of soil particles are significantly correlated with the coral distribution. Higher wave heights produce greater coverage of tabular coral and lower coverage of branching coral. A greater number of soil particles are related to less coverage of tabular coral. In contrast, the number of soil particles is not correlated with branching coral coverage. Averages of the diversity index of the coral types at the mouth and inner parts of the bay are lower than the average of the whole region, but

This chapter is based on work reported by Shimokawa et al. (2014b).

S. Shimokawa (✉) · T. Murakami
Storm, Flood and Landslide Research Division, National Research Institute for Earth Science and Disaster Resilience, Tsukuba, Japan
e-mail: simokawa@bosai.go.jp

T. Murakami
e-mail: tmurakami@bosai.go.jp

A. Ukai · K. Nakase
Environment Business Division, Penta-Ocean Construction Co., Ltd., Civil Engineering Headquarters, Tokyo, Japan
e-mail: Akiyuki.Ukai@mail.penta-ocean.co.jp

K. Nakase
e-mail: Kouta.Nakase@mail.penta-ocean.co.jp

H. Kohno · A. Mizutani
Okinawa Regional Research Center, Tokai University, Yaeyama, Japan
e-mail: hkohno@scc.u-tokai.ac.jp

A. Mizutani
e-mail: ma110267@tsc.u-tokai.ac.jp

S. Shimokawa et al. (eds.), *Geophysical Approach to Marine Coastal Ecology*, Springer Oceanography, https://doi.org/10.1007/978-981-15-1129-5_9

the average of diversity index at the intermediate part of the bay with the intermediate physical disturbances is higher than the average, which supports the intermediate disturbance hypothesis.

Keywords Coral · Environmental impact of assessment · Iriomote Island · Sakiyamawan–Amitoriwan Nature Conservation Area · The intermediate disturbance hypothesis · Physical observation · Numerical simulation

9.1 Introduction

The distributions of coral (see Sect. 1.4; Motokawa 2008; Sheppard et al. 2009) are diverse and are affected by various factors such as human activities (including red soil erosion caused by land development and sea temperature rise attributable to global warming), their susceptibility to infestation by crown-of-thorns starfish (*Acanthaster*) and a species of sea snail (*Drupella fragum*), and environmental properties related to waves and soil grains. Among these factors, environmental properties are the most important ones related to the long-term distribution of coral. Consequently, investigating the relation between coral distribution and environmental properties is useful for elucidating coral and its diversity.

This relation includes short-term and long-term physical processes along with direct responses. For example, regarding destruction by high waves, it is widely accepted that the structure of branching corals is more fragile than that of tabular corals. However, this destruction can also lead to a broader distribution because of the high regenerative power of corals: High waves can reduce the coral distribution in the short term, but can broaden it over the long term. Conversely, extreme wave heights that occur with strong typhoons can severely damage or destroy coral colonies (Dollar and Tribble 1993; Madin and Connolly 2006; Hongo et al. 2012; White et al. 2013). This damage is apparently related to the intermediate disturbance hypothesis (IDH) (Connell 1978), which postulates that local species diversity is maximized when environmental disturbances are neither too weak (or infrequent) nor too strong (or frequent). In fact, IDH is often used to investigate the relation between species diversity and environmental disturbances.

Environmental properties affect not only coral distributions but also coral life forms (Motokawa 2008; Sheppard et al. 2009). Most corals form colonies comprising numerous individuals called polyps. Coral of this type is called a colonial coral. All the corals in this study are classified as this type. Coral colonies have various forms such as tabular, branching, massive, foliose, and encrusting corals. They deform according to their environmental properties. Moreover, corals of the same species can show different forms. Reef-building coral classification is currently based on morphological features such as the shape of the individual polyps, their sequence manner on the colony, and the colony forms. However, classification is difficult because the surfaces of living corals have a molluscous covering (Fukami et al. 2010). In addition, although molecular phylogenetic analyses are

necessary for strict identification, when gene consistency within a species is lacking in some cases because gene exchanges among different species occur as a result of their unique mass-spawning trait (i.e., simultaneous release of eggs and sperm among different species; Hatta et al. 1999; Fukami et al. 2004, 2008). Currently, the right approach to investigate the relation between coral distribution and environmental properties is regarded as one which emphasizes the importance of habitat adaption and one which specifically examines life forms rather than species.

Amitori Bay, located in the northeast region of Iriomote Island, Japan (Sects. 1.1, 1.2 and Fig. 1.1), is 2 km wide at its mouth, 4 km long, with maximum depth of 70 m in the central mouth area. It receives discharge from two rivers (Ayanda and Udara) and the accompanying mangrove environments in the inner part of the bay. The bay has developed broad areas of coral: Their life forms, coverage, size, and species vary depending on the location. Amitori Bay has no access road. The bay perimeter is uninhabited. Therefore, this small bay, with its diverse environments and lack of human impact, is the most suitable area for studying the relation between coral distribution and environmental properties. This study (Shimokawa et al. 2014b) clarifies these relations in the Amitori Bay and Iriomote Island corals by observing the ocean, atmosphere, and rivers through numerical simulation using ocean and wave models along with particle tracking analysis.

In Sect. 9.2, we briefly state the investigation methods of the coral distribution and observation methods for the ocean, atmosphere and rivers, and the numerical simulation methods. Section 9.3 presents results. Additionally, we compare the coral distributions with our observational and numerical results and discuss the relation between coral distributions and environmental properties. Section 9.4 presents a consideration of the generality of results obtained in Sect. 9.3 by conducting statistical analyses related to the diversity index: a quantitative measure of the degree to which a dataset includes different types. It is related closely to the information entropy concept. The results are also discussed from an IDH perspective. We summarize and discuss our findings in Sect. 9.5.

9.2 Methods

9.2.1 Coral Distribution Investigation

Coral distributions were investigated at 44 locations in Amitori Bay, including 18 locations in 2009 and 26 locations in 2011 (Fig. 9.1). For the 2009 investigation, indicated by A–R in Fig. 9.1, three quadrats measuring 1 m on each side were placed at 1–4 points at various depths. We recorded the life form, coverage, and coral size (Ukai et al. 2010). For the 2011 investigation, denoted as 1–26 in Fig. 9.1, three quadrats measuring 2 m on each side were placed within a 3 m depth at the top of the reef slope and on the reef slope at a 5–8 m depth. The life form, coverage, and coral size were recorded (Murakami et al. 2012). The types of coral

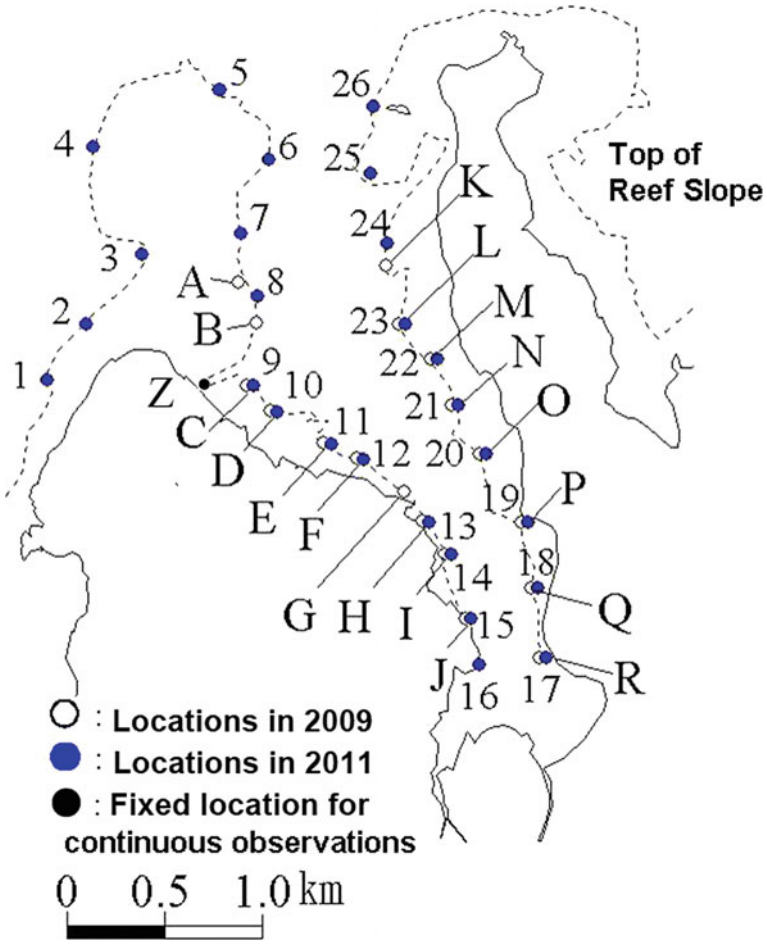

Fig. 9.1 Locations for coral distribution investigations in Amitori Bay. Stations A–R and 1–26, respectively, portray the locations in 2009 and 2011. Station Z shows the location for continuous measurements (position: 24° 19′ 51.6″ N, 123° 41′ 21.6″ E, and height: 4.2 m) (© 2014. American Geophysical Union. Used with permission from Shimokawa et al. (2014b) published by John Wiley and Sons)

life forms treated in this study are presented in Fig. 9.2. States of the coral investigations in Amitori Bay and an example of the photographs of the quadrats are shown in Fig. 9.3. Electronic weighing instruments were used to ascertain the weights of trace pieces cut from the photographs of the quadrats. Then, the coverage of each coral type was calculated. In this study, "coral individuals" and "coral size," respectively, denote the individuals and maximum diameters of a coral colony for a specific coral.

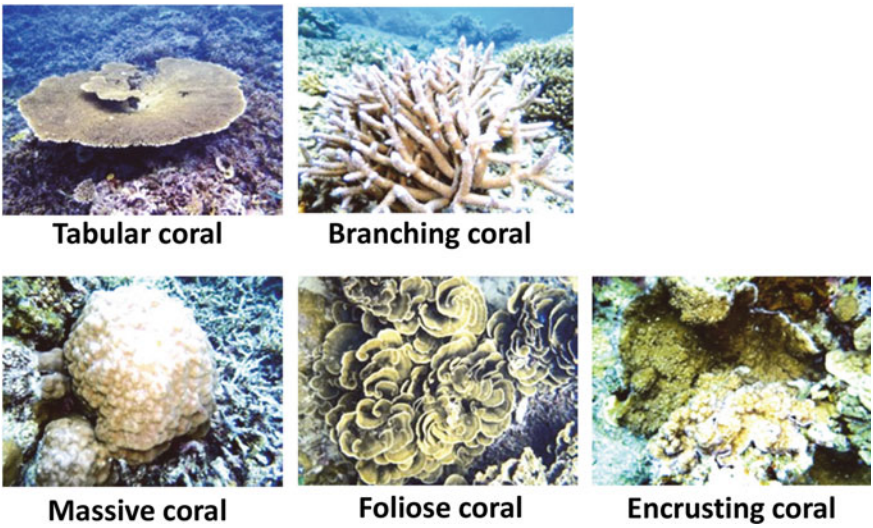

Fig. 9.2 Types of coral life forms treated in this study (© 2014. American Geophysical Union. Used with permission from Shimokawa et al. (2014b) published by John Wiley and Sons)

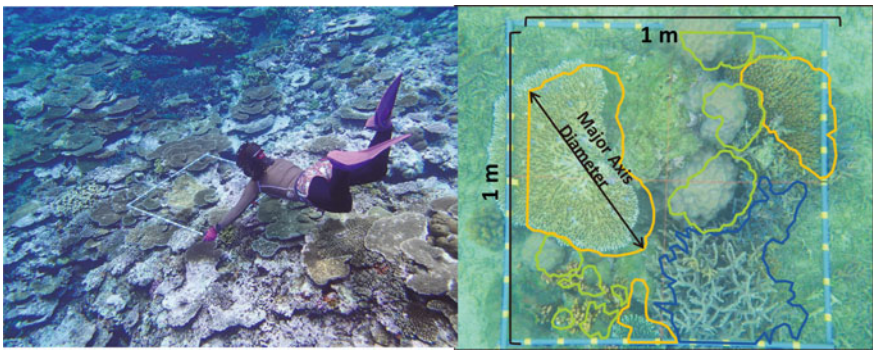

Fig. 9.3 Photographs of coral investigations in Amitori Bay (left) and an example of photographs of quadrats (right). Orange, green, and blue lines, respectively, portray tabular, branching, and massive corals

9.2.2 Physical Observations

Fixed-point observations were conducted to obtain data related to the sea level, sea pressure, and horizontal current velocities in Amitori Bay from July 2008 through October 2009 using a WH-403 wave height/wave direction/current speed measuring instrument (I.O. Technic Co. Ltd.; see Chap. 2). Two measurement instruments were placed at each of Stations 1 and 2 at depths of 10 and 20 m, respectively.

Measurements were conducted for 20-min periods at 1-h intervals. In addition, moving shipboard observations were conducted using a RINKO conductivity, temperature, and depth profiler (JFE Advantech Co. Ltd.; see Chap. 2) to ascertain the sea temperature and salinity of the bay on October 18, 19, and 24, November 9 and 22, and December 14, 2011. The number of observation sites varied between 15 and 31 depending on weather conditions. At each location, observations were conducted from the sea surface to the seafloor at 0.1-m intervals. At Station Z (Fig. 9.1), continuous measurements have been conducted since 1976 for the wind speed, wind direction, humidity, insolation, air temperature, sea surface temperature, and rainfall amount (see Sect. 1.3; Mizutani and Sakihara 2012). During the study, the measurement interval was 10 min, except for sea surface temperature measurements, for which it was 2 min.

Moreover, to obtain the flow rates of two rivers, the Ayanda and Udara (Fig. 9.1) from July 21 to October 3, 2011, an AEM213-D electromagnetic current meter (JFE Advantech Co. Ltd.; see Chap. 2) was placed in upstream reaches of each river. Water depths and cross-sectional area were also obtained at each location. The rain volumes were measured at Station Z. Then, a regression model equation was constructed to estimate the flow rate from the rainfall volume. This calculation was performed because the measurement of flow rates throughout the year was difficult because of the need for ongoing instrument maintenance. The correlation coefficients between the calculated results and the observations were high: over 0.8. Additional information about the observational methods is presented in Chap. 2.

9.2.3 Numerical Simulations

Numerical simulations were conducted to calculate wave heights and directions in Amitori Bay according to Ukai et al. (2010). The calculation was conducted during a one-year period from November 1, 2008, through October 31, 2009, and in the following two regions: the large region of 150 km × 100 km with 500-m grid spacing including Yaeyama Islands and the small region (i.e., Amitori Bay) of 4.5 km × 3 km with 20-m grid spacing. Offshore wave conditions from Japan Meteorological Agency Grid Point Value (JMA 2015) such as wave heights, directions, and periods were used as input data for calculations. Three basic wave heights and directions were found based on the offshore wave conditions. Nine case calculations, as combinations of the basic wave heights and directions, were conducted using an energy balance equation and a wave-breaking model developed by Isobe (1986). Then, a transformation table was created from the calculation results for every mesh in Amitori Bay, which was used to combine wave heights and directions in Amitori Bay with offshore wave conditions of the wave height, direction, and period. Using this table, time series data of wave heights and directions in Amitori Bay during the target term were obtained from the corresponding offshore wave conditions.

Moreover, Lagrangian particle tracking analysis (see Chap. 3) was conducted to elucidate the soil grain transport properties in Amitori Bay. For that purpose, numerical simulations were conducted to reproduce the flow fields in Amitori Bay from 1600 JST on October 18 to 0400 JST on October 25, 2011, using the coastal ocean current model (CCM, see Chap. 3; Murakami et al. 2011; Shimokawa et al. 2014a). The observed data (temperature, salinity, wind speed, wind direction, humidity, insolation, air temperature, and rainfall amount) and the flow rate from the regression model and astronomical tides calculated using the North Atlantic Oscillation Oceanic tide model (Matsumoto et al. 2000) were used as initial and boundary values for numerical simulations. Soil grain diameters were set to 0.1, 1, 3, 5, 8, 10, 15, 20, and 30 μm because sediment trap observations at the mouths of the rivers showed that the diameters were distributed from 0.1 to 50 μm (Shimokawa et al. 2014b). They were released every 15 s from the Ayanda and Udara rivers. Additional information for the numerical models and methods is given in Chap. 3. Details related to the emphasis of our study and the representativeness of the normal state in the numerical simulations above were reported by Shimokawa et al. (2014b).

9.3 Relation Between Coral Distributions and Environmental Properties

9.3.1 Distribution of Coral Life Forms

Figure 9.4 presents the ratios of coverage of each coral type in Amitori Bay during investigations in 2009 and 2011, classified according to the life form. Tabular and branching corals were dominant, covering a total area larger than 90%. The former were dominant at the top of the reef slopes. The latter were dominant on the reef slopes. On the east side of the bay, the coverage of tabular corals tended to decrease from the mouth of the bay (Station 26) to the inner bay (Station 17), although the tendency was not clear on the west side of the bay. These results suggest that Amitori Bay, although small, has corals of various types.

9.3.2 Relation Between Coral Distributions and Wave Heights

Figure 9.5a portrays a spatial distribution of wave heights with a corresponding 95% probability of non-exceedance calculated using the wave simulation described in Sect. 9.2.3. Wave heights at the mouth of the bay (Stations 4 and 26) were markedly higher than those in the inner bay (Station 17) and on the east side of the bay (Station 20). Figure 9.5b shows the relation between the coverage of tabular or

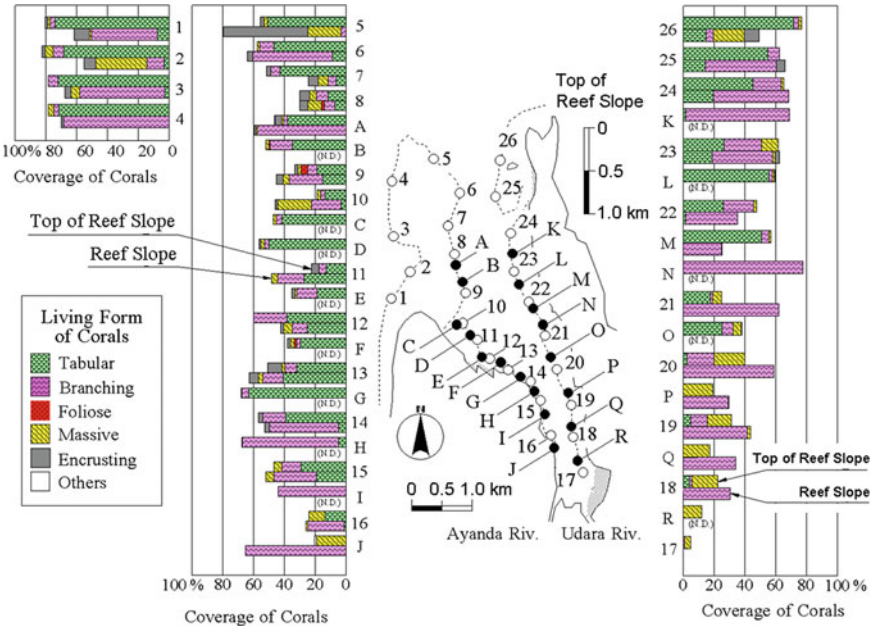

Fig. 9.4 Ratios of the coverages of respective coral types in Amitori Bay during the 2009 and 2011 investigations classified according to life form, and the corresponding investigation locations. N.D. indicates no data of reef slope. Types of coral life forms treated in this study are presented in Fig. 9.2 (© 2014. American Geophysical Union. Used with permission from Shimokawa et al. (2014b) published by John Wiley and Sons)

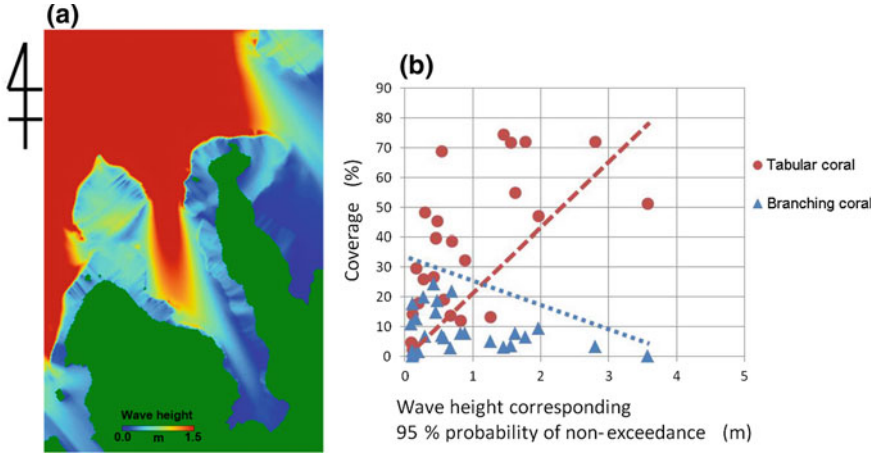

Fig. 9.5 **a** Spatial distribution of wave heights with a corresponding 95% probability of non-exceedance calculated using the wave simulation described in Sect. 9.2.3. **b** The relation between the coverage of tabular or branching corals and wave height. Red-dotted and blue-dotted lines, respectively, portray the lower boundary of coverage of the tabular corals and the upper boundary of coverage of the branching corals (© 2014. American Geophysical Union. Used with permission from Shimokawa et al. (2014b) published by John Wiley and Sons)

branching corals and wave height. Results demonstrated that greater coverage of tabular coral and smaller coverage of branching coral corresponded to larger wave heights. These results suggest that tabular coral is strengthened by high wave disturbances and that branching coral is readily broken by them, which is consistent with results of previous studies (Goreau 1959; Woodley et al. 1981).

9.4 Relation Between Coral Distributions and the Number of Soil Grains

Figure 9.6 shows the number of soil grains on the sea bottom calculated using the particle tracking analysis described in Sect. 9.2.3. It also shows the coverage of tabular and branching corals at Stations 1–26. Comparison between the number of soil grains on the sea bottom (Fig. 9.6a) and the coverage of the tabular corals (Fig. 9.6b) revealed that less coverage of the coral is related to the larger number of grains. Nevertheless, the same comparison with branching corals (Fig. 9.6c) revealed that the coral coverage was unrelated to the number of grains. These results suggest that tabular coral is affected by soil grains, but branching coral is not affected because the soil grains accumulate more easily on tabular coral than on branching coral as a result of their shape.

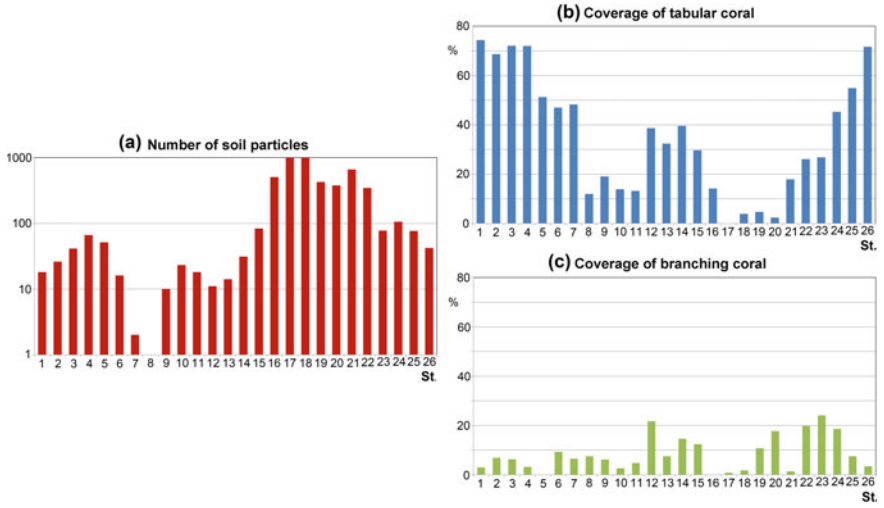

Fig. 9.6 **a** Number of soil grains that reached the seafloor by the end of the period (0400 JST on October 25, 2011), calculated using the particle tracking analysis described in Sect. 9.2.3 and coverage of **b** tabular coral and **c** branching coral at Stations 1–26. The diameters of grains counted in **a** were 1, 3, and 5 μm. The numbers of soil grains at Stations 17 and 18 in (a) were over 1000 (© 2014. American Geophysical Union. Used with permission from Shimokawa et al. (2014b) published by John Wiley and Sons)

9.5 Diversity Index Analysis

9.5.1 Diversity Index and Its Physical Meaning

In this section, the generality of the results is discussed by conducting a statistical analysis of data obtained in preceding sections. The diversity index H' is calculated (Shannon 1948; MacArthur and MacArthur 1961; Clarke and Warwick 2001; McCune and Grace 2002). It is defined as

$$H' = -\Sigma\, c_i \log_2 c_i, \tag{1}$$

where c_i represents the ratio of the ith group population to the total population. H' is a quantitative measure for the degree to which a dataset includes different types and is closely related to the information entropy concept. The value of H' is greater than zero, with no upper limit. It increases when both the number of types and evenness increase. For a given number of types, it is maximized when all types are equally abundant.

For example, a case with five individuals of only one type, i.e., $H' = -(5/5) \log_2 (5/5) = 0.0$. In this case, the result is zero when a sample has been taken because the type of the sample is determined. Conversely, in a case with one individual of each of five types, $H' = -(1/5) \log_2 (1/5) \times 5 = 2.32$. In this case, the result is greater than zero when a sample has been taken because the type of the sample presents multiple possibilities. In a case with a constant number of types, for example, cases with either one individual or 10 individuals of each of five types, i.e., $c_i = 1/5 = 10/50$, and thereby, $H' = 2.32$. In a case with a constant number of types and the same distribution of those types, H' is unaffected by the number of individuals. Conversely, in a case with a constant number of individuals, for example, a case with two individuals of each of five types, $H' = -(2/5) \log_2 (2/5) \times 5 = 0.53$, but in a case with one individual of each of 10 types, $H' = -(1/10) \log_2 (1/10) \times 10 = 3.32$. In a case with a constant number of individuals, the greater the number of types, the greater is H'. Consequently, H' can be regarded as an index that represents diversity and which incorporates the distribution of individuals, not the individuals themselves. Apart from this index, Simpson's λ index (Simpson 1949) represents diversity based on the numbers of types and individuals.

In our case, "group" refers to the coral type (Fig. 9.2). That is, the number of the groups is five although "group" is originally defined as the species (MacArthur and MacArthur 1961) because we have emphasized the coral type instead of the species, as stated in the *Introduction*. Additionally, we used coverage instead of population because corals form colonies, although c_i is defined originally as the ratio of the ith group population to the total population.

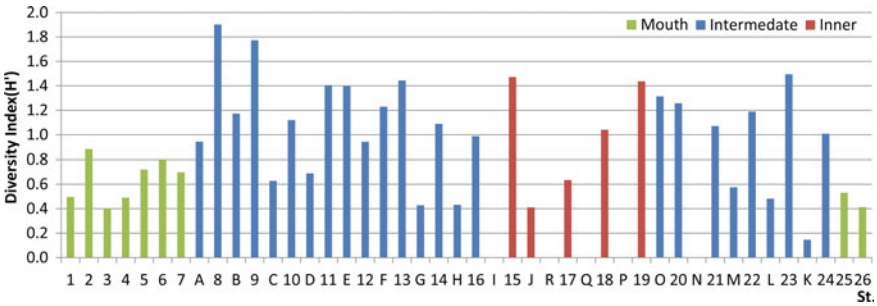

Fig. 9.7 Diversity index at Stations 1–26 and A–R. The mouth, intermediate, and inner area of the bay are displayed, respectively, in green, blue, and red (© 2014. American Geophysical Union. Used with permission from Shimokawa et al. (2014b) published by John Wiley and Sons)

9.5.2 Distribution of the Diversity Index and the IDH

Figure 9.7 presents the values of H' in Amitori Bay. The mouth, intermediate, and inner areas of the bay are portrayed, respectively, as green, blue, and red. Averages of H' at the mouth of the bay (0.60) and the inner area of the bay (0.62) were lower than the average value for the entire area (0.83). However, the average of H' at the intermediate area of the bay (0.97) was higher than the average for the entire area. These distributions of H' are respectively attributable to the existence of large environmental disturbances, i.e., large wave height and large numbers of soil grains, in the mouth and inner area of the bay.

The results seem to support the IDH reported by Connell (1978), which postulates that local species diversity is maximized when environmental disturbances are neither too weak (or infrequent) nor too strong (or frequent). Actually, IDH is often used to assess the relation between species diversity and environmental disturbances. When the strength or frequency of disturbances to a biological community is low, competitive elimination of certain species by more dominant species in the community occurs. The dominant species become the majority. When the strength or frequency of disturbances to a biological community is high, only specific species that are tolerant of the disturbances can survive. These species therefore become the majority: when disturbances are either low or high, diversity decreases. Consequently, diversity is maximized when disturbances are intermediate. In addition, IDH suggests that the environment is in a non-equilibrium state (i.e., because of the existence of disturbances and the subsequent recovery processes), which helps maintain diversity. In other words, if the environment is in a non-equilibrium state, then frequent disturbances can provide survival opportunities to those species which cannot survive in an equilibrium state; thereby, diversity is maintained.

For sites with good coral conditions, for example, Badul Island Waters, Ujung Kulon, Indonesia (Putri et al. 2012) and the Gulf of Aqaba and Ras Mohammed, Red Sea, Egypt (Shokry and Ammar 2011), H' averaged respectively 2.183 and

0.84. H', in this study (Fig. 9.7), was apparently slightly lower than the reported values. However, a simple comparison of H' among different areas and/or studies is difficult because H' is sensitive to the degree of sampling effort (e.g., the number of individuals and types) (Clarke and Warwick 2001). In this study, H' was calculated from only five types because the object for calculating H' was coral forms, not coral species. We believe this fact explains the slightly lower value of H' obtained in our study.

9.5.3 *Relation Between Diversity Index and Environmental Properties*

Next, the relations among H', wave height (Fig. 9.8), and the number of soil grains (Fig. 9.9) are discussed. In general, the H' value of organisms has a large dispersion. In addition, H' is dependent on the number of individuals. The dispersion of H' decreases with an increased number of individuals (Clarke and Warwick 2001). Consequently, a discussion of H' should be performed using maximum or average values. In the inner area of the bay with nearly constant (and low) wave height, no correlation between H' and wave height was found. Conversely, in the intermediate area of the bay with changes in wave height, the maximum (or average) of H' at a wave height increased with an increase in wave height up to 1 m. However, H' decreased sharply when the wave height was higher than 1 m (Fig. 9.8). Consequently, the diversity of coral types increases with increased wave disturbance. However, when the wave disturbances exceed a limit, coral types that are

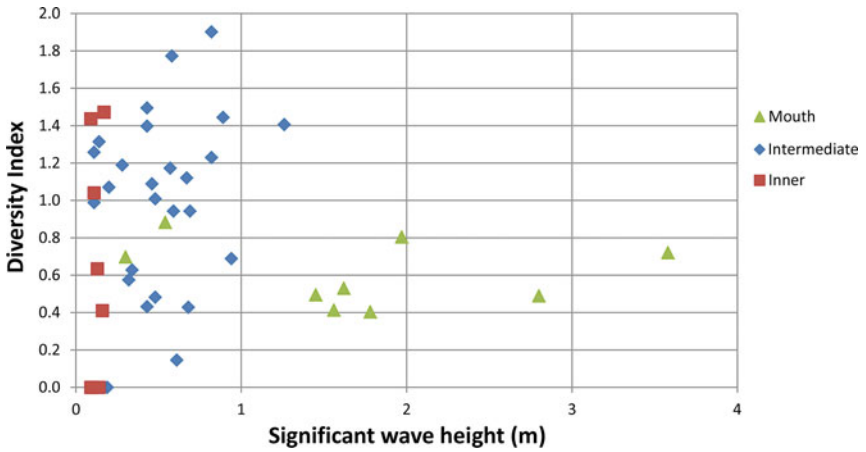

Fig. 9.8 Relation between diversity index and wave height at Stations 1–26 and A–R. The mouth, intermediate, and inner areas of the bay are displayed, respectively, as green, blue, and red (© 2014. American Geophysical Union. Used with permission from Shimokawa et al. (2014b) published by John Wiley and Sons)

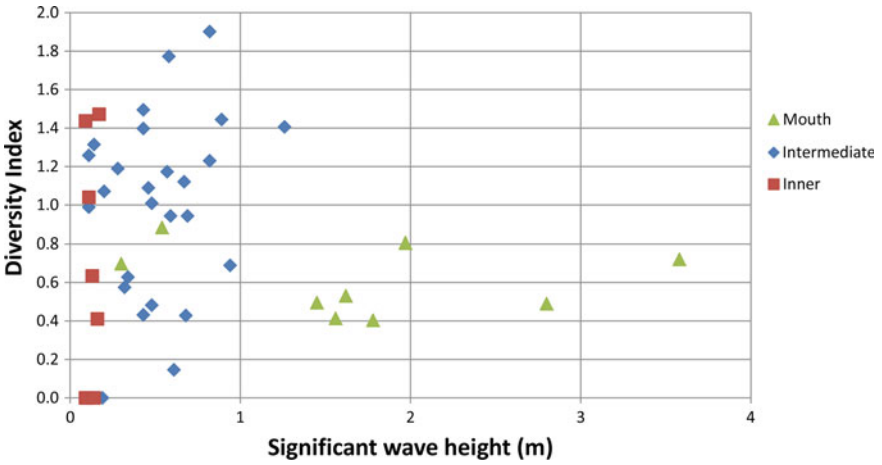

Fig. 9.9 Relation between diversity index and average number of soil grains reaching the seafloor per day at Stations 1–26 and A–R. The mouth, intermediate, and inner areas of the bay are displayed, respectively, as green, blue, and red. The numbers in the figure are the sums for all grain sizes (© 2014. American Geophysical Union. Used with permission from Shimokawa et al. (2014b) published by John Wiley and Sons)

vulnerable to such disturbances are limited. The diversity decreases. Conversely, H' peaked at average soil grain numbers of approximately 900 and 40,000 (Fig. 9.9), and the increased tendency of H' to increase with disturbances (up to a limit) is unclear when compared to the relation of H' to significant wave height. H' reached a maximum value at an average soil grain number of approximately 900 at Stations 8 and 9 in the intermediate area of the bay. At Stations 8 and 9, the ratio of tabular coral was low. Consequently, the ratios of other corals, especially foliose coral, were high (Fig. 9.4). These characteristics were not apparent at other locations. However, at Stations 8 and 9, they were regarded as the cause of high H' values. Foliose coral might prefer conditions with low numbers of soil grains and intermediate wave heights, which are typical of the conditions at Stations 8 and 9. When Stations 8 and 9 are excluded from Fig. 9.9, the tendency of H' to increase with an increase in disturbances (up to a limit in the average number of soil grains of approximately 40,000) becomes clearer. The distribution of H' in Fig. 9.7 is explained by these relations of H' to wave height and the number of soil grains.

High diversity does not indicate high coverage. Low diversity and low coverage indicate that the area is not a niche for organisms or biocoenosis distributed in the area. However, low diversity and high coverage indicate that the area is a niche only for organisms or biocoenosis distributed in the area. Figure 9.10 shows the relation between H' and the coverage of tabular or branching corals. For both corals, a high H' value (over 1.4), which is higher than the average of H' (0.83), corresponds to coverage from 5–30%. High coverage (over 50%) corresponds to an H' value lower than 0.6, which is lower than the average of H'. An area with high diversity of

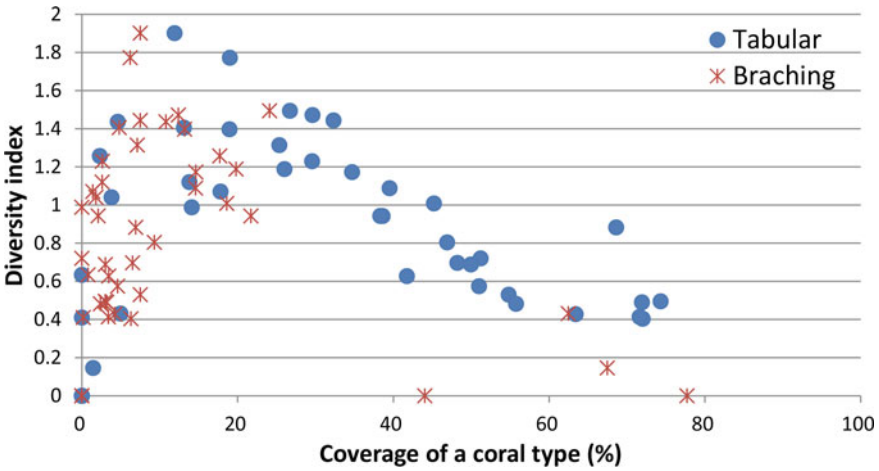

Fig. 9.10 Relation between diversity index and the coverage of tabular or branching corals at Stations 1–26 and A–R (© 2014. American Geophysical Union. Used with permission from Shimokawa et al. (2014b) published by John Wiley and Sons)

corals is not regarded as high coverage of a specific coral type (tabular or branching coral in this case) because the area is not a niche only for the species. An area with high coverage of a specific coral type is not regarded as having high diversity of corals because the area is a niche only for the species.

9.6 Conclusion

In this study, field observations were conducted to obtain data on coral distributions, sea temperature, sea salinity, wind speed, and the river flow rate. Ocean and wave model numerical simulations and soil grain tracking analysis were also conducted to obtain the spatial and temporal distributions of wave height and the number of soil grains. Using these observational and numerical data, the relation between coral distributions and environmental properties in Amitori Bay, Iriomote Island, Japan, were investigated. Moreover, diversity indices (which are a quantitative measure for the degree to which a dataset includes different types and which are related closely to information entropy concept) of coral distributions were calculated. Their relations to environmental properties were investigated. Our results demonstrated that the life forms, sizes, and species of corals varied significantly depending on their locations in the bay because the environmental properties differed significantly among these locations.

The main results of this study can be summarized as explained below.

(1) Coral distribution showed strong correlation with wave height and the number of soil grains. Larger coverage of tabular coral and smaller coverage of branching coral were correlated with larger wave heights. Smaller coverage of tabular coral related to a larger number of soil grains, although branching coral coverage were not correlated with the number of soil grains.
(2) Averages of the diversity index of the coral types at the mouth and inner area of the bay were lower than the average of the entire area. However, the average of the diversity index at the intermediate area of the bay with intermediate environmental disturbances was higher than the average of the entire area. This fact seems to support IDH as demonstrated by Connell (1978), which postulates that local species diversity is maximized when environmental disturbances are neither too weak nor too strong.

These results are expected to provide useful information for the assessment of physical characteristics' effects on coastal marine ecosystems in the Sakiyamawan–Amitoriwan Nature Conservation Area.

Acknowledgements We thank Prof. Kenshi Kimura of Tokai University for his helpful comments and Ms. Chiharu Yamaguchi of the National Research Institute for Earth Science and Disaster Prevention for helping in designing the figures. This work is supported by the Japan Society for the Promotion of Science through Grant No. 16K13879 and 18K04377.

References

Clarke KR, Warwick RM (2001) Changes in marine communities: an approach to statistical analysis and interpretation, 2nd edn. Plymouth Marine Laboratory: Primer-E Ltd., Plymouth, 176 pp

Connell JH (1978) Diversity in tropical rain forests and coral reefs. Science 199:1302–1310

Dollar SJ, Tribble GW (1993) Recurrent storm disturbance and recovery: a long-term study of coral communities in Hawaii. Coral Reefs 12:223–233

Fukami H, Budd AF, Paulay G, Sole-Cava A, Chen CA, Iwao K, Knowlton N (2004) Conventional taxonomy obscures deep divergence between pacific and atlantic corals. Nature 427:832–835

Fukami H, Chen CA, Budd AF, Collins A, Wallace C, Chuang YY, Chen C, Dai CF, Iwao K, Sheppard C, Knowlton N (2008) Mitochondrial and nuclear genes suggest that stony corals are monophyletic but most families of stony corals are not (Order Scleractinia, Class Anthozoa, Phylum Cnidaria). PLoS ONE 3:e3222

Fukami H, Tachikawa H, Suzuki G, Nagata S, Sugihara K (2010) Current status and problems with the identification and taxonomy of zooxanthellate scleractinian corals in Japan. J Japan Coral Reef Soc 12:17–31 (in Japanese)

Goreau TF (1959) The ecology of Jamaican coral reefs, 1. Species composition and zonation. J Ecol 40:67–90

Hatta M, Fukami H, Wang W, Omori M, Shimoike K, Hayashibara T, Ina Y, Sugiyama T (1999) Reproductive and genetic evidence for a reticulate evolutionary history of mass-spawning corals. Molecul Biol Evol 16:1607–1613

Hongo C, Kawamata H, Goto K (2012) Catastrophic impact of typhoon waves on coral communities in the Ryukyu Islands under global warming. J Geophys Res BioGeoSci 117, https://doi.org/10.1029/2011jg001902/full

Isobe M (1986) Calculation method for refraction, diffraction and breaking of irregular wave using parabolic equation. Ann J Coast Eng 33:134–138 (in Japanese)

Japan Meteorological Agency (JMA) (2015) Japan Meteorological Agency, Tokyo. http://gpvjma.ccs.hpcc.jp/gpvjma/

MacArthur RH, MacArthur JW (1961) On bird species diversity. Ecology 42:594–598

Madin JS, Connolly SR (2006) Ecological consequences of major hydrodynamic disturbances on coral reefs. Nature 444:477–480

Matsumoto K, Takanezawa T, Ooe M (2000) Ocean tide models developed by assimilating TOPEX/POSEIDON altimeter data into hydrodynamical model: a global model and a regional around Japan. J Oceanogr 56:567–581

McCune B, Grace JB (2002) Analysis of ecological communities. MjM Software Design, Oregon, 300 pp

Mizutani A, Sakihara T (2012) Atmospheric observation in Okinawa Regional Research Center. Study Rev Iriomote Is 2011:84–95 (in Japanese)

Motokawa T (2008) Story of coral reefs and coral—a strange ecosystem of the Southern Ocean, Chuokoron-shinsya, Tokyo, 273 pp (in Japanese)

Murakami T, Yoshino J, Yasuda T, Iizuka S, Shimokawa S (2011) Atmosphere–ocean–wave coupled model performing 4DDA with a tropical cyclone Bogussing scheme to calculate storm surges in an Inner Bay. Asian J Environ Disas Manag 3:217–228

Murakami T, Ukai A, Kohno H, Mizutani A, Shimokawa S, Nakase K, Yasuda T (2012) Relationships between distributions of coral and physical environments in Amitori Bay, Iriomote island, Japan. J Japan Soc Civil Eng B3(68):1133–1138 (in Japanese with English abstract)

Putri LSE, Hidayat AF, Sukandar P (2012) Diversity of coral reefs in Badul Island waters, Ujung Kulon, Indonesia. J Bio Sci 1:59–64

Shannon CE (1948) A mathematical theory of communication. Bell Syst Tech J 27:379–423 and 623–656

Sheppard CRC, Davy SK, Pilling GM (2009) The biology of coral reefs. Oxford University Press, Oxford, 339 pp

Shimokawa S, Murakami T, Iizuka S, Yoshino J, Yasuda T (2014a) A new typhoon bogussing scheme to obtain the possible maximum typhoon and its application for assessment of impacts of the possible maximum storm surges in Ise and Tokyo Bays in Japan. Nat Hazards 74:2037–2052. https://doi.org/10.1007/s11069-014-1277-2

Shimokawa S, Murakami T, Ukai A, Kohno H, Mizutani A, Nakase K (2014b) Relationship between coral distributions and physical variables in Amitori Bay, Iriomote Island, Japan. J Geophys Res Oceans 119:8336–8356. https://doi.org/10.1002/2014JC010307

Shokry M, Ammar A (2011) Coral diversity indices along the Gulf of Aqaba and Ras Mohammed, Red Sea, Egypt. Biodiversitas 12:92–98

Simpson EH (1949) Measurement of diversity. Nature 163:688

Ukai A, Kohno H, Nakase K, Shimaya M, Zinno M, Kimura K (2010) Influence of ocean waves on coral habitat environment of Amitori Bay. Ann J Civil Eng Ocean 26:363–368 (in Japanese with English abstract)

White KN, Ohara T, Fujii T, Kawamura I, Mizuyama M, Montenegro J, Shikiba H, Naruse T, McClelland TY, Denis V, Reimer JD (2013) Typhoon damage on a shallow mesophotic reef in Okinawa, Japan. Peer J 1:e151. https://doi.org/10.7717/peerj.151

Woodley JD, Chornesky EA, Clifford PA, Jackson JBC, Kaufman LS, Knowlton N, Lang JC, Pearson MP, Porter JW, Rooney MC, Rylaarsdam KW, Tunnicliffe VJ, Wahle CM, Wulff JL, Curtis ASG, Dallmeyer MDB, Jupp P, Koehl MAR, Neigel J, Sides EM (1981) Hurricane Allen's impact on Jamaican coral reefs. Science 214:749–755

Chapter 10
Coral Distributions and Physical Environments in Sakiyama Bay

Shinya Shimokawa, Hiroyoshi Kohno, Tomokazu Murakami and Akira Mizutani

Abstract This study was conducted to clarify the relation between coral distributions and physical variables in Sakiyama Bay, Iriomote Island, Japan. First, the distributions of coral coverage by the colony shapes and coral areas by the community types were investigated at 72 points around the bay. Next, physical variables such as oceanic flow and soil particle numbers were analyzed by numerical simulation under average summer and winter conditions in the region. The results were compared with the obtained coral distribution. From those results, we inferred the following: (1) Coral coverage shows a direct relation with bottom flows in the region; the bottom flows differ among coral community types. (2) Coral coverage shows an inverse relation with soil particle numbers in the region. *Enhalus acoroides* mainly inhabits areas with greater numbers of soil particles.

Keywords Reef building coral · Sakiyama Bay · Physical environment · Soil particle · Bottom flow · Numerical simulation

This chapter is based on the work reported by Shimokawa et al. (2016).

S. Shimokawa (✉) · T. Murakami
Storm, Flood and Landslide Research Division, National Research Institute for Earth Science and Disaster Resilience, Tsukuba, Japan
e-mail: simokawa@bosai.go.jp

T. Murakami
e-mail: tmurakami@bosai.go.jp

H. Kohno · A. Mizutani
Okinawa Regional Research Center, Tokai University, Yaeyama, Japan
e-mail: hkohno@scc.u-tokai.ac.jp

A. Mizutani
e-mail: ma110267@tsc.u-tokai.ac.jp

S. Shimokawa et al. (eds.), *Geophysical Approach to Marine Coastal Ecology*, Springer Oceanography, https://doi.org/10.1007/978-981-15-1129-5_10

10.1 Introduction

Sakiyama Bay, a part of the Amitoriwan–Sakiyamawan Nature Conservation Area (see Sect. 1.2), is adjacent to Amitori Bay. An earlier chapter (Chap. 9) described the relation between coral distributions and physical environments in Amitori Bay (Murakami et al. 2012; Shimokawa et al. 2014; Ukai et al. 2015; Shimokawa et al. 2015). Sakiyama Bay has Iriomote Island's leading communities of branching coral and a kind of seagrass (*Enhalus acoroides*: see Sect. 1.5), but Sakiyama Bay differs considerably from Amitori Bay in terms of its geographic characteristics such as depth, length, and shape. The relation between coral distributions and physical environments in Sakiyama Bay has remained unknown. Investigations of its characteristics have been strongly needed. Therefore, to clarify those various relations, we conducted investigations of distributions of coral coverage by colony shape and coral area for community types at 72 points around the bay. Then, we compared the obtained coral distributions with physical variables such as oceanic flow and soil particle numbers using numerical simulations under average summer and winter conditions in the region (Shimokawa et al. 2016).

10.2 Investigation Method of Coral Distributions

We conducted the following investigations of coral distributions during May–November in 2015.

(1) Investigation of coral coverage distributions by colony shape.

Coral distributions were investigated for 72 points on 19 lines, A–S in Sakiyama Bay (Fig. 10.1). Three quadrats measuring 2 m on each side were placed. Photographs were taken from just above at each point irrespective of the presence or absence of corals (Fig. 10.2). Then, according to the previous studies (Murakami et al. 2012; Shimokawa et al. 2014, 2015; Ukai et al. 2015), the types of coral life forms were classified as branching, tabular, massive, foliose, or encrusting corals as shown in Fig. 9.2. Subsequently, the coverage was calculated as the average on the three quadrats with 1% of the pitch width.

(2) Investigation of distributions of coral areas by community type.

We specifically examined branching and tabular corals with higher appearance frequencies in Sakiyama Bay. Particularly for branching coral, the community types were classified as long, short, or short–thin branching corals based on the measurement of lengths of the living parts and widths of the bases for randomly selected branches. To make an addition of *Enhalus acoroides* community to these communities, the areas of five community types (Fig. 10.3) were calculated using GPS measurements.

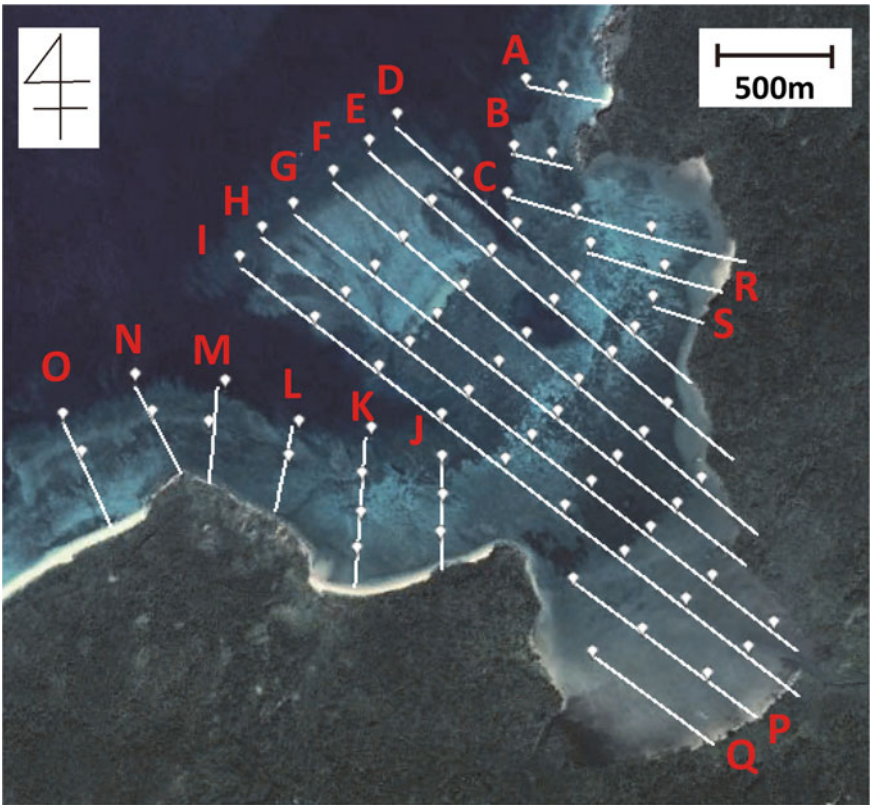

Fig. 10.1 Lines and points for investigating coral distributions. On lines A, B, J–O, investigation points were set approximately every 100 m; on other lines, they were set around every 200 m. Map data © 2016 Google (referred from Shimokawa et al. 2016)

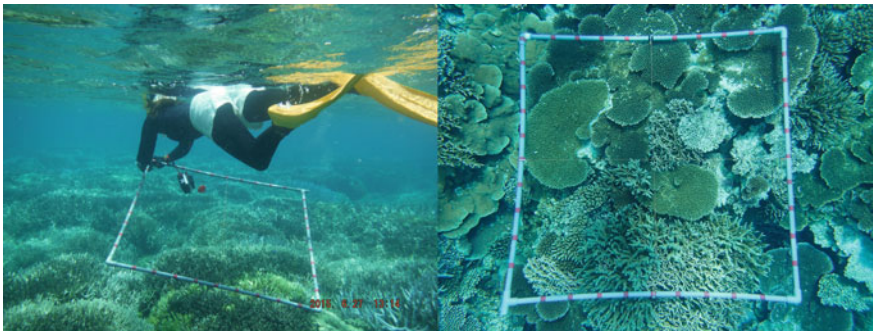

Fig. 10.2 Photographs of coral investigations (left) and quadrats (right) in Sakiyama Bay. A photograph of quadrats was taken at the offshore side point on line B (Fig. 10.1) (referred from Shimokawa et al. 2016)

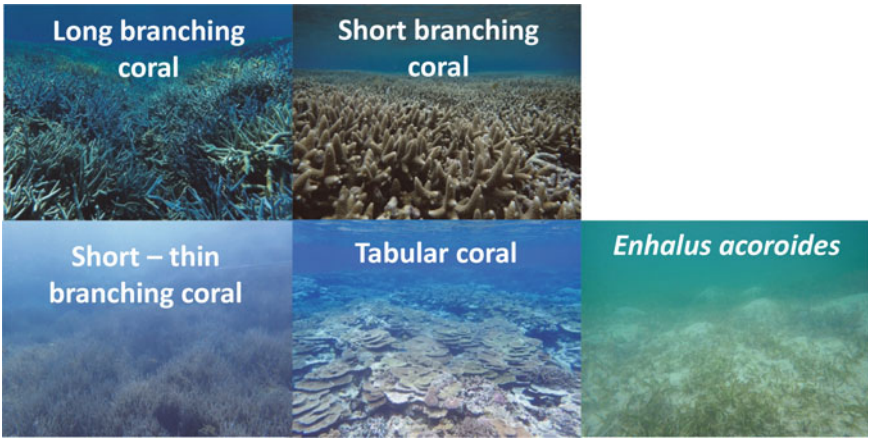

Fig. 10.3 Community types treated in this study (referred from Shimokawa et al. 2016)

10.3 Calculation Method of Physical Environments

Various factors such as physical, chemical, and biological factors affect the diverse distributions of corals (Motokawa 2008; Sheppard et al. 2009). Among them, this study addresses physical factors including ocean waves, ocean currents, sediments, salinity, and illuminance. Especially, the present study specifically elucidates the bottom flow speed and soil particle number because the distributions of corals inhabiting on sea bottom are affected by the bottom flow speed rather than the surface flow speed and wave strength. Moreover, in Sakiyama Bay, soil particle inflow from rivers at the inner bay can spread because of the flat bottom of the bay (Kawana 1990, see also Sect. 10.6).

For that purpose, we re-analyzed the results reported from earlier studies (Murakmai et al. 2013; Nakase et al. 2015) conducting numerical simulations for bottom flow speed and soil particle number under average conditions of summer and winter in Sakiyama Bay. Here, the Simulating Waves Nearshore (SWAN, Booji et al. 1999) and Coastal Ocean Current Model (CCM, Murakmai et al. 2015c) were used for simulations of the bottom flow speed (amplitude of orbital velocity). Lagrange particle tracing method (e.g., Cushman-Roisin and Beckers 2011) was used for the soil particle number. Details related to the simulation method are presented in Chap. 3 and in the original articles described above.

10.4 Distributions of Corals

In this section, we state the results of investigations of the distributions of coral coverage by the colony shape and coral area according to the community type in Sakiyama Bay.

Figure 10.4 portrays the distributions of coral coverage by colony shape. Tabular, foliose, and encrusting corals distribute mainly at the reef margin. Branching corals do so at the reef margin and the mouth of the bay. Massive corals are distributed at the mouth and central parts of the bay.

Among all 72 points of investigation, the numbers of points with 0% and >1% coverage were, respectively, 17 and 55. The coverage averaged at points with >1% coverage is 48%. For branching corals, the average, minimum, and maximum coverage and the number of points with the appearance of corals are, respectively, 39%, 1%, 100%, and 41%. For tabular corals, they are 15, 1, 49, and 28%. For

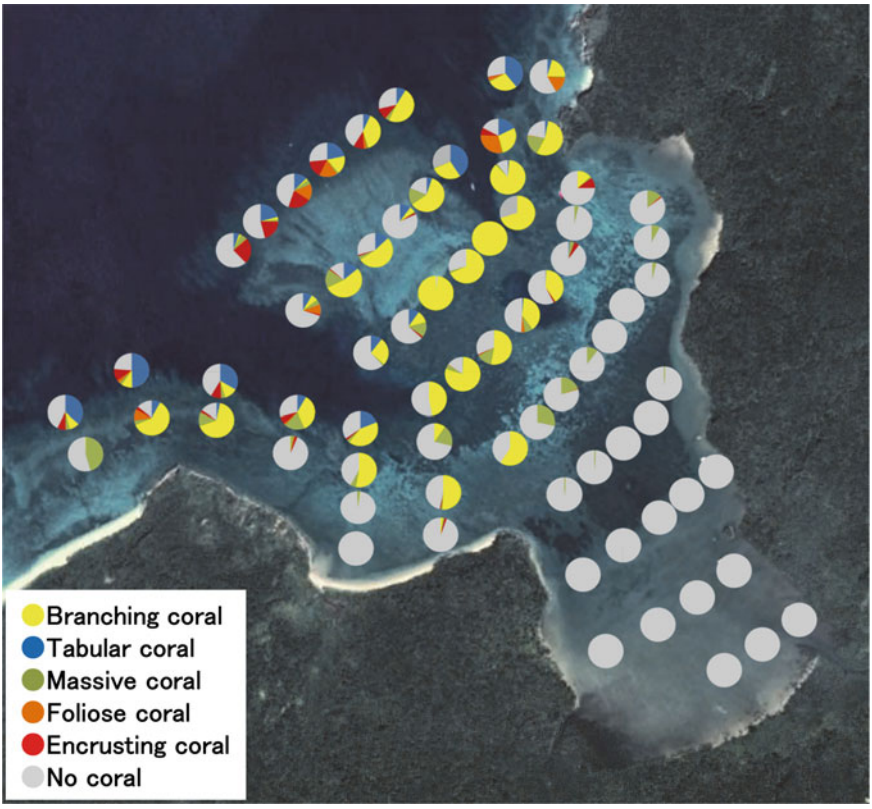

Fig. 10.4 Distributions of coral coverage by the colony shapes. The types of colony shapes are classified according to branching, tabular, massive, foliose, and encrusting corals shown in Fig. 9.2. Map data © 2016 Google (referred from Shimokawa et al. 2016)

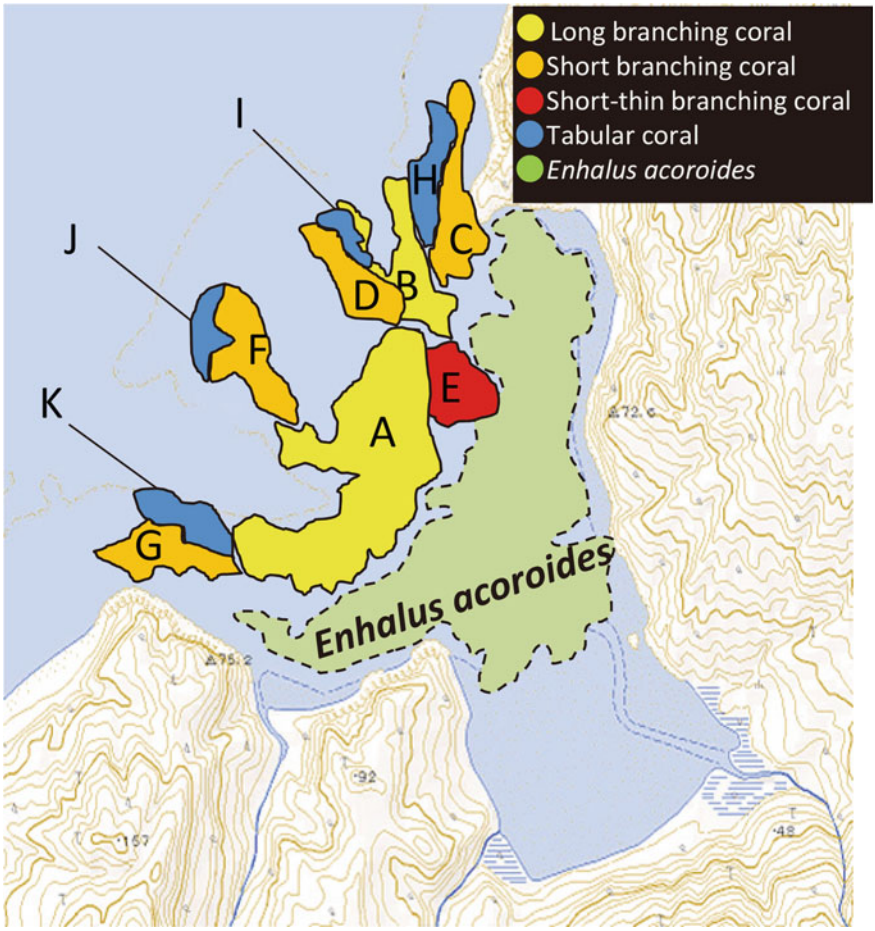

Fig. 10.5 Distributions of coral areas by community type. The community types were classified to long, short, short–thin branching, tabular corals, and *Enhalus acoroides* presented in Fig. 10.3 (referred from Shimokawa et al. 2016)

massive corals, they are 7, 1, 45, and 47%. For foliose corals, they are 6, 1, 29, and 19%. For encrusting corals, they are 7, 1, 24, and 25%.

Sakiyama Bay has seven branching coral communities (A–G in Fig. 10.5) and four tabular coral communities (H–K in Fig. 10.5). Average lengths of the living parts and width of the bases for the random selected branches in the branching coral communities are presented in Table 10.1. Based on the measurements, for the branching coral, the community types were classified as long, short, and short–thin branching corals. Average lengths of the living parts in the communities of long, short, and short–thin branching corals were, respectively, 15.9 cm, 9.4 cm, and

Table 10.1 Average lengths and widths of branches in branching coral communities (referred from Shimokawa et al. 2016)

Community	A	B	C	D	E	F	G
Average length (cm)	14.7	17.1	9.1	9.3	9.8	9.9	9.4
Average width (cm)	1.2	1.2	0.9	1.0	0.4	1.1	1.0

9.8 cm. Average widths of the bases in the communities of long, short, and short–thin branching corals were, respectively, 1.2 cm, 1.0 cm, and 0.4 cm.

Figure 10.5 presents the distributions of coral areas by community type presented in Fig. 10.3. Long branching coral communities are located mainly at the mouth of the bay, slightly distant from the reef margin. The number and total area size are, respectively, 2 and 16 ha. Short branching coral communities are located mainly at the reef margin with strong wave breaks. Their number and total area are, respectively, 4 and 11 ha. Short–thin branching coral communities of 200 m diameter are mainly located at the margin of reef pond at around 13 m depth in the east of the central part of the bay. Their number and total area size are, respectively, 1 and 2 ha. *Enhalus acoroides* communities are located mainly at the central and inner parts of the bay, along a shallow and flat bottom at approximately 1.2 m depth (Kawana 1990).

10.5 Relation Between Coral Distributions and Physical Variables

In this section, we explain the relation between coral distributions described in the previous section. We also explain the bottom flow speed and soil particle numbers obtained from numerical simulations conducted for Sakiyama Bay.

Figure 10.6 shows the total coverage of corals without distinction of colony shape. Broadly speaking, the total coverage is over 30% from the mouth of the bay to the central part of the bay, under 30% from the central part of the bay to the habitat of *Enhalus acoroides* (shown by dotted yellow line), and 0% at the innermost bay area. Therefore, we classified the investigation points as those with total coverage of 0, 1–30%, and over 30%. Moreover, we analyzed the relation between the coral distributions and the physical variables.

Figure 10.7 presents the relations among community type, total coverage, and bottom flow speed. Bottom flow is generated by waves, tides, wind, and river flows. Regarding the bottom flow speed by wave, irrespective of the season, the largest in terms of community type was tabular coral, followed in order by short branching coral, short–thin branching coral, and long branching coral (Fig. 10.7a). The largest in all coverage was points over 30%, followed in order by those of 1–30% and those of 0% (Fig. 10.7b). Particularly, the bottom flow speed in winter at points over 30% is twice as large as at points of 0%. However, for the bottom flow speed

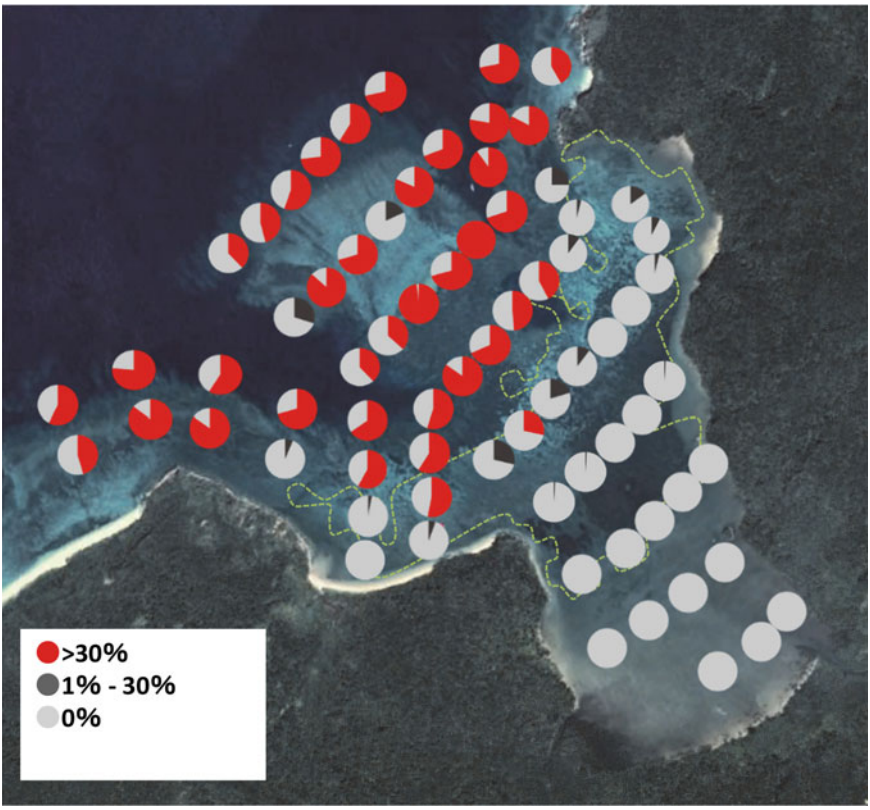

Fig. 10.6 Total coverage of corals without distinction of colony shape. Red, dark gray, and light gray, respectively, portray over 30, 1–30, and 0%. The dotted yellow line shows the presence of *Enhalus acoroides.* Map data © 2016 Google (referred from Shimokawa et al. 2016)

by tide and that by tide, wind, and river flow, their correlation between total coverage and the values themselves is weaker than that by waves (Figs. 10.7b–d). Therefore, considering the relation between coral distributions and bottom flow speed, that by waves, is regarded as fundamentally important.

From the above, in Sakiyama Bay, it can be inferred that the bottom flow speed differs depending on points of each community type: Also, a higher bottom flow speed at a point indicates greater total coverage at that point. The results reflect the different shape tolerance of corals against ocean current: branching coral tends to be a dominant species because it grows rapidly (Stoddart 1969; Motokawa 2008), but at higher flow speeds (particularly at points near the mouth of the bay), the branch changes are more likely to be short than long (Fig. 10.5) because of their low tolerance against ocean current. By contrast, tabular coral tends to be more common (Fig. 10.4) because it has high tolerance against ocean currents by virtue of its shape (Goreau 1959; Woodley et al. 1981; Motokawa 2008). At higher flow speeds,

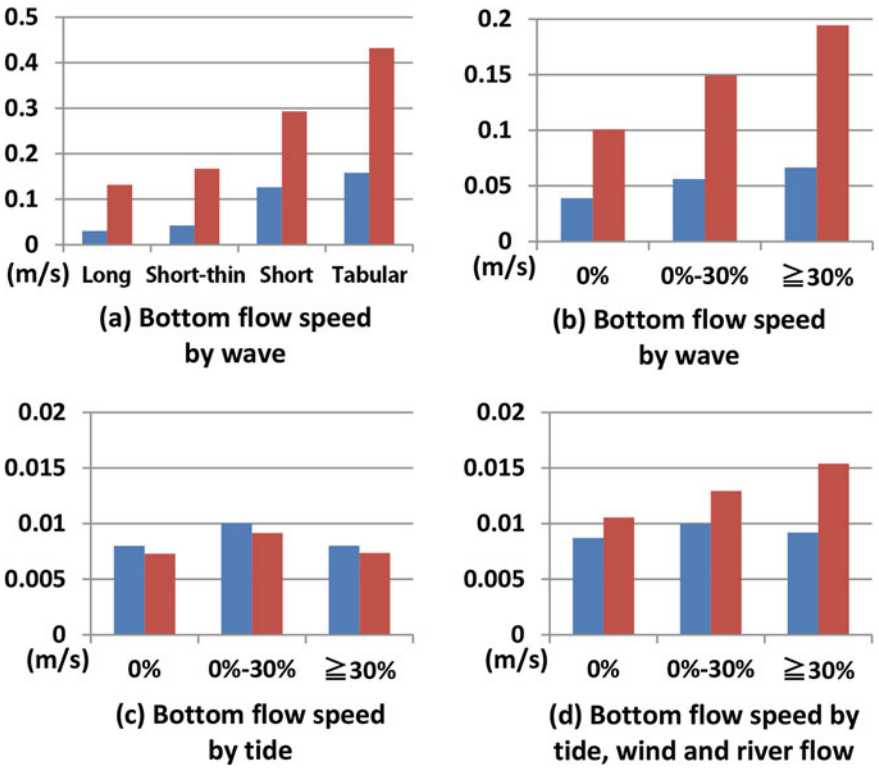

Fig. 10.7 Relations among (**a**) community types, **(b)**–**(d)** total coverage, and bottom flow speed. The bottom flow speeds show averages for summer (blue) and winter (red) seasons on points with each range of coverage (referred from Shimokawa et al. 2016)

it becomes increasingly common (as the object point nears the reef margin); massive and encrusting corals tend to be more common (Fig. 10.4) because they have higher tolerance against ocean current by virtue of their shape, although they grow slowly (Stoddart 1969; Motokawa 2008). Consequently, in Sakiyama Bay, high coverage can persist in a broad area from the reef margin to the central part of the bay. Here, it is noteworthy that although short–thin branching coral communities are located at almost equal distance from the reef margin as long branching coral communities, they inhabit areas surrounding a reef pond: a special location in Sakiyama Bay with a flat bottom (Kawana 1990). That habitat is regarded as different from those found at other locations.

Figure 10.8 exhibits the relation between coral coverage and soil particle number. The soil particle number, irrespective of the season and soil particle diameter, is extremely large at points of 0%. Points with coral appearance of 1–30% are more numerous than points greater than 30%. In Sakiyama Bay, soil particle numbers are larger at coral inhibited areas, where coral coverage is low, probably

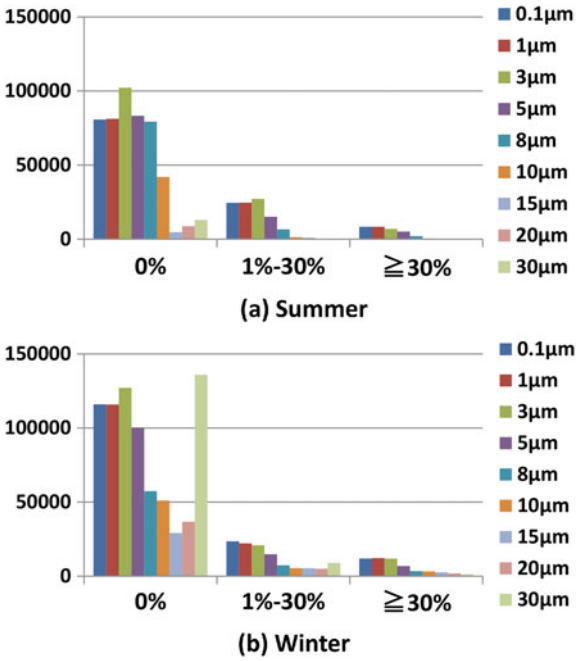

Fig. 10.8 Relation between coral coverage and soil particle number in **(a)** summer and **(b)** winter. The soil particle numbers show values of total of soil particle numbers in calculation grids including investigation points with each range of coverage divided by the number of investigation points (referred from Shimokawa et al. 2016)

because soil particle inflow from rivers at the innermost part of the bay spreads a certain extent and affects the distribution of corals with low tolerance against soil particles (Rogers 1990; Motokawa 2008). This point will be discussed in greater detail in the next section in reference to the comparison with findings for Amitori Bay.

Here, it is noteworthy that the total numbers of soil particles of each diameter do not always match because soil particles of each diameter released from rivers can be counted only when the particles exist in a calculation grid that includes an investigation point. Additionally, the number of 30 μm diameter soil particles in winter at points of 0% is extremely large because prevailing winds in winter in Sakiyama Bay are N–ENE (Kawana 1990). Therefore, large and heavy particles of 30 μm diameter move only slightly from the innermost part of the bay (i.e., the region for total coverage of 0%), in addition to the above.

10.6 Comparison Between the Cases of Sakiyama and Amitori Bays

In this section, we discuss the difference between the distributions of corals and *Enhalus acoroides* in Sakiyama Bay presented in previous sections and those in Amitori Bay (Chap. 9 and Shimokawa et al. 2014).

Amitori Bay has various corals (Murakami et al. 2012; Shimokawa et al. 2014, 2015; Ukai et al. 2015), but their diversity (here, diversity in types of the colony shape, strictly speaking, equality; Ohgaki 2008) is maximal at the center part of the bay (Shimokawa et al. 2014). Few *Enhalus acoroides* inhabit the area; no large community exists (Murakami et al. 2014, 2015a, b; Nakase et al. 2015). By contrast, in Sakiyama Bay, although various corals also exist, their diversity is maximal at the reef margin (Fig. 10.4). *Enhalus acoroides* inhabits a broad area from the center part of the bay to the inner part of the bay (Fig. 10.5). These differences in distributions of corals and *Enhalus acoroides* between the bays are related not only to physical factors but also to various factors. They cannot be explained by a specific factor. However, the difference in soil particle inflow related to the geographic environment gradient between both bays is regarded as strongly affecting differences in the distributions of corals and *Enhalus acoroides* in the two bays.

As explained in the *Introduction*, Sakiyama Bay is adjacent to Amitori Bay, but it differs considerably from Amitori Bay in terms of its geographic characteristics such as the depth, length, and shape. Amitori Bay has a large geographic environmental gradient: great length compared to the width of the mouth of the bay and a deep valley reaching 70 m depth at the center of the bay (Shimoji et al. 1990). Because of these geographic characteristics, the effects of soil particle inflow are strong at the innermost part of the bay and the deep valley in the center of the bay, and weak at the east and west sides of the bay, where the corals live (Murakmai et al. 2013). By contrast, Sakiyama Bay has a small geographic environmental gradient: a short length compared to the width of the mouth of the bay, shallow depth of around a few meters from the innermost part of the bay to the mouth of the bay, with a flat bottom except for the reef pond of around 13 m depth and 200 m diameter just east of the central part of the bay (E in Fig. 10.5) (Kawana 1990). Therefore, the soil particle inflow effects are spread easily throughout the bay, compared to Amitori Bay. In fact, the sediment is a mixture of fine brown sand and gray–black mud in the entire region of the inner part of the bay (Shimoji et al. 1990). That is, in Sakiyama Bay, the effects of soil particle inflow from rivers at the innermost part of the bay are widespread because of its smaller geographic environment gradient than that of Amitori Bay. Therefore, in the inner part of the bay, a coral community, which is difficult to grow at the place with much soil, cannot develop, but the *Enhalus acoroides* community, of which roots and subterranean stems easily take root on muddy sediments (Komatsu et al. 2004), can develop. Moreover, branching coral has high tolerance against soil particles because of its shape, which renders the soil particles more difficult to accumulate than tabular coral (Rogers 1990; Motokawa 2008). Consequently, the distribution in the order of *Enhalus acoroides*, branching coral, and tabular coral with distance from the river at the innermost part of the bay is clearer in Sakiyama Bay.

For tabular and branching corals, different effects of their tolerances against soil particles on their distributions are approximately proportional to their distance from the river mouth. Differences in their tolerances against ocean currents, which affect their distributions, as stated in the preceding section, are approximately proportional to their distance from the bay mouth. Therefore, if rivers are located at the

innermost part of the bay, as they are in Amitori and Saliyama Bays, then similar effects can be expected on their distances from the mouths of the respective rivers and bays.

In Amitori Bay, the diversity index is highest at the center part of the bay, although the intermediate disturbance hypothesis (IDH) (Connell 1978), which postulates that local species diversity is maximized when environmental disturbances are neither too weak (or infrequent) nor too strong (or frequent), is supported for waves, but not for soil particles; IDH is supported as a whole. The reason is the following. First, the locations where the two effects above can be reached are separated because the geographic environmental gradient is large (i.e., Amitori Bay has a greater length than the width of the mouth of the bay). As a result, the environment in which corals of various types can coexist (i.e., the diversity is high) can be realized in the center part of the bay, where the disturbance of waves is of an intermediate degree. By contrast, in Sakiyama Bay, locations at which the two effects above can be obtained are overlapped because the geographic environmental gradient is small (i.e., Sakiyama Bay has a small length compared to the width of the bay mouth). Therefore, works constructed in a direction to strengthen the two similar effects and to create an environment for their coexistence cannot be realized in any specific location of the bay. Consequently, the distribution areas of tabular corals, branching corals, and *Enhalus acoroides* must be regarded as distinctly and necessarily separate.

10.7 Summary

This study clarified the relation between coral distributions and physical variables in Sakiyama Bay, Iriomote Island, Japan. The results were compared to those obtained for Sakiyama Bay. Differences of geographic environmental gradients between both bays are regarded as affecting the distributions of corals and *Enhalus acoroides*. These results are expected to provide useful information for the assessment of the effects of physical variables on coastal marine ecosystems in the Sakiyamawan–Amitoriwan Nature Conservation Area.

Acknowledgements We thank Ms. Seina Miyauchi, Ms. Mayumi Suzuki, Mr. Yuichi Yoshioka, and Mr. Yuji Kitahara of Tokai University for their help, Mr. Kota Nakase of Penta-Ocean Construction Co., Ltd. for his helpful comments on *Enhalus acoroides*. This work is supported by the Japan Society for the Promotion of Science through Grant No. 16K13879 and 18K04377.

References

Booji N, Ris RC, Holthuijsen LH (1999) A third-generation wave model for coastal regions, 1. Moel description and validation. J Geophys Res 104:7649–7666

Connell JH (1978) Diversity in tropical rain forests and coral reefs. Science 199:1302–1310

Cushman-Roisin B, Beckers JM (2011) Introduction to geophysical dynamics, 2nd edn. Elsevier, Amsterdam, 828 pp

Goreau TF (1959) The ecology of Jamaican coral reefs, 1. Species composition and zonation. J Ecol 40:67–90

Kawana T (1990) Geomorphology, geology, climate and marine conditions in and around the Sakiyama Bay. Iriomote Island, The south Ryukyus, Japan. Report of investigation for Sakiyamawan nature conservation area (Ministry of the Environment, Government of Japan), pp 9–26 (in Japanese with English abstract)

Komatsu T, Umezawa Y, Nakakoka M, Supanwanid C, Kanamoto Z (2004) Water flow and sediment in *Enhalus acoroides* and other seagrass beds in the Andaman Sea, off Khao Bae Na, Thailand. Coast Mar Sci 29:63–68

Motokawa T (2008) Story of coral reefs and coral—a strange ecosystem of the Southern Ocean, Chuokoron-shinsha, Tokyo, 273 pp (in Japanese)

Murakami T, Ukai A, Kohno H, Mizutani A, Shimokawa S, Nakase K, Noguchi K, Yasuda T (2012) Relationships between distributions of coral and physical environments in Amitori Bay, Iriomote island, Japan. J Japan Soc Civil Eng B3(68):1133–1138 (in Japanese with English abstract)

Murakami T, Kohno H, Iwasaki A, Kuramochi T, Shimokawa S, Kimura K (2014) Particle tracking analysis based on ecological investigation of seeds of *Enhalus acoroides* in Amitori Bay. J Japan Soc Civil Eng B3(70):1074–1079 (in Japanese with English abstract)

Murakami T, Kohno H, Tamamoto M, Mizutani A, Shimokawa S (2015a) Numerical analysis of seed dispersal of *Enhalus acoroides* in the northwest sea area of Iriomote Island, Japan. J Japan Soc Civil Eng B3(71):951–956 (in Japanese with English abstract)

Murakami T, Shimokawa S, Yoshino J, Yasuda T (2015b) A new index for evaluation of risk of complex disaster due to typhoons. Nat Hazards 75:29–44. https://doi.org/10.1007/s11069-015-1824-5

Murakmai T, Ukai A, Noguchi K, Kohno H, Mizutani A, Shimokawa S, Nakase K, Yoshino J (2013) Numerical analysis of sediment transport in Amitori Bay, Irio-mote Island, Japan. J Japan Soc Civil Eng B3(69):928–933 (in Japanese with English abstract)

Murakmai T, Kohno H, Tamamoto M, Mizutani A, Shimokawa S (2015) Numerical analysis of fructification dispersal of *Enhalus acoroides* in the northwest sea area of Iriomote Island, Japan. J Japan Soc Civil Eng B2(71):1351–1356 (in Japanese with English abstract)

Nakase K, Murakami T, Ukai A, Mizutani A, Shimokawa S, Kohno H (2015) Distri-bution analysis of *Enhalus acoroides* vegetation, using hydraulic model, in the northwest sea area of Iriomote Island, Okinawa, Japan. J Japan Soc Civil Eng B3(71):957–962 (in Japanese with English abstract)

Ohgaki S (2008) Diversity and similarity—new taxonomic index. Argonauta 15:10–22 (in Japanese)

Rogers CS (1990) Responses of coral reefs and reef organisms to sedimentation. Mar Ecol Prog Ser 62:185–202

Sheppard CRC, Davy SK, Pilling GM (2009) The biology of coral reefs. Oxford University Press, Oxford, 339 pp

Shimoji N, Nakasone T, Nishidaira M, Yokote H (1990) Quality of water and sediments of Sakiyama bay nature conservation area, Iriomote Island. Report of investigation for Sakiyamawan nature conservation area (Ministry of the Environment, Government of Japan), pp 27–42 (in Japanese with English abstract)

Shimokawa S, Murakami T, Ukai A, Kohno H, Mizutani A, Nakase K (2014) Relationship between coral distributions and physical variables in Amitori Bay, Iriomote Island, Japan. J Geophys Res Oceans 119:8336–8356. https://doi.org/10.1002/2014JC010307

Shimokawa S, Kohno H, Murakami T, Mizutani A, Shibayama T, Yamamoto Y, Ukai A, Nakase K (2015) Relationship between massive coral distribution and physical variables in Amitori Bay, Iriomote Island, Japan. J Japan Soc Civil Eng B3(71):969–974 (in Japanese with English abstract)

Shimokawa S, Kohno H, Murakami T, Miyauchi S, Suzuki M, Mizutani A (2016) Relation between coral distributions and physical variables in Sakiyama Bay, Iriomote Island, Japan. J Japan Soc Civil Eng B2(72):1435–1440 (in Japanese with English abstract)

Stoddart DR (1969) Ecology and morphology of recent coral reefs. Biol Rev Cambridge Phil Soc 44:433–498

Ukai A, Murakami T, Mizutani A, Nakase K, Shimokawa S, Kohno H (2015) Estimation technique of spatial coral distribution in Amitori Bay, Iriomote Island, Japan. J Japan Soc Civil Eng B3(71):963–968 (in Japanese with English abstract)

Woodley JD, Chornesky EA, Clifford PA, Jackson JBC, Kaufman LS, Knowlton N, Lang JC, Pearson MP, Porter JW, Rooney MC, Rylaarsdam KW, Tunnicliffe VJ, Wahle CM, Wulff JL, Curtis ASG, Dallmeyer MDB, Jupp P, Koehl MAR, Neigel J, Sides EM (1981) Hurricane Allen's impact on Jamaican coral reefs. Science 214:749–755

Chapter 11
Estimation Technique for Horizontal Distribution of Coral

Akiyuki Ukai, Tomokazu Murakami, Akira Mizutani, Kouta Nakase, Shinya Shimokawa and Hiroyoshi Kohno

Abstract Amitori Bay, located in northwestern Iriomote Island, is characterized by its varied physical environments such as geographical features, wave height, and current in spite of its small size. It also exhibits a diverse distribution of coral reefs in response. Physical data acquired through numerical analysis, although including errors from actual measurements, provide much information by being interpolated spatially and are useful for the understanding of phenomena. However, the spatial distribution of corals is difficult to estimate using an ecosystem model because the coral ecology has numerous and important unknown characteristics. We have proposed a new technique for estimation of the horizontal distribution of coral coverage based on the relevance between coral coverage and physical data. We have conducted estimation of horizontal distribution of coral in Amitori Bay in this study. A technique using a piecewise linear function with artificial intelligence as the analytic method has yielded excellent results compared to those of multiple regression analysis.

This chapter is based on work reported by Ukai et al. (2015).

A. Ukai (✉) · K. Nakase
Environment Business Division, Penta-Ocean Construction Co., Ltd., Tokyo, Japan
e-mail: akiyuki.ukai@mail.penta-ocean.co.jp

K. Nakase
e-mail: kouta.nakase@mail.penta-ocean.co.jp

T. Murakami · S. Shimokawa
Storm, Flood and Landslide Research Division, National Research Institute for Earth Science and Disaster Resilience, Tsukuba, Japan
e-mail: tmurakami@bosai.go.jp

S. Shimokawa
e-mail: simokawa@bosai.go.jp

A. Mizutani · H. Kohno
Okinawa Regional Research Center, Tokai University, Yaeyama, Japan
e-mail: ma110267@tsc.u-tokai.ac.jp

H. Kohno
e-mail: hkohno@scc.u-tokai.ac.jp

S. Shimokawa et al. (eds.), *Geophysical Approach to Marine Coastal Ecology*, Springer Oceanography, https://doi.org/10.1007/978-981-15-1129-5_11

Keywords Amitori Bay · Coral distributions · Distribution of coral coverage · Numerical simulation · Genetic algorithm

11.1 Introduction

The relation between horizontal distribution of coral and various physical data in Amitori Bay and Sakiyama Bay of Iriomote Island (Sects. 11.1, 11.2, and Fig. 1.1) has been described in previous chapters (Chaps. 9 and 10) (see also Sect. 11.4 for the coral in Iriomote Island). Characteristic horizontal distribution of coral in Amitori Bay and Sakiyama Bay is evidently related to the physical environments typical in each bay, i.e., the distribution of coral coverage is affected strongly by the physical environment.

Results of analysis and various surveys conducted to date can serve as valuable information for elucidating the physical environments and the state of coral coverage in Amitori and Sakiyama bays at present. Although physical environments elucidated by local observations might have only limited information at a survey point, the detailed spatial distribution is obtainable by interpolation with the various numerical simulations described above.

However, field surveys of coral coverage require large amounts of labor, making it entirely unrealistic to measure many aspects of coral coverage; moreover, the number of observation points would be limited. It is also difficult to obtain horizontal distributions of coral such as physical data acquired through numerical simulation because the coral distribution mechanism remains unexplained.

In fact, understanding of phenomena related to physical environments has been enhanced by reproduction and detailed interpolation of their horizontal and three-dimensional distribution by numerical simulation. We consider that the detailed horizontal distribution of coral coverage will engender better understanding of the state of coral in the same fashion.

We apply an estimation technique for horizontal distribution of coral from the horizontal distribution of physical data of various kinds in this report using relations between coral coverage and physical environments that have been ascertained to date (Ukai et al. 2015).

11.2 Basic Concepts

The distribution of coral coverage obtained from field surveys (e.g., Figs. 9.4, 10.4) reflects the history of changes in physical environments up to the present and does not correspond one-to-one with observations of physical environments at present. Nevertheless, one can infer that the surviving coral is most strongly affected by today's physical environments and that the distribution of coral coverage at present is evidently related with physical environments (Chaps. 9 and 10). Accordingly, it

is reasonable to adopt the horizontal distribution of physical environments as input values for the estimation of the coral distribution.

Assuming that coral coverage at a certain point is expressed by the following equation as the sum of the multiple functions of physical data the point, then

$$F(x_1, x_2, \ldots, x_n) = c_0 + \sum_{i=1}^{n} f_i(x_i) \tag{11.1}$$

where $F(x_1, x_2, \ldots, x_n)$ stands for a function representing the estimate of coral coverage (%), c_0 is a constant, x_i signifies the ith physical data, f_i stands for a function representing the amount of coverage contribution by the ith physical data, and n denotes the number of object physical data.

These functions of physical data are selected and combined out of those regarded as affecting coral coverage. Although it is ideal that these functions are founded on a physical basis, the limited available information makes it difficult to implement such an expression. Moreover, considering that numerous physical environments are related and that coral coverage is not always expressed only with physical environments, it is unrealistic to seek such functions as a rigorous expression.

Therefore, the functions of physical data are derived statistically in this study. Some physical functions have been obtained to date as horizontal expressions using numerical simulation (Ukai et al. 2010; Murakami et al. 2013; Shimokawa et al. 2014). The functions of physical data representing coral coverage are derived statistically using these as input values.

The horizontal distribution of coral used was local observations of coral coverage obtained at 26 survey points presented in Fig. 11.1. In all, 52 measurements of coral coverage were obtained because the coral coverage was observed at two characteristic water depths, a reef edge and a reef slope, at each of the 26 observation points (Murakami et al. 2012).

The values of various physical data corresponding to each of 52 coral coverage measurements were extracted from the results of numerical simulation. A dataset including coral coverage and the values of various physical data was generated. Consequently, the function of physical data expressing coral coverage was obtained through statistical processing of these datasets.

The observation points of coral coverage were located over the mouth, center, and back of the bay according to the topographic characteristics. Coral was observed at all these points in varying sizes of coverage. However, some sites of Amitori Bay showed no coral distribution, such as sites with a large water depth from the bay mouth to the center and tidal flats at the bay head. It is fundamentally important that a function representing the coral coverage holds even at sites with no coral coverage as well as sites with coral.

Accordingly, 13 points with zero coral coverage at large depths and the bay head were added to the dataset described above. Consequently, the dataset employed for statistical processing included 65 points. Although coral coverage was classified

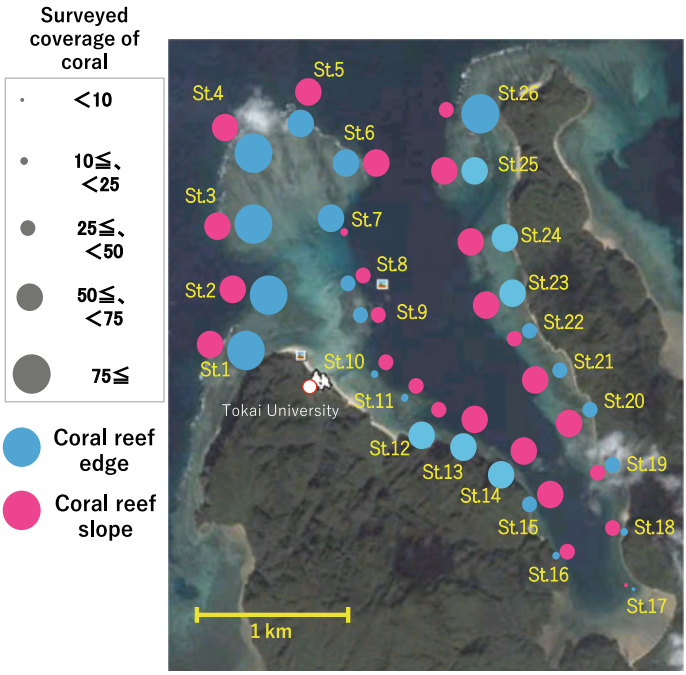

Fig. 11.1 Surveyed coverage of coral. Map data © 2015 Google (referred from Ukai et al. 2015)

according to the coral shape, this study treated the total coverage irrespective of its shape.

Physical environments to be used were limited to water depth, wave height, and turbidity (the number of floating soil particles), for simplification, by limiting the object to Amitori Bay. The influence of salinity and water temperature was removed from the objects because local observations (Murakami et al. 2011) revealed that low surface salinity concentration by inflow of freshwater from rivers and high water surface temperature by insolation would exert little effect at around the bottom on which coral was distributed. The wave height inside the bay computed from wave modification computations was used for wave height. The probability of non-exceedance was set to 5%, as obtained from time series data at each place point for six years (2008–2013) (Ukai et al. 2010) (Sect. 9.2.3 explains the computation method). The number of floating soil particles used as physical environments representing turbidity was obtained from load flow calculations and particle tracking analysis, as a result of computation at a typhoon (July 30–August 19, 2011) and a flood (September 28–October 18, 2011) (Murakami et al. 2013) (Chap. 3 presents the computation method). Values for wave height and the number of floating soil particles at the times of particular events such as typhoons were used instead of those obtained at ordinary times because the topographic characteristics of physical quantities are apt to emerge in spatial distribution at particular events

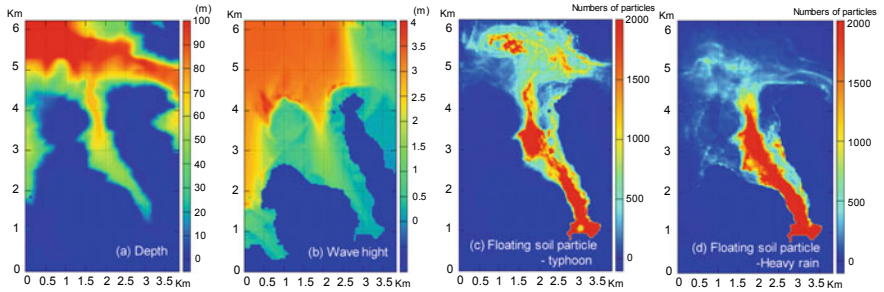

Fig. 11.2 Spatial distribution of physical environment. **a** Depth, **b** Wave hight, **c** Floating soil particle at the time of typhoon, **d** Floating soil particle at the time of heavy rain

rather than at ordinary times. Therefore, their effects on coral coverage have been clarified (Ukai et al. 2010).

Figure 11.2 presents an example of the horizontal distribution of physical data that are used. The values of physical environments at 65 points with coral coverage were extracted from this horizontal distribution and were compiled as a dataset.

11.3 Determination of Function

A dataset comprising 65 points into which coral coverage and physical data (water depth, wave height, number of floating soil particles) were compiled was subjected to statistical processing. Then, the functions of physical data that represent their influence on coral coverage were found.

The general function forms of physical data include a linear function and a quadratic function. The coefficients of these functions are calculable by the multiple regression analysis.

$$f_i(x_i) = a_i x_i^2 + b_i x_i \tag{11.2}$$

However, the influence of physical data on coral coverage might not be as simple as a linear or quadratic function; in reality, it might be more complicated. A higher-order expression by multiple regression analysis might be applied, but inappropriate association might cause harm as a ghost peak, we will only use up to a second-order expressions in this study.

We adopted a piecewise linear function as a simple function form with a high degree of freedom as a candidate. A piecewise linear function is a continuous function that is divisible into multiple sections, each of which is expressed as a linear function. Figure 11.3 depicts an exemplary graph of a piecewise linear function.

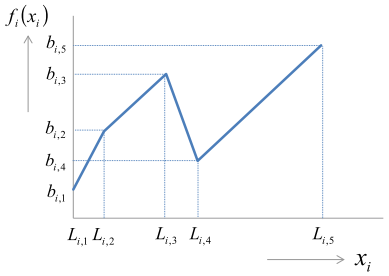

Fig. 11.3 Image of the piecewise linear function

Linear functions representing each section are given by the following equation.

$$f_i(x_i) = a_{i,j}\left(x_{i,j} - L_{i,j}\right) + b_{i,j} \tag{11.3}$$

The gradient of this piecewise linear function is given as shown below.

$$a_{i,j} = \frac{b_{i,j+1} - b_{i,j}}{L_{i,j+1} - L_{i,j}} \tag{11.4}$$

Therein, $L_{i,\,j}$ denotes a boundary value when physical environment x_i is divided into m sections. Also, $b_{i,\,j}$ expresses the value of $f_i\,(x_i)$ at the jth boundary value $L_{i,\,j}$. The gradient is given as $a_{i,\,j}$ when x_i is within a section $L_{i,\,j} \leq\ x_i < L_{i,\,j+1}$ (j = 1, 2, …, m).

Because this piecewise linear function represents the combination of a different function for each section, its coefficients cannot be defined using general methods such as the multiple regression analysis. We have evaluated the coefficients using a fundamental artificial intelligence (AI) model.

Research of AI has been conducted for some time, with efforts classified roughly into three types: neural networks that simulate the brain, expert systems that simulate the mode of thinking and decision-making of specialists, and genetic algorithms that simulate evolution. The technical fields of machine learning and deep learning, which have made remarkable breakthroughs lately, have developed modes of neural networks.

We have adopted a genetic algorithm for the present study, which is AI suitable for determining an optimum solution although a more fundamental AI model than either machine learning or deep learning. The genetic algorithm simulates the evolution of a gene and calculates an improved solution for every evolution. Herein, we describe the specific method applied to this study (Ukai et al. 2015) as reported by Morikawa (2000).

A physical function is expressed as a piecewise line divided into four sections, as presented in Fig. 11.3. The values of the five nodes are expressed by a list of numeric characters as gene information. The section division along the x-axis that gives each physical quantity is set up so that the number of data handled in each section might become equal.

The method of constructing gene information is the following. First, the value at each node is normalized into the range of −100 to 100 and is expressed with an array of a total of ten digits comprising 0 and 1. Many arbitrary setting methods are accepted. This study adopts a simple method. Because a physical function has five nodes in this case, it is expressed by 50 digits comprising 0 and 1. The estimate of coral coverage is expressed as the sum of six kinds of physical functions so that 50-gene information associated with each is connected as one digit sequence. The sequence of 300 digits comprising 0 and 1 serves as gene information. This sequence is altered in a procedure that simulates gene evolution to obtain a sequence that better fits a predetermined criterion for evaluation.

The evolutionary procedure is the following. First, 20 arrays of 300 digits comprising 0 and 1 given at random are prepared and treated collectively as one set. Each set is associated with the dataset at 65 measurement points. The values of estimated coverage and observed coverage are compared and sorted by the magnitude of the error. At this time, two sets of the largest error are discarded and replaced with two sets of genes generated by the crossover (mating) of gene information of two sets of the smallest error. Figure 11.4 expresses gene information with a sequence of digits (0, blue; 1, red). Mating is performed by exchanging gene information at a location of the digit sequence selected at random (Fig. 11.5). Furthermore, one of arbitrarily selected sequences is subjected to "mutation," by which 0 and 1 are inverted at a randomly selected part of the sequences (Fig. 11.6), and 20 offspring sets of the next generation are generated.

A piecewise linear function with a small error is obtained by repeating this procedure. Because genetic algorithms are based on accidental trials, they do not necessarily yield an optimum solution. However, the algorithms yield a plausible solution to a very complicated problem. A piecewise linear function was found in this study based on the result of one set with the smallest error during 30,000 iterations of generations.

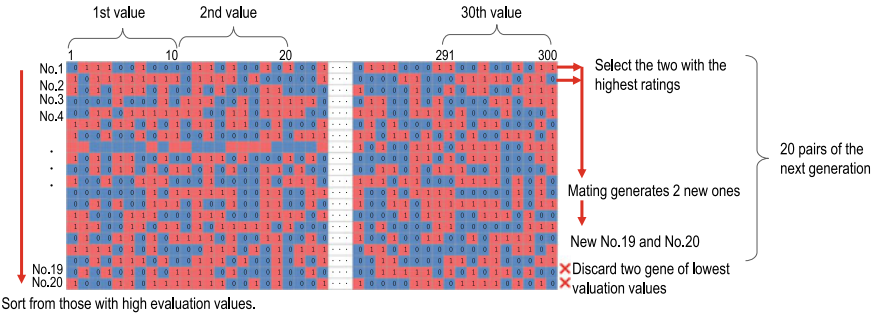

Fig. 11.4 Evolution procedure

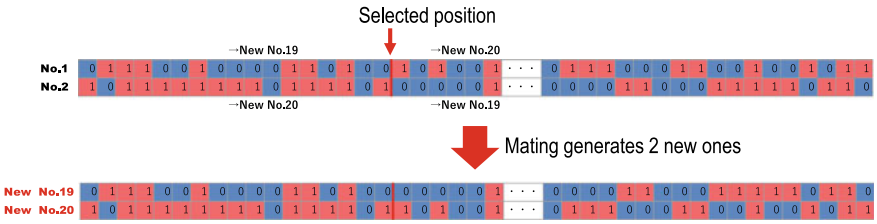

Fig. 11.5 Mating method

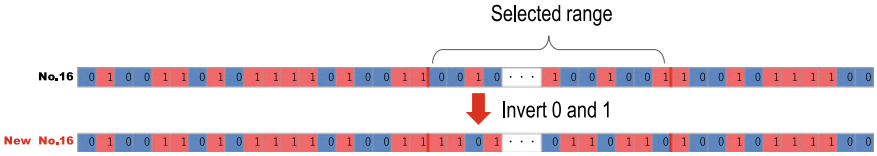

Fig. 11.6 Method of mutation

The evolutionary process of gene information is presented in Fig. 11.7, where one set consists of 20 arrays, each of which represents one function of gene information. The process from the initial random setting to 30,000 times of evolution is shown. An almost uniform state was attained after 3000 evolutions. A plausible result of estimated spatial coral distribution was obtained after 3000 evolutions from an initial random distribution, as presented in Fig. 11.8.

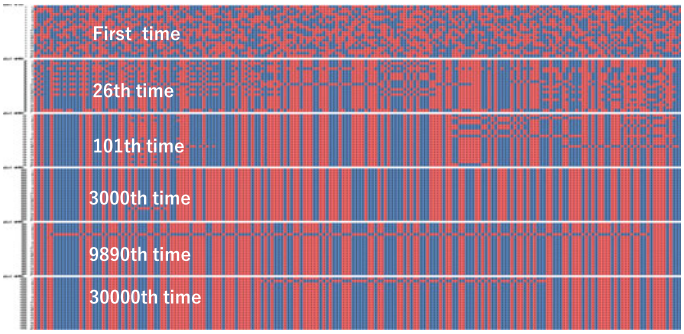

Fig. 11.7 Evolution process of genetic information

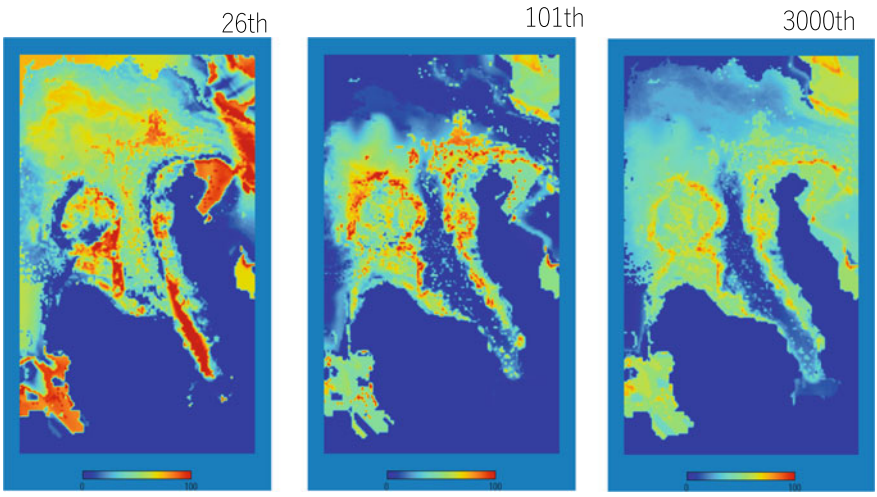

Fig. 11.8 Evolution process of estimation results of the coral horizontal distribution

11.4 Estimated Result of Coral Coverage

The degrees of association are compared between the estimated result obtained using linear and quadratic functions obtained using the multiple regression analysis and that using piecewise linear functions obtained using the AI model.

Figure 11.9 shows a correlation diagram of the estimate and observed values over the dataset at the 65 points. A quadratic function produced a better result than a linear function. A piecewise linear function produced a better result than a quadratic function, in spite of a similar trend over these three results.

Figure 11.10 presents the horizontal distribution of coral estimated using these three functions. Although these three results show a similar trend, a piecewise linear function provided the most satisfactory result as the estimate of spatial distribution. It is excellent because it assures high reproducibility of distribution at reef edges. Moreover, it yields no high ghost coral coverage in the bay head observed in the estimated result of a quadratic function.

11.5 Conclusion

We developed a technique for estimating the coral coverage distribution using numerical simulation results on physical data. Although this simple method is based on the relevance of coral coverage and physical data, a horizontal distribution that reproduces the site characteristics has been obtained well by expressing both relations using a piecewise linear function with a high degree of freedom. We

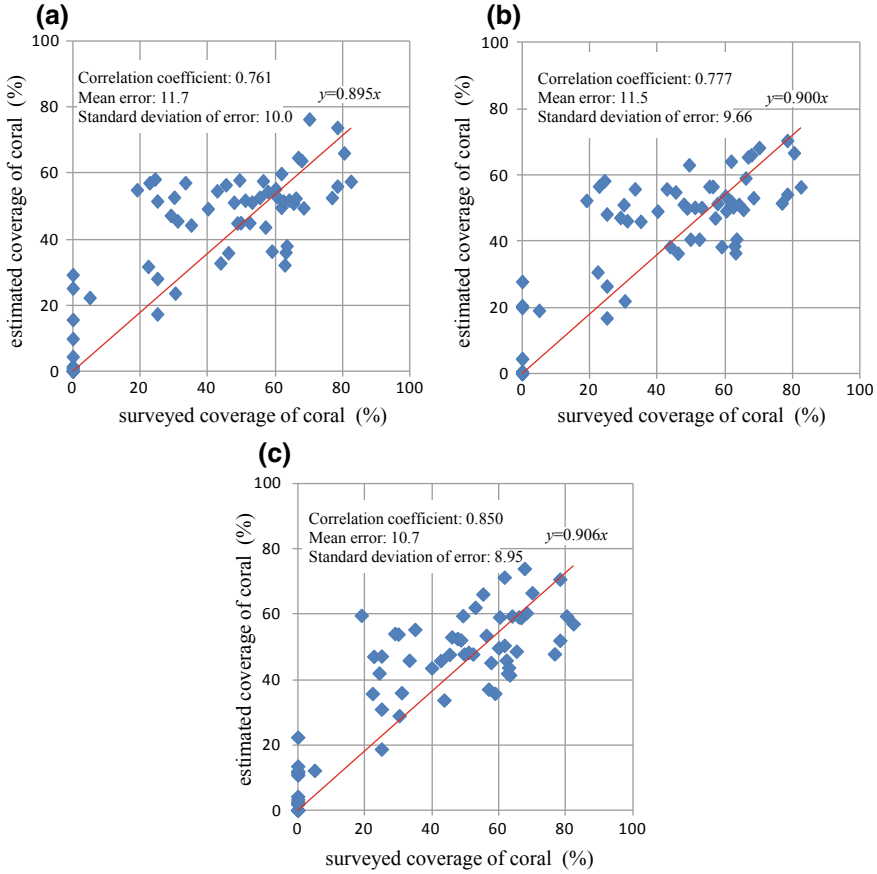

Fig. 11.9 Comparison of coral cover estimates and observed values: **a** linear function, **b** quadratic function, and **c** piecewise linear function

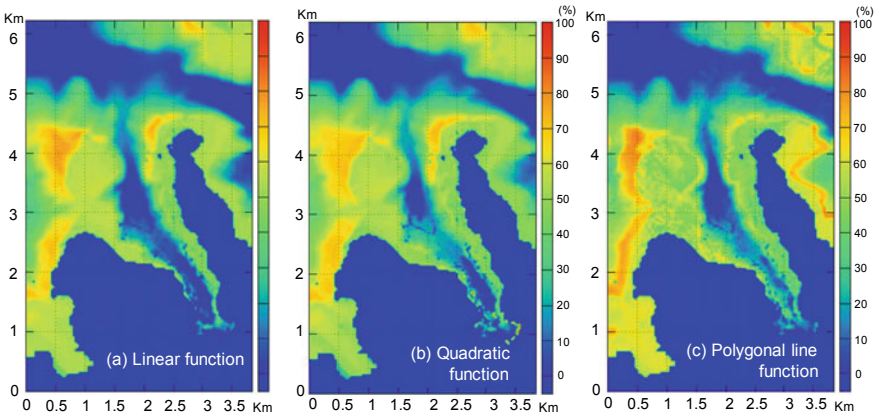

Fig. 11.10 Comparison of estimated coral horizontal distribution: **a** linear function, **b** quadratic function, and **c** piecewise linear function

expect that this method, if used considering more physical environments, can support an investigation of the changing trends of coral coverage distribution that occur along with the changes occurring in various physical data.

Acknowledgements We thank the staff of Tokai University, Mr. Kazuho Hiroshima and Ms. Naho Tanaka of Tokai University graduates 2011 for their help.

References

Morikawa Y (2000) Brain of a matchbox (AI)—a story of useful artificial intelligence, Shinkigensya, Tokyo, p 221 (in Japanese)

Murakami T, Mizutani A, Ukai A, Nakase K, Shimokawa S, Kohno H (2011) Observation of water temperature and salinity by portable multi-item water quality meter in Amitori Bay, Iriomote Island, Japan. The study review of Iriomote Island (Okinawa Regional Research Center, Tokai University), pp 61–66

Murakami T, Ukai A, Kohno H, Mizutani A, Shimokawa S, Nakase K, Noguchi K, Yasuda T (2012) Relationship between distributions of corals and physical environments in Amitori Bay, Iriomote Island, Japan. J Japan Soc Civil Eng B3(68):1133–1138. https://doi.org/10.2208/jscejoe.68.I_1133 (in Japanese with English abstract)

Murakami T, Ukai A, Noguchi K, Kohno H, Murakami A, Simokawa S, Nakase K, Yoshino J (2013) Numerical analysis of sediment transport in Amitori Bay, Iriomote Island, Japan. J Japan Soc Civil Eng B3(69):928–933. https://doi.org/10.2208/jscejoe.69.I_928 (in Japanese with English abstract)

Shimokawa S, Murakami T, Ukai A, Kohno H, Mizutani A, Nakase K (2014) Relationship between coral distributions and physical variables in Amitori Bay, Iriomote Island, Japan. J Geophys Res: Oceans 119:8336–8356 (https://doi.org/10.1002/2014jc010307)

Ukai A, Kohno H, Nakase K, Shimaya M, Zinno M, Kimura K (2010) Influence of ocean waves on coral habitat environment of Amitori Bay. Ann J Civil Eng Ocean 26:363–368 (in Japanese with English abstract)

Ukai A, Murakami T, Mizutani A, Nakase K, Shimokawa S, Kohno H (2015) Estimation technique of spatial coral distribution in Amitori Bay, Iriomote Island, Japan. J Japan Soc Civil Eng B3(71):963–968. https://doi.org/10.2208/jscejoe.71.I_963 (in Japanese with English abstract)

Chapter 12
Distribution of *Enhalus acoroides* According to Waves and Currents

Kota Nakase, Tomokazu Murakami, Hiroyoshi Kohno, Akiyuki Ukai, Akira Mizutani and Shinya Shimokawa

Abstract *Enhalus acoroides*, tropical sea grass also known as tape grass, is distributed throughout the Yaeyama Islands. It is listed as a vulnerable species (VU) on the Red List of the Ministry of Environment of Japan. Because this species is known to have poor seed dispersal characteristics, necessary conditions of its distribution must be elucidated to support its preservation. We have compared the present community distribution of *E. acoroides* with the horizontal distribution of numerically reproduced wave height and bottom velocity. Moreover, we have derived the conditions of water depth, waves, and bottom velocity required for the formation of *E. acoroides* distribution. The periphery of distribution of communities was determined using external forces during a high-wave period such as a typhoon period or a winter monsoon period.

Keywords *Enhalus acoroides* · Wave height · Bottom velocity · Physics simulation

This chapter is based on works reported by Nakase et al. (2015, 2016).

K. Nakase (✉) · A. Ukai
Environment Business Division, Penta-Ocean Construction. Co., Ltd., Tokyo, Japan
e-mail: kouta.nakase@mail.penta-ocean.co.jp

T. Murakami · S. Shimokawa
Storm, Flood and Landslide Research Division, National Research Institute for Earth Science and Disaster Resilience, Tsukuba, Japan

H. Kohno · A. Mizutani
Okinawa Regional Research Center, Tokai University, Yaeyama, Japan

S. Shimokawa et al. (eds.), *Geophysical Approach to Marine Coastal Ecology*, Springer Oceanography, https://doi.org/10.1007/978-981-15-1129-5_12

12.1 Introduction

Enhalus acoroides, tropical sea grass with a leaf width of 1–1.5 cm and grass height of 70 cm–1 m (Sect. 1.5), is distributed throughout tropical shallow sea areas of gravel and silt, especially near the equator. The northern limits of its distribution are the coasts of Ishigaki and Iriomote Islands of the Yaeyama Islands, Japan, reported Kuo et al. (2006). However, the large-scale decline and extinction of *E. acoroides* communities have been reported by Takeyama et al. (2014) recently in northwest sea areas of Iriomote Island (see Sects. 1.1 and 1.2, and Fig. 1.1). In fact, it is listed as a vulnerable species (VU) on the Red List published by the Ministry of the Environment, Government of Japan (2018).

Actually, *E. acoroides* has stages of blooming and fructification which differ from those of other sea grasses. The plants are characterized by their epihydrogamy and sinking and rising of seeds. Kuo et al. (2006) reported the distribution and ecology of *E. acoroides* as follows.

It blooms during September–January and fructifies all year round, except in July–August. Communities with grass height of 50 cm with spikes have been observed in Sakiyama Bay and Amitori Bay of Iriomote Island, although the plants sometimes form non-reproducing communities near Ishigaki Island. Only a few plants are alive in Amitori Bay today.

Lacap et al. (2002) reported that *E. acoroides* expands its community by seed dispersal with currents presumably. However, as Murakami et al. (2014) reported that the computed mean migration length of seeds by numerical reproduction of flow conditions indicates short migration distances of seeds, almost equivalent to the community size. This result agrees with reports by Nakajima et al. (2013) related to population genetics analysis using microsatellite markers in the northwest sea area of the Philippines. Reportedly, the frequency of long-distance dispersal of seeds and fruits of *E. acoroides* is low because *E. acoroides* exhibits large genetic divergence between points within a 15-km range (i.e., it has low mobility).

The stability of bottom sediment under waves and tidal currents is known to affect the distribution of sea grass communities over shallow coastal sites. Such approaches include studies of Maruyama et al. (1987) and Koch et al. (2006).

Nakase (2000) and Kanazawa and Mori (2003) have evaluated the distribution of eelgrass (*Zostera marina*) and typical sea grass in Japan using wave and current simulations.

However, few studies evaluate the physical conditions, such as waves and currents, for *E. acoroides*, which include current velocity measurement with suspended solids drifted inside and outside of a community by Rollon (1998), and measurement of the flow velocity distribution within a community using plaster balls by Komasu et al. (2004).

Accordingly, we have tried to extract the closed vegetation distribution conditions of *E. acoroides* by direct comparison for every computational mesh between the distribution range of *E. acoroides* communities in the northwest sea area of

Iriomote Island and the reproduction result of distribution of physical conditions such as waves and currents using numerical computation.

It is difficult for *E. acoroides* with poor dispensability to achieve spontaneous regeneration rapidly once its community becomes extinct. Transplantation or inoculation might be necessary for revitalization of communities. It is necessary to clarify the distribution status and growth environment conditions of *E. acoroides* to discuss its preservation.

The Yaeyama Islands are often struck by typhoons; high-wave conditions occur there every year. Furthermore, northwestern monsoons and high waves arrive daily in winter. Accordingly, waves are regarded as strongly affecting *E. acoroides* community formation in northwestern sea areas of Iriomote Island.

Measuring the horizontal distribution of wave height and current velocity over a wide area of a coast extending for tens of kilometers is difficult in terms of both workload and cost. Accordingly, their horizontal distribution was obtained by numerical simulation and was compared with the actual distribution of *E. acoroides* communities. The physical conditions of the distribution sites of *E. acoroides* were extracted.

12.2 Distribution Information of *Enhalus acoroides* at Western Sea Areas of Iriomote Island Used for Examination

Distribution survey of *E. acoroides*, measurements of external force, and numerical computations were carried for the northwestern coast of Iriomote Island, the Yaeyama Islands, Okinawa Prefecture (Fig. 12.1).

The closed vegetation distribution status 2013, compiled based on the survey results of *E. acoroides* distribution by undergraduate and graduate students of School of Marine Science and Technology, Tokai University, as graduation research in July–October 2013 along the coastline of 45 km long from Urauchi Bay to Sakiyama Bay in the northwest of Iriomote Island, was used as the distribution information of *E. acoroides*. These results were compiled by Takeyama et al. (2014). The presence of distribution, coverage, and grass height of *E. acoroides* was investigated with a line transect by the manta tow survey, in which an observer's boat was towed by a ship, and the coordinates at the respective peripheries of communities were identified using GPS in this survey.

Survey results published by the Environment Agency, Japan (1997), were employed to show the past community distribution status. This survey was administered by reading the distribution ranges of submarine forests in aerial photographs taken in 1977.

For comparison of survey results of community distributions with physical conditions, *E. acoroides* distributions were expressed on a computational mesh (50 m × 50 m) used for the numerical simulation of waves and currents.

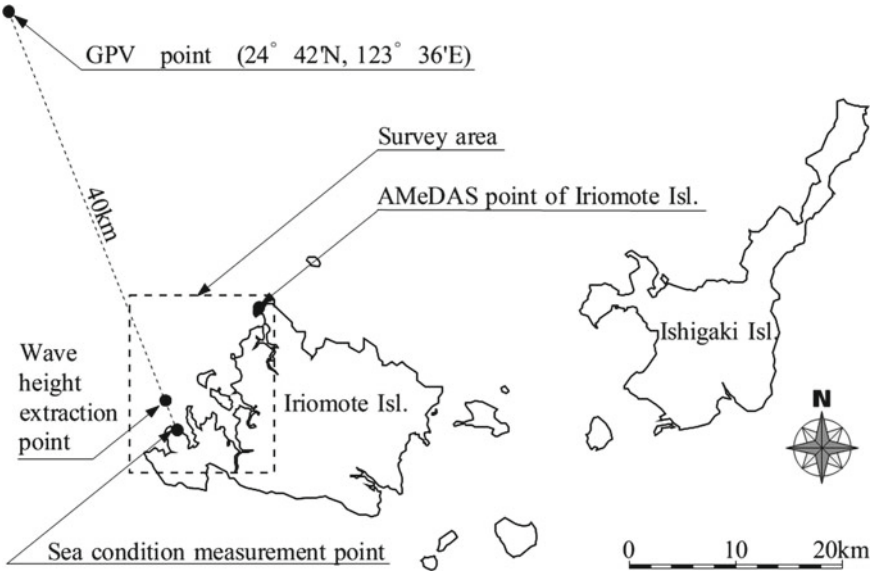

Fig. 12.1 Investigation site, Iriomote Island in Yaeyama Islands (referred from Nakase et al. 2015)

12.3 Reproduction Calculation of Physical Conditions of the Distribution Range of *Enhalus acoroides*

(1) Ascertaining weather and oceanographic conditions.

The horizontal distribution of numerically reproduced physical data should be compared with actual measurements. Accordingly, a current meter with an attached wave height meter was placed at 2 water depth points (10 and 20 m) in Amitori Bay, Iriomote Island, into which waves would enter from the open sea, and in which continuous observations of a total of four signals, including a water level, hydraulic pressure, and two components of current velocity, were conducted (for 20 min on the hour) during about one year and three months: July 2008–October 2009. The grid point data (GPD) of coastal wave model (CWM) (every 3 h) based on mesoscale model (MSM) data provided by Japan Meteorological Agency at about 40 km off the setting position of the wave height meters (Fig. 12.1) were used as offing wave conditions to be compared with measurements.

(2) Reproduction calculation of waves and currents.

The wave and current distributions were reproduced using Simulating WAves Nearshore (SWAN), a wave model for shallow water by Booij et al. (1996) (Chap. 3). The parameters to be reproduced were wave height, bottom velocity, and tidal residual currents.

Wave height, a physical force acting directly on *E. acoroides* grass bodies, is a force that damages sea grass directly. In the long run, it also contributes to the formation of geographical features and bottom sediment.

Actually, the mean bottom velocity, the root-mean-square of the amplitude of oscillating current velocity, represents substantial maximum amplitude. It is a physical force that influences the bottom sediment stability of *E. acoroides* distribution sites.

Mean tidal residual current velocity represents not high tidal current velocity but the difference of flow velocity at a high tide and low tide. Its large value implies that water mass is moving in a certain direction, i.e., the degree of passage. It thereby enables us to evaluate particle deposition characteristics indirectly.

Details of the computation method of significant wave height and bottom velocity are given by Booij et al. (1996). Weather conditions and the wind state used for computation were obtained by AMeDAS and GPD wind state data of Japan Meteorological Agency. Tidal residual currents, which reflect the influence of tides, were computed using the ocean model CCM by Murakami et al. (2004) (Chap. 3).

12.4 Correspondence of *E. acoroides* Distribution with External Force Distribution

To ascertain whether the *E. acoroides* distribution can be inferred from waves or currents by comparison with the external force distribution, we numerically reproduced the wave height, bottom velocity, and tidal residual current distribution using the wind state on January 14–18, 2013, and the tide during December 30, 2012–January 4, 2013, regarded as typical winter conditions, with wind direction and velocity data at the AMeDAS Iriomote Island observation point in December 2012–March 2013 for reference.

Surmising that the *E. acoroides* distribution could not be evaluated solely using a single physical parameter, we sought a combination of physical parameters that would be appropriate to interpret the *E. acoroides* distribution using the above-described *E. acoroides* distribution survey results from 2013 and the numerically reproduced external force at high waves in winter 2012–2013, using logistic regression analysis. We examined which combination of parameters would be sufficient to distinguish the presence of a distribution clearly using the presence of the *E. acoroides* distribution as an objective variable.

Next, the season with the most appropriate oceanographic conditions for evaluating the *E. acoroides* distribution was found by computing the time series of the horizontal distribution of wave height and the bottom velocity over the survey area for waves during January 1–31 December, 2015, using the method described above with GPD and AMeDAS data as input conditions.

A virtual offing wave height extraction point was set up at a depth point of 118 m in the offing of Amitori Bay to find the occurrence of weather events such as a typhoon and stormy weather and high-wave durations during monsoons. This point was defined as a "high-wave period" when the wave height was not less than 1 m and as a "calm period" otherwise in each month. External force was reproduced numerically using the following procedures. The hourly averages of wave height and bottom velocity for each mesh were obtained at both a "high-wave period" and a "calm period" of each month. Then, the arithmetic means of these averages over a month (720 h. if 30 days) were computed as the averages of the month. The correspondence was examined between the horizontal distribution of the reproduced external force for each month and the presence of distribution of *E. acoroides* communities. The mean ± standard deviation of each parameter of a mesh in which *E. acoroides* was present was extracted at this time. This range was defined as the estimated range of the *E. acoroides* distribution.

Then, computational meshes with the values of wave height and velocity falling within this estimated distribution range were extracted using the computational results of the external force. The fraction of meshes with the presence of sea grass presumed was defined as community reproducibility. Appropriate wave conditions for the evaluation of *E. acoroides* were examined.

12.5 Results and Discussion

(1) Distribution of *E. acoroides*

The community distribution range obtained from a graduation research project conducted for Tokai University in 2013 and a community distribution range confirmed in the northwest sea area of Iriomote Island based on aerial photography in 1977, published by the Environment Protection Agency in 1997, were expressed on a mesh (50 m × 50 m) used for reproduction calculation of external force (Fig. 12.2). The distribution range in 2013 had shrunk compared with that in 1977.

(2) Wave observation.

The situation in summer (July–October 2008) and winter (January–March 2009) of the monitored significant wave height ($H_{1/3}$) and the GPD (every 3 h.) are presented (Fig. 12.3).

The wave height was low on the coast where *E. acoroides* survived, even at high waves offshore. The wave height on the coast conformed to that of offshore waves by GPD.

Although the wave height was usually high in winter during October–March, the maximum wave heights observed during the observation period were recorded when typhoons struck: 1.25 m in the bay and 10.5 m offshore (by GPD).

The occurrence of offshore wave direction by the GPD obtained during the observation period and wind direction at the meteorological observation point in

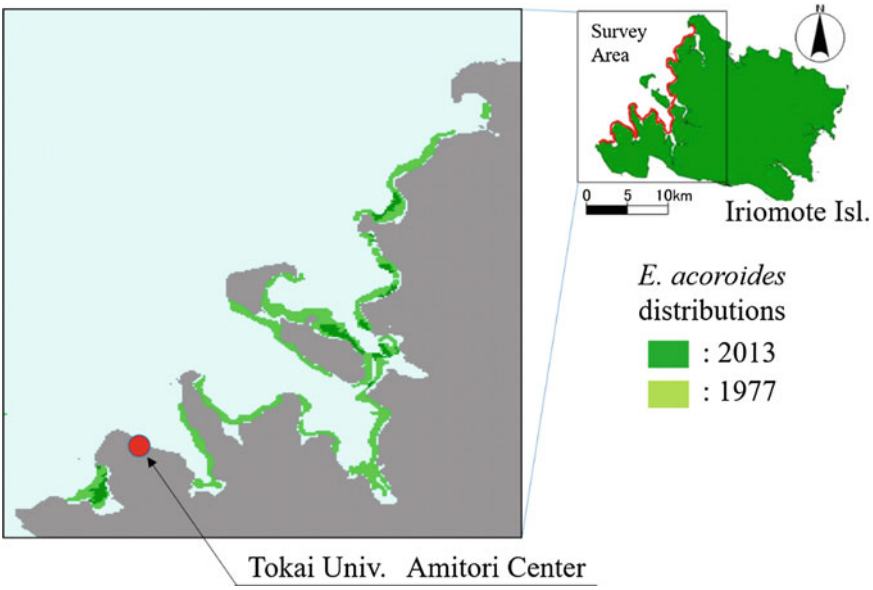

Fig. 12.2 Distributions of *E. acoroides* off northwestern Iriomote Island (referred from Nakase et al. 2015)

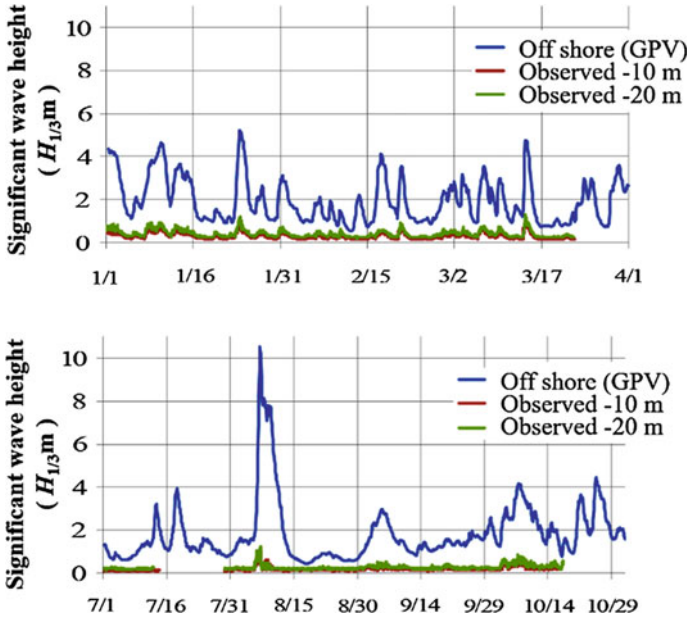

Fig. 12.3 Extracted wave condition in Amitori Bay off the northwestern coast of Iriomote Island (referred from Nakase et al. 2015)

Iriomote Island in 2008 (AMeDAS) (Fig. 12.4) suggest that the wind direction during October–March was almost along NE–NNE because of the winter monsoon, but a S–SSW component was also observed in April–September as a result of typhoons. The strong wind direction varied along with the course of a typhoon.

(3) Numerically reproduced external force distribution.

Figure 12.5 presents results reproduced from calculations of wave height, bottom velocity, and tidal residual current at the spring tide obtained based on local measurement results of wave conditions and GPD, using high-wave conditions usually observed at the northwest coast of Iriomote Island in winter. This figure also displays water depths and the location of communities confirmed by Tokai University in 2013.

High waves from the offing are reduced by coral reef edges at depths of 10 m or less. The mean bottom velocity is large at reef edges because high waves turn into flows when they are damped abruptly. The mean tide residual current velocity is high at straits between islands, capes, and the offshore side of reef edges. These are generally regarded as sites of good passage.

We extracted and identified 268 meshes with distribution of high-density communities confirmed from a line transect survey from 378 meshes with confirmed *E. acoroides* distribution. They were expressed in the scatter diagram of each physical parameter according to water depth. Meshes with *E. acoroides* distribution were concentrated on a specific part of the data dispersal region (Fig. 12.6).

The numbers of meshes with an *E. acoroides* distribution are shown in histograms according to the water depth and wave height, bottom velocity, and residual current velocity reproduced by numerical computation (Fig. 12.7). Table 12.1 presents the means and standard deviations of the respective parameters

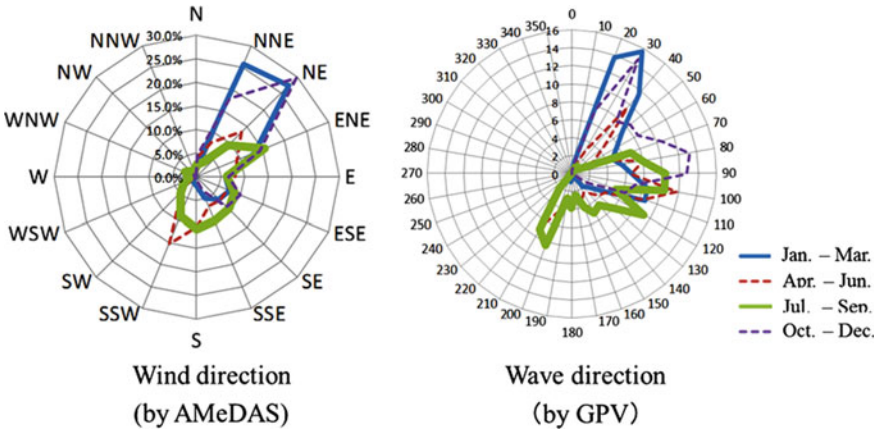

Fig. 12.4 Annual wave and wind directions off the northwestern coast of Iriomote Island (referred from Takeyama et al. 2014)

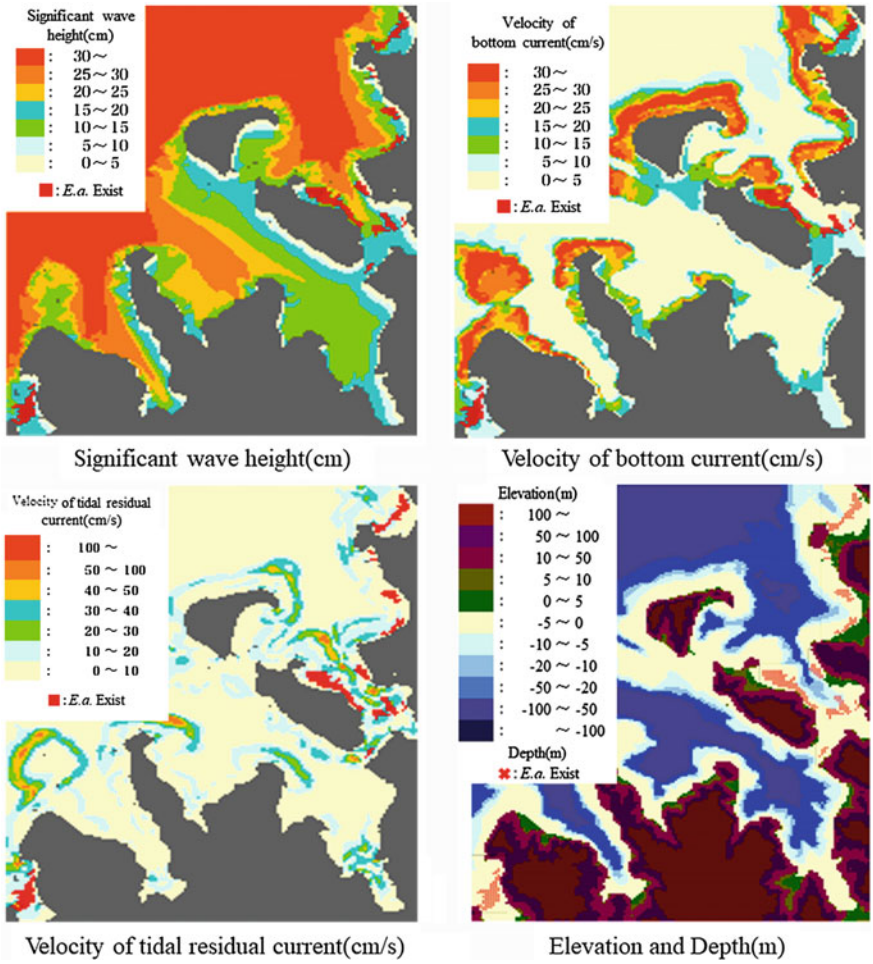

Fig. 12.5 Horizontal distribution of physical parameters duplicated by numerical simulation in typical winter high-wave conditions (referred from Takeyama et al. 2014)

in meshes with the *E. acoroides* distribution and meshes with the distribution of high-density communities.

The numbers of meshes with *E. acoroides* distribution obtained here are based on the reproduction calculation of a certain period in winter. Reproduction calculations yield different results depending on the computational conditions that are used. Whether the values obtained here are reasonable must be verified according to variation of the external force throughout the year.

(4) Seasonal conditions suitable for evaluating *E. acoroides*.

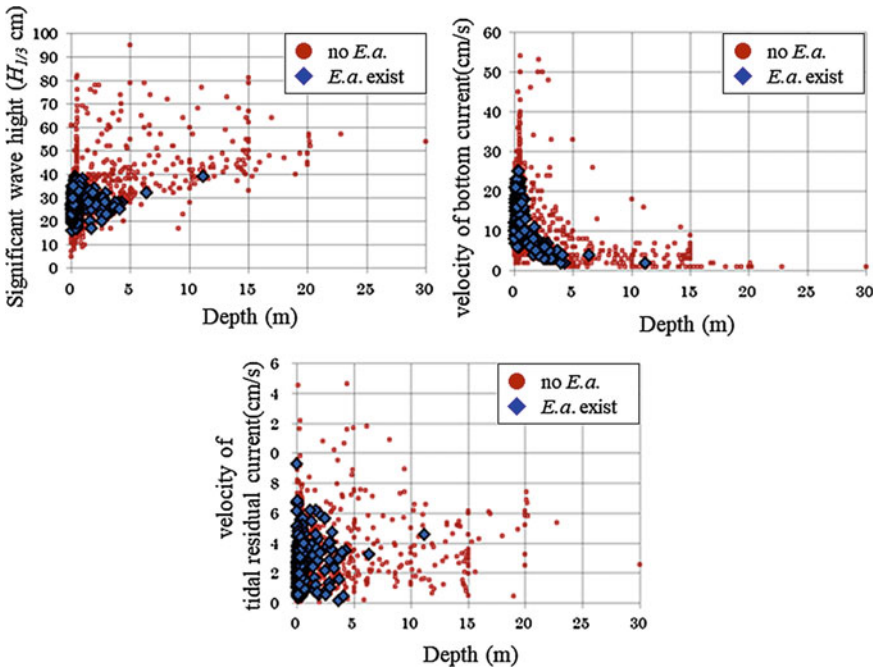

Fig. 12.6 Scatter plots of depth and each physical parameter, *E.a.*, exist (referred from Nakase et al. 2015)

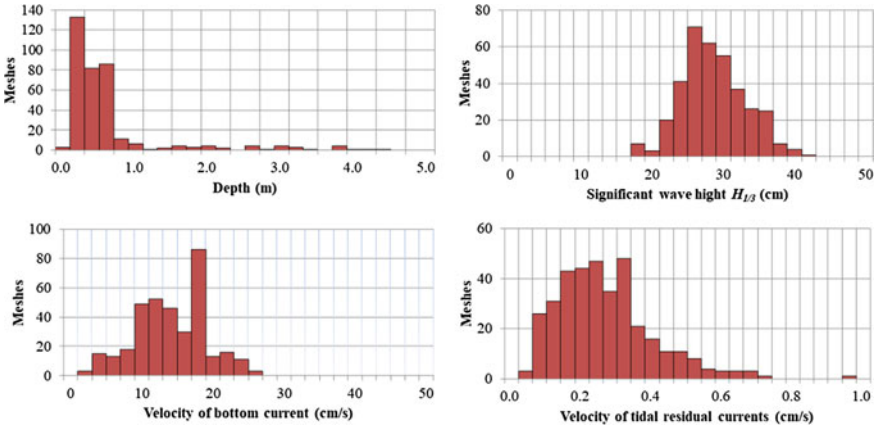

Fig. 12.7 Histograms of depth and physical parameters in meshes with *E. acoroides*

Parameters used for evaluating the *E. acoroides* community distribution include water depth and the numerically reproduced wave height, bottom velocity, and tide residual current velocity. Logistic regression analysis was conducted to ascertain a

Table 12.1 Average and SD of each parameter for meshes with *E. acoroides* (referred from Nakase et al. 2015)

	Unit	Existing		High density	
		Average	SD	Average	SD
Depth	m	−0.56	0.93	−0.41	0.35
Significant wave height ($H_{1/3}$)	m	0.28	0.05	0.28	0.04
Velocity of bottom current	cm/s	13.39	4.73	15.26	3.44
Velocity of tidal residual current	cm/s	0.24	0.13	0.19	0.08
Number of meshes		355		268	

suitable combination of them to interpret the community survival, by letting the presence (1) and absence (0) of *E. acoroides* distribution in a mesh be an objective variable and using the combination of water depth and numerically reproduced wave height, bottom velocity, and tide residual current velocity. Results show that logistic regression by the wave height and bottom velocity is sufficient for clear distinction between the presence and absence of *E. acoroides* (Fig. 12.8). Therefore, we chose to employ the wave height and bottom velocity for monthly evaluation.

(4) Monthly evaluation according to wave conditions.

The time series of the horizontal distribution of significant wave height and bottom velocity was computed in the survey area for one year during January 1 through

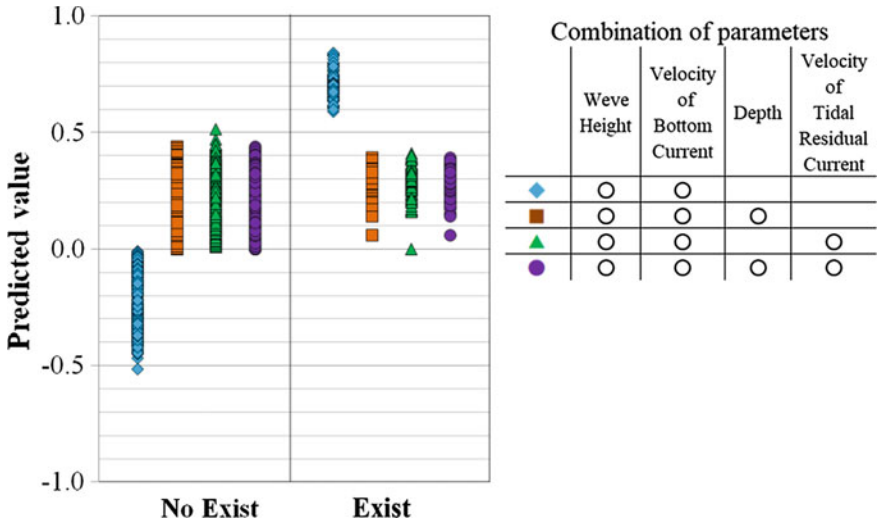

Fig. 12.8 Combination of parameters by logistic regression analysis (referred from Nakase et al. 2016)

December 31, 2015, using the SWAN wave model as numerically computed physical conditions.

(a) Other wave conditions.

The time series variation of daily mean significant wave height from January 1 through December 31, 2015, extracted at the extraction point of offshore waves presented in Fig. 12.1 by reproduction calculation is expressed in Fig. 12.9.

The sea area concerned is in a high-wave period in winter during December–March and is in a calm period in summer during May–September, except when a typhoon strikes. A large-scale typhoon struck on August 6–8, 2015. The maximum hourly mean significant wave height of 4.9 m was recorded at the time of this typhoon as the annual maximum wave height.

(b) Horizontal distribution of numerically reproduced external force of average in each month.

Figure 12.10 presents part of a monthly averaged horizontal distribution of numerically reproduced significant wave height. This figure shows monthly total average and average of monthly high-wave condition. August and December are high-wave seasons. June is the calmest month. In June, high-wave conditions of $H_{1/3} > 1.0$ m at an offshore wave extraction point are not observed. The SWAN wave model outputs the hourly average of wave height and bottom velocity for each mesh. They were averaged arithmetically over one month (720 h. if 30 days) as the monthly averages.

As for monthly mean significant wave height, the annual mean significant wave height was 0.17 m. The mean significant wave height in a high-wave period with wave height not lower than 1 m at an offshore wave extraction point was 0.31 m, in meshes with the *E. acoroides* distribution (2013) (Fig. 12.11). The monthly mean significant wave height in August with many typhoon attacks was 0.13 m, smaller than annual mean significant wave height of 0.17 m, whereas the mean significant

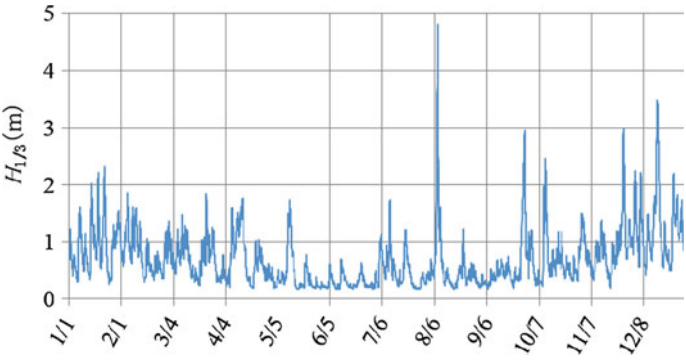

Fig. 12.9 $H_{1/3}$ at GPD point in 2015 (referred from Nakase et al. 2016)

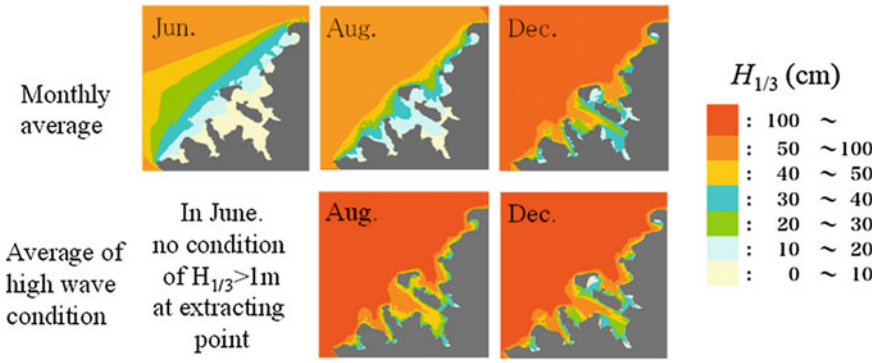

Fig. 12.10 Horizontal distribution of $H_{1/3}$ in June, August, and December of monthly average and average of high-wave condition (referred from Nakase et al. 2016)

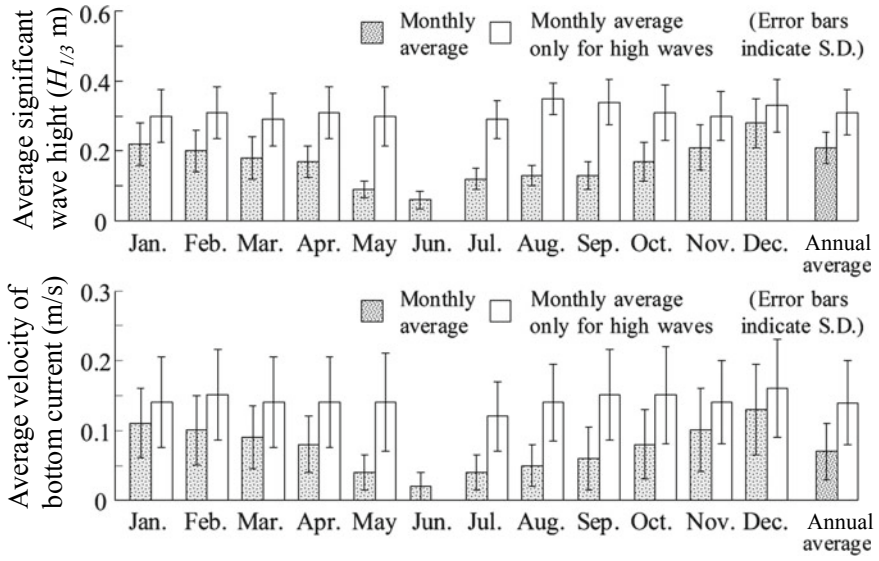

Fig. 12.11 Monthly average of $H_{1/3}$ and bottom current velocity of meshes, *E. acoroides* (referred from Nakase et al. 2016)

wave height at high waves in August was 0.35 m, reflecting the strong influence of typhoons.

The monthly mean significant wave height was 0.28 m in December with continuous high waves, almost as high as the mean significant wave height for high waves of 0.33 m, under the continuous conditions of high waves. The averages of

significant wave height $H_{1/3}$ at high waves and bottom velocity in meshes with *E. acoroides* community distribution showed little monthly variation: $H_{1/3} \approx 0.3$ m and bottom velocity ≈ 0.15 m. However, their monthly averages including a calm period indicated monthly fluctuations. They were significantly smaller in May–July. The mean and standard deviation of the significant wave height and bottom velocity in meshes with *E. acoroides* distribution were the calmest in June and in August and December during high-wave periods. Their annual means are presented in Table 12.2.

The distribution of *E. acoroides* was reproduced using the mean ± standard deviation of wave height and bottom velocity obtained here based on numerically reproduced in August and December (Fig. 12.12).

A distribution range reproduced for August in a high-wave situation with typhoons was quite narrower than that reproduced using the average of August because August is in a calm period except for the time of typhoon attacks.

Because December was in a high-wave period, the external force at high waves and that of the monthly average were almost equal. The reproduced range of the *E. acoroides* distribution was similar. The possible range of the *E. acoroides* distribution according to the conditions of August was narrower than in December if evaluated under the same high-wave conditions. Although little difference was found in the averages of significant wave height and bottom velocity in August and

Table 12.2 Average and SD of significant wave height and velocity of bottom current, meshes with *E. acoroides* in some conditions (referred from Nakase et al. 2016)

Condition			Significant wave height (m)		Velocity of bottom current (m/s)		Comment
			Average	SD	Average	SD	
Calm period	June	Total average	0.06	0.03	0.02	0.02	No high-wave conditions
High-wave period	August	Total average	0.13	0.05	0.05	0.06	A typhoon passed
		During high waves	0.35	0.07	0.14	0.06	
	December	Total average	0.27	0.07	0.13	0.06	High waves by seasonal wind continue
		During high waves	0.33	0.08	0.16	0.07	
Annual average		Total average	0.17	0.05	0.07	0.04	Overall average of the year
		During high waves	0.31	0.07	0.14	0.06	

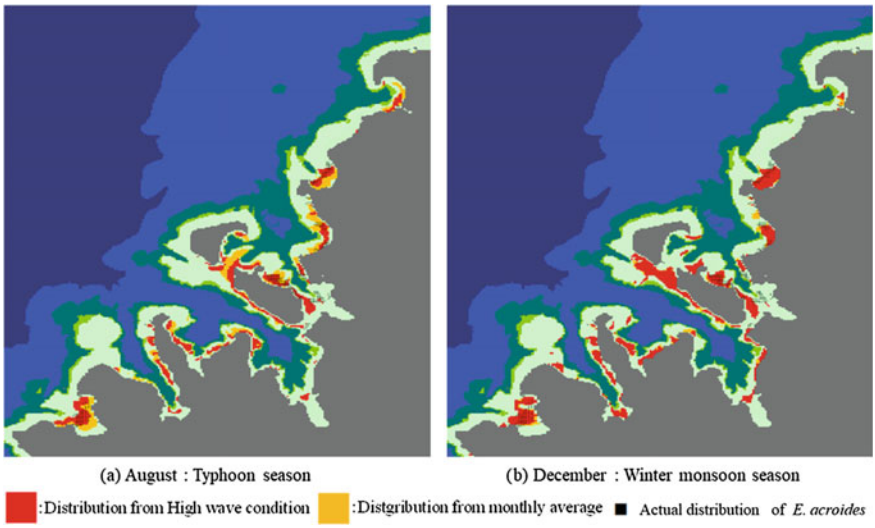

Fig. 12.12 *E. acoroides* distribution, reproduced from wave and flow simulation (referred from Nakase et al. 2016)

December (Table 12.2), waves from south–southwest were active in August, but scarce in December of the period under the influence of winter monsoon (Fig. 12.5). They enhanced the external force on areas facing southwest, thereby further restricting the range of meshes of possible *E. acoroides* distribution.

The mean ± standard deviation of physical parameters of each mesh with sea grass in 2013 was applied to the survey mesh. A mesh with presumed but no actual *E. acoroides* distribution was designated as an error mesh. Only about 60% of meshes with real community distribution were reproduced in any cases. The error meshes unable to reproduce a distribution range were evidently fewer during high-wave periods (Fig. 12.13).

High waves caused by typhoons are capable of damaging an entire community all at once. The sparse *E. acoroides* distribution on the shores or the inner part of bays directly facing southwest in the southwest coast of Iriomote Island at the present implies that high typhoon waves destroyed the *E. acoroides* communities. Accordingly, it is considered appropriate to adopt data at the occurrence of events such as a typhoon when the largest waves act during a year in the evaluation of *E. acoroides* distribution using numerically reproduced external forces.

The wave distribution should be reproduced for each season of various events such as a typhoon, and high waves occur during the winter when high waves from the northwest act continuously and during the typhoon season, when waves arrive also from southwest. Such seasons should be considered when determining wave conditions in which *E. acoroides* communities can survive.

The magnitude of external force was uniform throughout the year, with significant wave height $H_{1/3} \leq 0.3$ m and bottom velocity ≤ 0.15 m irrespective of

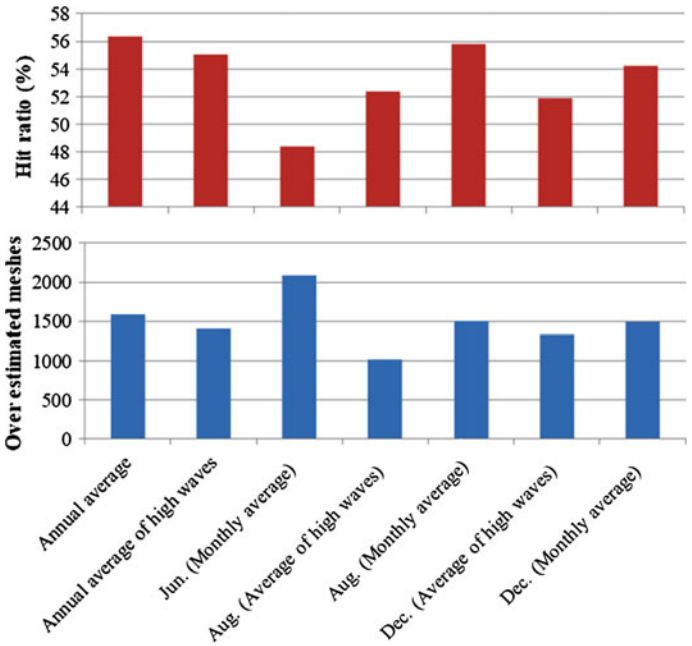

Fig. 12.13 Recall condition of *E. acoroides* distributions (referred from Nakase et al. 2016)

season. Waves beyond this magnitude might influence the bottom sediment through which *E. acoroides* extends its underground stems. These values were close to those acquired for the high-wave period in winter.

The presumed *E. acoroides* distribution range based on these physical conditions is broader than the actual distribution range. However, physical conditions determine only the outer boundary of a range inside which *E. acoroides* can survive, and determine the location in the possible physical distribution range a community is formed. That location is regarded as depending on various factors such as feeding damage and interspecies competition.

Finally, communities observed in 1977 were compared with those investigated in 2013 using the situation in a high-wave period in August. The number of meshes with an *E. acoroides* distribution decreased by 2296 during these 36 years: from 2674 to 378. Therefore, meadows equivalent to 574 ha disappeared: One mesh corresponds to 0.25 ha. The extinct area is expressed outside a plot group designated by wave height and bottom velocity at surviving communities in 2013 (Fig. 12.14). If the center portion of the plot group is assumed as the optimal range of distribution, then it can be inferred that communities were not able to be sustained any longer in areas where *E. acoroides* had "struggled" for survival.

Because Iriomote Island has undergone few artificial disturbances, communities have decreased in number strictly through natural causes. These causes are unknown at present, but are suspected to include feeding damage by *Chelonia mydas*, suggested by Takeyama et al. (2014).

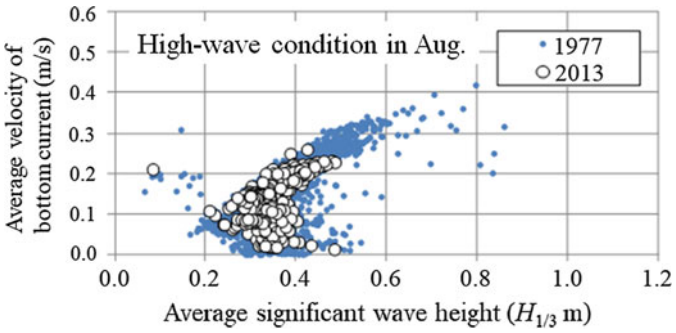

Fig. 12.14 Scatter plots of waves and currents, *E. acoroides*, exist in 1977 and 2013 (referred from Nakase et al. 2016)

12.6 Conclusion

Distribution of *E. acoroides* along about 40 km of the northwestern coast of Iriomote Island, the northern limit of its distribution, was evaluated by reproduction calculation of waves and currents. Numerical computation is a realistic approach to elucidating the wave height distribution over a wide sea area.

Large wave height and high bottom velocity are suitable for expressing the *E. acoroides* distribution among parameters obtained by numerical computation. It is desirable to adopt cases in which the waves of the annual maximum wave height are active, for example, when a typhoon strikes, as input conditions of numerical computation.

Computation with these conditions suggests that *E. acoroides* can survive to sustain the distribution physically in a range of $H_{1/3} \leq 0.3$ m and with bottom velocity ≤ 0.15 m under the largest waves of the year. Average water depth conditions were −76 cm in the possible distribution ranges and −41 cm in the dense distribution ranges.

The distribution range inferred from physical conditions was quite broader than the actual distribution range. The actual distribution of *E. acoroides* is affected by other factors within the physically possible distribution range.

Acknowledgements The authors extend their deepest gratitude to undergraduate and graduate students of the School of Marine Science and Technology, Tokai University, for their great endeavors on the surveillance study of *E. acoroides*.

This study has been conducted under joint research by Okinawa Regional Research Center of Tokai University, National Research Institute for Earth Science and Disaster Resilience, and Penta-Ocean Construction Co. Ltd.

References

Booij N, Holthuijsen LH, Ris RC (1996) The SWAN wave model for shallow water. In: Proceedings of 25th international conference on coastal engineering, vol 1, pp 668–676

Environment Agency Japan (1997) In: Environment Agency Japan (ed) Tidal flats, algal and sea-grass beds and coral reefs in Japan, vol 2. http://www.biodic.go.jp/reports/4-12/r00a.html. 15 July 2019 (in Japanese with English abstract)

Kanazawa T, Mori S (2003) Application of the Zostera bed creation method by sowing sheet. Ann J Coast Eng 50:1266–1270 (in Japanese)

Koch EW, Ackerman JD, Verduin J, van Keulen M (2006) Fluid dynamics in Seagrass ecology—from molecules to ecosystems. In: Larkum AWD et al (eds) Seagrasses: biology, ecology and conservation, Chapter 8, pp 193–225

Komasu T, Umezawa Y, Nakaoka M, Kanamoto C (2004) Water flow and sediment in *Enhalus acoroides* and other seagrass beds in the Andaman Sea, off Khao Bae Na, Thailand. Coral Mar Sci 29:63–68

Kuo J, Kanamoto Z, Iizumi H, Aioi K, Mukai H (2006) Seagrasses from the Nansei Islands, Southern Japanese archipelago: species composition, distribution and bio-geography. Mar Ecol 27:290–298

Lacap C, Vermaat J, Rollon R, Nacorda H (2002) Propagule dispersal of theSE Asian seagrasses *Enhalus acoroides* and *Thalassia hemprichii*. Mar Ecol Progr Ser 235:75–80

Maruyama K, Igarashi Y, Ishikawa Y (1987) Techniques for selecting appropriate site to create eelgrass meadows. Ann J Coast Eng 34:227–231 (in Japanese with English abstract)

Ministry of the Environment, Government of Japan (2018) https://www.env.go.jp/nature/kisho/hozen/redlist/RL2018_5_180604.pdf. July 15 2019

Murakami T, Yasuda T, Ohsawa T (2004) Development of a multi-sigma coordinate model coupled with an atmospheric model for the calculation of coastal currents. Ann J Coast Eng 51:366–370 (in Japanese)

Murakami T, Kohno H, Iwasaki A, Kuramochi T, Shimokawa S, Kimura K (2014) Particle tracking analysis based on ecological investigation of seeds of *Enhalus acoroides* in Amitori Bay, Iriomote Island, Japan. J Japan Soc Civil Eng B3(70):1074–1079 (in Japanese with English abstract)

Nakajima Y, Matsuki Y, Arriesgado D, Chun Lán L, Fortes M, Uy W, Campos W, Nakaoka M, Nadaoka K (2013) Elucidation of regional population maintenance mechanism of tropical sea grass *Enhalus acoroides* using genetic markers. In: Summary of the 60th national convention of the Japanese Ecological Society. https://updoc.site/download/pdf–5b41c5cd71648_pdf. July 15 2019 (in Japanese)

Nakase K (2000) Quantitative estimation of eelgrass distribution from the viewpoint of external forces, at Takeoka Beach, Tokyo Bay, Japan. In: Proceedings of fourth international seagrass biology workshop, pp 397–400

Nakase K, Murakami T, Ukai A, Mizutani A, Shimokawa S, Kohno H (2015) Distribution analysis of *Enhalus acoroides* using hydraulic model, in the northwest sea area of Iriomote Island, Okinawa, Japan. J Japan Soc Civil Eng B3, 71:957–962 (in Japanese with English abstract)

Nakase K, Murakami T, Mizutani A, Kohno H, Ukai A, Shimokawa S (2016) Estimation of the *Enhalus acoroides* distribution using monthly condition n of external forces by wave model in northwest coast of the Iriomote Island. J Japan Soc Civil Eng B2(72):1429–1434 (in Japanese with English abstract)

Rollon RN (1998) Spatial variation and seasonality in growth and reproduction of *Enhalus acoroides* (L.f.) royle populations in the coastal waters off cape Bolinao, NW Philippines First Edition. A.A. Balkema, Rotterdam, pp 9–35

Takeyama K, Kohno H, Kuramochi T, Iwasaki A, Murakami T, Kimura K, Ukai A, Nakase K (2014) Distribution and growth conditions of *Enhalus acoroides* on iriomote island. J Japan Soc Civil Eng B3(70):1068–1073 (in Japanese with English abstract)

Data Source

AMeDAS: Japan Meteorological Agency (2008–2009, 2012–2013, 2015). https://www.jma.go.jp/jma/en/Activities/amedas/amedas.html. 15 July 2019

GPV: Japan Meteorological Business Support Center (2008–2009, 2012–202013, 2015). http://www.jmbsc.or.jp/en/index-e.html. 15 July 2019

Part IV
Relationship Between Dispersals of Seeds, Fructification, Spawns, and Larvae of Marine Costal Life and Physical Environments

Chapter 13
Numerical Analysis of Initial Dynamic State of Bundle of *Acroporidae* spawning in Amitori Bay

Tomokazu Murakami, Hiroyoshi Kohno, Akira Mizutani and Shinya Shimokawa

Abstract This study was conducted to assess numerical simulation methods used to examine the initial dynamic state of coral bundle that has not been studied because of a shortage of observational data. For that purpose, we conducted field observations of spawning of *Acroporidae* in Amitori Bay, Iriomote Island, Japan. Results revealed spawning sites of *Acropora digitifera*, of which mass spawning were observed, the number of the spawning egg–sperm bundle and the rise rate of the bundle. After we conducted numerical simulations of the initial dynamic state of *Acropora digitifera* bundles based on observational data, we reproduced initial dynamic state characteristics such as the bundle rise and dispersion.

Keywords *Acropora digitifera* · Amitori Bay · Egg–sperm bundle · Numerical simulation

This chapter is based on work reported by Murakami et al. (2015).

T. Murakami (✉) · S. Shimokawa
Storm, Flood and Landslide Research Division, National Research Institute for Earth Science and Disaster Resilience, Tsukuba, Japan
e-mail: tmurakami@bosai.go.jp

S. Shimokawa
e-mail: simokawa@bosai.go.jp

H. Kohno · A. Mizutani
Okinawa Regional Research Center, Tokai University, Yaeyama, Japan
e-mail: hkohno@scc.u-tokai.ac.jp

A. Mizutani
e-mail: ma110267@tsc.u-tokai.ac.jp

S. Shimokawa et al. (eds.), *Geophysical Approach to Marine Coastal Ecology*, Springer Oceanography, https://doi.org/10.1007/978-981-15-1129-5_13

13.1 Introduction

Hermaphrodite and broadcast-spawning corals, using the most common mode of reproduction of corals, release capsules (bundles), each of which contains about ten unfertilized eggs and 1 million or more sperm, all at once during a spawning period. The released bundles rise and break near the sea surface, and a sperm and an egg of the same kind from different colonies are fertilized. A belt-like accumulation zone called a slick in which eggs and sperm are intermingled is sometimes formed in such an event (Oliver and Willis 1987).

A fertilized egg starts cell division, metamorphoses into a planula larva within about 1–3 days, and starts adhesion (Hayashibara et al. 1993; Nozawa and Harrison 2008). Its adhesion capability reaches a peak in one week to 10 days after fertilization. Then the settled larva metamorphoses into a polyp and becomes a part of a coral colony (Nozawa and Harrison 2008).

Preservation of coral reefs has become a subject of global concern today. Devised measures for this issue include the simulation of slick formation and transportation of eggs and larvae (e.g., Takayama et al. 2013). This research theme is important, leading to the prediction of development and decline of coral reefs.

However, no simulation treating the early behavior of bundles like rise and dispersion performed before the process of slick formation or transportation of eggs and larvae has been carried out because of shortage of observational data such as the release sites and rise rate of bundles.

Accordingly, many questions related to the actual conditions of the early behavior of bundles are left unsolved. Furthermore, the initial conditions of the simulation of slick formation and transportation of eggs and larvae are left indefinite because they are provided by the early behavior of bundles, which determines the formation sites of slicks, the sites of distribution of eggs and larvae, and their magnitude.

Therefore, it is demanded that a simulation be proposed to reproduce and predict the early behavior of bundles correctly and which can contribute to elucidation of the realities of the early behavior of bundles and the precision improvement of the simulation of slick formation and transportation of eggs and larvae for the preservation of coral reefs conducted to date.

This study was conducted to propose a simulation of the early behavior of bundles. For that purpose, we have conducted observation of spawning and distribution survey, etc., of corals at Amitori Bay. We present data of the release sites and the rise rate of bundles and the usage of these data in a simulation. Then using the proposed simulation we reproduce early behavior such as rise and dispersion of bundles in Amitori Bay.

13.2 Field Survey and Results

We conducted a submersible survey at 24°19′ north latitude and 123°41′ east longitude in Amitori Bay, Iriomote Island to acquire data related to the spawning of corals. The survey was performed on a total of 38 days in 2014 including May 15–20 (around a full moon), May 29–30 (around a new moon), June 2–4, June 12–21 (around a full moon), July 12–20 (around a full moon), and August 13–21 (around a full moon). Observations were carried out around 20:00–24:00 on each day of observation. We looked for corals that were about to spawn, waited until spawning started if bundles were found to have been set to polyps, and recorded the start and finish times of spawning, the number of colonies, and the situation of the circumference, etc. The species of coral spawned were identified based on Nishimori and Veron (1995). Table 13.1 presents the results.

Table 13.1 Coral spawning observations at Amitori Bay, Iriomote Island in 2014 (referred from Murakami et al. 2015)

Mo.	Day	Spawning species	Population	Start time	Finish time	High tide at night	Tide
5	17	*Goniastrea retiformis*		22:16		21:42	Middle
5	18	*Acropora grandis*	Multi-colony	21:55	22:40	22:33	Middle
5	18	*Acropora millepora*	Single colony	22:03	22:40	22:33	Middle
5	19	*Acropora grandis*	2–3 colonies	21:48	22:20	23:31	Middle
5	19	*Acropora millepora*	2–3 colonies	21:50	22:20	23:31	Middle
5	19	*Acropora formosa*	Multi-colony	22:08	22:17	23:31	Middle
5	19	*Acropora microphthalma*	Multi-colony	22:08	22:20	23:31	Middle
5	19	*Acropora florida*	Single colony	22:14		23:31	Middle
5	19	*Acropora digitifera*	Multi-colony	22:20	22:40	23:31	Middle
5	19	*Acropora gemmifera*		22:35	22:58	23:31	Middle
6	15	*Montipora stellata*	2–3 colonies	21:30	21:55	21:33	Middle
6	16	*Acropora brueggemanni*	Single colony	22:14	22:32	22:20	Middle
6	17	*Acropora brueggemanni*	Single colony	22:20	22:40	23:09	Middle
6	17	*Acropora gemmifera*	Single colony	22:24	22:42	23:09	Middle
6	18	*Porites lutea*		22:06	22:18	0:01 (Next day)	Middle

(continued)

Table 13.1 (continued)

Mo.	Day	Spawning species	Population	Start time	Finish time	High tide at night	Tide
6	19	*Porites lutea*	Single colony	21:55	22:10	0:56 (Next day)	Middle
6	19	*Goniastrea pectinata*	Single colony	22:09	22:30	0:56 (Next day)	Middle
6	19	*Favia favus*	Single colony	22:23	22:45	0:56 (Next day)	Middle
7	19	*Acropora secale*	Single colony	21:35	21:59	0:08 (Next day)	Neap
8	17	*Acropora brueggemanni*	2–3 colonies	21:36	22:00	0:08 (Next day)	Neap
8	17	*Acropora divaricata*	Single colony	23:00	23:20	0:08 (Next day)	Neap

Spawning of *Acroporidae* was observed frequently in May and June. Especially, spawning of seven species of corals was observed mostly simultaneously at around 22:00 on May 19. As for their three species, *A. digitifera*, *A. formosa*, and *A. microphthalma*, many colonies simultaneously spawned only once on May 19. These were regarded as mass spawning.

Spawning of *A. grandis* and *A. millepora* was observed on both May 18 and 19. Spawning of *A. gemmifera* was observed on May 19 and June 17, on the specific days of successive months. Spawning of *A. brueggemanni* was observed on June 17, June 18, and August 17, on specific days two months apart. These were regarded as split spawning.

Two species of *A. secale* and *A. divaricata* spawned, respectively, on July 19 and August 17. These spawning periods were later compared with those of other *Acroporidae*. Moreover, these were spawning only by a single colony, respectively; no synchronized spawning with other colonies was observed.

Spawning of almost all species took 11–30 min. According to spawning patterns, three species of *A. digitifera*, *A. formosa*, and *A. microphthalma*, which carried out mass spawning, finished spawning in a short time, for about 9 min at the shortest and about 20 min at the longest. By contrast, *A. grandis*, *A. millepora*, *A. gemmifera*, and *A. brueggemanni*, which conducted split spawning required longer spawning time compared with species that conducted mass spawning, 18 min at the shortest and 37 min at the longest.

The spawning of *Acroporidae* was performed nearly at high tide on the night following each day of spawning. All *Acroporidae* started spawning at about 30–90 min before a high tide in May. Spawning of all the *Acroporidae* started by about 60 min before a high tide in June. *A. secale* spawned about 2.5 h before high tide in July. This spawning was earlier compared with that of *Acroporidae*, which spawned in May and June. *A. brueggemanni* and *A. divaricata* spawned about 2.5 and 1 h before high tide, respectively, in August.

As for the relation between the day of spawning and tide, spawning was carried out in the middle tide in May and June, but during the neap tide in July and August. No spawning in the spring tide was observed from observational research in 2014 of this study.

This study specifically examines *A. digitifera* of the Acroporidae family, which demonstrated the most remarkable mass spawning. This study also specifically addresses simulation of the early behavior of its bundles. Figure 13.1 portrays the *A. digitifera* spawning behavior.

The spatial distribution of *A. digitifera* in Amitori Bay is necessary for the simulation of the early behavior of bundles at Amitori Bay.

The coverage distribution was investigated using the quadrat method in 2009 and 2014. Specifically, quadrats were installed at 61 points over the whole Amitori Bay (four quadrats of 1 m × 1 m, a total area of 4 m^2 at each point), and photographed. The *A. digitifera* recognized in photographs taken at each point were contoured on tracing paper. The coverage was found by measuring the weight of the cut-off part of the paper using an electronic balance.

Then coverage was subjected to spatial interpolation by inverse distance weighting, and coverage distribution over the whole Amitori Bay was estimated. The result is shown in Fig. 13.2. The weighting factor of inverse distance weighting

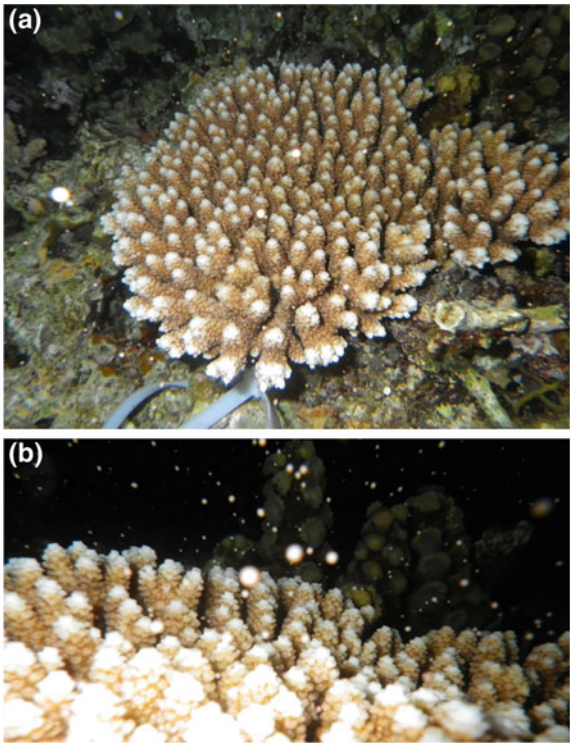

Fig. 13.1 Appearance and bundle release of *Acropora digitifera*; **a** shows Acropora digitifera; **b** shows the bundle release behavior (referred from Murakami et al. 2015)

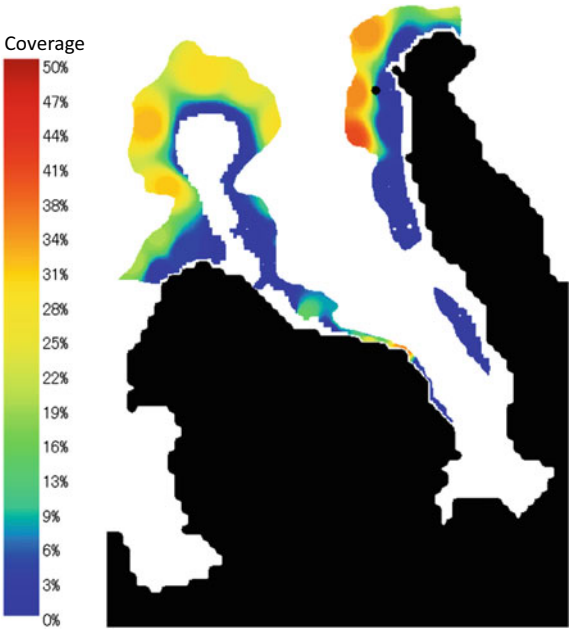

Fig. 13.2 Spatial distribution of coverage of *Acropora digitifera* in Amitori Bay (referred from Murakami et al. 2015)

was optimized and determined using 32 coverage data obtained from an additional survey for verification.

Kitada (2002) reported a relation $y = 0.62\,x^{3.78}$ between the diameter of *A. tenuis* x cm and the number of released eggs y. No convincing proof exists that this relation also holds for *A. digitifera*, the target of this study. Nevertheless, it was assumed that the relational expression for *A. tenuis* holds also for *A. digitifera* in consideration of the fact that the relation between the diameter and the number of released eggs of *A. digitifera* was unknown, and that *A. tenuis* and *A. digitifera* were the same corymbose corals.

Next, the number of bundles released at each site was estimated based on the spatial distribution of coverage shown in Fig. 13.2. Letting the average major axis of *A. digitifera* be R, the number of colonies of *A. digitifera* within a calculation lattice of 6.25 m × 6.25 m described later be n, coverage be c. and assume the area of *A. digitifera* to be expressed as circular, then the following relation is obtained.

$$\pi(R/2)^2 \times n = 6.25 \times 6.25 \times c/100 \tag{13.1}$$

Given the number of colonies n from Eq. (13.1), the following relation is obtained by multiplying the previously described relational expression between the diameter and the number of released eggs of *A. tenuis* by the number of colonies n.

$$y = 0.62\,(100R)^{3.78} \times 6.25 \times 6.25 \times c / \left\{ 100\,\pi\,(R/2)^2 \right\} \tag{13.2}$$

Given the average major axis of *A. digitifera* R m and the coverage of *A. digitifera* c, the number of released eggs of *A. digitifera* in a calculation lattice of 6.25 m × 6.25 m can be estimated.

This study adopted values shown in Fig. 13.2 as the coverage of *A. digitifera*. The average major axis of *A. digitifera* was set as 0.27 m: the average of measurements from the photographs of the quadrat survey (sample number: 211).

The number of eggs contained in one bundle of *A. digitifera* is known to be 5.7 (Kitada 2002). The number of released bundles of *A. digitifera* in a calculation lattice of 6.25 m × 6.25 m is determined using this value and Eq. (13.2).

Data of the rise rate of bundles are fundamentally important to compute the early behavior of the bundles immediately after spawning with sufficient accuracy.

Accordingly, the rise rate of bundles was measured. However, measurements were conducted with *A. nasuta* because the rise rate of bundles of *A. digitifera*, the target of this study, could not be measured.

Measurements were carried out by setting a transparent acrylic box with five surfaces (open bottom) above the target coral about to start spawning in order to remove current components, and by recording the behavior of rising bundles with a video camera (Fig. 13.3). A calibration board with scale marks of a 5 cm interval

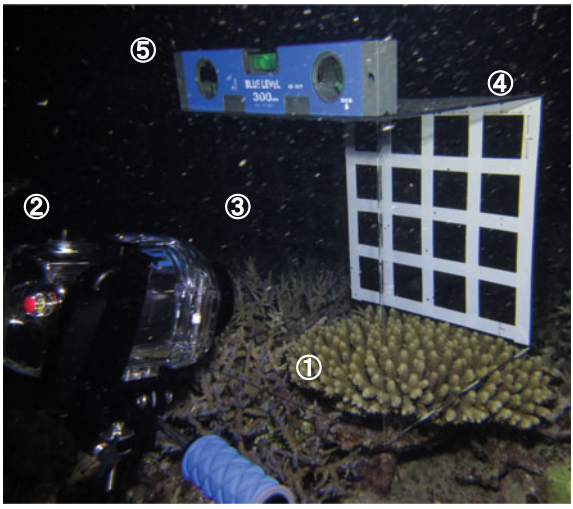

Fig. 13.3 Measurement method for the rise rate of bundles (referred from Murakami et al. 2015)

(1) Observation target coral
(2) Underwater video camera
(3) Transparent acrylic box
(4) Calibration board
(5) Level gauge

was also attached. The velocity of bundles passing in front was computed. The result indicated the average rise rate of bundles as 0.88 cm/s (standard deviation, 0.25; sample number, 60).

13.3 Numerical Simulation

A seawater current required in the simulation of dispersion of bundles was reproduced using the coastal ocean current model with a multi-sigma coordinate system (CCM) described in Chap. 3. The calculation period was set as May 18–21, 2014 including May 19, 2014, the day of spawning of *A. digitifera*.

The wind velocity and direction data monitored at the coast of Amitori Bay, the estimated river flow rate of the Udara River and the Ayanda River (Murakami et al. 2012), and astronomical tide data obtained using the NAO model (Matsumoto et al. 2000) were used as the initial and boundary values for the ocean model CCM.

Bundles were regarded as particles in a reproduced seawater current field and were tracked according to the Lagrangian method. The specific computational conditions, in that case, were the following.

A calculation lattice was a square of 6.25 m × 6.25 m. The number of released bundles from the lattice was estimated using the described previously method. It is noteworthy that one particle represented 300,000 bundles in this computation because of calculation costs. The particles were released from spawning start time 22:20 to the spawning finish time 22:40 of *A. digitifera* presented in Table 13.1. The rise rate of 0.88 cm/s described above was adopted as that of a bundle, which was data of *A. nasuta*.

13.4 Computational Results

Figures 13.4, 13.5 and 13.6, respectively, present the simulation results of the early behavior of bundles of *A. digitifera* in Amitori Bay, at 22:21, 22:25, and 23:00 on May 19, 2014. All the bundles rose to the surface at a moderate rise rate of 0.88 cm/s in Fig. 13.4 at 22:21 on May 19 immediately after the spawning start. Because the tide was about to turn (a high tide was at 23:31) and because the wind velocity was as low as 1.8 m/s at 22:21 on May 19, the seawater current was also very weak. Although bundles would undergo the influence of a sea water current even during rising, they were regarded as staying near the spawning site caused by such weak seawater current.

Bundles that had arrived at the sea surface and those in the course of rising coexisted at 22:25 on May 19 (Fig. 13.5). Although all bundles had risen by 23:00 on May 19, no large migration from near the spawning site was observed caused by the previously described weak seawater current (Fig. 13.6).

Next, the prolonged computation was performed until 10:00 on May 21 with the position of bundles at 23:00 on May 19 shown in Fig. 13.6 as the initial conditions.

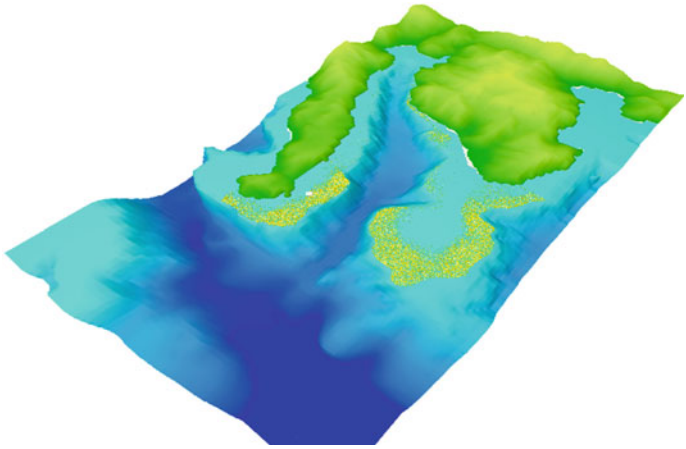

Fig. 13.4 Simulation of early behavior of bundles at 22:21 on May 19, 2014; yellow circles and red circles, respectively, denote bundles rising and drifting on the sea surface (referred from Murakami et al. 2015)

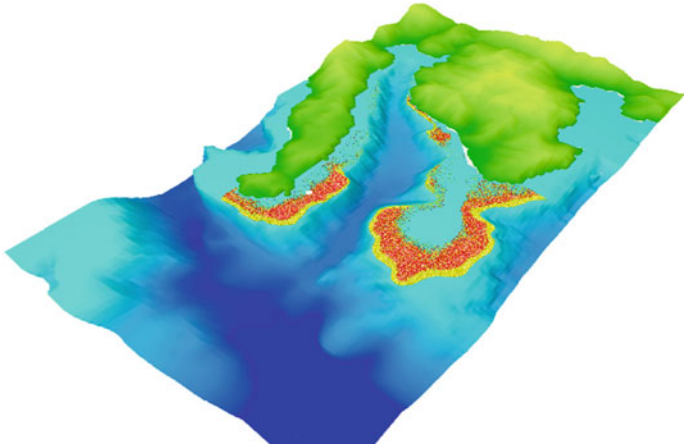

Fig. 13.5 Simulation of early behavior of bundles at 22:25 on May 19, 2014; yellow circles and red circles, respectively, denote bundles rising and drifting on the sea surface (referred from Murakami et al. 2015)

Figures 13.7 and 13.8, respectively, present the results obtained at 22:00 on May 20 and 10:00 on May 21. Slicks had formed inside the bay simultaneously as the bundle flew toward the open sea at 22:00 on May 20 in Fig. 13.7.

Although almost all bundles had moved out of the calculation domain by 10:00 on May 21, some bundles were observed to remain inside the bay (Fig. 13.8). Therefore, early behaviors of bundles such as rise and dispersion in Amitori Bay were reproduced using the method explained for this study.

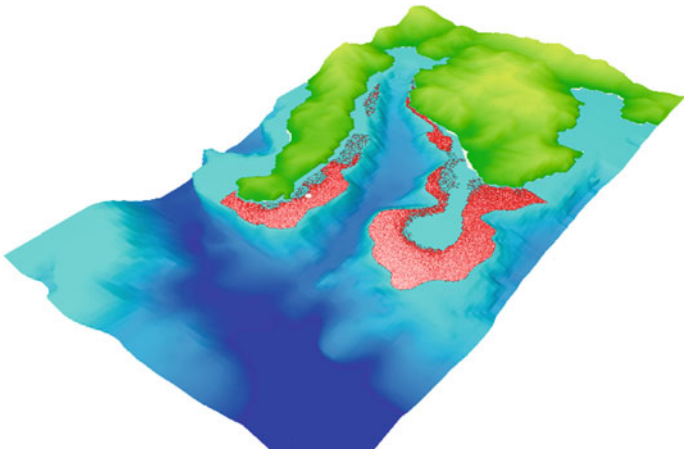

Fig. 13.6 Simulation of early behavior of bundles at 23:00 on May 19, 2014: yellow circles and red circles, respectively, denote bundles rising and drifting on the sea surface (referred from Murakami et al. 2015)

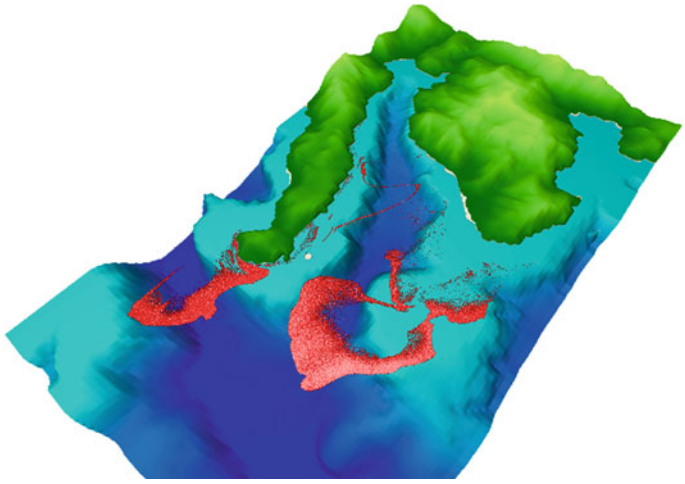

Fig. 13.7 Simulation of behavior of bundles at 22:00 on May 20, 2014 (referred from Murakami et al. 2015)

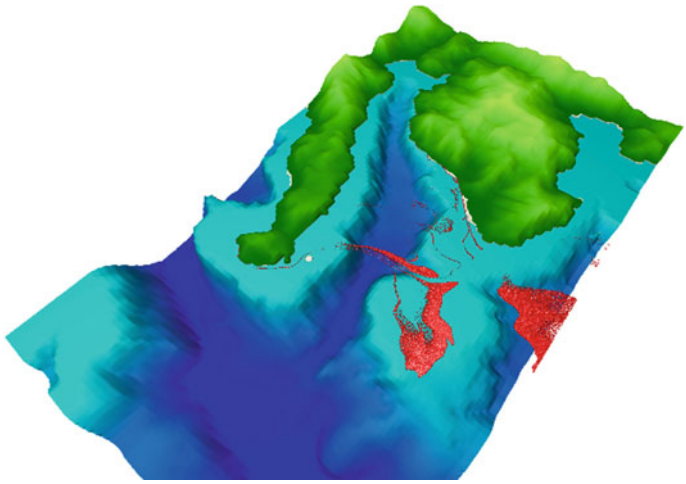

Fig. 13.8 Simulation of behavior of bundles at 10:00 on May 21, 2014 (referred from Murakami et al. 2015)

13.5 Conclusion

We have observed Acroporidae spawning in Amitori Bay, Iriomote Island, Japan in this study. The results elucidated data including the release sites of bundles of *A. digitifera*, for which mass spawning was observed and the rise rate of bundles of *A. nasuta*. We have also proposed a simulation of the early behavior of bundles based on these data and demonstrated that early behavior of bundles such as rise and dispersion were reproducible.

However, this study leaves some issues unresolved, including the fact that the relation between the diameter and the number of released eggs of *A. tenuis* was applied to *A. digitifera*, and that the rise rate of bundles of *A. nasuta* measured in this study was applied as that of *A. digitifera*. For that reason, the authors believe it important to perform continuous observation of spawning of corals and to accumulate data related to the bundle release of many species into a database.

Acknowledgements The field survey in this study was carried out with the cooperation of Hiroyuki Inoue who was then a research student with the Okinawa Regional Research Center, and Masaki Jinno, Mio Tanaka, Kazuho Hiroshima, and Yuiko Yamamoto who were then students of School of Marine Science and Technology, Tokai University. The authors extend their deepest gratitude for this kind of support.

References

Hayashibara T, Shimoike K, Kimura T, Hosaka S, Heyward A, Harrison P, Kudo K, Omori M (1993) Pattern of coral spawning at Akajima Island, Okinawa, Japan. Mar Ecol Prog Ser 101:253–262

Kitada H (2002) Fecundity of *Acropora tenuis* at Akajima Island, Midoriishi, No. 13, pp 26–19

Matsumoto K, Takanezawa T, Ooe M (2000) Ocean tide models developed by assimilating TOPEX/POSEIDON altimeter data into hydrodynamical model: a global model and a regional around Japan. J Oceanography 56:567–581

Murakami T, Ukai A, Kohno H, Mizutani A, Shimokawa S, Nakase K, Yasuda T (2012) Relationships between distributions of coral and physical environments in Amitori Bay, Iriomote Island, Japan. J Japan Soc Civil Eng B2 B3 68:1133–1138 (in Japanese with English abstract)

Murakami T, Kohno H, Yamamoto Y, Mizutani A, Shimokawa S (2015) Numerical simulation for initial dynamic state of bundle based on field observations of Acroporidae spawning in Amitori Bay, Iroomote Island, Japan. J Japan Soc Civil Eng B2 71:I_1225–I_1230 (in Japanese with English abstract)

Nishimori M, Veron JEN (1995) Hermatypic corals of Japan. Kaiyusha, Tokyo, pp 32–409 and 412–413 (439 p)

Nozawa Y, Harrison PL (2008) Temporal patterns of larval settlement and survivorship of two broadcast-spawning acroporid corals. Mar Biol 155:347–351

Oliver JK, Willis BL (1987) Coral-spawn slicks in the Great Barrier Reef: preliminary observations. Mar Biol 94:521–529

Takayama Y, Katakura N, Ito K, Sumihiro T, Hiroshima H (2013) A numerical case study of coral Larva transport in South Coast of the Arabian Gulf. J Japan Soc Civil Eng B3 69:I_ 1102–I_1107 (in Japanese with English abstract)

Chapter 14
Numerical Analysis of Dispersals of *Enhalus acoroides* Seeds and Fruits in the Northwest Sea Area of Iriomote Island

Tomokazu Murakami, Hiroyoshi Kohno, Akira Mizutani and Shinya Shimokawa

Abstract This study used numerical analysis to evaluate *Enhalus acoroides* seed and fruit dispersal in the northwestern sea area of Iriomote Island, Japan. Input data for numerical simulations were provided based on results of an ecological investigation of *Enhalus acoroides* and field observations of physical phenomena. Reproductions of coastal currents in the northwestern sea area of Iriomote Island were conducted using an ocean current model: CCM. *Enhalus acoroides* seed and fruit dispersal characteristics were examined using particle tracking analysis.

Keywords *Enhalus acoroides* · Seed dispersal · Fruit dispersal · Numerical analysis · Iriomote Island

This chapter is based on work reported by Murakami et al. (2015a, b).

T. Murakami (✉) · S. Shimokawa
Storm, Flood and Landslide Research Division, National Research Institute for Earth Science and Disaster Resilience, Tsukuba, Japan
e-mail: tmurakami@bosai.go.jp

S. Shimokawa
e-mail: simokawa@bosai.go.jp

H. Kohno · A. Mizutani
Okinawa Regional Research Center, Tokai University, Yaeyama, Japan
e-mail: hkohno@scc.u-tokai.ac.jp

A. Mizutani
e-mail: ma110267@tsc.u-tokai.ac.jp

S. Shimokawa et al. (eds.), *Geophysical Approach to Marine Coastal Ecology*, Springer Oceanography, https://doi.org/10.1007/978-981-15-1129-5_14

14.1 Introduction

Enhalus acoroides, a tropical seagrass, is considered important from the viewpoint of the maintenance management of marine resources because it forms a habitat as described in Sect. 14.5. The habitat serves as a prey field and growth field for various fishes. Moreover, its unique propagation system of epihydrogamy with male flowers has become a valuable tourist attraction in Yaeyama province, Okinawa-ken.

Enhalus acoroides is listed as a vulnerable species (VU) on the Red List of the Ministry of Environment of Japan. The decline and extinction of *Enhalus acoroides* communities in the northwest sea area of Iriomote Island, Okinawa-ken were reported recently (Chap. 12). For that reason, it has been demanded that the causes of the decline and extinction of *Enhalus acoroides* communities of Iriomote Island be elucidated, and that preservation and recovery measures be proposed. To meet these demands, it is necessary to elucidate the life history, the present situation of meadow distribution, biological and physical conditions in connection with distribution, and ecological and physical environmental causes of the decline and extinction of *Enhalus acoroides* in Iriomote Island, some of which have been clarified by the author and colleagues (Chap. 12).

In addition to these efforts is also indispensable to formulate and execute effective measures for the preservation and recovery of *Enhalus acoroides* communities to elucidate its dispersal characteristics, such as migration distance of seeds and fruits, and the mutual effects of those and other factors among communities. This latter point is extremely important because it is involved with the power of spontaneous recovery of a meadow. Moreover, it determines the distribution and magnitude of a meadow.

Accordingly, the simulation of dispersal of seeds and fruits is conducted in this study for *Enhalus acoroides* communities in the northwest sea area of Iriomote Island, based on observations and experimental data related to *Enhalus acoroides* seeds by Kohno et al. (unpublished).

14.2 Ecological Survey of *Enhalus acoroides* Seeds and Results

The seeds of *Enhalus acoroides* are released from dehiscent fruit (Fig. 14.1a). Its seed coat carries an air bubble inside. For that reason, seeds rise to the sea surface as a result of their buoyancy (Fig. 14.1b). Then seeds are dispersed by seawater currents on the sea surface. They sink to the sea bottom when the coat comes off (Fig. 14.1c).

Reproduction of such behavior through numerical simulation requires data including (1) the day of seed release, (2) the site of seed release, (3) the number of released seeds, (4) the floating period of seeds, and (5) the rising and sinking rates

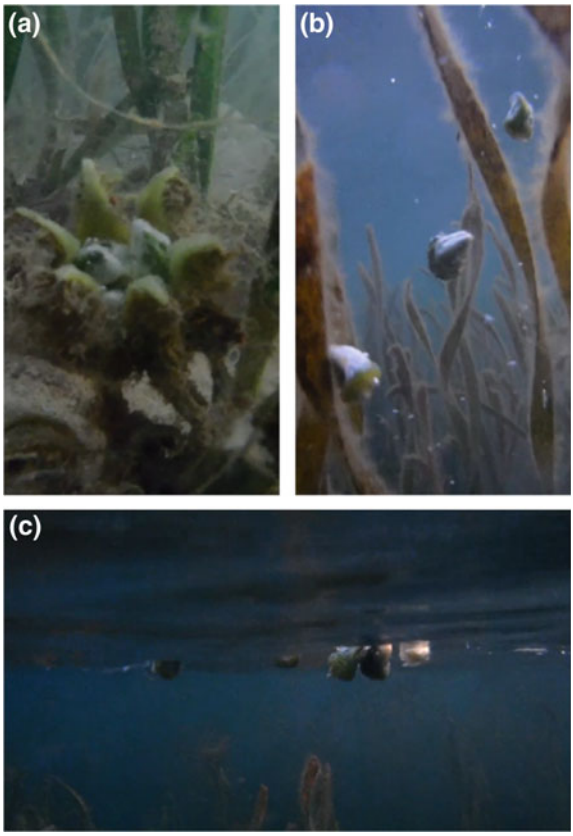

Fig. 14.1 *Enhalus acoroides* seeds: **a** seeds in dehiscent fruit, **b** seeds rising because of their air bubble coats, and **c** seeds drifting on the sea surface (referred from Murakami et al. 2015a)

of seeds. This chapter presents a description of these data based on observations and experimentation by Kohno et al. in 2013–14 (unpublished).

(1) Days of seed release: 2–3 quadrats of a 4 m × 4 m square were prepared in the Sonai meadow (Meadow 2 in Fig. 14.2). Observation of their progress was performed until seed release after simultaneous blooming. *Enhalus acoroides* bloomed in June, July, August, and September in 2014 and released seeds, respectively, in August 26–September 1, September 22–29, October 21–28, and December 15–20 in 2014.
(2) Sites of seed release: A field survey using aerial photography and GPS revealed surviving communities at 12 sites, shown as Communities 1–12 in Fig. 14.2. Aerial photography in 1974 and an on-site interview verified that communities had existed but that they had become extinct at 17 sites shown as Communities 13–29 in Fig. 14.2.

The area of each meadow was ascertained from image analysis using aerial photography as described above.

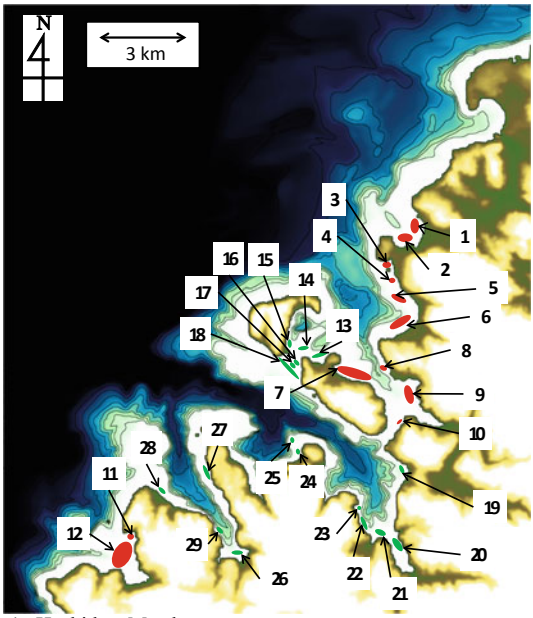

Fig. 14.2 Distribution of *Enhalus acoroides* communities in the northwest sea area of Iriomote Island (referred from Murakami et al. 2015a)

1. Hoshidate Meadow
2. Sonai Meadow
3. first Sonai Harbor Meadow
4. second Sonai Harbor Meadow
5. first Midarahama Meadow
6. second Midarahama Meadow
7. Uchibanari Island Meadow
8. first Shirahama Meadow
9. second Shirahama Meadow
10. Hayasaka Channel Meadow
11. first Sakiyama Meadow
12. second Sakiyama Meadow
13. first Sotobanari Island Meadow
14. second Sotobanari Island Meadow
15. third Sotobanari Island Meadow
16. fourth Sotobanari Island Meadow
17. fifth Sotobanari Island Meadow
18. sixth Sotobanari Island Meadow
19. first Funauki Meadow
20. second Funauki Meadow
21. third Funauki Meadow
22. fourth Funauki Meadow
23. fifth Funauki Meadow
24. sixth Funauki Meadow
25. seventh Funauki Meadow
26. first Amitori Bay Meadow
27. second Amitori Bay Meadow
28. third Amitori Bay Meadow
29. fourth Amitori Bay Meadow

(3) Number of released seeds: The fruit pieces were counted at 2 or 3 quadrats of 4 m × 4 m prepared in the observation of (1). The number of fruit pieces per unit area was computed. The average numbers of fruit pieces per square meter (average number (the maximum and minimum of one quadrat, the number of quadrats)) of *Enhalus acoroides* that bloomed in June, July, August, and September, 2014 were, respectively, 0.34 (5, 6, 2), 0.08 (2, 0, 3), 0.08 (2, 0, 3), and 0.04 (2, 0, 3).
Fruits were sampled outside of the quadrats prepared in the observation of (1) in the Sonai meadow (Meadow 2 in Fig. 14.2). The contained seeds were counted. The average numbers of seeds per fruit (average ± standard deviation (the maximum and minimum, the number of samples)) of *Enhalus acoroides* that bloomed in June, July, August, and September in 2014 were, respectively, 4.60 ± 1.64 (8, 3, 15), 9.47 ± 2.39 (13, 5, 15), 9.40 ± 1.87 (14, 5, 30), and 10.20 ± 1.79 (12, 8, 5).
Then the numbers of released seeds in each month of blooming at each surviving meadow presented in Fig. 14.2 were estimated using data of the area of each meadow, the number of average fruits per square meter, and the number of average seeds per fruit revealed by image analysis of (2). The results are presented in Table 14.1.

(4) Floating period of seeds: Five pieces each of fruit were sampled outside of the quadrats prepared for the observation of (1) in the Sonai meadow (Meadow 2 in Fig. 14.2). Sampling was conducted on September 24, September 29, October

Table 14.1 Estimate of the number of released seeds in each month of blooming at each meadow (Fig. 14.2); tabulated based on data from Kohno et al. (unpublished)

		Bloomed in June Seeds released during August 26–September 1, 2014	Bloomed in July Seeds released during September 22–29, 2014	Bloomed in August Seeds released during October 21–28, 2014	Bloomed in September Seeds released during December 15–20, 2014
Meadow No.	1	58,190	29,031	28,827	15,640
	2	106,513	53,140	52,765	28,628
	3	5091	2540	2522	1368
	4	3329	1661	1649	895
	5	133,711	66,708	66,239	35,938
	6	27,972	13,955	13,857	7518
	7	312,281	155,798	154,701	83,933
	8	58,490	29,181	28,976	15,721
	9	99,413	49,597	49,248	26,720
	10	16,698	8331	8272	4488
	11	6748	3367	3343	1814
	12	217,975	108,748	107,982	58,586

Figure 14.2 presents the meadow numbers (referred from Murakami et al. 2015a)

3, October 9, October 14, and December 11 in 2014, which were, respectively, 27, 22, 18, 12, 7, and 4 days before the starting day of seed release. Seeds were taken out of the collected fruits. Then the seeds floating on a still water surface in a beaker were counted every 30 min. Results showed the maximum floating period after seven days as 7.1 h.

(5) Rising and sinking rates of seeds: The rising time of *Enhalus acoroides* seeds from the sea bottom with depth of about 1.2–1.5 m, where *Enhalus acoroides* was commonly distributed to the sea surface, was about 11 s. The sinking time from the sea surface to the sea bottom was about 7 s.

14.3 Ecological Survey of *Enhalus acoroides* Fructification and Results

Male and female flowers of *Enhalus acoroides* bloom all at once at low tide in the daytime on several days around the full moon from early summer to autumn. Pollination (epihydrogamy with male flowers) occurs on the sea surface. Pollinated female flowers sink at the root of the strain of *Enhalus acoroides*, mature as fruits, and dehisce to release seeds (Fig. 14.3).

This study includes numerical analysis of cases in which fruits detach from the plant and drifts away before seed release. Data required for this purpose include data with respect to (1) the detachment period of fruits carrying germinable seeds, (2) the location and area of communities, (3) the number of fruit pieces at each meadow, and (4) drifting of fruits. This chapter presents a description of these data based on observations and experimentation by Kohno et al. in 2013–14 (unpublished).

(1) Detachment period of fruits carrying germinable seeds: 2–3 quadrats of a 4 m × 4 m square were prepared in the Sonai meadow (Meadow 2 in Fig. 14.2), and observation the plant progress was conducted until seed release

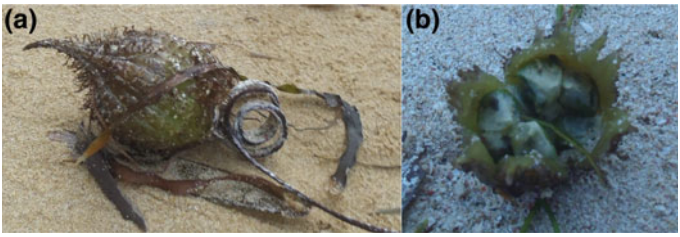

Fig. 14.3 Detached fruits of *Enhalus acoroides*: **a** shows fruit of *Enhalus acoroides*; **b** seeds are visible in a dehiscent fruit (referred from Murakami et al. 2015a, b)

after simultaneous blooming. *Enhalus acoroides* bloomed in June 13, July 12–13, and August 10 in 2014, respectively, released seeds spontaneously in August 26–September 1, September 22–29, and October 21–28 in 2014.

Five pieces each of *Enhalus acoroides* fruit were sampled outside of the quadrats in the Sonai meadow (Meadow 2 in Fig. 14.2) 45, 50, 54, 60, and 65 days after the blooming in August. Then seeds were taken out and germination experiments were conducted in seawater in a beaker. The germination rates at 45, 50, 54, 60, and 65 days after blooming were, respectively, 0, 0, 95, 100, and 100% (numbers of sample seeds: 46, 52, 43, 44, and 50). Consequently, seeds would become germinable no sooner than 54 days after blooming, even when contained inside detached fruits.

These findings imply that the detachment period of fruits that carry germinable seeds extends from 54 days after blooming to the last day of spontaneous release of seeds, which are August 6–September 1, September 5–29, and October 3–28 in 2014, respectively, for *Enhalus acoroides* that bloomed in June, July, and August in 2014.

(2) Location and area of communities: sites of seed release: a field survey using aerial photography and GPS revealed surviving communities at 12 sites shown as Communities 1–12 in Fig. 14.2. Aerial photography in 1974, an on-site interview, and records by Kohno, one coauthor of this study, and his colleagues who have conducted marine organism surveys since 1976 in this sea area verified that communities had existed but that they have been extinct at present at 17 sites shown as Communities 13–29 in Fig. 14.2.

The area of each meadow was also determined using image analysis with the aerial photography described above.

(3) Numbers of fruits in respective communities: The fruit pieces were counted in 2 or 3 quadrats of 4 m $\times$ 4 m prepared in the observation of (1). The numbers of fruit pieces per unit area were computed. The average numbers of fruit pieces per square meter [average number (the maximum and minimum of one quadrat, the number of quadrats)] of *Enhalus acoroides* that bloomed in June, July, and August, 2014 were, respectively, 0.34 (5, 6, 2), 0.08 (2, 0, 3), and 0.08 (2, 0, 3). The numbers of fruit pieces in each month of blooming at each meadow presented in Fig. 14.2 were estimated using data of the area of each meadow and the average number of fruit pieces per square meter that were revealed by image analysis of (2).

(4) Drifting of fruits: Five pieces each of fruit were sampled outside of the previously described quadrats 60 and 65 days after the blooming of *Enhalus acoroides* in August. The fruits were put in seawater in a beaker. Then the behavior was investigated. All ten fruit pieces continued floating for two months or more. It was also observed that fruits were drifting on the sea (at the Sonai meadow in Fig. 14.2) as presented in Fig. 14.4.

Fig. 14.4 Drifting fruits of *Enhalus acoroides*: photographed in the Sonai meadow as presented in Fig. 14.2 on September 29, 2014 (referred from Murakami et al. 2015a, b)

14.4 Numerical Simulation of Seed Dispersal

Seawater currents required in the simulation of seed dispersal were reproduced using the coastal ocean current model with a multi-sigma coordinate system (CCM) as described in Chap. 3.

Wind velocity data from the mesoscale model (MSM) of Japan Meteorological Agency, river flow rate data for the Yonada River, the Udara River, and the Ayanda River measured by the present authors, river flow rate data for the Urauchi River, the Nakara River, and the Kuira River measured by Watanabe with the Iriomote Project, Research Institute for Humanity and Nature (RIHN) (Murakami et al. 2012), and astronomical tide data by the NAO model (Matsumoto et al. 2000) were used as the initial and boundary values for the ocean model CCM.

A calculation period for reproducing seawater current using the ocean model CCM was set as August 25–September 2 (bloomed in June), September 21–30 (bloomed in July), October 20–29 (bloomed in August), and December 14–21 (bloomed in September) so that the days of seed release described in Chap. 2 were included. The average wind velocities at the Uchibanari Island meadow (Meadow 7 in Fig. 14.2) in each period were 1.8 m/s, 4.8 m/s, 4.2 m/s, and 6.4 m/s, respectively, whereas the mean wind directions were 151°, 122°, 60°, and 27° (where 0° denotes a north wind and 90° denotes an east wind), respectively. Such wind velocity and direction are common for Iriomote Island, and there was no large weather event, such as the approach of a typhoon, during the calculation period of this study.

Enhalus acoroides seeds were regarded as particles in a reproduced seawater current field and were tracked according to the Lagrangian method. The specific computational conditions in that case were the following.

Numbers of released seeds: particles of the same number of seeds were released.

Release time of seeds: The release periods of *Enhalus acoroides* seeds that bloomed in June, July, August, and September in 2014 were, respectively, August

26–September 1, September 22–29, October 21–28, and December 15–20 in 2014, as described above. However, the time of seed release was not recorded. Accordingly, computations were conducted assuming that seeds were released uniformly at 10 min intervals at each seed release period.

Seed floating time: Particle tracking computations were performed for this study during the seed release period. As described above, the maximum floating period during seven days after seed release was 7.1 h. This study used 7.1 h as the longest floating period; particle tracking computations were performed for 7.1 h after seed release. As an average floating period for examining average dispersal characteristics, an estimated average of 2.4 h at 3.5 days after the start of seed release (median of the starting day and finishing day of seed release) was adopted. However, the longest floating period of 7.1 h and the estimated average floating period of 2.4 h were the results of experiments conducted in still water. Therefore, the actual floating period on the site might be regarded as shorter because of disturbance by waves, etc.

Miscellaneous computational conditions: because the time required for rising and sinking of seeds is extremely short as described above, the particle tracking analysis of this study did not incorporate rising or sinking. Moreover, because a seed would float with its coat carrying an air bubble, a seed was assumed to be always located on the water surface. Sedimentation by its own weight was not considered in computations either.

14.5 Numerical Simulation of Fruit Dispersal

Seawater currents required in the simulation of fruit dispersal were reproduced using the coastal ocean current model with a multi-sigma coordinate system (CCM) described in Chap. 3. The initial and boundary values of CCM were set similarly to the numerical simulation of seed dispersal.

Although an ecological survey of the fruit of *Enhalus acoroides* was conducted in 2014, the result was assumed to be applicable during 2007–2014 to increase opportunities for discussion of the possibility of fruit dispersal. Then a total of 24 cases of seawater current computation were conducted for August 5–September 1, September 4–29, and October 2–28 in each year of 2007–2014, respectively, so that the detachment periods of fruits carrying germinable seeds should be included. It is noteworthy that these calculation periods covered the approach of typhoons for which the maximum instantaneous wind velocity exceeded 20 m/s at the Iriomote Island AMEDAS observatory, including No. 0712 (37.4 m/s on September 18, 2007), No. 0715 (28.5 m/s on October 6, 2007), No. 0813 (27.2 m/s on September 12, 2008), No. 0908 (22.2 m/s on August 7, 2009), No. 1011 (33.9 m/s on September 19, 2010), No. 1215 (20.3 m/s on August 28, 2012), and No. 1323 (23.2 m/s on October 6, 2013).

The fruits of *Enhalus acoroides* were tracked using the Lagrangian method under the reproduced seawater current field. Specific computational conditions in such cases are described below.

Numbers of detached fruit: The actual numbers of fruits detached from the plant were not found. Accordingly, computations were performed in this study under conditions of a case in which all fruits detached (100% detachment assumption) and a case in which 1% of fruits detached (1% detachment assumption) as presumed states. Thereby, we examined the maximum migration distance of fruit dispersal.

Time and site of fruit detachment: For the number of detached fruit, 100 and 1% detachment assumptions were divided equally in each detachment period of fruits carrying germinable seeds: August 6–September 1, September 5–29, and October 3–28. The detached fruits were released from a total of 29 surviving/extinct communities as presented in Fig. 14.2.

Miscellaneous computational conditions: Fruits continued floating for two months or more as described above. Accordingly, the Lagrangian tracking analysis of this study assumed that fruits remained always on the water surface. Sedimentation by its own weight was not considered in computation.

14.6 Computational Results of Seed Dispersal

Figure 14.5 presents the seed dispersal behavior of *Enhalus acoroides* (bloomed in June) at 0:00 on September 1, 2014. Seeds released from each meadow presented in Fig. 14.2 were distributed under the influence of tides, drift currents, hyperpycnal inflows from rivers, etc.

Figure 14.6 shows the migration distance of seeds from their release sites. The average, maximum, and minimum values in this figure are of all the seeds over the total computational period and from all communities. The average moving distance after an average floating time of 2.4 h was 261 m. This migration distance of 261 m was considered small compared with the scale of the northwest sea area of Iriomote Island of about 10 km from east to west and about 15 km from north to south (Fig. 14.2). Even the maximum migration distance after 2.4 h was 1198 m at most.

The maximum migration distance after 7.1 h, the longest floating period, was 4012 m. This distance was considerably long, even at the scale of the northwest sea area of Iriomote Island, so that seeds could be delivered to distant communities. It is noteworthy, however, that this migration distance of 4012 m was of a very rare case with the longest floating period and the maximum migration distance. It is also possible that the longest floating period of 7.1 h might be shortened because of disturbance by waves, etc., at the site, as described above. Consequently, a migration distance of 4012 m is regarded as almost the greatest of all the realistic cases.

Next, details of average migration distances after an average floating period of 2.4 h are examined. Figure 14.7 shows the average migration distances of 2.4 h after seed release for each meadow and each month of blooming. Migration

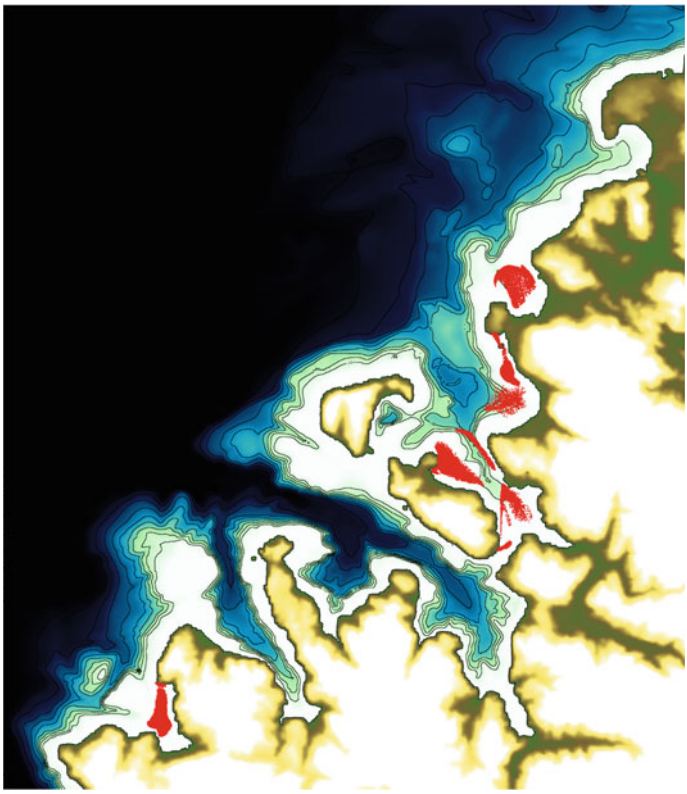

Fig. 14.5 Behavior of seed dispersal at 0:00 on September 1, 2014 (bloomed in June); red circles denote released seeds (referred from Murakami et al. 2015a)

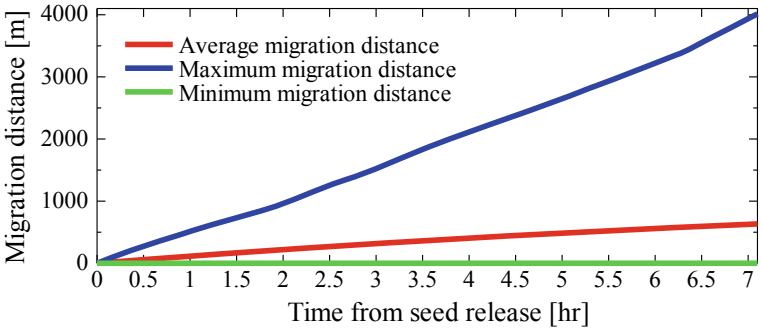

Fig. 14.6 Migration distance from sites of seed release: the average, maximum, and minimum values are of all the seeds over the total computational period and from all communities (referred from Murakami et al. 2015a)

distances evidently varied according to the meadow and the month of blooming. It is a characteristic that the migration distances of seeds of *Enhalus acoroides* that bloomed in September were prolonged at Communities 3–8 and 10 (Fig. 14.2). Moreover, although the migration distance of *Enhalus acoroides* that bloomed in June tended to be less than those of other months of blooming, the migration distance of *Enhalus acoroides* that bloomed in June was greatest only for Communities 2 and 9.

Figure 14.8 shows the sea surface flow velocity at each meadow. Its average and maximum were, respectively, 0.01–0.04 m/s and 0.03–0.14 m/s in spite of differences among communities. The current velocity was considerably weak over the sea area in which communities were formed, which suggests that the short migration distances of seeds shown in Figs. 14.6 and 14.7 were also attributable to weak flow velocity in the sea area where communities were formed, although mainly owed to the short floating period of seeds.

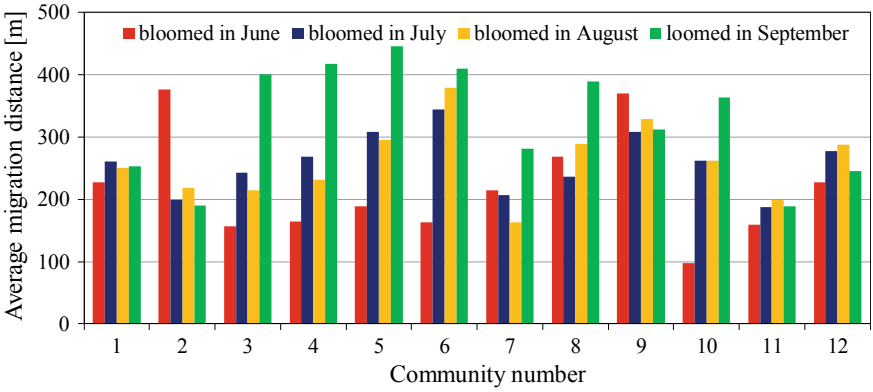

Fig. 14.7 Average migration distance 2.4 h after seed release according to the meadow and month of blooming (referred from Murakami et al. 2015a)

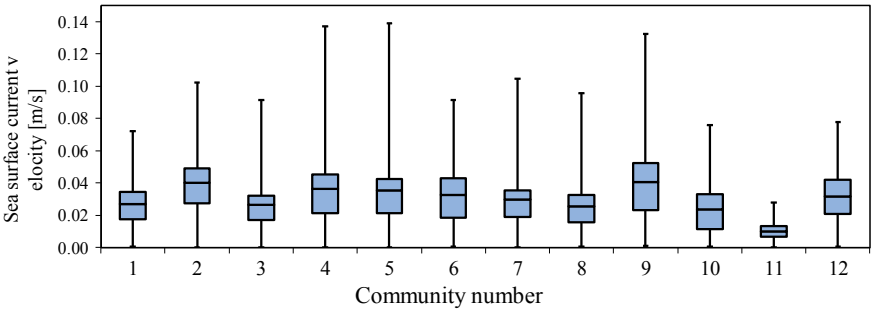

Fig. 14.8 Sea surface flow velocity at each meadow (referred from Murakami et al. 2015a)

These findings imply extremely low probabilities of seeds reaching communities that had already been extinct.

14.7 Computational Results of Fruit Dispersal

Figure 14.9 shows the fruit dispersal behavior in the case of 1% detachment assumption at 0:00 on September 1, 2007. Fruits were released from each meadow (Fig. 14.2) under the computational conditions described in Chap. 3, and were then distributed under the influence of the tide, drift current, hyperpycnal inflow from rivers, etc.

Figure 14.10 portrays the average and maximum migration distances of fruits of all 24 cases of 100% detachment assumption. The average migration distance was 879–2494 m, although it varied among communities. This was large compared with the average migration distance of 261 m during the average floating period of seeds of 2.4 h. The maximum migration distance was 9727–15,403 m, which implies that fruit detachment out of any meadow can reach everywhere throughout the northwest sea area of Iriomote Island at the maximum. It is noteworthy that, when fruits passed the border of the calculation domain, the migration distance beyond the border was not counted in the average and maximum migration distances presented in Fig. 14.10. For that reason, the actual average and maximum migration distances might be longer than those shown here.

The number of fruit pieces detached out of each meadow under the 1% detachment assumption that reached other communities was counted, although the

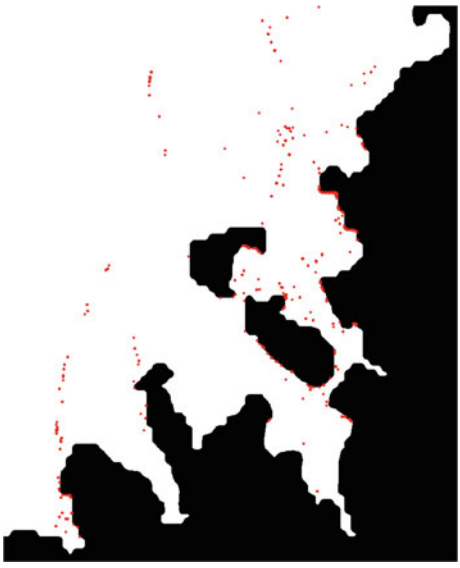

Fig. 14.9 Behavior of fruit dispersal of 1% detachment assumption at 0:00 on September 1, 2007; red circles denote fruits (referred from Murakami et al. 2015a, b)

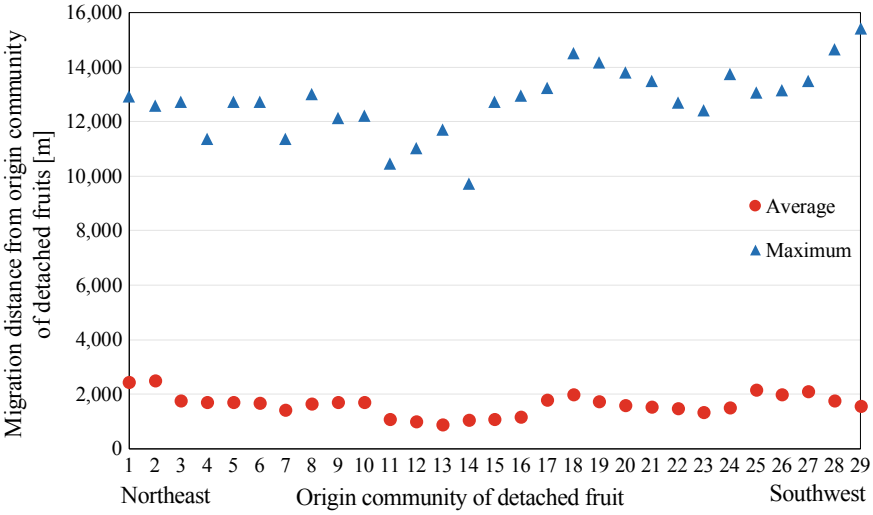

Fig. 14.10 Average and maximum migration distances of fruits of all the 24 cases of the 100% detachment assumption. When fruits passed the border of the calculation domain, migration distance beyond the border are not counted (referred from Murakami et al. 2015a, b)

results are not shown. The Hoshidate meadow (Meadow 1) and the second Sakiyama meadow (Meadow 29) were most distantly separated (about 13.25 km). However, two fruit pieces travelled from the Hoshidate meadow to the second Sakiyama meadow and one vice versa. These are events of extremely low probability because this is the number of events during the eight years of 2007–2014. Nevertheless, this result demonstrates the possibility of interchange of fruits among communities.

Moreover, all the communities including the already extinct communities (Communities 13–27) received fruits detached from other communities. Consequently, a possibility of recovery of lost communities is demonstrated by fruit dispersal, although it is of extremely low probability similarly to the case of the described above interchange between communities. It is characteristic that fewer fruit pieces arrived at the already extinct communities located in Amitori Bay (Communities 24–27) than in other communities. It is noteworthy that such physiographic characteristics also affect the possibility of recovery of lost communities.

Figure 14.11 displays the distribution of the number of fruit pieces integrated over the computation time for all 24 cases of the 100% detachment assumption. Detached fruits tend toward sites with many integrated number of fruit pieces easily. Figure 14.11a, representing the total number of detached fruits, released from all communities, indicates numerous integrated numbers of fruit pieces, even at points A and B where no meadow had been observed (see Fig. 14.2). Consequently, a new meadow might occur if ecological and physical conditions

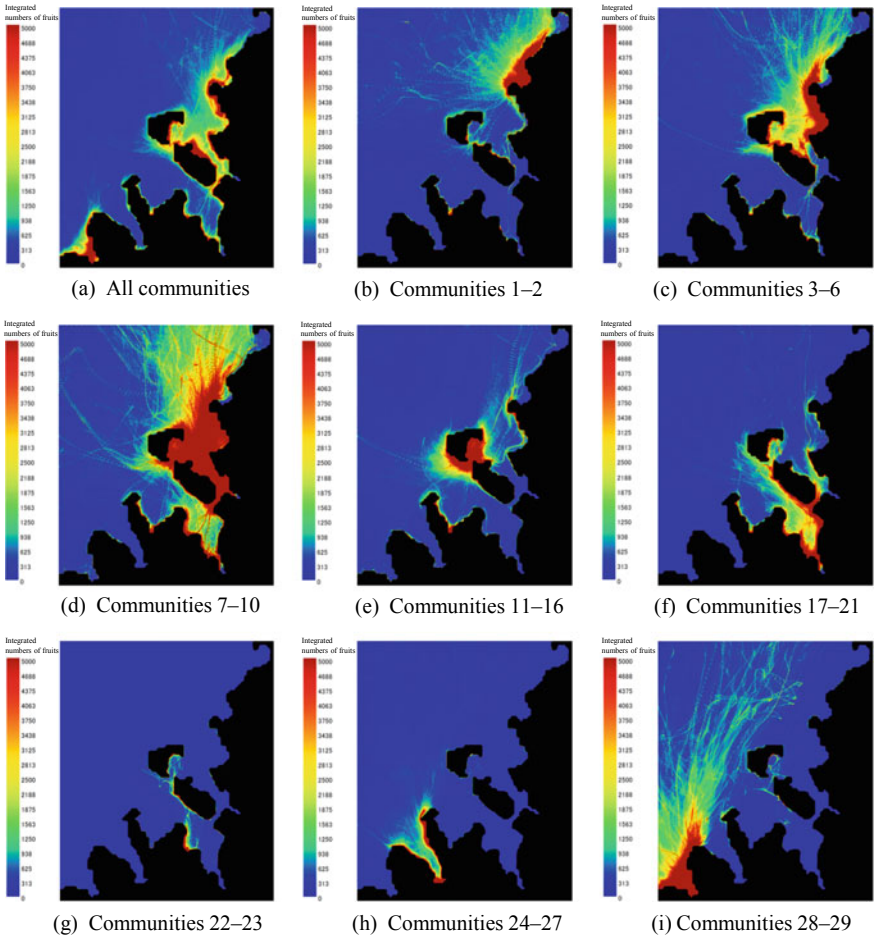

Fig. 14.11 Distribution of the number of fruit pieces integrated over the computation time for all 24 cases of 100% detachment assumption: **a** when fruits are released from all communities, **b–i** when fruits are released from each meadow; detached fruits tend toward sites with many integrated numbers of fruit pieces easily (referred from Murakami et al. 2015a, b)

suitable for habitation of *Enhalus acoroides* are met. By contrast, only a few integrated numbers of fruit pieces were observed near the Urauchi River mouth and in Amitori Bay (see Fig. 14.2), which suggests their geographical features would keep fruits from establishing plants.

Figure 14.11a also suggests that a region ranging from the Hoshidate meadow (Meadow 1) to Sotobanari and Uchibanari Islands (see Fig. 14.2) received many fruit pieces, most of which had travelled from Communities 1–21 (Fig. 14.11b–f). However, many fruit pieces detached at Communities 22–27 (Fig. 14.11g and h) were distributed near their release sites. The fruits only rarely reached a region

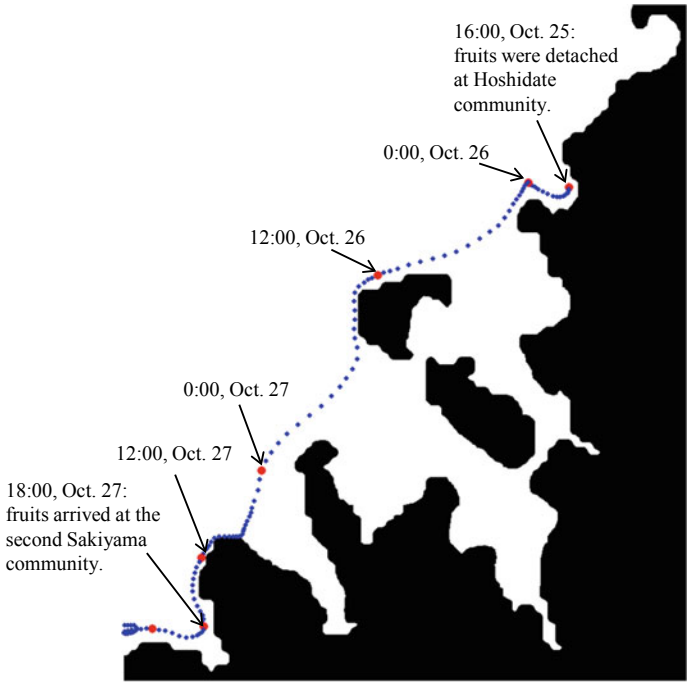

Fig. 14.12 Trajectory of a piece of fruit detached from Hoshidate meadow at 16:00 on October 25, 2007 (referred from Murakami et al. 2015a, b)

ranging from the Hoshidate meadow (Meadow 1) to Sotobanari and Uchibanari Islands. Moreover, fruits detached from Communities 11–12 located in Sakiyama (See Fig. 14.11i) dispersed northward easily but only slightly toward Amitori Bay or Funauki Bay beyond Capes Uruchizaki and Sabazaki (Fig. 14.2).

Figure 14.12 presents the trajectory of a piece of fruit detached from the Hoshidate meadow at 16:00 on October 25, 2007. It exhibits the behavior of the fruit: detached at the Hoshidate meadow (Meadow 1) because of weather and oceanographic conditions at that time, passed offshore of Sotobanari Island (Fig. 14.2) at 12:00 on October 26, and arrived at the second Sakiyama meadow (Meadow 12) at 18:00 on October 27.

14.8 Conclusion

This study has numerically evaluated the dispersal characteristics of the seeds and fruits of *Enhalus acoroides* in the northwest sea area of Iriomote Island based on observational and experimental data. Results revealed the fact that the average migration distance of seeds during an average flotation period of 2.4 h was only

261 m. The interchange situation of seeds between communities was such that almost no seeds from other communities would join already extinct communities. Fruit dispersal with a large migration distance allows seeds to be distributed over a wide area. However, the possibility of fruit dispersal is much lower than seed dispersal. Furthermore, this study has evaluated the possibility of fruit interchange among communities in the northwest sea area of Iriomote Island and the recovery of already extinct communities.

Nevertheless, these results indicate that the dispersal characteristics of *Enhalus acoroides* seeds are extremely weak. Consequently, if a meadow once declined and disappeared for biological or physical reasons, the possibility of spontaneous recovery is extremely low. Accordingly, it is necessary to take preventive measures before decline and extinction of *Enhalus acoroides* communities. Fruit dispersal extends to a greater migration distance than seed dispersal, implying the possibility of contribution of fruit dispersal to the relation between the Yaeyama population and the eastern Philippine population of *Enhalus acoroides* communities and suggests the importance of fruit dispersal.

Acknowledgements The simulation used for this study used river flow rate data on the Urauchi River, the Nakara River, and the Kuira River measured by Osamu Watanabe with the Iriomote Project, Research Institute for Humanity and Nature (RIHN). Field surveys for this study were conducted through cooperation of Michiru Tamamoto, Ayaka Iwasaki, Toshie Kuramochi, and Natsumi Kawada who were then students of School of Marine Science and Technology, Tokai University. The authors extend their deepest gratitude for that kind support.

References

Matsumoto K, Takanezawa T, Ooe M (2000) Ocean tide models developed by assimilating TOPEX/POSEIDON altimeter data into hydrodynamical model: a global model and a regional around Japan. J Oceanogr 56:567–581

Murakami T, Ukai A, Kohno H, Mizutani A, Shimokawa S, Nakase K, Yasuda T (2012) Relationships between distributions of coral and physical environments in Amitori Bay, Iriomote Island, Japan. Ann J Civil Eng Ocean B3(68):1133–1138 (in Japanese with English abstract)

Murakami T, Kohno H, Tamamoto M, Mizutani A, Shimokawa S (2015a) Numerical analysis of seed dispersal of *Enhalus acoroides* in the northwest sea area of Iriomote Island, Japan. Ann J Civil Eng Ocean B3 71:951–956 (in Japanese with English abstract)

Murakmai T, Kohno H, Tamamoto M, Mizutani A, Shimokawa S (2015b) Numerical analysis of fruit dispersal of *Enhalus acoroides* in the northwest sea area of Iriomote Island, Japan. Ann J Civil Eng Ocean B2(71):1351–1356 (in Japanese with English abstract)

Chapter 15
Coral Recruitment on a Local Scale in Amitori Bay, Iriomote Island, Estimated by Filed Surveys and Numerical Analyses

Masako Nakamura, Tomokazu Murakami, Hiroyoshi Kohno and Akira Mizutani

Abstract Recruitment of new individuals is essential for community sustainability and resilience. Spatial variation in coral recruitment was quantified for nine sites in Amitori Bay of Iriomote Island, Okinawa Prefecture, Japan, and compared with adult abundance. In addition, potential source sites for recruits, larval trajectories from source to sink sites, and travel distances of larvae were estimated by numerical modeling using real biological and physical data at the main spawning periods. As a result, acroporid recruitment was dominant in Amitori Bay and was positively correlated with adult abundance. Numerical modeling demonstrated a potential that recruits in Amitori Bay could be originated from nearby areas, and that most of recruits traveled less than 400 m with the maximum travel distance of less than 5.5 km. Therefore, estimated dispersal distance of larvae could be relatively short as the mouth of Amitori Bay is about 2 km across and the length of the bay is 4 km. These suggested that the acroporid community in Amitori Bay could be maintained by recruits from within the bay and from immediately surrounding areas.

Keywords Coral · *Acropora* · Recruitment · Dispersal · Numerical model

This chapter is based on work reported by Nakamura et al. (2017).

M. Nakamura (✉)
School of Marine Science and Technology, Tokai University, Shizuoka, Japan
e-mail: mnakamura@tsc.u-tokai.ac.jp

T. Murakami
Storm, Flood and Landslide Research Division, National Research Institute for Earth Science and Disaster Resilience, Tsukuba, Japan
e-mail: tmurakami@bosai.go.jp

H. Kohno · A. Mizutani
Okinawa Regional Research Center, Tokai University, Yaeyama, Japan
e-mail: hkohno@scc.u-tokai.ac.jp

A. Mizutani
e-mail: ma110267@tsc.u-tokai.ac.jp

S. Shimokawa et al. (eds.), *Geophysical Approach to Marine Coastal Ecology*, Springer Oceanography, https://doi.org/10.1007/978-981-15-1129-5_15

15.1 Introduction

For the last several decades, scleractinian corals have been facing serious biological and physical disturbances, and it is estimated that 50–80% of the world's scleractinian corals have been destroyed (Gardner et al. 2003; De'ath et al. 2012). Recently, mass bleaching of corals, followed by mass mortality, has been reported in most of the world's coral reefs due to abnormally high seawater temperatures during the summer of 2016 (GBRMPA 2016; Biodiversity Center of Japan 2016). Because decreased coral abundance reduces diversity and abundance of other coral reef fauna (Jones et al. 2004; Graham et al. 2015), mechanisms to protect, maintain, and recover coral communities after severe disturbances are necessary in order to effectively protect coral reef ecosystems.

Maintenance and recovery of heavily damaged coral communities depend on numbers of newly recruited individuals and their species composition, acquired via planktonic larval dispersal (Connell et al. 1997; Hughes et al. 2000). Trajectories of dispersing larvae have been estimated using current circulation models and/or by analyzing genetic connectivity among different populations (Treml et al. 2008; Cowen et al. 2009). In addition to these analyses, substantial larval supply and recruitment data are essential for understanding the processes.

Larvae of acroporid corals, which are broadcast-spawners, have been thought to disperse over long distances by strong, stable currents such as the Kuroshio Current. In contrast, acroporid larvae have also been estimated from surveys on recruitment and GPS-equipped surface drifters to disperse locally via local coastal currents and to recruit within several tens of kilometers of their origins. Therefore, larval dispersal and recruitment in an inland bay might be affected by currents working at this scale, e.g., estuary circulation patterns. However, studies focusing on larval dispersal patterns in relation to current circulation patterns and subsequent larval supply at local scales, such as an inland bay, are scarce. As a result, knowledge of larval dispersal and subsequent recruitment patterns at this scale is limited. This limitation could be due to difficulties of observation and the paucity of numerical analyses with high accuracy and high resolution.

In this study, using field surveys and a coastal ocean current model with a multi-sigma coordinate system (CCM, see Chap. 3) to overcome difficulties in numerical analyses, we quantified larval supply and estimated source areas, dispersal trajectories, and distances traveled by supplied larvae in Amitori Bay, where mass bleaching occurred in the summer of 2016. This study should lead to a better understanding of spatio-temporal variability in larval supply and subsequent recruitment, and it should permit us to estimate connectivity among populations and to construct substantial protective measures for corals in Amitori Bay and for coral communities in similar inland bays.

15.2 Materials and Methods

(1) Research Sites

Nine sites were selected along both banks from the entrance to the end of Amitori Bay. These sites, including five sites on the west bank (AmSt.1–5) and four sites on the east bank (SaSt.1–4), encompass significant environmental gradients due to topographical characteristics and river flow (see Sect. 1.1) (Fig. 15.1). Three subsites were also established at each site.

(2) Field Surveys

Surveys of larval supply and community structure of corals were conducted at these nine sites. Larval supply was quantified using artificial settlement plates, which consisted of a pair of 10 × 10 cm panels made of fiber-reinforced cement (Fig. 15.2). To precondition the plates, ten plates were deployed at each subsite (30 plates per site) about one month before the predicted major coral spawning periods. These were retrieved about one month later, after the observed spawning on May 19, 2016 in the field. Retrieved plates were bleached with a chlorine solution to eliminate organic matter and then dried for observation under a stereomicroscope.

Fig. 15.1 Research sites along Amitori Bay, Iriomote Island, Okinawa Prefecture, Japan (referred from Nakamura et al. 2017). Map data © 2018 Google

Fig. 15.2 Artificial settlement plate (referred from Nakamura et al. 2017)

Settled juvenile corals on the plates were identified by skeletal morphology and classified to family (Acroporidae, Pocilloporidae, Poritidae, etc.) (Fig. 15.3), and the numbers of individuals pertaining to each family were counted.

Community structures were quantified using the belt transect method with 1 m × 1 m quadrats. One 10 m × 2 m belt transect was established per subsite (three transects per site). Pictures of five randomly selected 1 m × 1 m quadrats were taken and % cover of Acroporidae, Pocilloporidae, Poritidae, and other families were determined using Image J. Relationships between larval supply and % cover were analyzed with Pearson's correlation analysis.

(3) Numerical Analyses

Visual observation of coral larval trajectories from source to sink cannot be made because of small larval sizes. Therefore, a coastal ocean current model with a multi-sigma coordinate system (CCM, see Chap. 3) was employed for estimation of sources and trajectories of larvae supplied to Amitori Bay. Initial values for CCM were wind speed data from mesoscale model I (MSM) of the Japan Meteorological Agency, flow data for the Yonada, Udara, and Paita Rivers from our own observations, and those of the Urauchi, Nakara, and Kuira Rivers from Prof Osamu

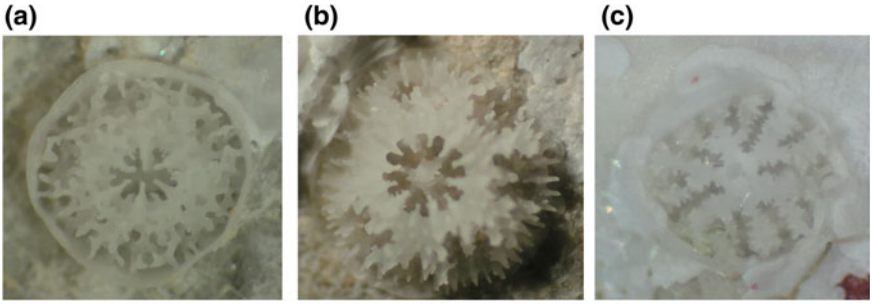

Fig. 15.3 Juvenile corals settled on artificial settlement plates. **a** Acroporidae, **b** Pocilloporidae, and **c** Poritidae (referred from Nakamura et al. 2017)

Watanabe from the Iriomote Project of the Research Institute for Humanity and Nature, as well as astronomical data on tides from the NAO model. Particles were considered as coral larvae under reproduced ocean flow field and tracked with a Lagrangian description. Other detailed conditions for analyses were as given below.

Date and time for larval releases: Large slicks of coral eggs and embryos were observed along the northwestern coast of Iriomote Island from 9:00 to 11:00 am on May 20, 2016 (Fig. 15.4). Slicks were not observed before this day. Therefore, mass spawning of corals occurred during the night of May 19, 2016, establishing the date of larval release. In addition, release time was set as 22:00–22:25, in accordance with Murakami et al. (2015).
Areas of larval release: Using 15-m topographic grids, areas less than 5 m deep were considered as regions of potential larval release.
Number of released larvae: From each 225 m^2 quadrat of potential larval release, 10 particles, considered as coral larvae, were released from 22:00 to 22:25 (Murakami et al. 2015). In total, 616,180 particles were released.
Settlement timing: According to Suzuki et al. (2011), particles treated as coral larvae could settle within 4–15 days after release. Therefore, in this analysis, anytime a particle passed through one of the nine research sites within 15 days, it was considered to have "settled."

Fig. 15.4 Slicks of coral eggs and embryos observed along the northwestern coastal area of Iriomote Island (referred from Nakamura et al. 2017)

15.3 Results and Discussion

(1) Larval Supply and Community Structure

Acroporids were the most abundant juveniles established on settlement plates in Amitori Bay, comprising 63% of all juveniles settled on the installed plates. These included 223.7 ± 62.4 acroporids, 49.8 ± 19.6 pocilloporids, 41.0 ± 11.7 poritids, and 37.4 ± 11.4 others (Fig. 15.5). This was not surprising, given that acroporid corals are the major component of coral communities along both banks of Amitori Bay, covering 66.4%.

The number of settled juveniles decreased toward the apex of the bay on both banks (Fig. 15.6). On the west bank, Am.St2 showed the highest number, 19.7 ± 3.5 per plate, and the lowest number was found at Am.St5, 2.5 ± 0.5. Numbers at sites on the east bank were lower than those on the west bank. The highest number was observed at Sa.St1, 6.2 ± 5.8 and the lowest was at Sa.St4, 0.6 ± 0.2.

Positive correlations were observed between the number of settled juveniles (larval supply) and % cover for acroporid corals on both banks of Amitori Bay. A stronger relationship was found with the east bank (Fig. 15.7; west bank, $r = 0.70$, and east bank, $r = 0.90$). These results suggested that sites with higher acroporid cover have higher larval supply and/or that survival rates of settled juveniles are higher at sites with higher acroporid cover, resulting higher coral cover. That is, larval supply or survival rates of settled individuals may decrease from the mouth to the apex of the bay. In Amitori Bay, influenced by flow rates of

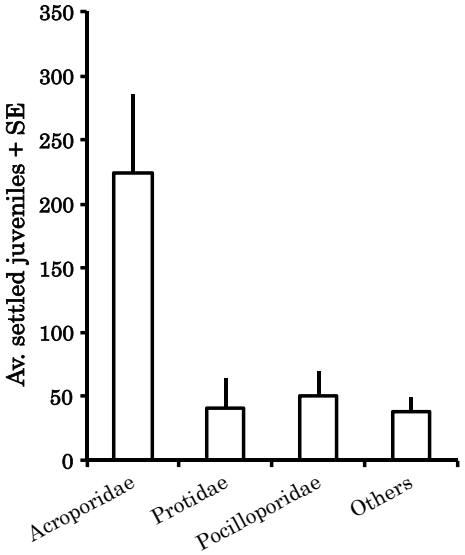

Fig. 15.5 Average numbers of juveniles settled on settlement plates in Amitori Bay (referred from Nakamura et al. 2017)

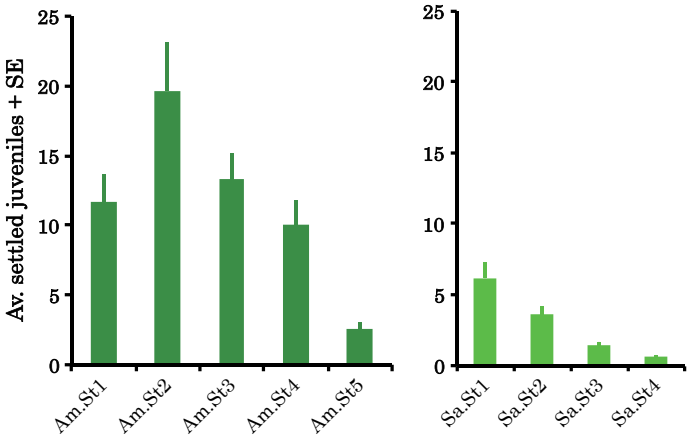

Fig. 15.6 Average numbers of juveniles settled on settlement plates at nine sites in Amitori Bay (referred from Nakamura et al. 2017)

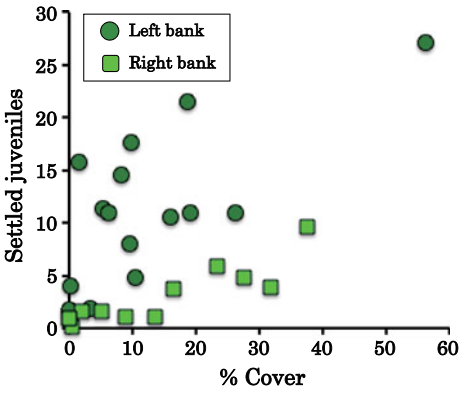

Fig. 15.7 Relationship between the number of settled juveniles and % cover for acroporid corals at sites on both banks of Amitori Bay (referred from Nakamura et al. 2017)

the Ayanda and Udara Rivers, daily fluctuations in salinity and sediment inflow were higher near to the apex (Murakami et al. 2012), factors that can affect larval settlement and survival. In addition, our results also suggest the potential for self-seeding within Amitori Bay. Previous studies of larval settlement and % cover of acorporid corals have not found any such correlation; therefore, acroporid larvae were thought to have come from other areas (Hughes et al. 1999; Nakamura and Sakai 2010). However, larval settlement and % cover of acorporid corals in Amitori Bay showed strong positive correlations; thus larval supply may originate nearby.

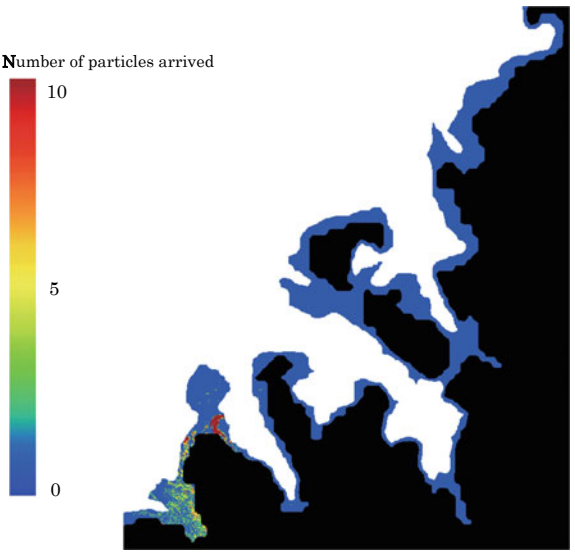

Fig. 15.8 Estimated source areas of juveniles settled in Am.St2 (referred from Nakamura et al. 2017)

(2) Estimation of Larval Sources

Figure 15.8 shows probable source areas for juveniles settled at site Am.St2. This suggests that juveniles settled at Am.St2 came from near Am.St2 and a relatively high number of juveniles originated from Sakiyama Bay. The other eight sites (Am. St1, 3–5 and Sa.St1–4) showed similar patterns that juveniles could be originated from nearby areas.

Dispersal distances of juveniles settled at each study site were calculated (Fig. 15.9). Most juveniles traveled <1,200 m and the maximum distances were within 4.0 km for the west bank and within 5.5 km for the east bank. Moreover, 26.0–97.7% of juveniles settled at Am.St2–St5, Sa.St3, and Sa.St4 traveled <400 m. Considering that the mouth and depth of the Bay are about 2 km and 4 km, respectively, acroporid larvae arriving in the bay disperse relatively short distances.

It has been reported that acroporid larvae start to settle three days after mass spawning and that the main settlement occurs within 8 days (Suzuki et al. 2011). In addition, coral larvae can travel over 10 km in three days with coastal currents and several tens km within seven days (Nakamura et al. 2015). However, estimated dispersal distances of larvae in Amitori Bay were relatively short while distances increased toward the entrance of the bay. This may have resulted from larval retention due to tidal fluctuations and local currents resulting from the complex topography of the bay. Therefore, further studies with numerical analyses based on detailed physical field observations are necessary.

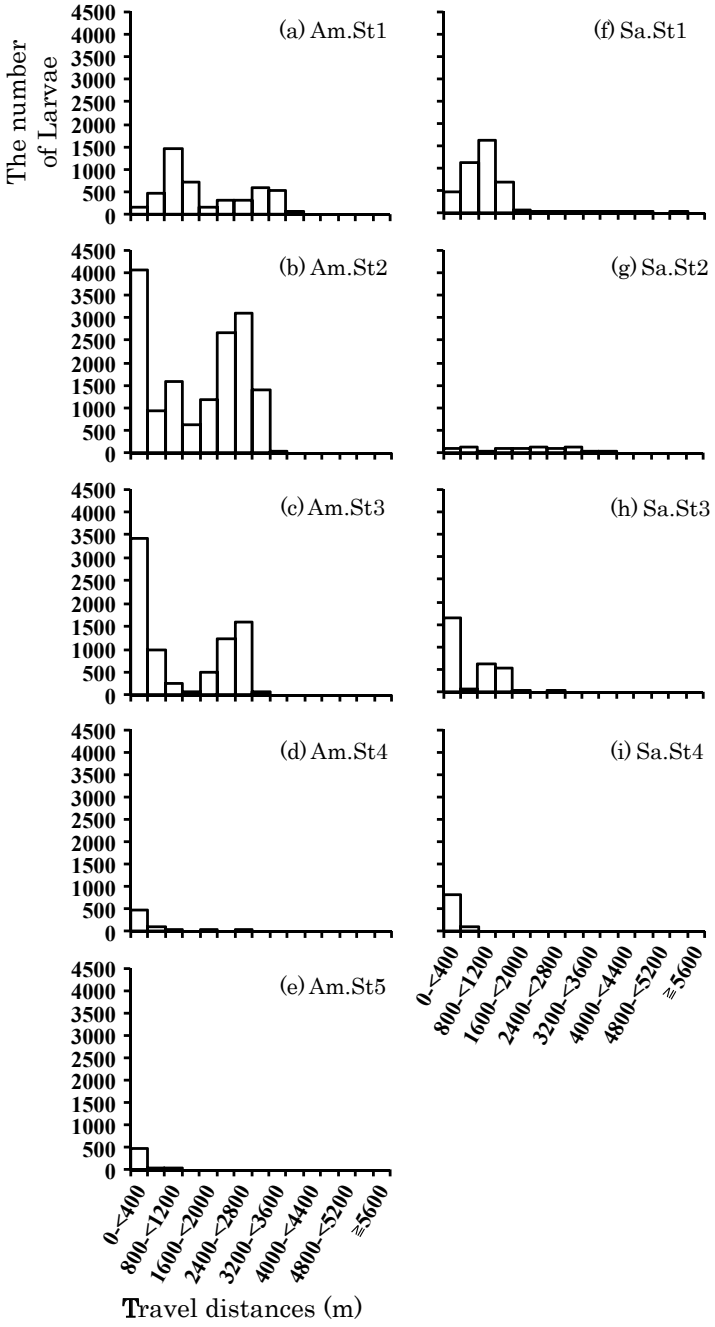

Fig. 15.9 Frequency of larvae in relation to travel distances from estimated source to sink areas (referred from Nakamura et al. 2017)

15.4 Conclusions

This study quantified larval supply through settlement on artificial plates in coral communities inhabiting an inner bay and demonstrated a positive correlation with % local coral cover. Moreover, numerical analyses estimated that source areas of larvae are often located within 400 m of the settlement sites. These results suggest the potential of larval supply from nearby areas. That is, coral communities in an inner bay might be maintained by self-seeding. Therefore, to sustain acroporid coral communities in Amitori Bay, protection and maintenance of existing corals, especially sexually mature colonies, is the highest priority. In addition to the further studies mentioned above, it could be useful to conduct a study estimating larval supply from wider areas.

Acknowledgement We are very grateful to Wataru Noda and Yusuke Matsushita for helping to conduct this research. This study was supported by JSPS KAKENHI Grant Numbers 16K07527. We also thank OIST's technical editor, Dr. Steven D. Aird, for helping to polish this manuscript.

References

Biodiversity Center of Japan (2016) Report on monitoring 1000 coral reef survey in fiscal year 2016. The Ministry of the Environment, Japan

Connell JH, Hughes TP, Wallace CC (1997) A 30-year study of coral abundance, recruitment, and disturbance at several scales in space and time. Ecol Monogr 67:461–488

Cowen RK, Sponaugle S (2009) Larval dispersal and marine population connectivity. Ann Rev Mar Sci 1:443–466

De'ath G, Fabricius KE, Sweatman H, Puotinen M (2012) The 27-year decline of coral cover on the Great Barrier Reef and its causes. Proc Natl Acad Sci 109(44):17995–17999

Gardner TA, Côté IM, Gill JA, Grant A, Watkinson AR (2003) Long-term region-wide declines in caribbean corals. Science 301:958–960

GBRMPA (Great Barrier Reef Marine Park Authority) (2016) Interim report: coral bleaching event on the Great Barrier Reef. GBRMPA, Townsville, pp 1–27

Graham NAJ, Jennings S, MacNeil MA, Mouillot D, Wilson SK (2015) Predicting climate-driven regime shifts versus rebound potential in coral reefs. Nature 518:94–97

Hughes TP, Baird AH, Dinsdale EA, Moltschanlwskyj NA, Pratchett MS, Tanner JE, Wills BL (1999) Patterns of recruitment and abundance of corals along the Great Barrier Reef. Nature 396:59–63

Hughes TP, Baird AH, Dinsdale EA, Moltschaniwskyj NA, Pratchett MS, Tanner JE, Willis BL (2000) Supply-side ecology works both ways: the link between benthic adults, fecundity, and larval recruits. Ecology 81:2241–2249

Jones GP, McCormick MI, Srinivasan M, Eagle V (2004) Coral decline threatens fish biodiversity in marine reserves. Proc Natl Acad Sci 101(21):8251–8253

Murakami T, Ukai A, Khono H, Mizutani A, Shimokawa S, Nakase K, Noguchi K, Yasuda T (2012) Relationships between distributions of corals and physical environments in Amitori Bay, Iriomote Island, Japan. J Japan Soc Civil Eng B3, 68:I_1133–I_1138

Murakami T, Khono H, Yamamoto Y, Mizutani A, Shimokawa S (2015) Numerical simulation for initial dynamic state of bundle based on field observations of Acroporidae spawning in Amitori Bay, Iriomote Island, Japan. J Japan Soc Civil Eng B2 71(2):I_1225–I_1230 (In Japanese with English abstract)

Nakamura M, Sakai K (2010) Spatiotemporal variability in recruitment around Iriomote Island, Ryukyu Archipelago, Japan: implications for dispersal of spawning corals. Mar Biol 157:801–810

Nakamura M, Kumagai NH, Sakai K, Okaji K, Mitarai S (2015) Spatial variability in recruitment of acroporid corals and predatory starfish along the Onna coast, Okinawa, Japan. Mar Ecol Prog Ser 540:1–12

Nakamura M, Murakami T, Khono H, Noda W, Matsushita Y, Mizutani A (2017) Coral recruitment on a local scale in Amitori Bay, Iriomote Island, estimated by settlement plates and numerical analysis. J Japan Soc Civil Eng B2 72(2):I_1279–I_1284 (In Japanese with English abstract)

Suzuki G, Arakaki S, Hayashibara T (2011) Rapid in situ settlement following spawning by Acropora corals at Ishigaki, southern Japan. Mar Ecol Prog Ser 421:131–138

Treml EA, Halpin PN, Urban DL, Pratson LF (2008) Modeling popualtion connectivity by ocean currents, a graph-theoreric apporach for marine conservation. Landscape Ecol 23:19–36

Chapter 16
Numerical Analysis of the Dynamic State of *Coenobita brevimanus* Larvae in Amitori Bay

Wataru Doi, Tomokazu Murakami, Akira Mizutani, Shinya Shimokawa and Hiroyoshi Kohno

Abstract Understanding pelagic larval dynamics is fundamentally necessary for biological conservation in marine biology. We analyzed larval transportation and recruitment of the land hermit crab *Coenobita brevimanus* during July 2010 in Amitori Bay on Iriomote Island by performing particle tracking analysis based on field observations of larval releases and weather conditions. Larval release was observed for several days before and after the new moon between July and September. It coincided well with the nighttime high tide. During July 10–14, 2010, it was estimated that 39 females released 780,000 zoeae. An average of about 10% of the larvae remained in the area near the release site. Many larvae were transported outside the bay rather than returning to the population. Therefore, the population of *C. brevimanus* in Amitori, which consists of many large crabs, is regarded as important as a source of recruits for adjacent habitats.

Keywords Larval dispersal · Anomura · Crustacean · Land hermit crab

This chapter is based on work reported by Murakami et al. (2014).

W. Doi (✉)
Faculty of Fisheries, Kagoshima University, Kagoshima, Japan
e-mail: doiw@fish.kagoshima-u.ac.jp

T. Murakami · S. Shimokawa
Storm, Flood and Landslide Research Division, National Research Institute for Earth Science and Disaster Resilience, Tsukuba, Japan
e-mail: tmurakami@bosai.go.jp

S. Shimokawa
e-mail: simokawa@bosai.go.jp

A. Mizutani · H. Kohno
Okinawa Regional Research Center, Tokai University, Yaeyama, Japan
e-mail: ma110267@tsc.u-tokai.ac.jp

H. Kohno
e-mail: hkohno@scc.u-tokai.ac.jp

S. Shimokawa et al. (eds.), *Geophysical Approach to Marine Coastal Ecology*, Springer Oceanography, https://doi.org/10.1007/978-981-15-1129-5_16

16.1 Introduction

Similarly to most semiterrestrial crustaceans with pelagic larval stages, the land hermit crabs *Coenobita brevimanus* (see Sect. 1.6) expand their geographical distributions through their initial stage of life history. After mating, egg laying, and egg incubating in the terrestrial environment, ovigerous females of *C. brevimanus* migrate to the sea and release their larvae (Fig. 16.1; Nio et al. 2014, 2019). The larval stage of this crab consists of four or five zoeal stages and a single megalopal stage (Fig. 16.2; Hamasaki et al. 2014, 2015a; Kohno et al. 2014). The size of the *C. brevimanus* larvae is <2.3 mm in carapace length (Hamasaki et al. 2014; Kohno et al. 2014). For most coastal marine species, the larval phase is the dominant dispersal stage. Therefore, considerable emphasis is assigned to this stage and the processes that influence it when addressing issues of population connectivity in marine systems (Cowen and Sponaugle 2009). The zoeal duration of *C. brevimanus* is 13–22 days. Megalopae migrate onto land by around 16–18 days after metamorphosis at about 28 °C in rearing experiments (Hamasaki et al. 2014, 2015a; Kohno et al. 2014). Therefore, the larval dispersal duration of *C. brevimanus* is probably 4–5 weeks during the reproductive season in summer in Japan. The larval growth and development patterns of *C. brevimanus* were initially larger larvae and smaller growth increments: a shorter pathway in the coenobitid crabs (Hamasaki et al. 2015a). Therefore, their population networks through larval dispersals are expected to be limited. However, Hamasaki et al. (2015b) reported no evidence for population genetic structure and isolation by distance in the samples collected from Ishigakijima Island, Guam Island, Peleliu Island, or Peniou Island within their wide geographic distribution throughout the Indo-Pacific (Sect. 1.1.5).

In addition to the genetic markers, analyzing dispersion in the waters of plankton larvae numerically using biophysical models is effective as a method to study

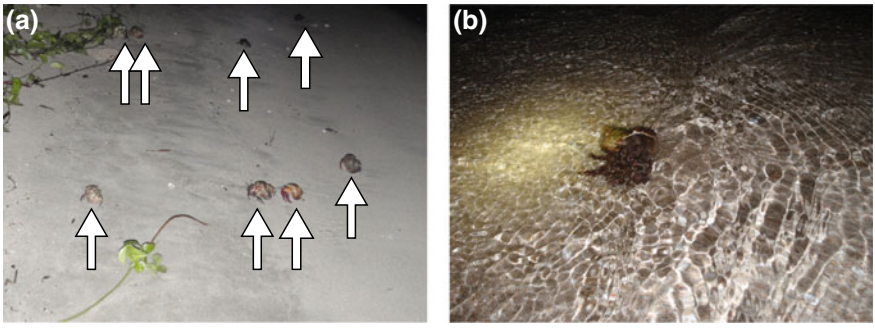

Fig. 16.1 Sequence of larval release of female *Coenobita brevimanus*. Some ovigerous females (arrows) started descending from the vegetation behind shore (**a**). An ovigerous female immersion of the body in seawater to release the larvae (**b**)

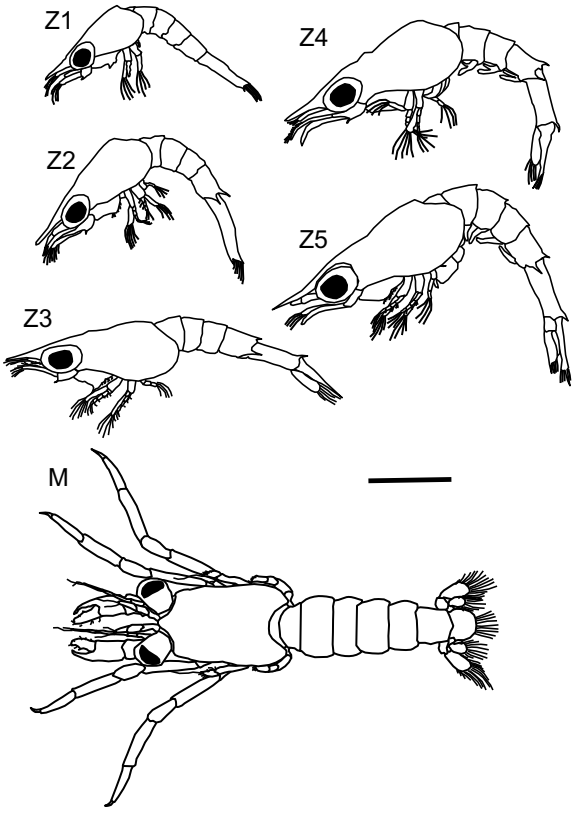

Fig. 16.2 Five zoeal stages (Z1–Z5) and megalopa (M) of *Coenobita brevimanus* (referred from Kohno et al. 2014). Scale bar = 1 mm

population network of marine species (Cowen and Sponaugle 2009). The larval releases of the land hermit crabs are synchronized with lunar and tidal rhythms (Nakasone 2001; Nio et al. 2014; Doi et al. 2016, 2018). Spatial and temporal data of larval release are important parameters that determine the survival and transportation of early larvae. Fortunately, the larval release of semiterrestrial crustaceans is accompanied by seaward migration to the coast. For that reason, it can be observed easily.

Therefore, Murakami et al. (2014) used ecological facts of larval release obtained using field observations (Nio et al., 2019) as parameters of particle tracing by the Lagrangian method and high-resolution Coastal ocean Current Model (CCM) (Chap. 3). They estimated the dynamic state of *C. brevimanus* larvae. We review this study (Murakami et al. 2014) in this chapter.

16.2 Materials and Methods

16.2.1 Study Site

The field study was conducted on a sandy beach and dune plant areas in Amitori on the northwestern part of Iriomote Island (24°24′ N, 123°46′ E; see also Sects. 1.1 and 1.2, and Fig. 1.1), located on the southern Ryukyu Islands, Japan. A dense population composed of large individuals of *C. brevimanus* is found inside and around Amitori (Mizutani and Kohno 2012; Doi et al., 2019; see also Sect. 1.6). The sampling area was located on the sandy beach near the Amitori (hereinafter designated as Amitori beach) measuring 300-m long.

16.2.2 Visual Observation

During May–November 2009, a single researcher walked and searched crabs on a sandy beach along a 300-m-long shoreline in Amitori (Fig. 16.3a) every two hours from the sunset until next morning at 6:00. The times and locations at which the crabs were found were recorded. The anterior and whole parts of crabs were photographed.

During May–December 2010, the crabs that migrated on a selected 180-m-long shoreline of the beach were observed by two researchers on the artificial revetment neighboring the beach from the sunset until 00:00. This occurred because most crabs migrated to the beach near the revetment between sunset and 00:00 in the 2009 survey. Some behavioral patterns by the individual crabs on the beach were observed. Before the crabs walked back to the dune plants, the anterior and whole parts of crabs were photographed. The times when the crabs entered into the sea were recorded on selected days in the new moon periods.

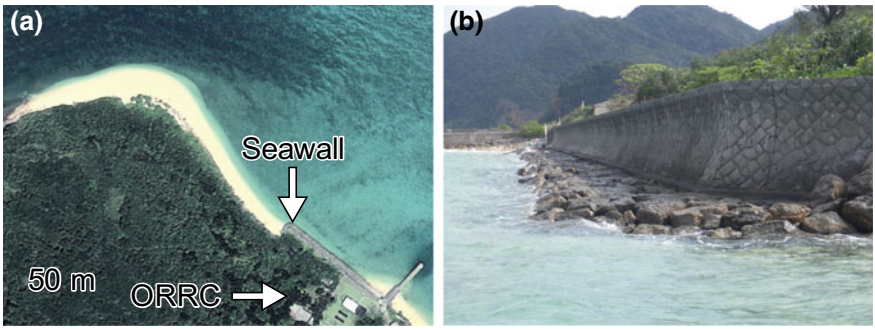

Fig. 16.3 Study site and the flaring shaped seawall. Location of the study site on Amitori Beach near Okinawa Regional Research Center (ORRC) of Tokai University (**a** Map data © 2018 Google). Photograph of the flaring shaped seawall (**b**)

16.2.3 Ocean Model and Particle Tracking

The measurements of wind velocity, wind direction, and river flow rate, and astronomical tide computed with the NAO model (Matsumoto et al. 2000) were given to the Coastal ocean Current Model with a multi-sigma coordinate system (CCM) (Chap. 3), and seawater current in Amitori Bay on July 10–30, 2010 was reproduced. The average wind speed and the most frequent wind direction during this period were 2.7 m and south–southeast, respectively, representing the average meteorological conditions in Amitori Bay in summer, with no weather event such as a typhoon (Sect. 1.3).

Zoea larvae under the reproduced seawater current field were tracked using the Lagrange method (Chap. 3). The sites and times of their release were set as values observed by field survey. 500 individual larvae were treated as one particle. Tracking computations of each particle were conducted for 16 days until the end of the larval stage. Murakami et al. (2014) took no account of the sinking and swimming abilities of larvae. It was estimated that a total of 780,000 larvae were released in the larval release by 39 individuals of *C. brevimanus* observed on 10–14 July 2010. The calculation period was set to July 30, for the zoeal duration of 16 days (Hamasaki et al. 2014; Kohno et al. 2014).

The megalopae of *Coenobita* land on the seashore (Hamasaki et al. 2014, 2015a; Kohno et al. 2014). However, the collected population of juveniles of *C. brevimanus* is so modest that it is unknown what kind of environment larvae choose as a settlement site. Murakami et al. (2014) defined the seashore of the release site of larvae as a return site (Fig. 16.3a) and assumed the number of larvae that lingered there at the end of a calculation period as the amount of recruitment, inspired by the fact that young crabs of the close species of the same genus immediately after landing were found near the habitat of their adults.

16.3 Results and Discussion

16.3.1 Larval Release

The coast in front of the Amitori Village was covered by the flaring shaped seawall with a gentle slope (Fig. 16.3b). Because the hermit crabs cannot descend or ascend the seawall, many females migrated and released the larvae near the wall's western edge (Fig. 16.4). A total of 1546 individuals of *C. brevimanus* were observed to migrate in the sandy beach during the two-year research period (Fig. 16.5). The occurrence period was between 10 May and 21 October in 2009 (n = 639) and between 13 May and 7 November in 2010 (n = 907). The beginning of the main migrating season was July, but the season ended on September in 2009 and October in 2010 (only one individual was found on five research days on November in 2010). The monthly number of seaward migrating crabs increased drastically from

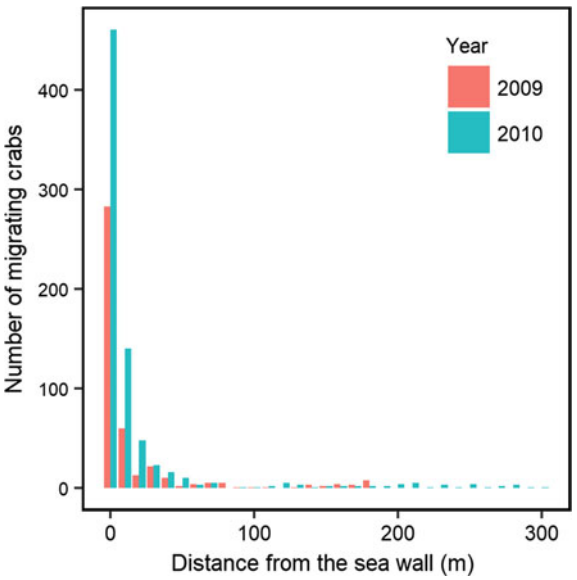

Fig. 16.4 Relation between the number of seaward migrating crabs and distance (m) from the seawall

July, peaked in August and/or September. It then decreased abruptly in October or November. The daily number of seaward migrating crabs varied according to the tidal phase and lunar age.

In the spring tide around the new moon phase, 0–68 (mean ± SD, 12.6 ± 17.3) crabs occurred in 2009 (n = 39 days) and 0–84 (17.0 ± 15.3) in 2010 (n = 47 days). In the spring tide around the full moon phase, 0–18 (2.8 ± 4.1) crabs occurred in 2009 (n = 35 days) and 0–10 (2.2 ± 2.0) in 2010 (n = 36 days). During neap tides, 0–19 (2.3 ± 4.6) crabs occurred in 2012 (n = 48 days) and 0–7 (2.5 ± 1.8) in 2013 (n = 13 days).

The time ranges of larval release by *C. brevimanus* were 19:00–22:50 in 2010 (Fig. 16.6). Larval release occurred only after sunset. The time shifted slightly from earlier hours to later hours, except for September. The timing of larval release coincided well with high tide in the earlier days of the larval releasing period of each month, but in the later days, it occurred almost always before nocturnal high tides.

Timing of the reproductive activities in intertidal and supratidal brachyuran crabs has been well studied (Forward 1987; Morgan 1995; Christy 2003, 2011), suggesting that the most common pattern is for larval hatching to occur at night during high tide on larger-amplitude tides on a biweekly or monthly cycle of tidal amplitude (Christy 2011). The adaptive significance of this pattern was believed to be that by moving quickly to the ocean at night; larvae might escape visual detection by planktivorous fishes that are especially abundant in shallow waters (Christy 2003).

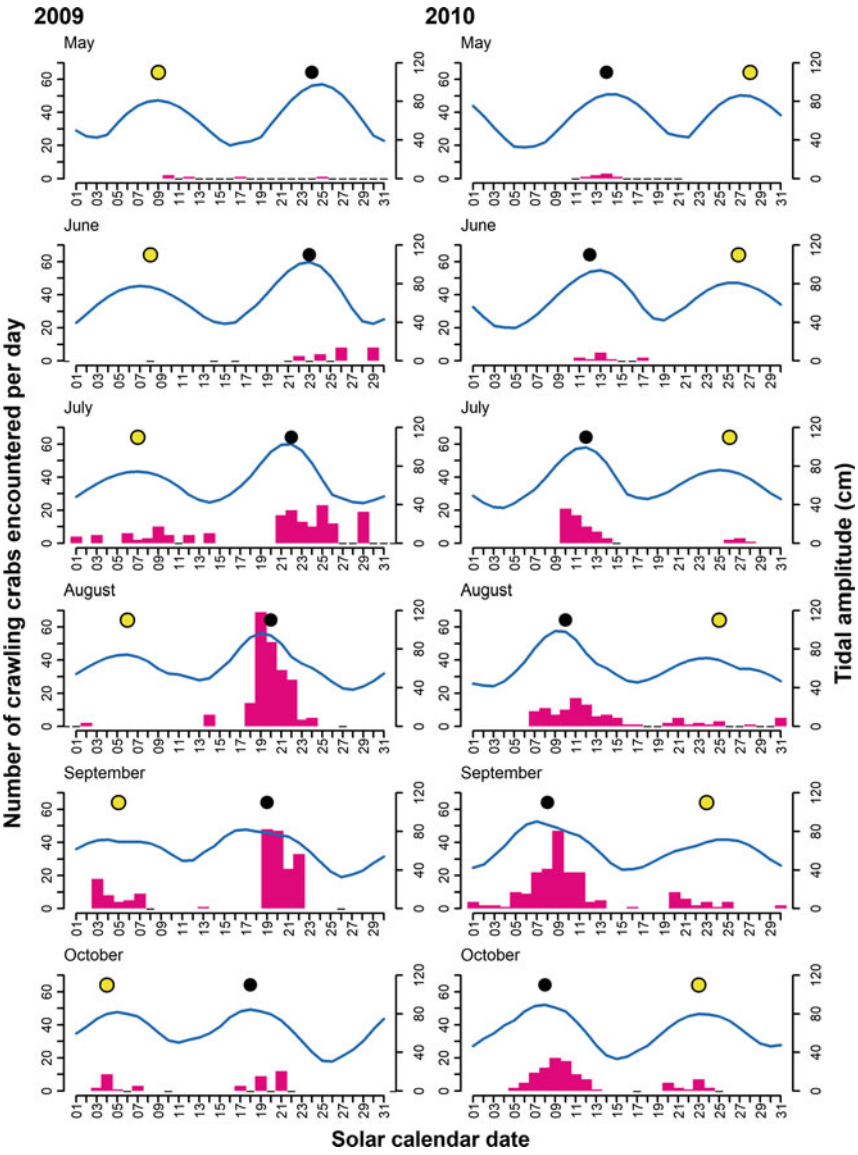

Fig. 16.5 Temporal changes in the number of crawling individuals of *Coenobita brevimanus* at Amitori beach, Iriomote Island, Japan during May–October 2009 and 2010. Black bars represent no crabs observed. Solid blue lines represent the maximum tidal amplitude. Yellow and closed circles, respectively, represent the full moon and the new moon. *Data source* Nio et al. (2019)

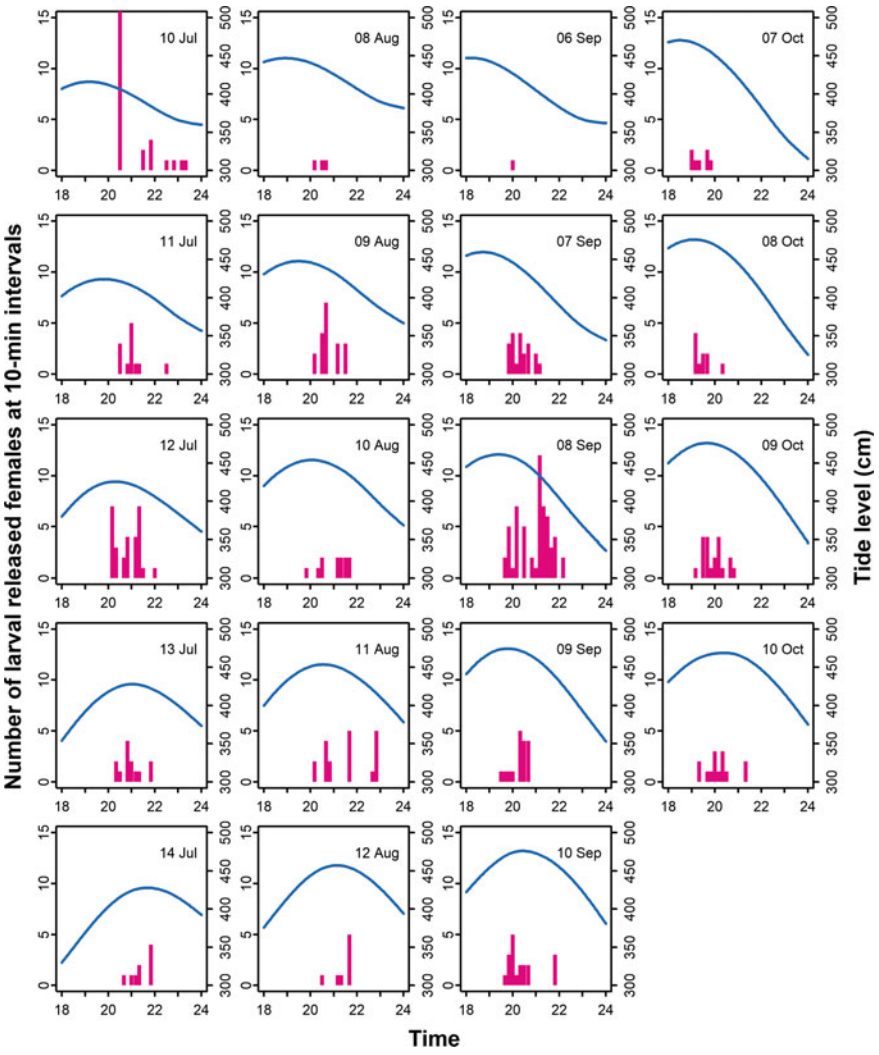

Fig. 16.6 Number of *Coenobita brevimanus* individuals releasing larvae at 10-min intervals and temporal changes of tidal levels in the Amitori Beach, Iriomote Island, Japan during the new moon periods during July–October 2010. *Data source* Nio et al. (2019)

16.3.2 Numerical Analysis

The dynamic state of larvae at 9:00 on July 30, 2010 is presented in Fig. 16.7, which indicates that almost all individuals of zoeae released from ovigerous females on the Amitori coast were conveyed northward toward the open sea. For larvae that settled on the seashore to migrate onto land, shell resources suitable for their small

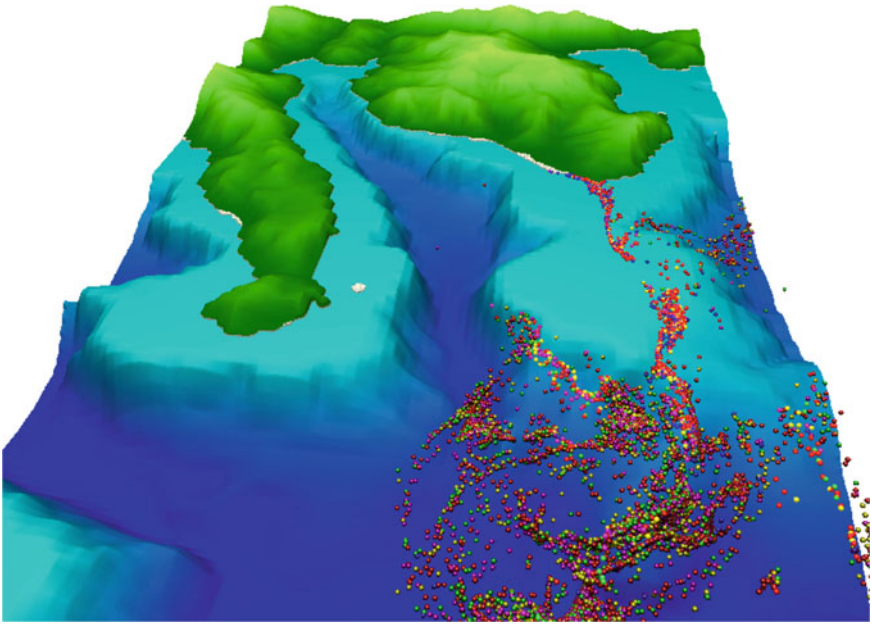

Fig. 16.7 Dynamics of the larvae of *Coenobita brevimanus* at 09:00 on July 30, 2010. The colors of particles represent the date of release: green, yellow, red, pink, and blue, respectively, denote 10–14 July (modified from Murakami et al. 2014)

bodies are fundamentally important. It is also necessary to exchange their shells suitable for their body size at their subsequent growth. For that reason, larvae are expected to settle near a larvae release site where middle-sized and large individuals of *C. brevimanus* reside. Murakami et al. (2014) defined sites presented in Fig. 16.3a as the vicinity of the release site and analyzed the temporal change of the population of the larvae that lingered there. As Fig. 16.8 shows, larval release was observed on July 10–14, incidentally on the spring tide.

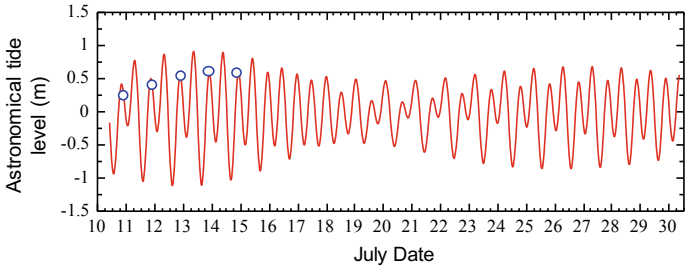

Fig. 16.8 Temporal changes of astronomical tide level between 10 July and 30 July 2010 in Amitori Bay (modified from Murakami et al. 2014). Blue circles represent the time at which larval release occurred

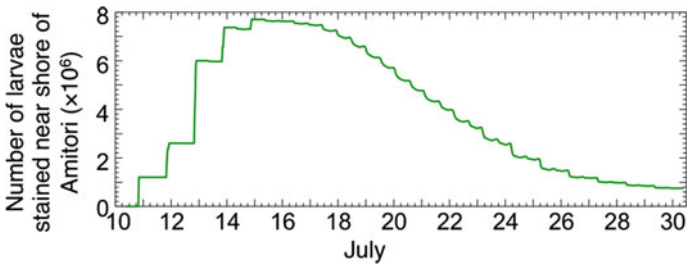

Fig. 16.9 Daily changes of number of larvae stained in the area near the place where the larval release occurred (modified from Murakami et al. 2014)

Larval release was conducted continuously during July 10–14. The number of larvae lingering near the release site increased: 76,999,000 larvae accumulated at the peak (Fig. 16.9). The number of staying larvae declined monotonously, showing a slight increase or decrease on and after July 15 when no subsequent larval release was conducted. This pattern suggests a very low probability that larvae which once left the release site would return, although larvae move in and out around the release site along with the tidal rhythms.

Next, the low probability of larvae that once left the release site would return was examined based on physical factors. The mean sea level current velocity during the calculation period is presented in Fig. 16.10, which exhibits that a northward current toward the open sea prevails in the seawater current field during this period. As described above, the most frequent wind direction during the calculation period was south–southeast, by which the current field was affected. This northward current conveys larvae to the open sea from the release site, although it makes it difficult for larvae drifted from the release site to the open sea to return to the original release site. Consequently, the larvae observed near the release site are regarded as having stayed near the release site.

Figure 16.11 shows the relation between lapsed days from larval release and a stay ratio. The stay ratio was 96% four days after larval release during the larval distribution to the surface layer had been observed. It then decreased to an average of 66% eight days after the release when the zoeal stage of migration to the lower layer was completed. It declined to 11% on the 16th when the zoeal stages finished. These estimates do not include wear by predation. Many individuals are assumed to be conveyed outside the vicinity of the release site. This result agrees with the fact that the population of these species is hereditarily identical. The population of *C. brevimanus* at Amitori is regarded as important as a supply source of its larvae to other regions because the population includes many large individuals.

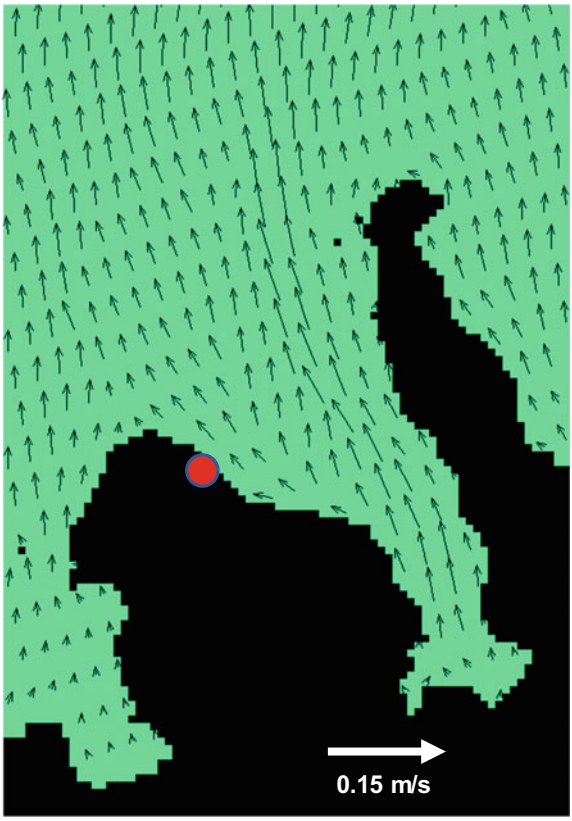

Fig. 16.10 Mean sea surface current (m/s) during particle tracking experiments (referred from Murakami et al. 2014). Red circles represent the location where larval release occurred

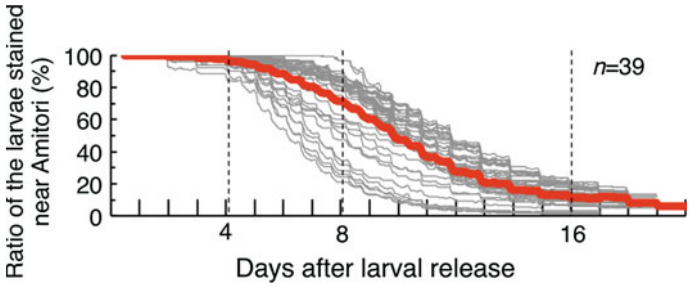

Fig. 16.11 Relation between days after larval releasing and ratio of the larvae stained near Amitori. Redline represents the mean value (modified from Murakami et al. 2014)

16.3.3 Conclusion

The dynamic state of larvae has been elucidated in this study with an ocean model and the particle tracking method, using as a parameter the spatiotemporal pattern of larval release of *C. brevimanus* determined by field observation. About 10% of the larvae were consumed for self-recruitment. The other larvae were conveyed to the outside of Amitori Bay. It will be necessary for our future study to elucidate the dynamic state of larvae in a wide area including surrounding remote islands as well as in Amitori Bay, because many larvae drift away from the bay. It is also important to clarify the sinking, rising, and vertical movement of larvae by laboratory experimentation, to incorporate it into the model and to verify its accuracy by sampling of larvae.

References

Christy JH (2003) Reproductive timing and larval dispersal of intertidal crabs: the predator avoidance hypothesis. Rev Chil Hist Nat 76:177–185

Christy JH (2011) Timing of hatching and release of larvae by brachyuran crabs: patterns, adaptive significance and control. Integr Comp Biol 51:62–72

Cowen RK, Sponaugle S (2009) Larval dispersal and marine population connectivity. Ann Rev Mar Sci 1:443–466

Doi W, Mizutani A, Kohno H (2016) Larval release and associated tree-climbing behavior of the land hermit crab *Coenobita violascens* Heller, 1862 (Anomura: Coenobitidae). J Crustacean Biol 36:279–286

Doi W, Mizutani A, Kohno H (2018) Larval release rhythm of the land hermit crab *Coenobita cavipes* Stimpson, 1858 (Anomura, Coenobitidae) on Iriomote Island, Japan. Crustaceana 91:199–211

Doi W, Mizutani A, Yoshioka M, Kawai K, Kohno H (2019) Aspects of local population and gastropod shell use of the land hermit crab *Coenobita brevimanus* (Decapoda: Anomura) in Amitori, an abandoned village on Iriomote Island, Japan. Jpn J Benthology 73:75–83 (in Japanese with English abstract)

Forward RBJ (1987) Larval release rhythms of decapod crustaceans: an overview. Bull Mar Sci 41:165–176

Hamasaki K, Kato S, Hatta S, Murakami Y, Dan S, Kitada S (2014) Larval development and emigration behaviour during sea-to-land transition of the land hermit crab *Coenobita brevimanus* Dana, 1852 (Crustacea: Decapoda: Anomura: Coenobitidae) under laboratory conditions. J Nat His 48:1061–1084

Hamasaki K, Iizuka C, Ojima A, Sugizaki M, Sugimoto A, Dan S, Kitada S (2015a) Genetic diversity and demographic history of the terrestrial hermit crabs *Birgus latro* and *Coenobita brevimanus* in the North-Western Pacific Region. J Crustacean Biol 35:793–803

Hamasaki K, Kato S, Murakami Y, Dan S, Kitada S (2015b) Larval growth, development and duration in terrestrial hermit crabs. Sex Early Dev Aquat Organ 1:93–107

Kohno H, Jinno M, Mizutani A, Nio T (2014) The larval development, behavior and shell-selection of the land hermit crab *Coenobita brevimanus* Dana, 1852 (Crustacea: Decapoda: Anomura: Coenobitidae). Stud Rev Iriomote Is 2013:7–21 (in Japanese)

Matsumoto K, Takanezawa T, Ooe M (2000) Ocean tide models developed by assimilating TOPEX/POSEIDON altimeter data into hydrodynamical model: a global model and a regional around Japan. J Oceanogr 56:567–581

Mizutani A, Kohno H (2012) Distribution of *Coenobita brevimanus* in Amitori, Iriomote Island. Stud Rev Iriomote Is 2011:30–39 (in Japanese)

Morgan SG (1995) The timing of larval release. In: McEdward L (ed) Ecology of marine invertebrate larvae. CRC Press, Florida

Murakami T, Kohno H, Mizutani A, Jinno M, Shimokawa S (2014) Particle tracking analysis of larvae of land hermit crab *Coenobita brevimanus* in Amitori Bay, Iri-omote Island, Japan. J Japan Soc Civil Eng B2(70):1136–1140 (in Japanese with English abstract)

Nakasone Y (2001) Reproductive biology of three land hermit crabs (Decapoda: Anomura: Coenobitidae) in Okinawa, Japan. Pac Sci 55:157–169

Nio T, Doi W, Mizutani A, Kohno H (2019) Seaward migration and larval release of the land hermit crab *Coenobita brevimanus* Dana, 1852 (Anomura: Coenobitidae) on Iriomote Island, Japan. Crust Res 48:67–80

Nio T, Suguri A, Mizutani A, Doi W, Kohno H (2014) Emergence of the mole crab *Hippa marmorata* around the land hermit crab *Coenobita brevimanus* releasing larvae. Cancer 23:39–42 (in Japanese)